Chapter 4. Examination of Tsunami Propagation Calculations

4.1. Governing equations and numerical scheme

4.1.1. Governing equations and numerical scheme for near-field tsunami propagation

The governing equations and numerical schemes based on the method proposed by Goto (Goto and Ogawa, 1982) are shown below.

(1) Governing equations

1) Continuity equation

$$\frac{\partial \eta}{\partial t} + \frac{\partial M}{\partial x} + \frac{\partial N}{\partial y} = 0$$

2) Momentum equations

$$\frac{\partial M}{\partial t} + \frac{\partial}{\partial x}\left(\frac{M^2}{D}\right) + \frac{\partial}{\partial y}\left(\frac{MN}{D}\right) + gD\frac{\partial \eta}{\partial x} - K_h\left(\frac{\partial^2 M}{\partial x^2} + \frac{\partial^2 M}{\partial y^2}\right) + \gamma_b{}^2 \frac{M\sqrt{M^2+N^2}}{D^2} = 0$$

$$\frac{\partial N}{\partial t} + \frac{\partial}{\partial x}\left(\frac{MN}{D}\right) + \frac{\partial}{\partial y}\left(\frac{N^2}{D}\right) + gD\frac{\partial \eta}{\partial y} - K_h\left(\frac{\partial^2 N}{\partial x^2} + \frac{\partial^2 N}{\partial y^2}\right) + \gamma_b{}^2 \frac{N\sqrt{M^2+N^2}}{D^2} = 0$$

where x and y are horizontal axes, t is time, η is the vertical displacement of water surface above the still water surface, M and N are the flow rate per unit width in the x and y directions, h is the still water depth, D is total water depth ($D = h + \eta$), g is the gravitational acceleration, K_h is horizontal eddy viscosity coefficient, $\gamma_b{}^2$ is friction coefficient ($= gn^2 / D^{1/3}$), n is Manning's coefficient of roughness.

(2) Numerical scheme

An overview of numerical scheme is given below.

- The time integration scheme is principally based upon the Leap-frog method.
- The arrangement of variables is based on the staggered grid (Figures 4.1.1-1 and 4.1.1-2).
- The primary upwind difference method is used for conservative advection terms.
- Friction terms are implicitly approximated for stable of calculation.

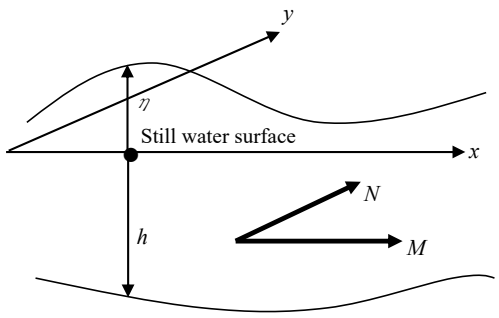

Figure 4.1.1-1 The arrangement of variables

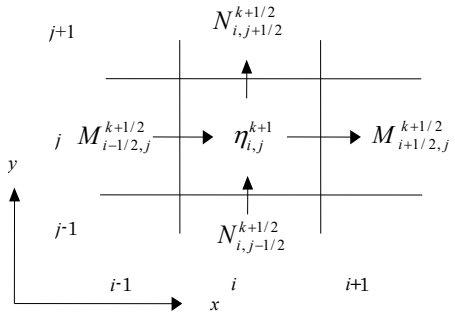

Figure 4.1.1-2 The point schematics for the staggered grid

(3) Truncation error

For simplicity, when the governing equations are:

$$\frac{\partial \eta}{\partial t}+\frac{\partial M}{\partial x}=0$$

$$\frac{\partial M}{\partial t}+\frac{\partial}{\partial x}\left(\frac{M^2}{D}\right)+gD\frac{\partial \eta}{\partial x}=0$$

Then truncation error is given using the following equations.

$$\frac{\partial \eta}{\partial t}+\frac{\partial M}{\partial x}+\frac{1}{24}\underbrace{\left\{(\Delta t)^2\frac{\partial^3 \eta}{\partial t^3}+(\Delta x)^2\frac{\partial^3 M}{\partial x^3}\right\}}_{\text{A}}=0$$

$$\frac{\partial M}{\partial t}+\frac{\partial}{\partial x}\left(\frac{M^2}{D}\right)+gD\frac{\partial \eta}{\partial x}+\frac{1}{24}\underbrace{\left\{(\Delta t)^2\frac{\partial^3 M}{\partial t^3}+gD(\Delta x)^2\frac{\partial^3 \eta}{\partial x^3}\right\}}_{\text{B}}-\underbrace{\Delta x\left|\frac{M}{D}\right|\frac{\partial^2 M}{\partial x^2}}_{\text{C}}=0$$

A and B, which are underlined in the above equation, are numerical variance terms, and C is the numerical viscosity term. Numerical viscosity term C is derived from the advection term and functions so that wave height does not attenuate, and its effect also increases the greater $\triangle x$ becomes. The numerical variance terms have a greater effect when there is significant forward tilting of the wave.

4.1.2. Governing equations and numerical schemes for far-field propagation of tsunamis

(1) Governing equations

The linear Boussinesq theory (Boussinesq, 1872), which takes into account Coriolis force, is used.

1) Continuity equation

$$\frac{\partial \eta}{\partial t}+\frac{1}{R\cos\lambda}\left[\frac{\partial(M\cos\lambda)}{\partial\lambda}+\frac{\partial N}{\partial\phi}\right]=0$$

2) Momentum equations

$$\frac{\partial M}{\partial t}+\frac{gh}{R}\frac{\partial \eta}{\partial \lambda}=-fN+\frac{1}{R}\frac{\partial}{\partial\lambda}\left[\frac{h^3}{3}F\right]$$

$$\frac{\partial N}{\partial t}+\frac{gh}{R\cos\lambda}\frac{\partial \eta}{\partial \phi}=fM+\frac{1}{R\cos\lambda}\frac{\partial}{\partial\theta}\left[\frac{h^3}{3}F\right]$$

However,

$$F=\frac{1}{R\cos\lambda}\left[\frac{\partial^2}{\partial t\partial\lambda}(u\cos\lambda)+\frac{\partial^2 v}{\partial t\partial\phi}\right]$$

$$u=M/\ (\eta+h), v=N/\ (\eta+h)$$

where, λ and ϕ are latitude and longitude, η is the vertical displacement of water surface above the still water surface, M and N are the flow rate per unit width in the λ and ϕ directions, h is still water depth, g is the gravitational acceleration, f is Coriolis coefficient, and R is Earth's radius.

(2) Numerical scheme

In accordance with Goto and Sato (1993) and Goto et al. (1988) are shown below.

- Arrangement of variables: Staggered mesh
- Time integration scheme: Implicit method

4.1.3. Dispersive wave theory

(1) Linear dispersive wave theory

In cases where the conditions for hydraulic quantities are:

- Wave height-water depth ratio $\varepsilon=\eta/h\ll1$
- Relative water depth $\sigma=h/L\ll1$
- Ursell number $U_r=\varepsilon/\sigma^2\ll1$

Then, the linear Boussinesq equations are used as shown below.

$$\frac{\partial \eta}{\partial t}+\frac{\partial M}{\partial x}+\frac{\partial N}{\partial y}=0$$

$$\frac{\partial M}{\partial t}+gh\frac{\partial \eta}{\partial x}=\frac{\partial}{\partial x}\left(\frac{h^3}{3}Q_1\right)-\frac{\partial h}{\partial x}\left(\frac{h^2}{2}Q_1\right)$$

$$\frac{\partial N}{\partial t}+gh\frac{\partial \eta}{\partial y}=\frac{\partial}{\partial y}\left(\frac{h^3}{3}Q_1\right)-\frac{\partial h}{\partial y}\left(\frac{h^2}{2}Q_1\right)$$

where, $Q_1 = \dfrac{\partial^2 \overline{u}}{\partial t \partial x} + \dfrac{\partial^2 \overline{v}}{\partial t \partial y}$

(2) Nonlinear dispersive wave theory

In cases where the conditions for hydraulic quantities are:

- Wave height-water depth ratio $\varepsilon=\eta/h \ll 1$
- Relative water depth $\sigma=h/L \ll 1$
- Ursell number $U_r=\varepsilon/\sigma^2 \sim 1$

Then, the equations of Peregrine (1967) are used as shown below.

$$\frac{\partial \eta}{\partial t} + \frac{\partial M}{\partial x} + \frac{\partial N}{\partial y} = 0$$

$$\frac{\partial M}{\partial t} + \frac{\partial}{\partial x}\left(\frac{M^2}{D}\right) + \frac{\partial}{\partial y}\left(\frac{MN}{D}\right) + g(h+\eta)\frac{\partial \eta}{\partial x} = \frac{\partial}{\partial x}\left(\frac{h^3}{3}Q_1 + \frac{h^2}{2}Q_2\right) - \frac{\partial h}{\partial x}\left(\frac{h^2}{2}Q_1 + hQ_2\right)$$

$$\frac{\partial N}{\partial t} + \frac{\partial}{\partial x}\left(\frac{MN}{D}\right) + \frac{\partial}{\partial y}\left(\frac{N^2}{D}\right) + g(h+\eta)\frac{\partial \eta}{\partial y} = \frac{\partial}{\partial y}\left(\frac{h^3}{3}Q_1 + \frac{h^2}{2}Q_2\right) - \frac{\partial h}{\partial y}\left(\frac{h^2}{2}Q_1 + hQ_2\right)$$

where,

$$Q_1 = \frac{\partial^2 \overline{u}}{\partial t \partial x} + \frac{\partial^2 \overline{v}}{\partial t \partial y}$$

$$Q_2 = \frac{\partial}{\partial t}\left(\overline{u}\frac{\partial h}{\partial x}\right) + \frac{\partial}{\partial t}\left(\overline{v}\frac{\partial h}{\partial y}\right)$$

Moreover, in cases where

- Wave height-water depth ratio is $\varepsilon=\eta/h \sim 1$
- Relative water depth is $\sigma=h/L \ll 1$
- Ursell number is $U_r=\varepsilon/\sigma^2 \gg 1$

Then, the equations of Goto (1984) are used as shown below.

$$\frac{\partial \eta}{\partial t} + \frac{\partial M}{\partial x} + \frac{\partial N}{\partial y} = 0$$

$$\frac{\partial M}{\partial t} + \frac{\partial}{\partial x}\left(\frac{M^2}{D}\right) + \frac{\partial}{\partial y}\left(\frac{MN}{D}\right) + g(h+\eta)\frac{\partial \eta}{\partial x}$$

$$= \frac{\partial}{\partial x}\left(\frac{(h+\eta)^3}{3}H_1 + \frac{(h+\eta)^2}{2}H_2\right) - \frac{\partial h}{\partial x}\left(\frac{(h+\eta)^2}{2}H_1 + (h+\eta)H_2\right)$$

$$\frac{\partial N}{\partial t} + \frac{\partial}{\partial x}\left(\frac{MN}{D}\right) + \frac{\partial}{\partial y}\left(\frac{N^2}{D}\right) + g(h+\eta)\frac{\partial \eta}{\partial y}$$

$$= \frac{\partial}{\partial y}\left(\frac{(h+\eta)^3}{3}H_1 + \frac{(h+\eta)^2}{2}H_2\right) - \frac{\partial h}{\partial y}\left(\frac{(h+\eta)^2}{2}H_1 + (h+\eta)H_2\right)$$

where,

$$H_1 = \left(\frac{\partial}{\partial t} + \overline{u} \frac{\partial}{\partial x} + \overline{v} \frac{\partial}{\partial y} \right) \left(\frac{\partial \overline{u}}{\partial x} + \frac{\partial \overline{v}}{\partial y} \right) - \left(\frac{\partial \overline{u}}{\partial x} + \frac{\partial \overline{v}}{\partial y} \right)^2$$

$$H_2 = \left(\frac{\partial}{\partial t} + \overline{u} \frac{\partial}{\partial x} + \overline{v} \frac{\partial}{\partial y} \right) \left(\overline{u} \frac{\partial h}{\partial x} + \overline{v} \frac{\partial h}{\partial y} \right)$$

4.1.4. Examination of dispersibility

4.1.4.1. Examination of tsunami numerical models accounting for dispersibility and wave breaking

When a tsunami propagates across a gently shelving coastline, the wave crest may fragment. This is known as soliton fission, which results from the effects of the wave's nonlinearity and dispersibility. When soliton fission occurs, the height of the tsunami wave is further amplified and it turns into a wave breaking later on. Matsuyama et al. (2005) conducted shallow water deformation hydraulic model experiments of tsunami along gently shelving coastlines to ascertain the characteristics of soliton fission phenomena and wave breaking Using these results, Matsuyama et al. (2006) reviewed the applicability of variance terms and made improvements in the wave breaking model.

(1) Experiments on soliton fission and wave breaking (Matsuyama et al., 2005)

Matsuyama et al. (2005) reproduced tsunami soliton fission using non-distortion experiments simulating a continental shelf to ascertain phenomena near wave breaking and examine wave breaking conditions, and then, using water level time-series data from experiment results, proposed a method for calculating the ratio of water surface current velocity to wave velocity, which is shown below, and the water surface slope as indicators of the wave breaking threshold.

$$\frac{u_S}{c} = \frac{\eta}{D} - \frac{h}{3Dc^2} \left\{ D \frac{\partial^2 \eta}{\partial t^2} - 2 \left(\frac{\partial \eta}{\partial t} \right)^2 \right\}$$

where, t is time, η is the vertical displacement of water surface above the still water surface, u_s is water surface horizontal current velocity, h is still water depth, D ($=h+\eta$) is total water depth, and c is wave velocity.

The results of applications of experiment data show that the maximum water surface slope for the wave breaking threshold is between 20 and 50° and the ratio of the water surface flow current velocity to wave velocity is generally between 0.5 and 1.2, clearly indicating larger wave breaking threshold values than those previously used.

(2) Variance term

When numerical calculations were conducted of variance term DT in a nonlinear dispersive

wave equation using a one-dimensional cross-section and comparisons made of spatial tsunami shape error and wave form just prior to breaking, it became clear that the use of variance terms proposed by Peregrine (1967) as well as Madsen and Sørensen (1992), which are given below, provides results approaching those obtained during experiments.

Peregrine (1967) : $DT = \frac{1}{3}h^2 \frac{\partial^3 M}{\partial t \partial x^2}$

Madsen and Sørensen (1992) : $DT = \frac{2}{5}h^2 \frac{\partial^3 M}{\partial t \partial x^2} + \frac{1}{15}gh^3 \left(\frac{\partial^3 \eta}{\partial x^3} \right)$

(3) Wave breaking model (Matsuyama et al., 2006)

To express the attenuation of breaking soliton fission waves, Iwase et al. (2001) and Sato (1995) incorporated a diffusion-type wave breaking attenuation term in the equation of motion. Iwase et al. (2001) indicated that amplification could not be reproduced of highly nonlinear waves where models for weak nonlinear dispersive waves exceed a ratio of 0.6 for the maximum water level to water depth. Then, Iwase et al. (2001) provided a negative diffusion coefficient just prior to the wave breaking to reproduce wave height amplification immediately prior to the wave breaking This model specifies the wave height amplification region just prior to the wave breaking and the attenuation region just prior to the wave breaking. However, it uses the ratio of maximum water level to water depth as an indicator for detecting the region giving the artificial amplification term, so there is a problem in that detection is delayed in the calculation with respect to leading waves preceded by drawback and the wave breaking are also delayed. So, Matsuyama et al. (2006) improved the detection indicator and diffusion coefficient. Figure 4.1.4-1 provides an overview of this. The points improved are described below.

As for the parameters for initiation of the artificial amplification term, the following parameters are used. Also, Split wave height H is used in place of the previously used water level for the representative length in the diffusion coefficient when the wave is breaking.

$$\omega = -\frac{D}{3}\frac{\partial^2 \eta}{\partial x^2}$$

$$\nu_\beta = \mu \sqrt{gD}\, H$$

where, ν_β is diffusion coefficient and μ is coefficient, and the values are determined by experiment data. ω_s is the non-dimensional curvature of the water surface across the entire water depth, and increases as soliton fission develops short-period waves. For wave height H, a large value is adopted from among the heights from the wave crests to wave troughs when a trough is cut out from troughs in split waves. These improvements have increased the reproducibility of soliton fission phenomena at the head of the leading wave after the backrush.

Reproducibility was the best when calculations were performed using the following values

which are based on parametric studies conducted of wave breaking locations and wave breaking heights (water levels) as well as upon experiment data from three parametric studies: ω_s when the artificial amplification term is initiated, coefficient μ for the artificial amplification term, and the wave breaking threshold γ ($=u_s/c$).

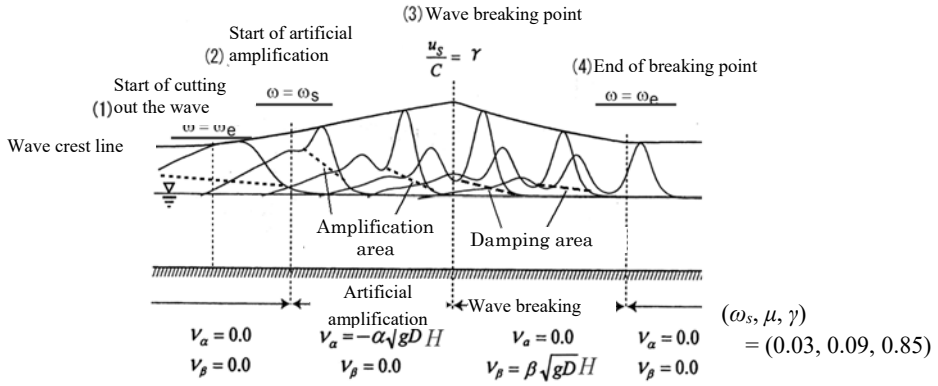

Figure 4.1.4-1 Improved model of wave breaking (JSCE, 2007)

4.1.4.2. Examination of the occurrence of dispersive waves

(1) Examination of dispersibility in deep sea areas

According to Iwase et al. (2002), when high-frequency content is included in the initial tsunami source, there are cases where wave number dispersibility may not be disregarded even for a tsunami that occurs in areas closer than 100km from shore. The effect of wave number dispersibility in deep-sea areas is attenuation of the water level of the first tsunami wave, and is expressed in the extension of wavelength and generation of a variance wave series. Iwase et al. (2002) proposed an indicator value I_D that quantitatively expresses the effect of this wave number dispersive effect.

$$I_D = \alpha\left(\bar{h}/W\right)^{\beta} \qquad (\alpha = 10^{1.76+0.001\delta},\ \beta = 1.28 - 0.005\delta)$$

where, $\bar{h}$ is the mean water depth at the tsunami source region, W is the fault width, and δ is the fault dip angle. Iwase et al. (2002) focused on the elongation rate of the length of the first wave, and stated that wave number dispersibility in deep-sea areas may be disregarded in cases where the indicated value is smaller than 1.

The water level is focused here and a parametric study was conducted by a one-dimensional propagation calculation using a nonlinear dispersive wave model and a nonlinear longwave model. The relationship among fault upper edge depth, sea bottom topography slope, slip amount and strike with respect to the indicator values is investigated and the applicability of the indicator values is examined.

1) Parameters accounting for variation

For the following parameters, their variations are taken into account. Those marked with a ● are items not included in the I_D indicator value equation proposed by Iwase et al. (2002).

■ Tsunami source location depth	:	1,000m, 2,000m
■ Fault width	:	15km, 50km, 100km
■ Dip angle	:	90°, 60°, 30° and 15°
● Sea bottom topography slope	:	1/100, 1/200
● Strike	:	0° (land-side hanging wall), 180° (land-side foot wall)
● Upper edge depth	:	1.0km, 2.5km, 4.0km
● Slip amount	:	4.0m, 7.0m

2) Computational region

Two patterns of sea bottom topography with slopes 1/100 and 1/200 are applied, and the land-side region extends up to location of a water depth of 150m (Figure 4.1.4-2).

3) Initial water level

The initial water level is set as the level of the central cross-section of the ground deformation distribution obtained by the method proposed by Mansinha and Smylie (1971).

4) Calculation results

Calculations are performed using the nonlinear dispersive wave model and nonlinear long-wave model, and a comparison made of chronological tsunami shapes at points where the water depth is 200m to find the correlation between the maximum water level ascent ratio (nonlinear long-wave / nonlinear dispersive wave) and the I_D.

First, the impact is verified that parameters, which are not included in the I_D, have on the water level at points where the water depth is 200m. With respect to the direction of fault dip angle, in cases where the land is a hanging wall, the results for the nonlinear wavelength model for all cases exceed the results for the nonlinear dispersive wave model (Figure 4.1.4-3a). With respect to slip amount, the distribution of the water level ratio is almost the same for cases of 4m and 7m (Figure 4.1.4-3b). With respect to the differences in sea bottom topography slope, no correlation with the I_D is observed (Figure 4.1.4-3c). With respect to the upper edge depth, a trend was observed: the deeper the edge became, the closer the ratio to 1, but no correlation with the I_D indicator value is observed (Figure 4.1.4-3d).

Figure 4.1.4-4 shows four patterns divided, according to size compared to the I_D of 1 and a 10% error in the water level ratio.The issue here is that, in the cases where the I_D is less than 1 and the water level ratio is greater than or equals to 10% respectively, the calculated water level is greater for the nonlinear long-wave model in most cases. Although the calculated water

levels are lower for the nonlinear long-wave model in several cases, the setting of these cases are not realistic because of a fault width of 100km and a dip angle of 60° (Table 4.1.4-1).

On the other hand, in several cases where the I_D and the water level ratio are greater than or equals to 1 and 10% respectively, there are cases that the calculated water level is smaller for the nonlinear long-wave model and the source setting is realistic.

Therefore, it is believed to be no issues present for the use of the I_D as an indicator for determining whether or not to take into account the effect of wave number distribution in deep-sea areas from the standpoint of the offshore water level.

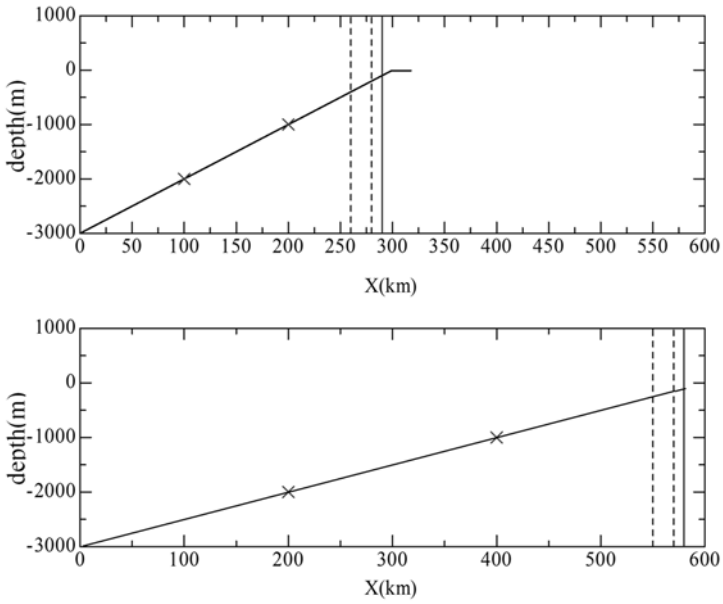

Figure 4.1.4-2 Computational Region

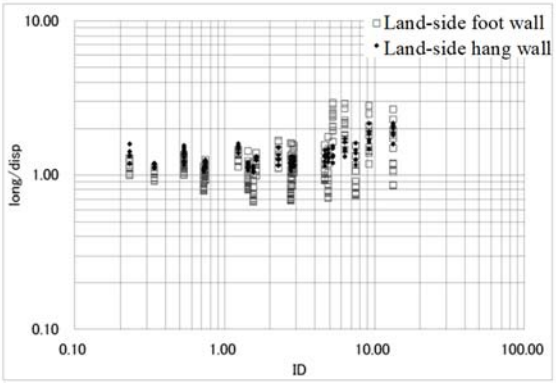

a Effect of the fault dip angle direction

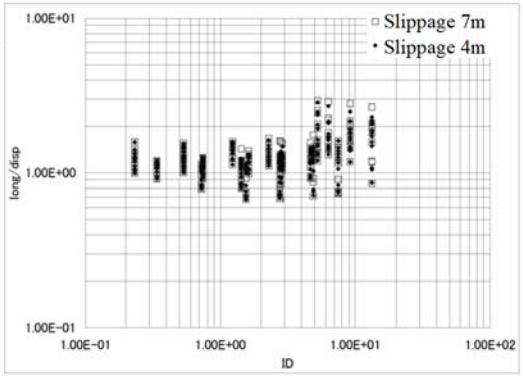

b Effect of the slip amount

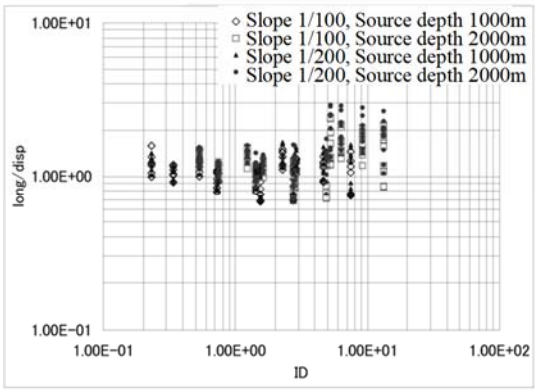

c Effect of the topography slope

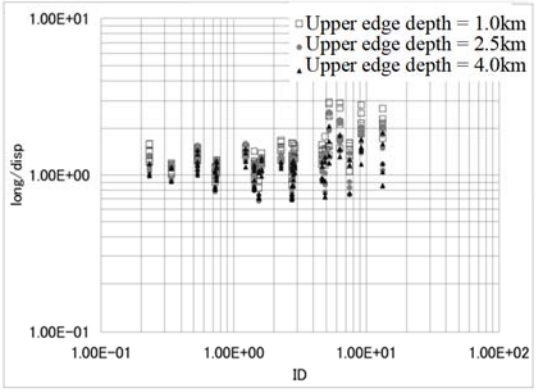

d Effect of the upper edge depth

*long/disp (Nonlinear long-wave model / Nonlinear dispersive wave model)

Figure 4.1.4-3 The relationship between the maximum depth ratio where the depth is 200m (Nonlinear long-wave model / Nonlinear dispersive wave model) and the I_D indicator value (1))

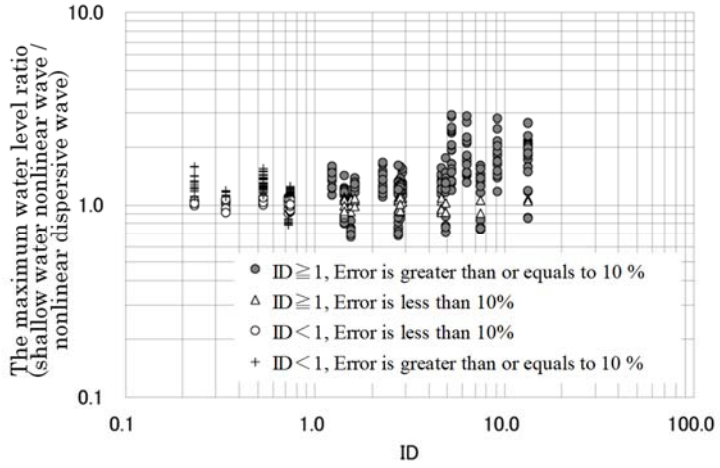

Figure 4.1.4-4 The relationship between the maximum water level ratio where the depth is 200m (Nonlinear long-wave model / Nonlinear dispersive wave model) and the I_D indicator value (2))

Table 4.1.4-1 The cases of which I_D is less than 1 and the maximum water level ratio is less than or equals to 0.9

*long/disp（Nonlinear long-wave model/Nonlinear dispersive wave model）

Source location depth(m)	Sea bottom topography slope	Width (km)	Slip amount (m)	Fault dip angle (°)	Direction of fault dip	Upper edge depth (km)	I_D	long/ disp
1,000	1/100	100	4	60	Land-side foot wall	2.5	0.72	0.79
						4		0.84
			7			2.5		0.79
						4		0.84
	1/200		4			2.5		0.81
						4		0.82
			7			2.5		0.84
						4		0.81

(2) Examination of grid partitioning for deep sea areas

Calculations are performed using a nonlinear dispersive wave model with a one-dimensional cross-section and varied grid sizes for a case in which variance waves occurred offshore, and then comparisons are conducted of spatial and chronological tsunami shapes at points having a water depth of 400m to examine grid partitioning in deep-sea areas.

1) Computational region

Figure 4.1.4-5 shows topography of the computational region for the examination of grid sizes in deep sea areas.

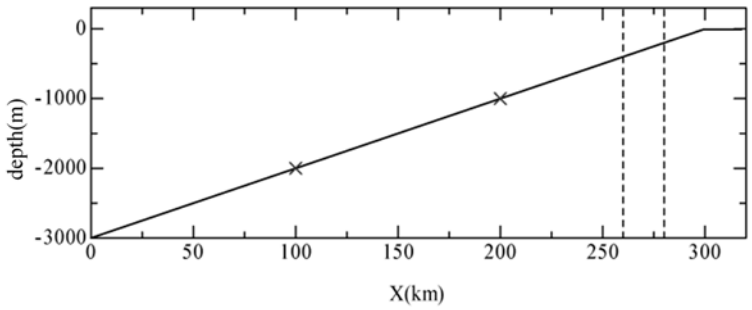

Figure 4.1.4-5 The computational region for the examination of grid sizes in deep sea areas

2) Tsunami source specifications, etc.

- Width 15km, dip angle 90°, slip angle 90°, slip amount 7m, upper edge depth 2.5km, initial movement of leading wave
- Sea bottom topography slope: 1/100
- Tsunami source location depth: 1,000m and 2,000m

3) Initial water level

The initial water level is set as the level of the central cross-section of the ground deformation distribution obtained by the method proposed by Mansinha and Smylie (1971).

4) Calculation cases (grid sizes)

Other than CASE 0, calculations are performed up to a water depth of 150m at fixed grid sizes for the entire region in all cases, and transmission conditions are set for the coastal boundary. CASE 0 is calculated up to the coastline.

CASE 0: 30m grids for water depths deeper than 80m
and 10m grids for water depths shallower than 80m
CASE 1: 1,600m grid
CASE 2: 800m grid
CASE 3: 400m grid
CASE 4: 200m grid
CASE 5: 1,920m grid
CASE 6: 960m grid
CASE 7: 480m grid
CASE 8: 240m grid

5) Calculation results

Comparisons are conducted focusing on the first wave of the main tsunami using 30m grids as the base case for spatial and chronological tsunami shape (Figures 4.1.4-6 and 4.1.4-7). The difference is small between tsunami shapes of 800m grids and 30m grids.

Next, wave height and inherent period for the main tsunami and variance waves are defined as shown in Figure 4.1.4-8 to find the water level and inherent period (peak to peak) from the first to the fifth waves (Table 4.1.4-2) and the ratios in comparison to CASE 0 are arranged in Table 4.1.4-3. The results show that the 800m grid (CASE 2) is within 5% for both the case of a tsunami source location depth of 1,000m at 0.96 and the case of a tsunami source location depth of 2,000m at 0.97. It is found that, in partitioning grids for deep sea areas, a 1,600m grid is too rough, but the precision may be assured if the grid is set at 800m.

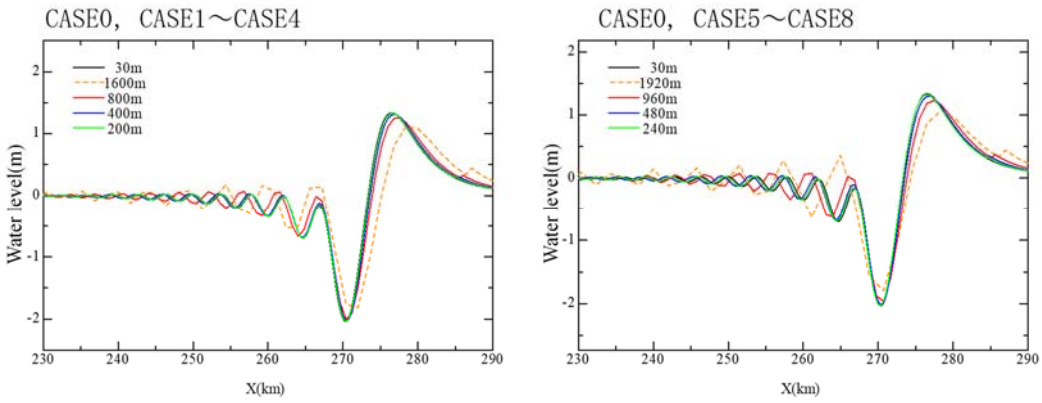

a) Spatial tsunami shapes after 1,000 second (Tsunami source location depth 1,000m)

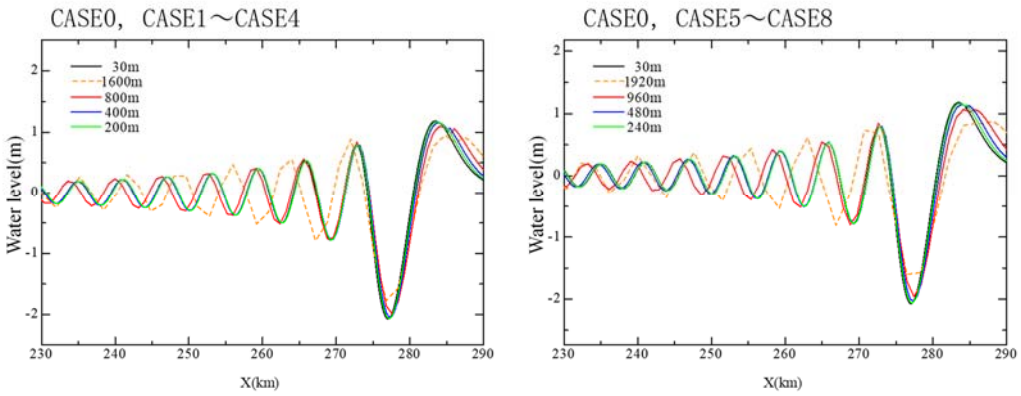

b) Spatial tsunami shapes after 2,000 seconds (Tsunami source location depth 2,000m)

Figure 4.1.4-6 Comparison of spatial tsunami shapes

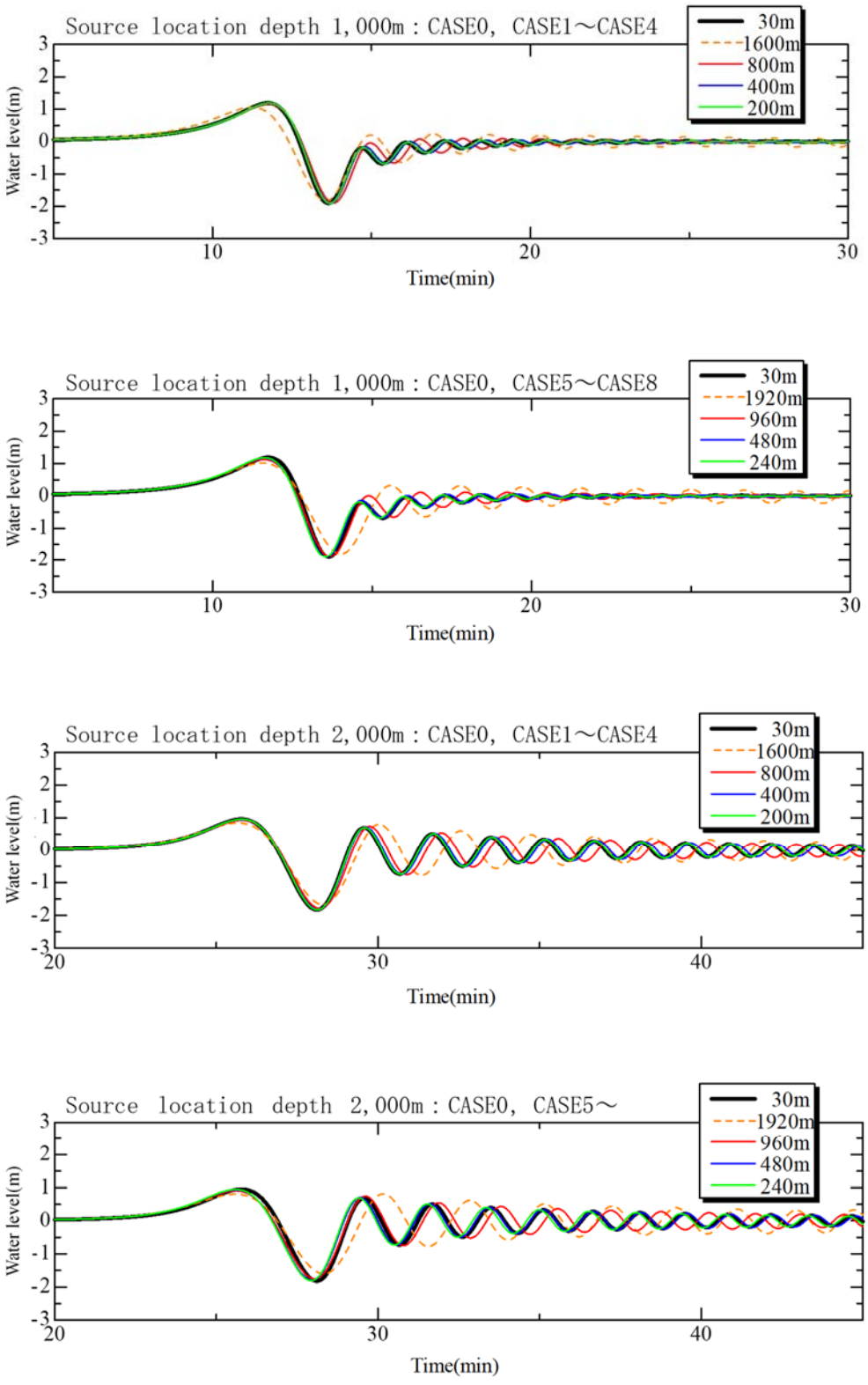

Figure 4.1.4-7 Chlonogical tsunami shapes at where the depth is 400m

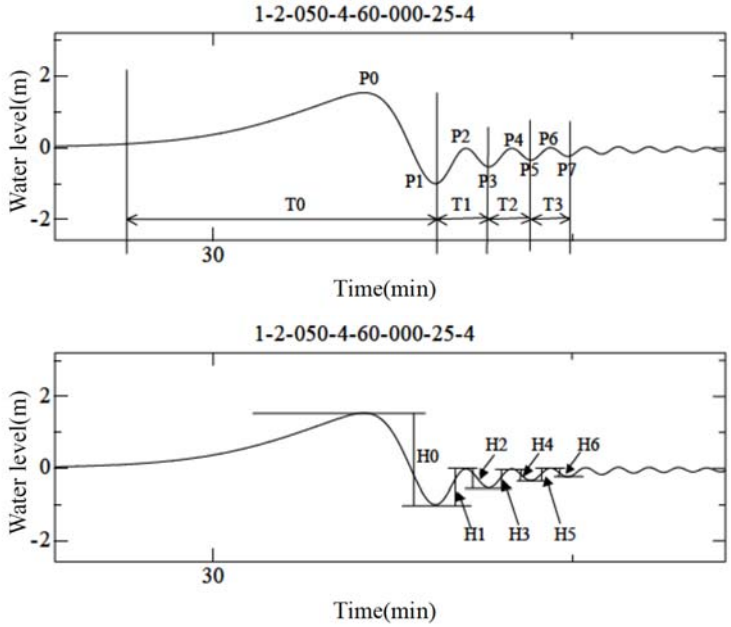

P0: Rise peak of the main tsunami

P1: The first inflection point since the water level went below zero after P0.

P2~P7: Peaks of dispersive waves after P1

T0: The elapsed time from the timing when water level first displaced by 10cm from the initial level, and P1

T1: The elapsed time between P1 and P3

T2: The elapsed time between P3 and P5

T3: The elapsed time between P5 and P7

T = (T1+T2+T3) /3 … Mean period of three dispersive waves

H0: Wave height of the main tsunami (P0-P1)

H1~H6: Wave heights of dispersive waves (|P(n+1)-P(n)|)

H = (H1+H2+H3+H4+H5+H6) /6 … Mean height of three dispersive waves

Figure 4.1.4-8 The definition of wave height and inferential period of the main tsunami and dispersive waves

Table 4.1.4-2 The water level and inherent period (peak to peak) from the first to the fifth waves

* Unit: Water level(m), Period(minutes)

Source location depth: 1,000m

	P1	P2	P3	P4	P5	T1	T2	T3	T4
CASE0	1.19	-0.20	-0.03	0.02	0.03	2.96	1.39	1.20	1.10
CASE1	1.06	0.20	0.24	0.22	0.20	3.76	1.97	1.74	1.62
CASE2	1.15	-0.04	0.08	0.09	0.09	3.21	1.56	1.36	1.25
CASE3	1.18	-0.15	0.00	0.04	0.05	3.03	1.43	1.24	1.14
CASE4	1.19	-0.19	-0.02	0.02	0.04	2.98	1.40	1.21	1.12
CASE5	1.02	0.32	0.32	0.28	0.25	4.03	2.19	1.95	1.83
CASE6	1.13	0.01	0.11	0.12	0.11	3.30	1.62	1.42	1.31
CASE7	1.17	-0.14	0.01	0.05	0.05	3.05	1.45	1.26	1.16
CASE8	1.18	-0.18	-0.02	0.03	0.04	2.97	1.40	1.22	1.12

Source location depth: 2,000m

	P1	P2	P3	P4	P5	T1	T2	T3	T4
CASE0	0.96	0.69	0.51	0.40	0.33	3.80	2.12	1.80	1.64
CASE1	0.84	0.80	0.60	0.49	0.42	4.37	2.52	2.16	1.96
CASE2	0.93	0.74	0.54	0.43	0.36	3.96	2.22	1.89	1.72
CASE3	0.95	0.71	0.52	0.41	0.34	3.84	2.14	1.83	1.66
CASE4	0.96	0.70	0.51	0.40	0.33	3.81	2.12	1.81	1.64
CASE5	0.81	0.82	0.62	0.51	0.45	4.58	2.68	2.30	2.10
CASE6	0.91	0.74	0.55	0.44	0.37	4.02	2.27	1.93	1.75
CASE7	0.94	0.71	0.52	0.41	0.34	3.85	2.15	1.84	1.67
CASE8	0.95	0.70	0.51	0.40	0.33	3.81	2.12	1.81	1.64

Table 4.1.4-3 The ratios in comparison to CASE 0 of the water level and inherent period (peak to peak)

Source location depth: 1,000m

	P1	P2	P3	P4	P5	T1	T2	T3	T4
CASE0	1.00	1.00	1.00	1.00	1.00	1.00	1.00	1.00	1.00
CASE1	0.89	-1.02	-7.89	11.93	6.04	1.27	1.42	1.45	1.47
CASE2	0.96	0.22	-2.46	5.06	2.76	1.08	1.12	1.13	1.13
CASE3	0.99	0.77	-0.01	2.17	1.49	1.02	1.03	1.03	1.03
CASE4	1.00	0.93	0.69	1.35	1.14	1.01	1.01	1.01	1.01
CASE5	0.86	-1.61	-10.29	15.05	7.60	1.36	1.58	1.62	1.66
CASE6	0.95	-0.03	-3.58	6.43	3.38	1.11	1.17	1.18	1.18
CASE7	0.98	0.68	-0.40	2.61	1.68	1.03	1.04	1.05	1.05
CASE8	0.99	0.90	0.57	1.48	1.20	1.00	1.01	1.01	1.01

Source location depth: 2,000m

	P1	P2	P3	P4	P5	T1	T2	T3	T4
CASE0	1.00	1.00	1.00	1.00	1.00	1.00	1.00	1.00	1.00
CASE1	0.88	1.15	1.18	1.22	1.26	1.15	1.19	1.20	1.20
CASE2	0.97	1.06	1.06	1.07	1.08	1.04	1.05	1.05	1.05
CASE3	0.99	1.02	1.02	1.02	1.02	1.01	1.01	1.01	1.01
CASE4	1.00	1.00	1.00	1.00	1.00	1.00	1.00	1.00	1.00
CASE5	0.84	1.18	1.22	1.28	1.34	1.21	1.27	1.28	1.28
CASE6	0.95	1.07	1.07	1.09	1.10	1.06	1.07	1.07	1.07
CASE7	0.98	1.02	1.02	1.02	1.02	1.01	1.02	1.02	1.02
CASE8	0.99	1.00	1.00	1.00	1.00	1.00	1.00	1.00	1.00

(3) Examination of grid partitioning for shallow sea areas

For shallow regions (water depths between 50m and 400m), an examination of the grid partitioning is conducted for performing calculations using a nonlinear dispersive wave model. For the examination, numerical tests are conducted using one-dimensional tsunami propagation calculations similar to the examination conducted of deep sea areas. For tsunami having a 180-second period, grid sizes are set so that they were 1/20 or less of the wavelength for each section representing water depth, and comparisons are conducted between cases where these grid sizes were the base case (1/20 of the wavelength) and a case where the grid size was halved.

The initial water level for calculation is the level of the central cross-section of the ground deformation distribution obtained by the method proposed by Mansinha and Smylie (1971). The sea bottom topography slope is the same as that used in the examination of deep-sea areas, and the tsunami source set position is 1,000m. Also, transmission conditions are configured for both offshore and on land.

For the default parameters, the five tsunami sources shown in Table 4.1.4-4 are used, and comparisons conducted of the chronological tsunami shapes at a depth of 50m as well as the maximum water level ascent and descent. Also, the base case for regions having a water depth of greater than 80m used a grid size of 30m and for regions where the water depth was 80m or shallower, the grid size for the base case is 10m, and the ratio in relation to the base case is investigated (Tables 4.1.4-5 to 4.1.4-7).

The ratios of the maximum water level ascent and descent are within 5% in relation to the base case, for both base case and the halved base case. It was confirmed, from the verification of chronological tsunami shapes in Figure 4.1.4-9, that no significant difference is found on fluctuation of the water level of the first wave, even when the grid size is set as 800m for regions deeper than 400m, and set as base case for regions of 50m to 400m depth.

Although a delay in arrival time is observed, this is because the grid size offshore is set as 800m, and not because of setting the grid size for regions shallower than 400m.

Table 4.1.4-4 The fault parameters for the examination of grid sizes in shallow sea area

Source	Width (km)	Fault dip angle (°)	Upper edge depth (km)	Slip amount (m)	Slip angle (°)	Direction of fault dip
F1	100	15	2.5	7	90	Land-side foot wall
F2	17.3	60	2.5	9.44	90	Land-side hang wall
F3	50	20	2.5	9.7	90	Land-side foot wall
F4	15	90	2.5	4.16	90	Land-side hang wall
F5	50	45	0	5	270	Land-side hang wall

Table 4.1.4-5 The grid sizes for the tsunami of a 180-second period

Depth (m)	Wave length (m)	Wave length/20 (m)	base case grid size (m)	Halved base case grid size (m)
20	2,520	126	100	50
30	3,086	154	100	50
40	3,564	178	100	50
50	3,984	199	200	100
60	4,365	218	200	100
70	4,714	236	200	100
80	5,040	252	200	100
90	5,346	267	200	100
100	5,635	282	200	100
150	6,901	345	200	100
200	7,969	398	400	200
250	8,910	445	400	200
300	9,760	488	400	200
350	10,542	527	400	400
400	11,270	563	400	400

Table 4.1.4-6 The maximum water level ascent at a depth of 50m

	grid size 30m and 10m (A)	base case grid size (B)	Halved base case grid size (C)	(B) / (A)	(C) / (A)
F1	3.26	3.23	3.24	0.99	0.99
F2	3.96	3.84	3.86	0.97	0.98
F3	4.88	4.87	4.86	1.00	1.00
F4	1.16	1.10	1.12	0.95	0.96
F5	1.28	1.34	1.30	1.05	1.02

Table 4.1.4-7 The maximum water level descent at a depth of 50m

	grid size 30m and 10m (A)	Base case grid size (B)	Halved base case grid size (C)	(B) / (A)	(C) / (A)
F1	-1.77	-1.77	-1.78	1.00	1.01
F2	-2.64	-2.71	-2.74	1.02	1.04
F3	-1.58	-1.62	-1.59	1.03	1.01
F4	-1.87	-1.85	-1.87	0.99	1.00
F5	-2.99	-2.94	-2.96	0.98	0.99

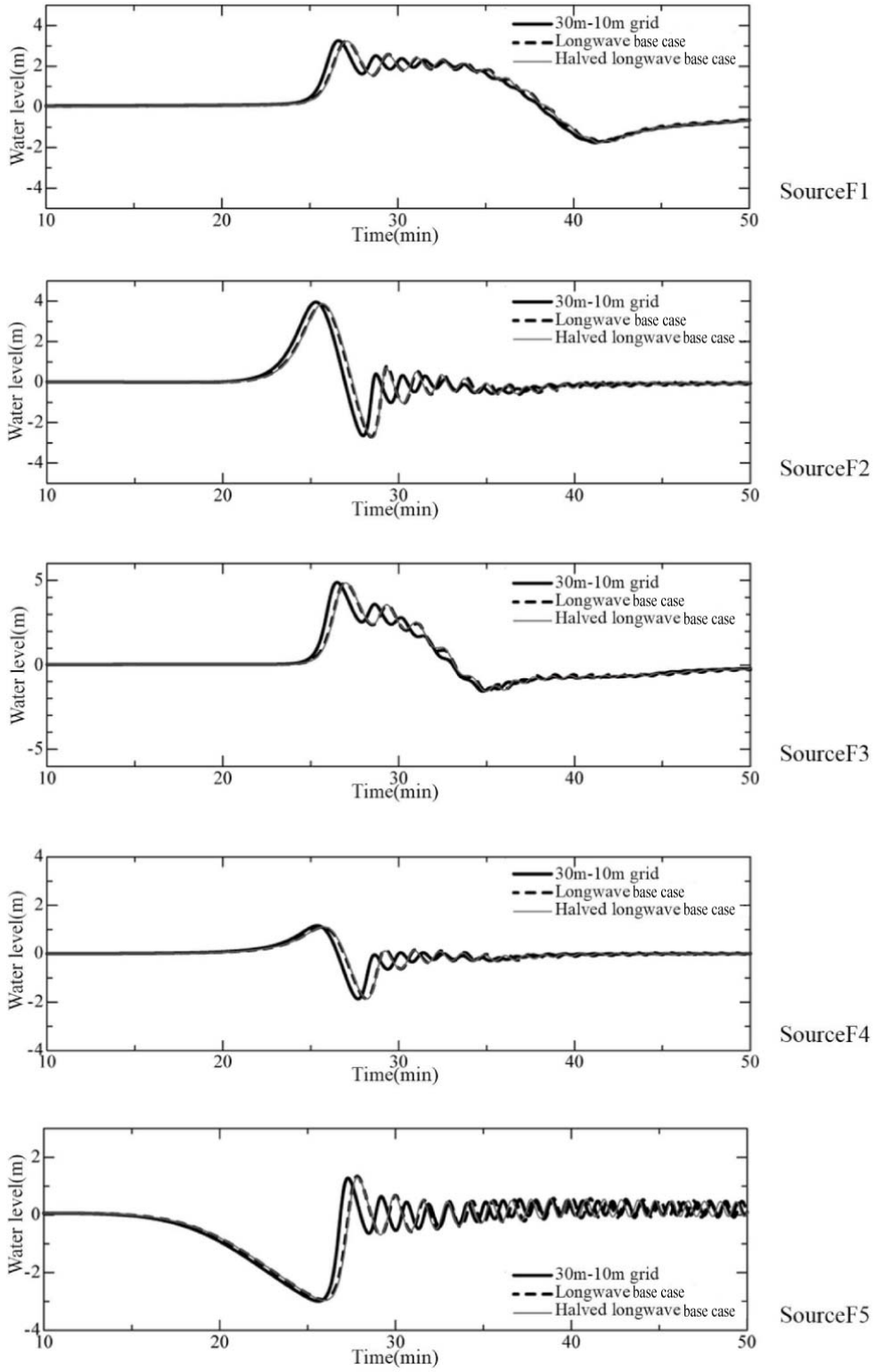

Figure4.1.4-9 Chronogical tsunami shapes at a depth of 50m

4.1.5. Examination of field applicability of the nonlinear dispersive wave model

(1) Calculation conditions

A nonlinear dispersive wave model having a two-dimensional plane was used for a tsunami analysis to examine applicability in the field. The tsunami, which was the object of the examination, was the 1933 Showa Sanriku tsunami, and the fault model is shown in Table 4.1.5-1. The principal calculation conditions are consolidated in Table 4.1.5-2. Also, Kuji Bay was the site for the case study in this examination. The grid partitioning of the Sanriku coastline is shown in Figures 4.1.5-1 and 4.1.5-2.

Table 4.1.5-1 Parameters of the fault model for the 1933 Showa Sanriku tsunami (JSCE, 2002)

Reference point	M_W	Length L (km)	Width W (km)	Depth of upper edge of the fault plane d(km)	Strike direction θ(degree)	Dip angle δ(degree)	Slip angle λ(degree)	Slip amount D(m)
40.16°N 144.5°E	8.4	185	50	1	180	45	270	6.6

Table 4.1.5-2 Calculation conditions

	Non-linear dispersive wave theory	Non-linear long-wave theory	Note
Grid sizes	800 ~ 12.5 m	800 ~ 12.5 m	
Computation time interval	0.1 s	0.1 s	
Simulating time	2 hours	2 hours	
Manning's coefficient of roughness	0.03	0.03	
Advection term	central difference scheme	1st-order upwind difference scheme	
Artificial amplification term	Matsuyama et al.(2006)	-	ω_E =0.01, α=0.09
Wave breaking term	Matsuyama et al.(2006)	-	ω_s =0.03, β=0.23, γ=0.85
Variance term	Peregrine(1967)	-	

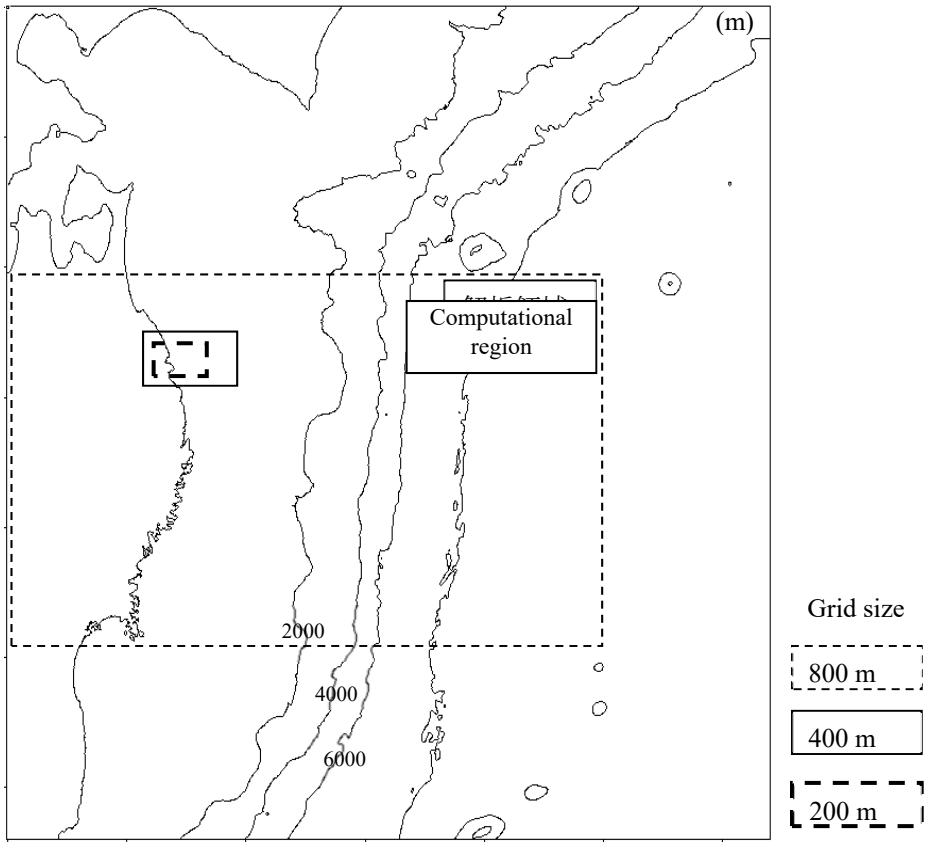

a) Computational region

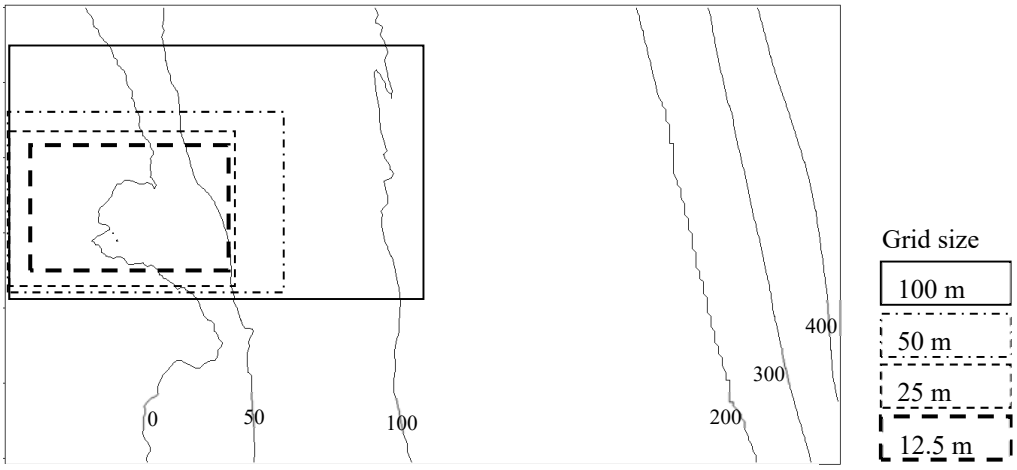

b) Enlarged view

Figure 4.1.5-1 Grid division and water depth

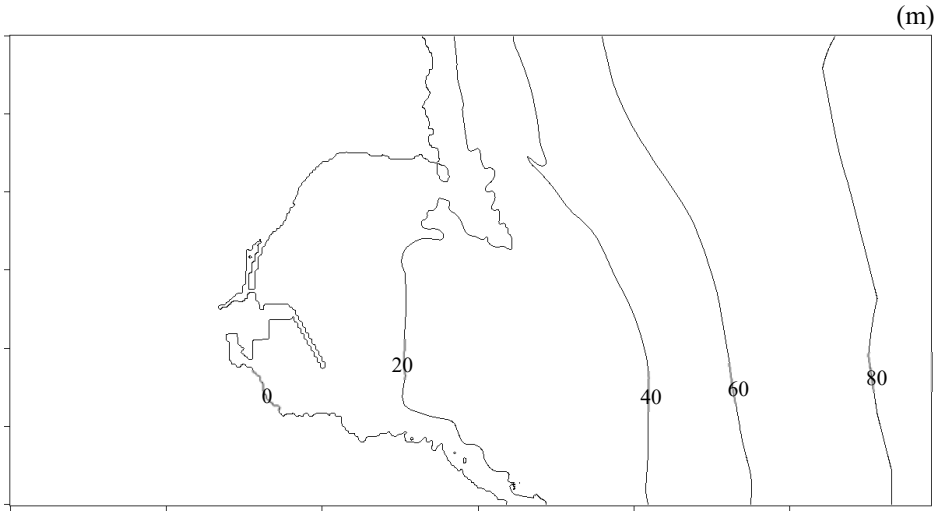

Figure 4.1.5-2 Water depth of 12.5m grid region

(2) Calculation results

In Figure 4.1.5-3, the propagation conditions of a tsunami from the tsunami source to the coastline are shown with a spatial distribution of the water level, and a comparison is shown between the dispersive wave model and the nonlinear long-wave model. According to these diagrams, short-period waves repeatedly occur in tsunami source regions coastal regions one after another with the nonlinear dispersive wave model. As the result, it may be said that it is desirable to use the nonlinear dispersive wave model when precise of tsunami wave shapes occurring at tsunami sources is an issue.

A cross-sectional view of the water level distribution of the target section of Kuji Bay given in Figure 4.1.5-4 is shown in Figure 4.1.5-5. In the dispersive wave model, soliton fission begins to occur as the tsunami arrives at the bay entrance until the vicinity of the central area (water depth shallower than 20m), and becomes more pronounced as it nears the coastline. As a result, the water rises due to the wave splitting near the shoreline. Also, soliton fission clearly occurs in front of breakwaters and other such areas, and an examination that takes into account soliton fission is necessary in areas where split waves are predominant. Figures 4.1.5-6 and 4.1.5-7 show the maximum tsunami height and the cross-sectional views analyzed using the dispersive wave model and nonlinear long-wave model. This shows that in contrast to the nonlinear long-wave model, the dispersive wave model affords a tendency for tsunami height along the coastline to be greater locally due to the effects of soliton fission and other factors, but there is almost no change with respect to areas inundated or tsunami height in tsunami run-up areas.

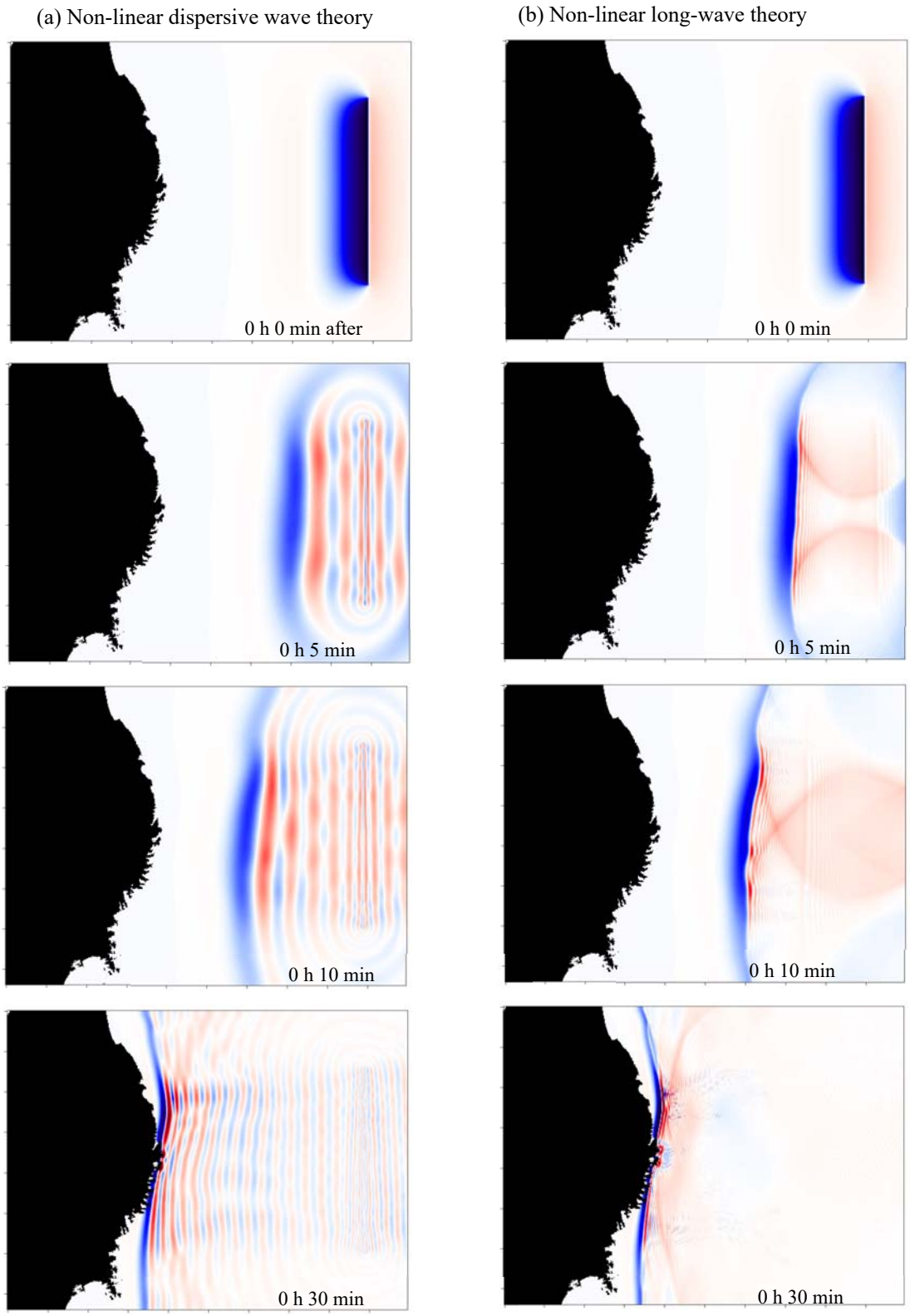

Figure 4.1.5-3 Comparison of the spatial distribution of tsunami water level

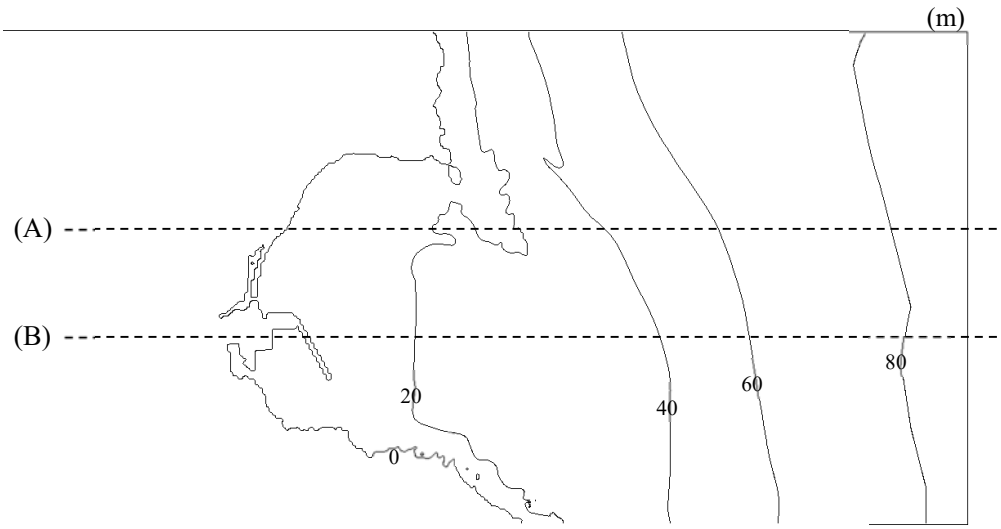

Figure 4.1.5-4 Cross section to compare the results

43 minutes after

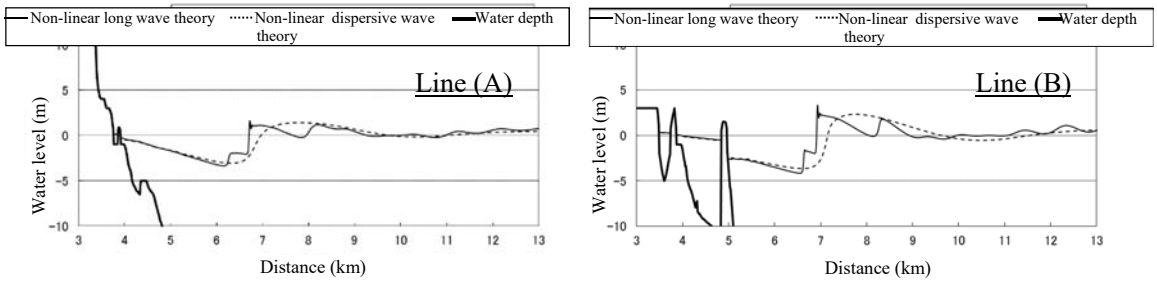

45 minutes after

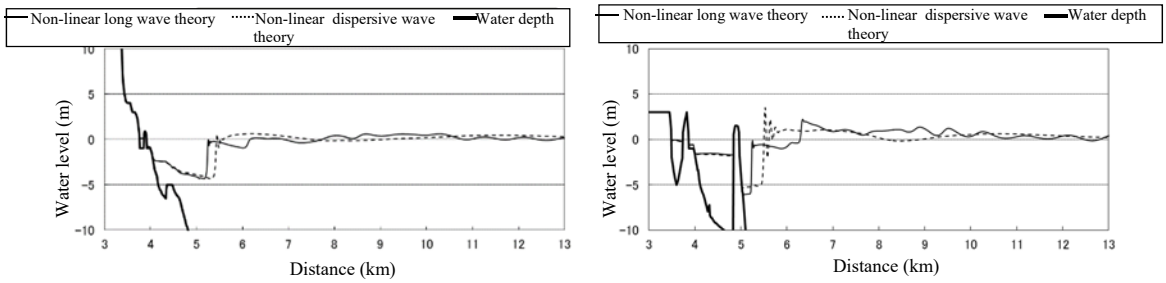

47 minutes after

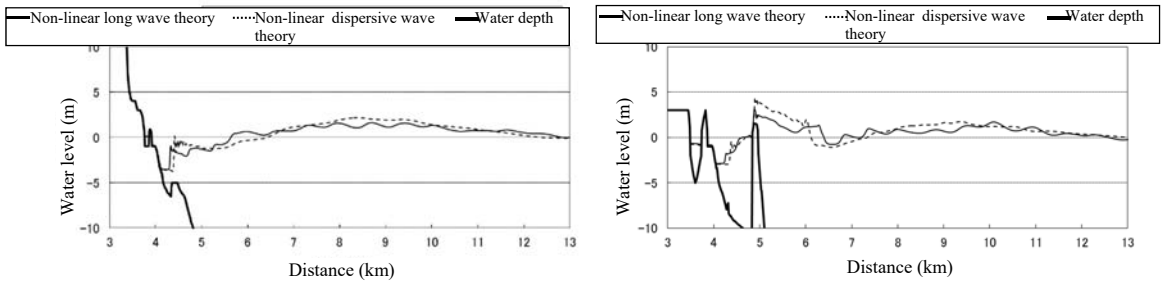

Figure 4.1.5-5 Cross section of tsunami water level

(a) Non-linear dispersive wave theory (b) Non-linear long-wave theory

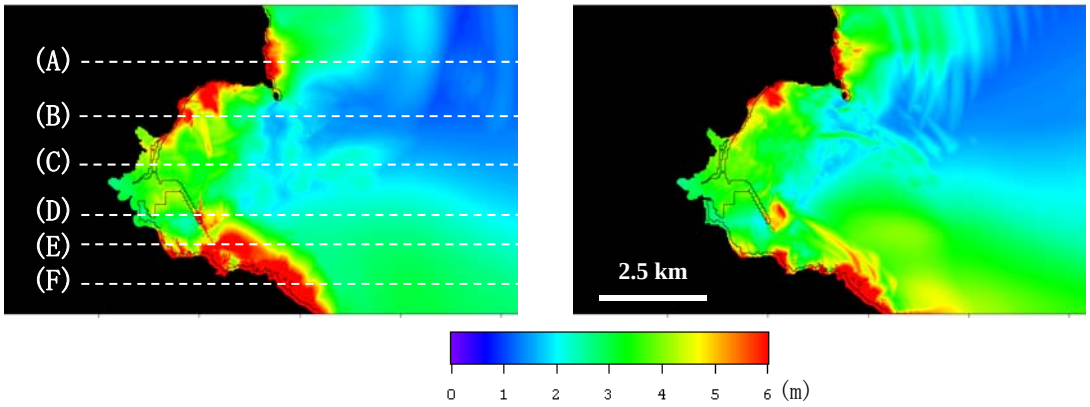

Figure 4.1.5-6 Maximum water level distribution

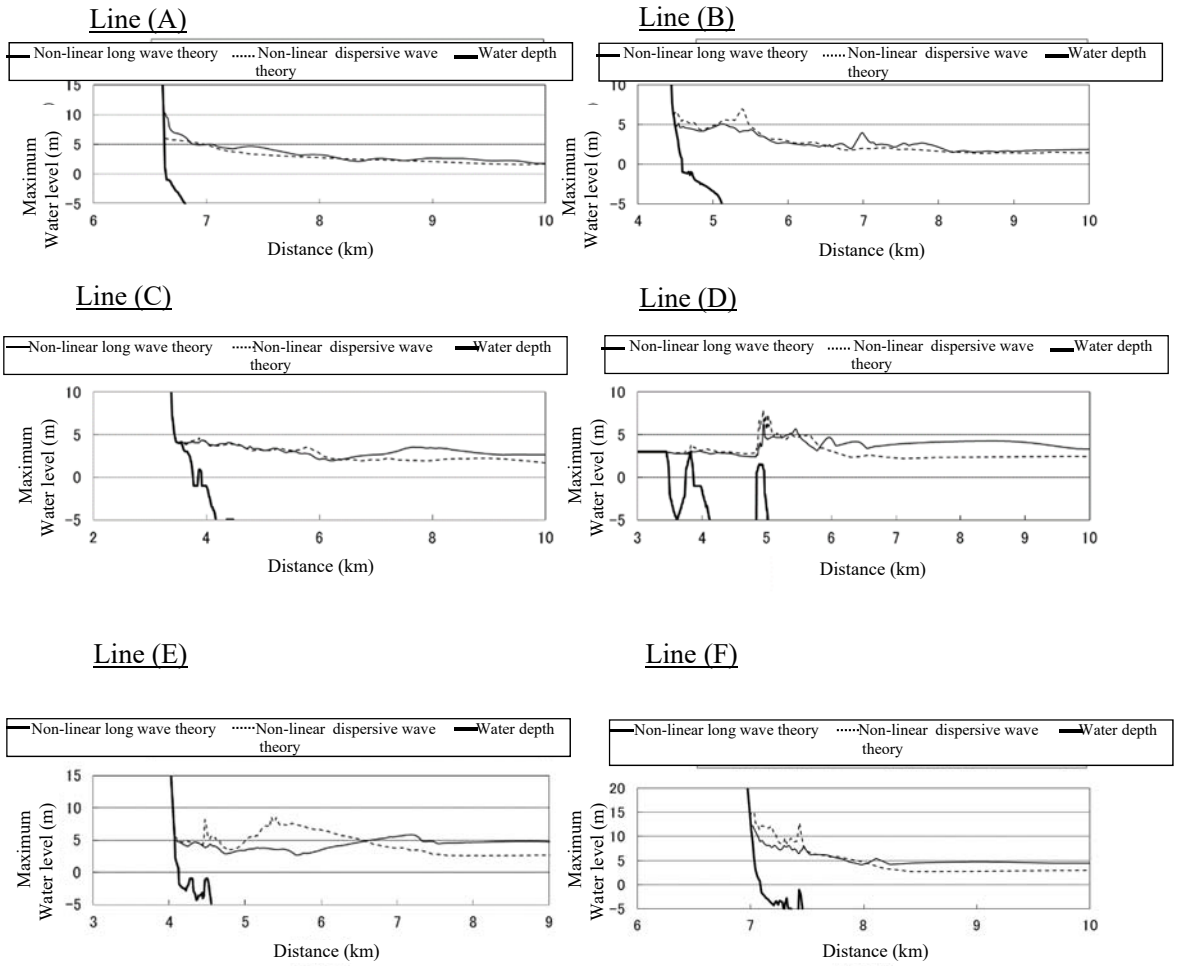

Figure 4.1.5-7 Cross section of maximum water level distribution

4.1.6. Verification of the appropriateness of three-dimensional models using simulation analysis of previous hydraulic model experiment results

In cases focusing on tsunami coastal propagation and land run-up, numerical models with a plane two-dimensional field (plane two-dimensional model) that apply nonlinear long-wave theory (shallow water equation) are often used. On the other hand, in recent years the development of fluid analysis technology has also made it possible to apply three-dimensional fluid dynamics models (three-dimensional models) that directly calculate three-dimensional basic equations.

Here, case studies have been consolidated of previous analyses of leading three-dimensional models, and numerical simulations of previous hydraulic model experiments have been conducted to verify the appropriateness of three-dimensional models.

(1) Case studies of previous analyses of representative three-dimensional models

Three-dimensional models are broadly classified into models that assume hydrostatic pressure approximation and models that do not. STOC-ML and C-HYDRO3D are three-dimensional models that consider hydrostatic pressure approximation, and CADMAS-SURF/3D, OpenFOAM, STOC-IC, DOLPHIN-3D and tsunami complex disaster prediction model, and others are examples of three-dimensional models that do not consider hydrostatic pressure.

1) CADMAS-SURF/3D

CADMAS-SURF/3D is a non-hydrostatic pressure-type three-dimensional model, which was researched and developed by the Coastal Development Institute of Technology (2010), and has the capability not only to calculate the behavior and pressure of tsunami running up onto land, but also analyses that are coupled with gases, ground and solids. Arikawa et al. (2005) verified the appropriateness of results of analyses of fluid behavior and tsunami wave pressure conducted using CADMAS-SURF/3D based on comparisons with the results of hydraulic model experiments on run-up tsunami (Figure 4.1.6-1).

2) OpenFOAM

Open source Field Operation and Manipulation (OpenFOAM) is a fluid analysis model released as free and open source software under GNU General Public License (GPL). Fam et al. (2012) and Kawasaki et al. (2013) applied the OpenFOAM interFoam solver to numerical simulations of problems of water column collapse and hydraulic model experiments of run-up tsunami, and conducted comparative validations with the results of experiments on fluid behavior and tsunami wave pressure.

3) Storm Surge and Tsunami Simulator (STOC)

The Storm Surge and Tsunami Simulator in Oceans and Costal Areas (STOC) is a hybrid model capable of connecting, as necessary, the quasi-three-dimensional hydrostatic pressure

multi-level model STOC-ML to the three-dimensional non-hydrostatic pressure flow model STOC-IC. Tomita and Kakinuma (2005), Tomita and Honda (2008), and Takahashi and Tomita (2013) used STOC to verify the model's appropriateness and precision based upon comparisons with hydraulic model experiments using factors such as slope, tsunami breakwaters, actual topography, etc.

4) DOLPHIN-3D

Dynamic numerical model Of muLti-Phase flow with Hydrodynamic INteractions-3 Dimension version (DOLPHIN-3D) is a three-dimensional model of the non-hydrostatic pressure type that is capable of calculating the dynamic behavior of debris, interaction between structures and tsunami, and behavior of run-up tsunami and other elements. Kawasaki et al. (2006) as well as Kawasaki and Hakamata (2007) applied DOLPHIN-3D to numerical simulations of hydraulic model experiments on tidal bore accompanying water column collapse as well as collision and drift of rectangular rigid bodies to conduct a comparison and validation of the model against the results of experiments on fluid behavior and wave pressure.

5) Tsunami complex disaster predication model

The tsunami complex disaster prediction model is a non-hydrostatic pressure-type three-dimensional model capable of calculating fluid motion as well as vessel motion and mooring cable tension. Yoneyama et al. (2008) and Yoneyama and Nagashima (2009) used the tsunami complex disaster prediction model to verify the appropriateness of results of analyses of run-up tsunami behavior as well as debris behavior based upon comparisons with the results of hydraulic model experiments.

6) C-HYDRO3D

C-HYDRO3D is a hydrostatic pressure-type three-dimensional model that calculates tsunami propagation from the tsunami source region to the coastline as well as overflow and run-up flow in addition to calculations of the motion of debris and topography change caused by tsunami. Kihara and Matsuyama (2010) and Kihara et al. (2012) verified the reproducibility of tsunami behavior and topography change for the area around bays in Sri Lanka that were caused by the 2004 earthquake tsunami off the coast of Sumatra as well as hydraulic model experiments, and they also validated the vertical distribution of suspended sediment concentrations using a comparison with moving-bed open channel experiments.

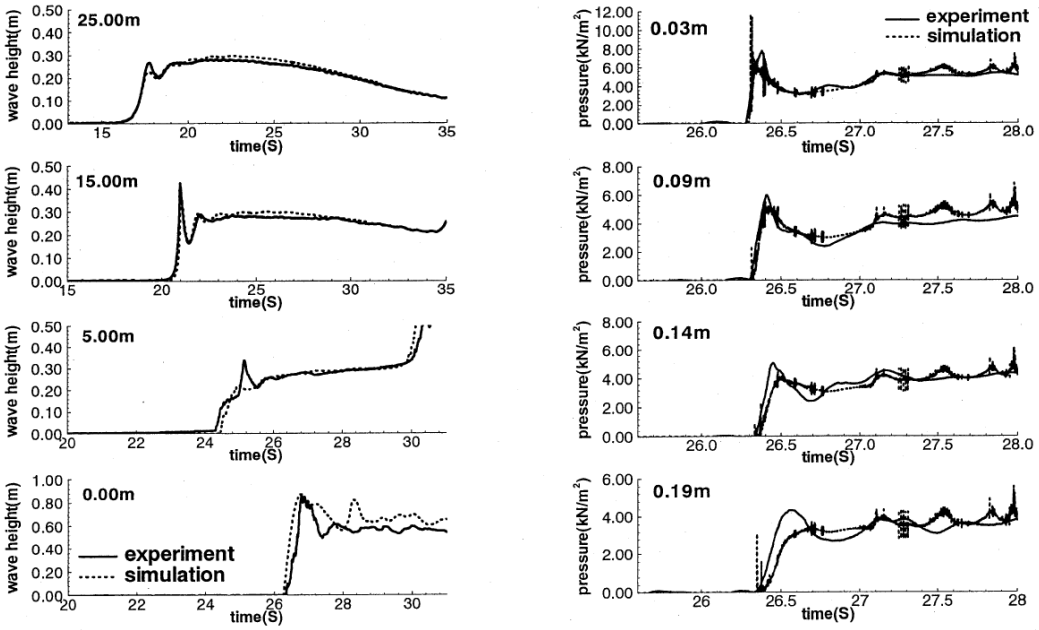

(1) Time series of wave height (2) Wave pressure acting on the seawall

Figure 4.1.6-1 Comparison of analysis results by CADMAS-SURF/3D with experimental results (Arikawa et al., 2005)

(2) Numerical simulations of hydraulic model experiments reproducing tsunami behavior overflowing seawalls and other facilities

Numerical simulations were conducted which applied a plane two-dimensional model and three-dimensional model to hydraulic model experiments simulating tsunami behavior when overflowing seawalls to verify the appropriateness of both models.

1) Experiment overview

Arimitsu et al. (2012) used a rectangular water channel (height: 0.5m, width: 0.5m, length: 18m), and quickly opened the gate to a water storage section, thereby causing a tidal-like tsunami. The tsunami propagated through a uniform water depth (length: 3.2m), overflowing subsequent seawalls (heights: 0.02m and 0.05m) and running up onto a flat land area (length: 6.8m). During the experiments, seawall height, storage water position, shape of structure models, and the position where the structures settings were varied.

2) Examination conditions

[1] Plane two-dimensional model

In analyzing tsunami, a method (Goto and Ogawa, 1982) was used that employs a staggered leapfrog method to differentiate continuity equation and nonlinear long-wave theory.

The computational region, ground height, initial water level and other calculation

conditions were the same as those adopted for the experiments (Table 4.1.6-1, Figure 4.1.6-2). Also, for seawalls, two methods were used, one that uses the Honma model (Honma formula) to calculate the overflow rate along the overflow boundary, and the other that calculates the flow rate per unit width using nonlinear long-wave theory for the topography. From the experiment conditions used by Arimitsu et al. (2012), a storage water level of 0.15m was used and there were no structure models, and three calculation cases configured setting the seawall heights at 0.00m (no seawall), 0.02m, and 0.05m.

[2] Three-dimensional model

For this examination, CADMAS-SURF/3D (Coastal Development Institute of Technology, 2010), a numerical wave motion water channel program, is used.

The numerical experiment water channel, which is used for the numerical simulations, is the same as that for the plane two-dimensional model (Figure 4.1.6-2). Also the simulating conditions of the three-dimensional model are shown in Table 4.1.6-2. The calculation cases are the same three cases as for the plane two-dimensional model.

3) Numerical simulation results

The following knowledge was gained from the results of a comparison made of the empirical results and analytical results of spatial tsunami shapes in the area around seawalls as well as chronological tsunami shapes of water level and flow velocity at the geodetic points in the experiment.

[1] Tsunami behavior in sea areas

From chronological tsunami shapes of water levels in sea areas as shown in Figure 4.1.6-3, the plane two-dimensional model was not able to reproduce the variance effect of the tsunami head as observed in experiments and three-dimensional models, and the phase of the water level peak was also early, but, with the exception of these points, it was confirmed that experiments were able to be nicely reproduced. Also, it was found that the three-dimensional model properly reproduces the empirical results for both spatial tsunami shapes and chronological tsunami shapes of water levels.

[2] Tsunami behavior on land

Using chronological tsunami shapes of water level and flow velocity in land areas as shown in Figures 4.1.6-4 and 4.1.6-5, with the exception of the area around seawalls, the results of calculations using the plane two-dimensional model and three-dimensional model were consistent with respect to conditions after run-up, and created good reproductions of inundation depth and flow velocity in the empirical results. However, from spatial tsunami shapes during overflow of seawalls as shown in Figure 4.1.6-6, the plane two-dimensional model is not able to reproduce water surface shapes very near seawalls, so the three-dimensional model is regarded as effective in cases where the inundation depth and flow

velocity need to be more appropriately ascertained.

Table 4.1.6-1 Simulating condition of two-dimensional model in the reproduction calculation of hydraulic model experiments of Arimitsu et al. (2012)

Item		Setting value
Governing equations		Nonlinear long-wave theory
Computational region		The same region as the hydraulic model experiment
Grid sizes		1cm interval
Computation time interval		0.0002s (Considering C.F.L. condition)
Initial conditions		The same condition as the hydraulic model experiment
Boundary conditions	Offshore boundary conditions	Water storage wall: Complete reflection condition Water channel side wall: Full reflection condition Land part: Free transmission condition
	Onshore boundary conditions	Wave front condition
	Overflow boundary conditions	Honma model
Manning's coefficient of roughness		n=0.010 $m^{-1/3}$·s
Simulating time		20s

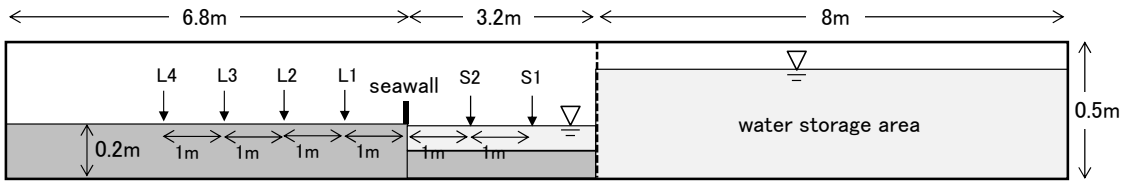

* Water channel width: 0.5m, S1, S2, L1～L4: Measurement points of water level and flow velocity

Figure 4.1.6-2 The numerical experiment water channel for the reproduction calculation of hydraulic model experiments of Arimitsu et al. (2012)

Table 4.1.6-2 Simulating condition of three-dimensional model in the reproduction calculation of hydraulic model experiments of Arimitsu et al. (2012)

Item		Setting value
Initial conditions		The same condition as the hydraulic model experiment
Computational region		The same region as the hydraulic model experiment
Grid sizes	Δx	0.01 ~ 0.03m
	Δy	0.01m
	Δz	0.01 ~ 0.025m
Time control	Computation time interval Δt	Automatic
	Simulating time	15s
Difference scheme		VP-DONOR
Boundary conditions	Velocity and pressure	Logarithmic law
	VOF function	FREE
Physical property values	Density	1,000kg/m^3
	Acceleration of gravity	9.8m/s^2
	Viscosity	None
Option	Bubble rising speed	0.2m/s
	Water droplets falling speed	Free fall
	Flow velocity of surface cell	Zero gradient

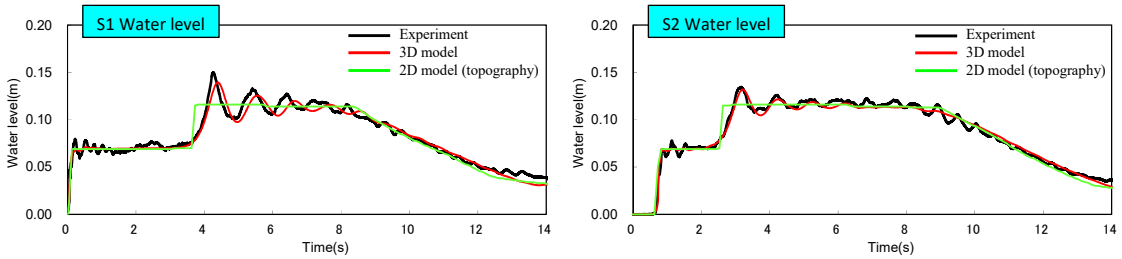

(1) In the case seawall height at 0.00m (No seawall)

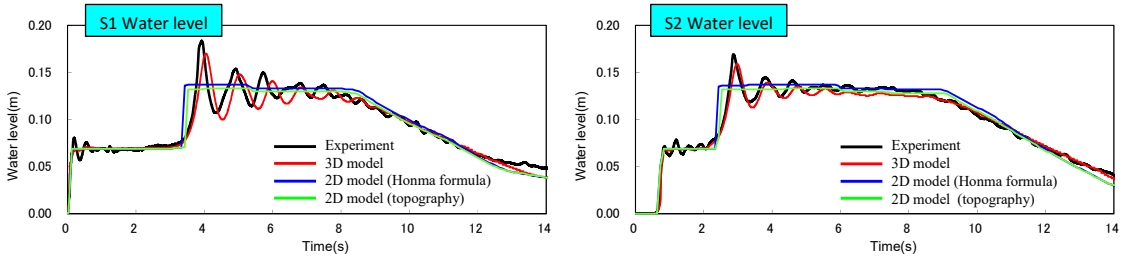

(2) In the case seawall height at 0.05m

Figure 4.1.6-3 Time series of water level at S1 and S2

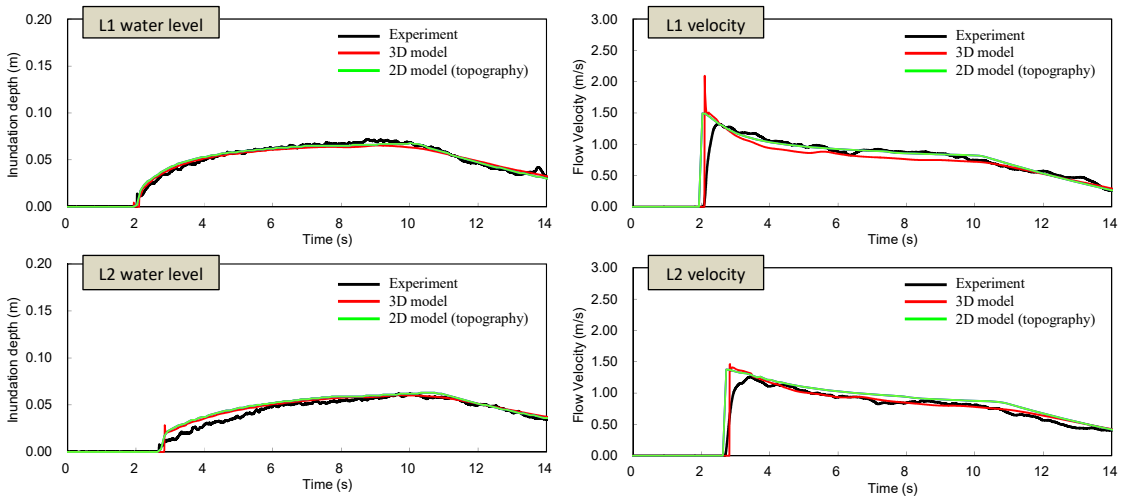

Figure 4.1.6-4 Time series of water level and flow velocity at L1 and L2

(In the case seawall height at 0.00m)

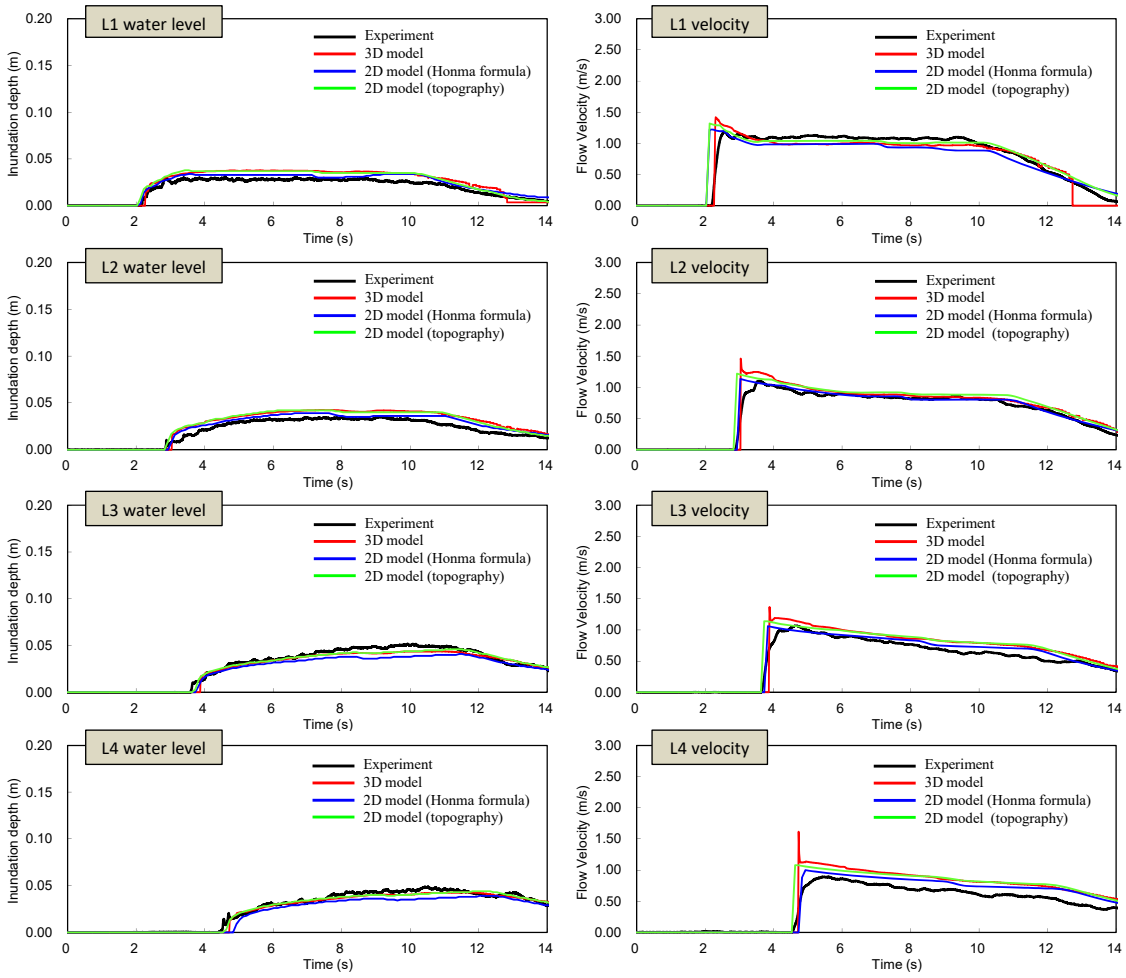

Figure 4.1.6-5 Time series of water level and flow velocity at L1 and L2

(In the case seawall height at 0.05m)

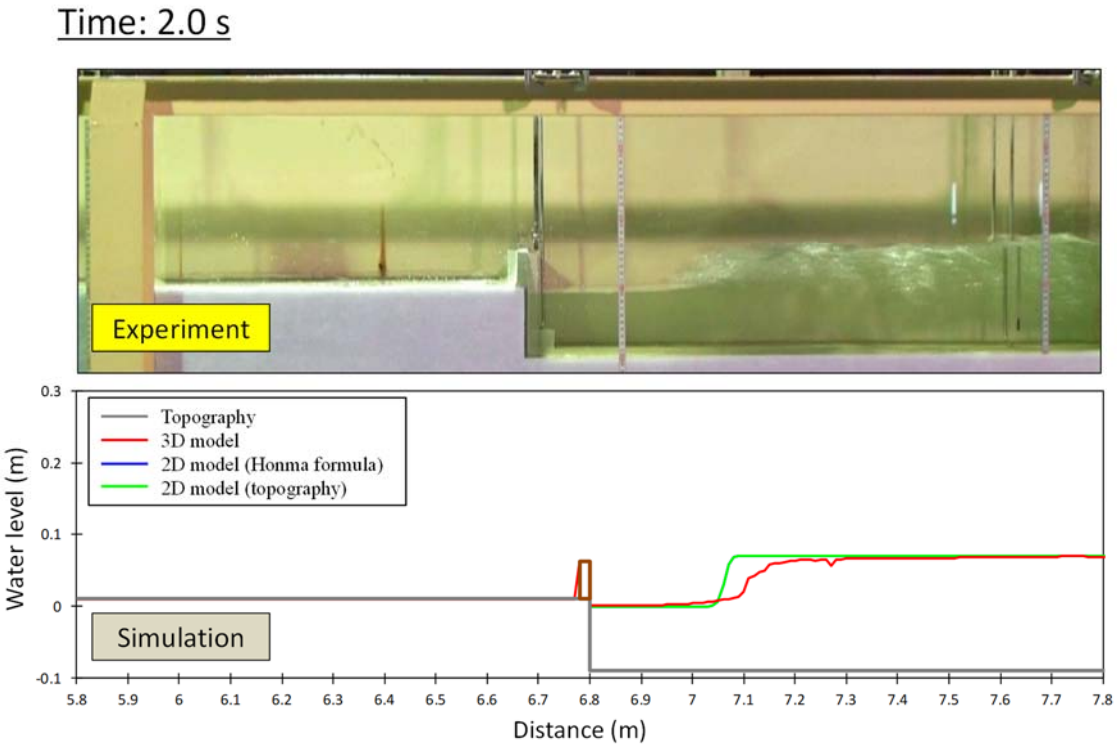

Figure 4.1.6-6 Spatial waveform of the tsunami overflowing the seawall

(3) Numerical simulations of hydraulic model experiments simulating tsunami behavior running up to buildings and other structures in land areas

Numerical simulations were conducted which applied a plane two-dimensional model and three-dimensional model to hydraulic model experiments simulating the behavior of tsunami running up to buildings on land.

1) Experiment overview

Arimitsu et al. (2013) used one side of the plane water tank (length: 38m, width: 20m, height: 1.2m) shown in Figure 4.1.6-7 that was partitioned by guided wave panels in the center and a wave-making machine to create solitary ways simulating a tsunami. The tsunami propagates across an even floor 4.2m in length and the slope of sea bottom of 1/10 and 1/50, overflows over an upright embankment that is 0.11m high, and runs up onto a flat land terrain. The arrangement of the structure models is into patterns: a case where a rectangular structure (length: 0.1m, width: 0.1m, height: 0.4m) is arranged in a single unit (single unit) and a case where two of the same structures are set up offshore (group of structures) as shown in Figure 4.1.6-7. In the experiments, the height of the solitary waves as well as the position of the structure settings were varied, and measurements taken of the water level and horizontal flow velocity in the sea area (H1 ~ H3), as well as the inundation depth (L0 ~ L3) and flow velocity (L3) in the land area.

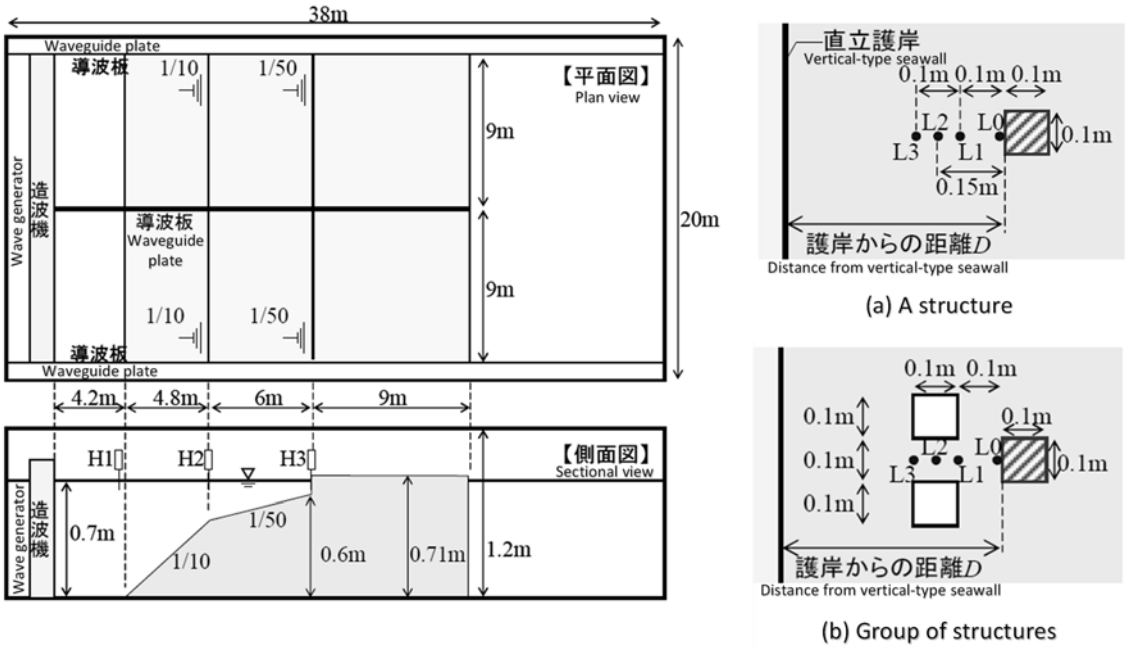

Figure 4.1.6-7 Experimental equipment and arrangement of the structures

2) Examination conditions

[1] Plane two-dimensional model

In analyzing tsunami, a method (Goto and Ogawa, 1982) was used that employs a staggered leapfrog method to differentiate continuity equation and nonlinear long-wave theory. The computational region ranged from the H2 point on one side (width: 9m) of the plane water tank to the tip of the land terrain as shown in Figure 4.1.6-7. Also, the analysis focused on experimental cases where the arrangement of the structures was as a “group of structures”.

The simulating conditions for the plane two-dimensional model are given in Table 4.1.6-3. The conditions for the ground height and the initial water level are both the same as for the experiments, and the water level at observation point H2, which was obtained from the experiment, was set as the incident tsunami shape, and was launched from the offshore boundary. The grid sizes were set for a total of six patterns, which were 1cm, 2cm, 2.5cm, 3.33cm, 5cm and 10cm so that the number of grids between structures (10cm) was 10 grids, 5 grids, 4 grids, 3 grids, 2 grids, and 1 grid.

Table 4.1.6-3 Simulating condition of two-dimensional model in the reproduction calculation of hydraulic model experiments of Arimitsu et al. (2013)

Item		Setting value
Governing equations		Nonlinear long-wave theory
Grid sizes		1cm, 2cm, 2.5cm, 3.33cm, 5cm, 10cm
Computation time interval		0.0002 ~ 0.0010s (Considering C.F.L condition)
Boundary conditions	Offshore boundary conditions	Sea area: Inputting time series of water level of solitary wave which tsunami height is 3cm Water channel side wall: Full reflection condition Land area: Free transmission condition
	Onshore boundary conditions	Wave front condition
Manning’s coefficient of roughness		n=0.010 $m^{-1/3}\cdot s$
Simulating time		15s

[2] Three-dimensional model

CADMAS-SURF/3D (Coastal Development Institute of Technology, 2010), a numerical wave motion water channel program, was used for the three-dimensional model. The computational region and calculation cases were the same as for the plane two-dimensional

model.

The simulating conditions for the three-dimensional model are shown in Table 4.1.6-4. The incident tsunami shape of a solitary wave (same tsunami shape as the plane two-dimensional model) was input from the wave-making boundary of the sea area. With respect to the grid sizes in the height direction, the minimum grid sizes were varied using 0.25cm, 0.5cm, and 1cm so that the number of grids for the inundation depth at L0 point in the experiment would be 20 grids, 10 grids and 5 grids. The grid sizes in the horizontal direction were set so that the ratio of the grid sizes in a horizontal direction to the height direction would be either 2:1 or 1:1.

Table 4.1.6-4 Simulating condition of three-dimensional model in the reproduction calculation of hydraulic model experiments of Arimitsu et al. (2013)

Item		Setting value
Grid sizes	$\triangle x \times \triangle y \times \triangle z$	・0.5cm×0.5cm×0.25cm ・0.5cm×0.5cm×0.5cm ・1cm×1cm×0.5cm ・2cm×2cm×1cm
Time control	Computation time interval $\triangle t$	Automatic
	Simulating time	15s
Offshore boundary conditions		Inputting time series of water level of solitary wave which tsunami height is 3cm
Difference scheme		VP-DONOR
Boundary conditions	Velocity and pressure	SLIP
	Scalar quantity	FREE
Physical property values	Density	1,000kg/m^3
	Acceleration of gravity	9.8m/s^2
	Viscosity	None
Option	Bubble rising speed	0.2m/s
	Water droplets falling speed	Free fall

3) Reproduction calculation results

With regard to the reproducibility of inundation depth and flow velocity for tsunami overflowing seawalls or other structures up to the flooding of the site, the following knowledge was gained from the results of analyses conducted that focused on the appropriate number of grids between structures and other elements, and the tsunami circling around behind the

structures.

[1] Plane two-dimensional model

Based on Figure 4.1.6-8, it is difficult for the plane two-dimensional model to reproduce sudden rises of water masses in front of structures. However, with the exception of such localized phenomena, the plane two-dimensional model allows for calculations of inundation depth and flow velocity with good precision overall. However, in cases where the number of grids between structures is either one or two, the reproducibility of inundation depth after passing between the structures is significantly reduced, so it is desirable to set the number of grids between structures at a minimum of three.

[2] Three-dimensional model

Based on Figures 4.1.6-9 and 4.1.6-10, the three-dimensional model allows for calculation with good precision overall of sudden rises in water mass in front of structures, and use of the three-dimensional model is effective in cases where it is necessary to ascertain in more detail the behavior of tsunami around structures. However, there are cases where calculation precision of hydraulic quantity is reduced when grid sizes in a vertical direction are rough, so this point needs to be kept in mind when setting grid sizes in the vertical direction.

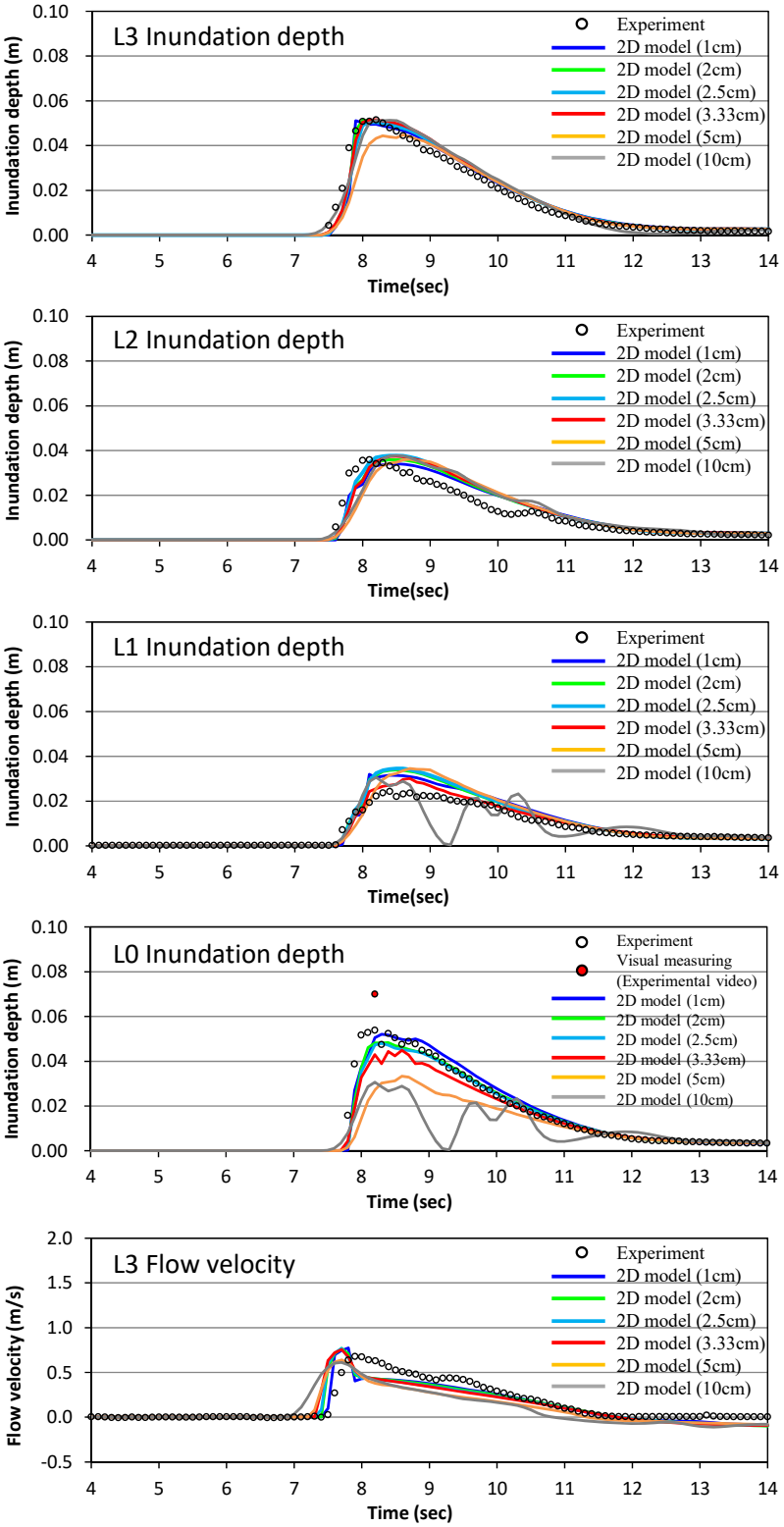

Figure 4.1.6-8 Time series of inundation depth and flow velocity by experimental results of Arimitsu et al. (2013) and numerical simulation results of plane two-dimensional model

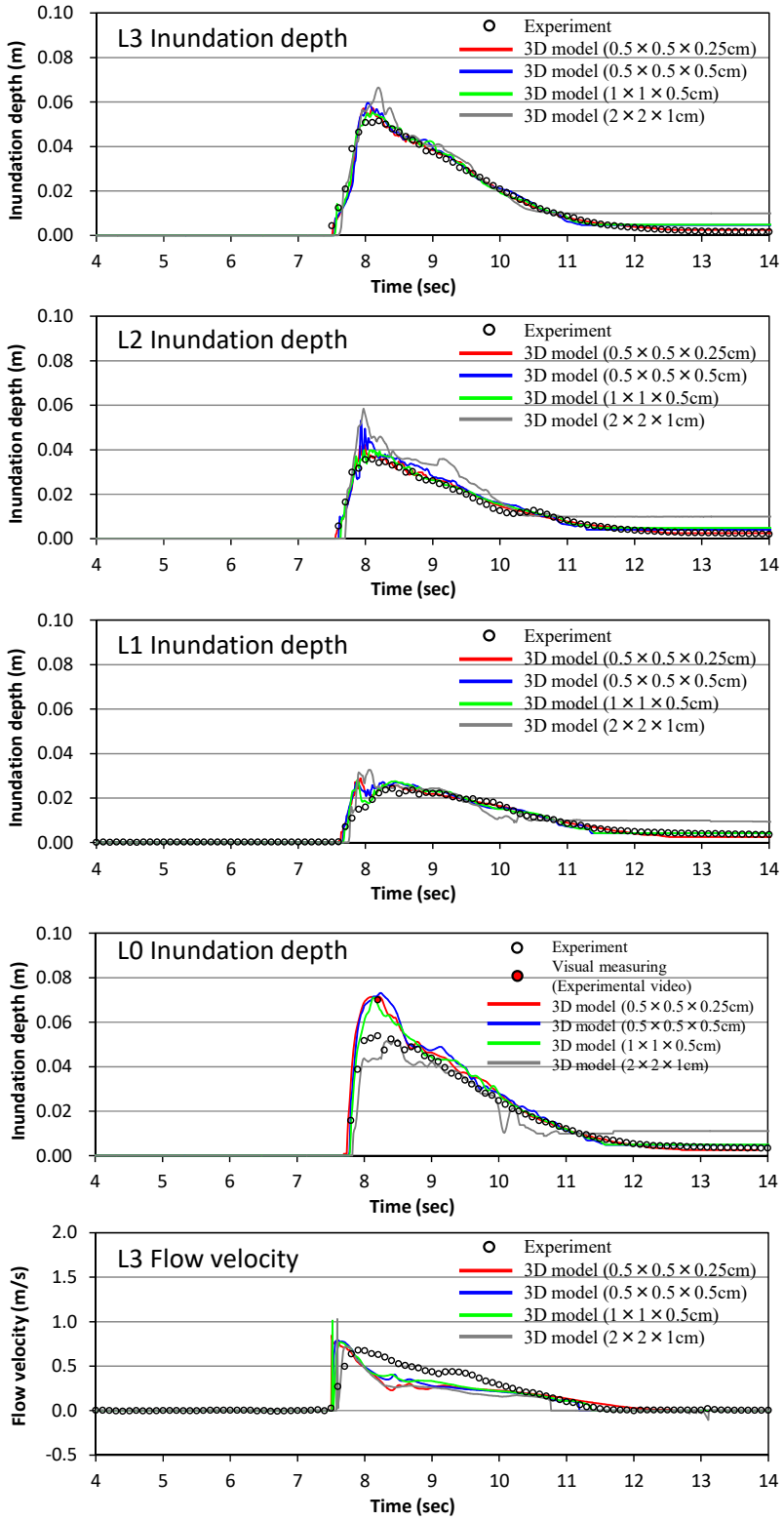

Figure 4.1.6-9 Time series of inundation depth and flow velocity by experimental results of Arimitsu et al. (2013) and numerical simulation results of three-dimensional model

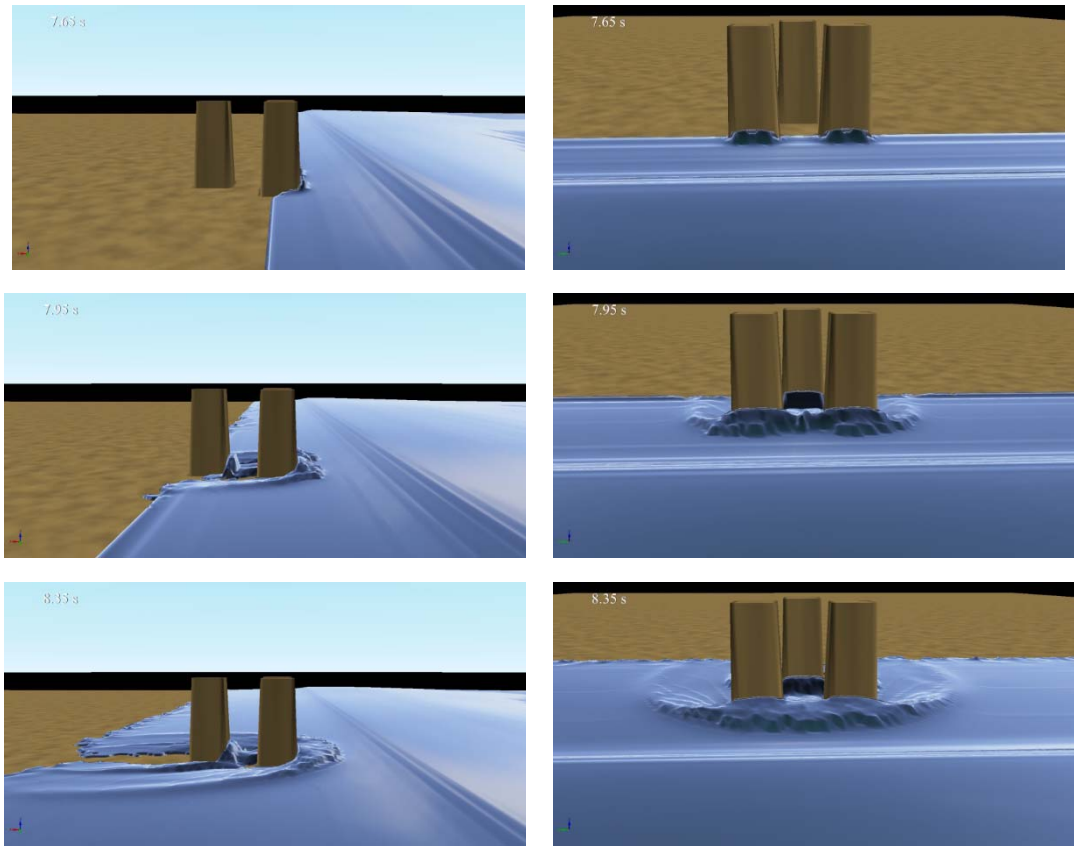

(a) Side-view (b) Front-view

Figure 4.1.6-10 Tsunami behavior around structures of three-dimensional model ($\triangle x \times \triangle y \times \triangle z$ = 1cm × 1cm × 0.5cm)

4.2. Calculation method for distribution of vertical displacement on sea bottom surface

4.2.1. Method proposed by Mansinha and Smylie (1971)

In the initial conditions for tsunami propagation calculation, it is necessary to configure the distribution of vertical displacement on the sea bottom surface. With respect to this vertical displacement distribution, methods proposed by Mansinha and Smylie (1971) as well as by Okada (1985) have been used for calculating the distribution of displacement of the surrounding ground accompanying earthquake fault motion, which assume that the ground where an earthquake occurs is an isotropic and homogeneous elastic body. Here, the method proposed by Mansinha and Smylie (1971) is shown below.

Displacement u_i of the surrounding area due to the amount of discrepancy Δu_i in arbitrary closed surface Σ of elastic half-space has been given below from Skeketee (1958).

$$u_i = \int_\Sigma \Delta u_j \left[\delta_{jk} \lambda \frac{\partial u_i^\ell}{\partial \xi_\ell} + \mu \left(\frac{\partial u_i^j}{\partial \xi_k} + \frac{\partial u_i^k}{\partial \xi_j} \right) \right] \nu_k \, dS \tag{4.2.1}$$

where, δ_{jk} is the Kronecker delta, λ and μ are Lame's constants, v_k is the normal direction cosine of *dS*, and u_i^j is displacement in direction *i* of points (x_1, x_2, x_3) due to units of power working in *j* direction at points (ξ_1, ξ_2, ξ_3).

For the local rectangular coordinates, as shown in Figure 4.2-1, the fault plane is extended and the line (strike) intersecting with the sea bottom surface is x_1, the point where the center of the longitudinal direction of the fault plane intersects with x_1 is the origin (*O*), and the x_2 axis proceeds to the right from *O*, and the x_3 axis downward. Also, the line passing through the center of the fault plane at *O* is the ξ axis (the ξ axis is within plane $x_2 - x_3$).

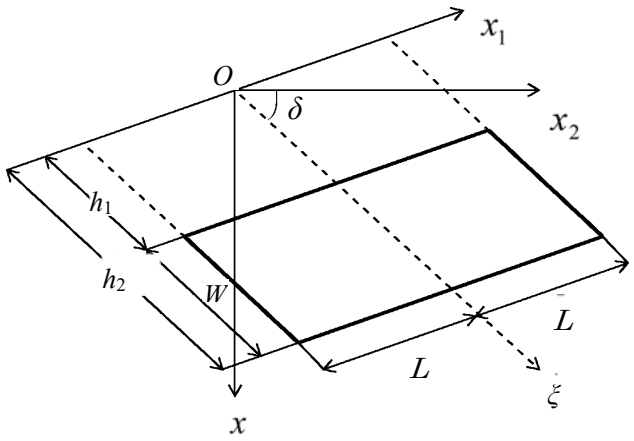

Figure 4.2-1 Fault geometry and coordinate system

The fault specifications are defined so that 2*L* is the fault length, h_1 the length from the origin along the ξ axis to the upper edge of the fault as shown in Figure 4.2-2, h_2 the length down to the lower edge of the fault (h_2-h_1 is width *W* of the fault), and δ the fault dip angle as measured clockwise from the x_2 axis. Also, as shown in Figure 4.2-3, λ is the angle formed by the slip direction and fault direction, *D* the magnitude of the slip, and ϕ the strike angle.

The ground is assumed to be Poisson solid ($\lambda = \mu$ with the Poisson ratio =1/4).

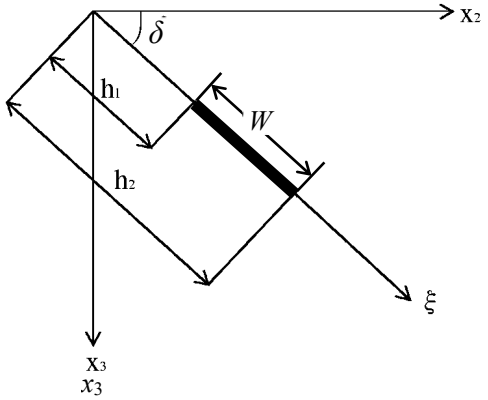

Figure 4.2-2 Vertical cross section in the local coordinate system

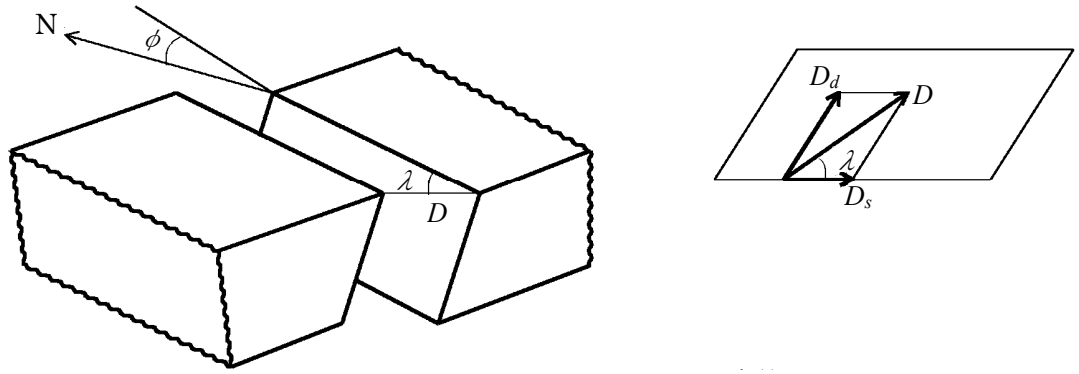

Figure 4.2-3 Definition of fault parameters

Assuming that:

$$\left.\begin{array}{ll} \text{Strike slip} & D_s = D\cdot\cos\lambda \\ \text{Dip slip} & D_d = D\cdot\sin\lambda \end{array}\right\} \tag{4.2.2}$$

Then for strike slip:

$$u_i = \mu D_s \int_\Sigma \left[\left(\frac{\partial u_i^1}{\partial \xi_2}+\frac{\partial u_i^2}{\partial \xi_1}\right)\sin\delta - \left(\frac{\partial u_i^1}{\partial \xi_3}+\frac{\partial u_i^3}{\partial \xi_1}\right)\cos\delta\right] dS \tag{4.2.3}$$

For dip slip:

$$u_i = \mu D_d \int_\Sigma \left[\left(\frac{\partial u_i^2}{\partial \xi_2}-\frac{\partial u_i^3}{\partial \xi_3}\right)\sin 2\delta - \left(\frac{\partial u_i^2}{\partial \xi_3}+\frac{\partial u_i^3}{\partial \xi_2}\right)\cos 2\delta\right] dS \tag{4.2.4}$$

If the equations (4.2.3) and (4.2.4) are converted to ξ coordinate systems, then for strike slip:

$$u_i = \mu D_s \int_{h1}^{h2} \int_{-L}^{L} \left[\left(\frac{\partial u_i^1}{\partial \xi_2} + \frac{\partial u_i^2}{\partial \xi_1} \right) \sin \delta - \left(\frac{\partial u_i^1}{\partial \xi_3} + \frac{\partial u_i^3}{\partial \xi_1} \right) \cos \delta \right] d\xi_1 d\xi \tag{4.2.5}$$

For dip slip:

$$u_i = \mu D_d \int_{h1}^{h2} \int_{-L}^{L} \left[2 \left(\sin \delta \frac{\partial u_i^2}{\partial \xi} - \cos \delta \frac{\partial u_i^3}{\partial \xi} \right) + \left(\frac{\partial u_i^3}{\partial \xi_2} - \frac{\partial u_i^2}{\partial \xi_3} \right) \right] d\xi_1 d\xi \tag{4.2.6}$$

where, $-L \le \xi_1 \le L$, $h_1 \le \xi \le h_2$. The variables are set as given below for integration of equations (4.2.5) and (4.2.6).

$$\left.\begin{aligned}
\xi_2 &= \xi \cos \delta \\
\xi_3 &= \xi \sin \delta \\
R^2 &= (x_1 - \xi_1)^2 + (x_2 - \xi_2)^2 + (x_3 - \xi_3)^2 \\
Q^2 &= (x_1 - \xi_1)^2 + (x_2 - \xi_2)^2 + (x_3 + \xi_3)^2 \\
r_2 &= x_2 \sin \delta - x_3 \cos \delta \\
r_3 &= x_2 \cos \delta + x_3 \sin \delta \\
q_2 &= x_2 \sin \delta + x_3 \cos \delta \\
q_3 &= -x_2 \cos \delta + x_3 \sin \delta \\
h^2 &= q_2^2 + (q_3 + \xi)^2 \\
k^2 &= (x_1 - \xi_1)^2 + q_2^2
\end{aligned}\right\} \tag{4.2.7}$$

Also, if the indefinite integral is assumed to be $u(\xi_1, \xi)$, then the definite integral is given as:

$$\left[\left[u(\xi_1, \xi) \right]_{-L}^{L} \right]_{h1}^{h2} = u(\xi_1, \xi) \| = u(L, h_2) - u(L, h_1) - u(-L, h_2) + u(-L, h_1) \tag{4.2.8}$$

If the amount of displacement is directions x_1, x_2, x_3 due to strike slip D_s is U_{1s}, U_{2s}, U_{3s} and the amount due to dip slip D_d is U_{1d}, U_{2d}, U_{3d}, the displacement of arbitrary points (x_1, x_2, x_3) is given using the following equations depending upon the pattern of the definite integral across the fault plane.

$$\begin{aligned}
12\pi \frac{U_{1s}}{D_s} = \Bigg\| \Bigg[& (x_1 - \xi_1) \left\{ \frac{2r_2}{R(R + r_3 - \xi)} - \frac{4q_2 - 2x_3 \cos \delta}{Q(Q + q_3 + \xi)} - \frac{3 \tan \delta}{Q + x_3 + \xi_3} + \frac{4q_2 x_3 \sin \delta}{Q^3} \right. \\
& \left. - 4q_2 q_3 x_3 \sin \delta \frac{(2Q + q_3 + \xi)}{Q^3 (Q + q_3 + \xi)^2} \right\} \\
& - 6 \tan^2 \delta \tan^{-1} \left\{ \frac{(k - q_2 \cos \delta)(Q - k) + (q_3 + \xi) k \cdot \sin \delta}{(x_1 - \xi_1)(q_3 + \xi) \cos \delta} \right\} \\
& + 3 \tan^{-1} \frac{(x_1 - \xi_1)(r_3 - \xi)}{r_2 R} - 3 \tan^{-1} \frac{(x_1 - \xi_1)(q_3 + \xi)}{q_2 Q} \Bigg] \Bigg\|
\end{aligned} \tag{4.2.9}$$

$$12\pi\frac{U_{2s}}{D_s}=\Big[\sin\delta\Big\{3\tan\delta\cdot\sec\delta\cdot\ell n(Q+x_3+\xi_3)-\ell n(R+r_3-\xi)-(1+3\tan^2\delta)\ell n(Q+q_3+\xi)\Big\}$$
$$+\frac{2r_2{}^2\sin\delta}{R(R+r_3-\xi)}+\frac{2r_2\cos\delta}{R}-2\sin\delta\frac{\{2x_3(q_2\cos\delta-q_3\sin\delta)+q_2(q_2+x_2\sin\delta)\}}{Q(Q+q_3+\xi)}$$
$$-3\tan\delta\frac{(x_2-\xi_2)}{Q+x_3+\xi_3}+2\frac{(q_2\cos\delta-q_3\sin\delta-x_3\sin^2\delta)}{Q}$$
$$+4q_2x_3\sin\delta\frac{\{(x_2-\xi_2)+q_3\cos\delta\}}{Q^3}-4q_2{}^2q_3x_3\sin^2\delta\frac{2Q+q_3+\xi}{Q^3(Q+q_3+\xi)^2}\Big]\Big\| \qquad (4.2.10)$$

$$12\pi\frac{U_{3s}}{D_s}=\Big[\cos\delta\Big\{\ell n(R+r_3-\xi)+(1+3\tan^2\delta)\ell n(Q+q_3+\xi)-3\tan\delta\sec\delta\cdot\ell n(Q+x_3+\xi_3)\Big\}$$
$$+\frac{2r_2\sin\delta}{R}+2\sin\delta\frac{(q_2+x_2\sin\delta)}{Q}-\frac{2r_2{}^2\cos\delta}{R(R+r_3-\xi)}$$
$$+\frac{4q_2x_3\sin^2\delta-2(q_2+x_2\sin\delta)(x_3+q_3\sin\delta)}{Q(Q+q_3+\xi)}+4q_2x_3\sin\delta\frac{\{(x_3+\xi_3)-q_3\}}{Q^3}\frac{\cos\delta}{\sin\delta}$$
$$-4q_2{}^2q_3x_3\cos\delta\sin\delta\frac{2Q+q_3+\xi}{Q^3(Q+q_3+\xi)^2}\Big]\Big\| \qquad (4.2.11)$$
(4.2.11)

$$12\pi\frac{U_{1d}}{D_d}=\Big[(x_2-\xi_2)\sin\delta\Big\{\frac{2}{R}+\frac{4}{Q}-4\frac{\xi_3x_3}{Q^3}-\frac{3}{Q+x_3+\xi_3}\Big\}$$
$$-\cos\delta\Big\{3\ell n(Q+x_3+\xi_3)+2\frac{(x_3-\xi_3)}{R}+4\frac{(x_3-\xi_3)}{Q}+4\frac{\xi_3x_3(x_3+\xi_3)}{Q^3}\Big\}$$
$$+\frac{3}{\cos\delta}\Big\{\ell n(Q+x_3+\xi_3)-\sin\delta\cdot\ell n(Q+q_3+\xi)\Big\}$$
$$+6x_3\Big\{\frac{\cos\delta}{Q}-\frac{q_2\sin\delta}{Q(Q+q_3+\xi)}\Big\}\Big]\Big\| \qquad (4.2.12)$$

$$12\pi\frac{U_{2d}}{D_d}=\Big[\sin\delta\Big[-\ell n(R+x_1-\xi_1)+\ell n(Q+x_1-\xi_1)-\frac{4\xi_3x_3}{Q(Q+x_1-\xi_1)}+\frac{3(x_1-\xi_1)}{(Q+x_3+\xi_3)}$$
$$+(x_2-\xi_2)^2\Big\{\frac{2}{R(R+x_1-\xi_1)}+\frac{4}{Q(Q+x_1-\xi_1)}-4\xi_3x_3\Big(\frac{2Q+x_1-\xi_1}{Q^3(Q+x_1-\xi_1)^2}\Big)\Big\}\Big]$$
$$-\cos\delta\Big[(x_2-\xi_2)\Big\{\frac{2(x_3-\xi_3)}{R(R+x_1-\xi_1)}+\frac{4(x_3-\xi_3)}{Q(Q+x_1-\xi_1)}+4\xi_3x_3(x_3+\xi_3)\Big(\frac{2Q+x_1-\xi_1}{Q^3(Q+x_1-\xi_1)^2}\Big)\Big\}$$
$$+6\tan^{-1}\Big\{\frac{(x_1-\xi_1)(x_2-\xi_2)}{(h+x_3+\xi_3)(Q+h)}\Big\}-3\tan^{-1}\Big\{\frac{(x_1-\xi_1)(r_3-\xi)}{r_2R}\Big\}+6\tan^{-1}\Big\{\frac{(x_1-\xi_1)(q_3+\xi)}{q_2Q}\Big\}\Big]$$
$$+6\Big[\frac{1}{\cos\delta}\tan^{-1}\Big\{\frac{(k-q_2\cos\delta)(Q-k)+(q_3+\xi)k\sin\delta}{(x_1-\xi_1)(q_3+\xi)\cos\delta}\Big\}$$
$$+x_3\Big\{\frac{(\sin^2\delta-\cos^2\delta)(q_3+\xi)+2q_2\cos\delta\sin\delta}{Q(Q+x_1-\xi_1)}+\frac{(x_1-\xi_1)\sin^2\delta}{Q(Q+q_3+\xi)}\Big\}\Big]\Big\| \qquad (4.2.13)$$

$$12\pi\frac{U_{3d}}{D_d}=\left[\sin\delta\left[(x_2-\xi_2)\left\{\frac{2(x_3-\xi_3)}{R(R+x_1-\xi_1)}+\frac{4(x_3-\xi_3)}{Q(Q+x_1-\xi_1)}-4\xi_3x_3(x_3+\xi_3)\left(\frac{2Q+x_1-\xi_1}{Q^3(Q+x_1-\xi_1)^2}\right)\right\}\right.\right.$$

$$-6\tan^{-1}\left\{\frac{(x_1-\xi_1)(x_2-\xi_2)}{(h+x_3+\xi_3)(Q+h)}\right\}+3\tan^{-1}\left\{\frac{(x_1-\xi_1)(r_3-\xi)}{r_2R}\right\}-6\tan^{-1}\left\{\frac{(x_1-\xi_1)(q_3+\xi)}{q_2Q}\right\}\Bigg]$$

$$+\cos\delta\left[\ell n(R+x_1-\xi_1)-\ell n(Q+x_1-\xi_1)-\frac{2(x_3-\xi_3)^2}{R(R+x_1-\xi_1)}-\frac{4\left\{(x_3+\xi_3)^2-\xi_3x_3\right\}}{Q(Q+x_1-\xi_1)}\right.$$

$$\left.-4\xi_3x_3(x_3+\xi_3)^2\left(\frac{2Q+x_1-\xi_1}{Q^3(Q+x_1-\xi_1)^2}\right)\right]$$

$$\left.\left.+6x_3\left[\cos\delta\sin\delta\left\{\frac{2(q_3+\xi)}{Q(Q+x_1-\xi_1)}+\frac{x_1-\xi_1}{Q(Q+q_3+\xi)}\right\}-q_2\frac{(\sin^2\delta-\cos^2\delta)}{Q(Q+x_1-\xi_1)}\right]\right]\right\| \tag{4.2.14}$$

where, displacement u_1,u_2,u_3 in dirctions x_1,x_2,x_3 is given as:

$$\left.\begin{aligned}u_1&=U_{1s}+U_{1d}\\u_2&=U_{2s}+U_{2d}\\u_3&=U_{3s}+U_{3d}\end{aligned}\right\} \tag{4.2.15}$$

For the global coordinates (calculation coordinate system), as shown in Figure 4.2-4, the origin is the same as for the (x_1,x_2,x_3) system. If the *X* axis takes direction E, the *Y* axis direction N, and the *Z* axis downward and φ (eastern route from the *Y* axis is positive) is the angle formed by the *Y* and x_1 axes, then the conversion of the amount of displacement (u_x,u_y,u_z) of the (X,Y,Z) system is given according to the following equation when (u_1,u_2,u_3) is the amount of displacement of the (x_1,x_2,x_3) system.

$$\left.\begin{aligned}u_x&=u_1\sin\phi+u_2\cos\phi\\u_y&=u_1\cos\phi-u_2\sin\phi\\u_z&=u_3\end{aligned}\right\} \tag{4.2.16}$$

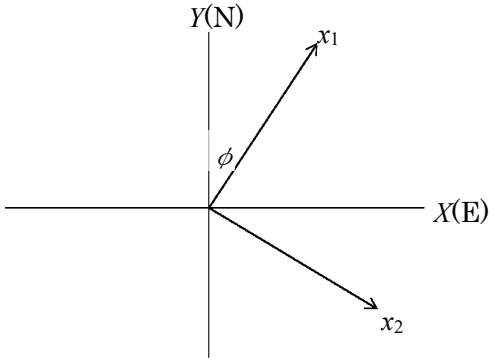

Figure 4.2-4 Local coordinate system and the calculation coordinate system

The equation (4.2.14) is the correction given by Okada (1985) of the misprint in the original

paper by Mansinha and Smylie (1971).

4.2.2. Method using three-dimensional sea bottom movement analysis

In cases where examinations are conducted of tsunami that take into consideration the effect that three-dimensional underground structures have on tsunami as well as the time change of sea bottom displacement, a method may be applied that uses analysis of sea bottom movements capable of taking into account three-dimensional heterogeneous underground structures (Tsuchiya et al., 2013). This method is presented below.

4.2.2.1. Three-dimensional sea bottom movement analysis

First, a three-dimensional sea bottom movement analysis is employed to calculate the time change in ground displacement from a ground motion analysis that takes into consideration three-dimensional heterogeneous underground structures.

The National Research Institute for Earth Science and Disaster Resilience's Ground Motion Simulator (GMS), which is a tool for ground motion analysis using a three-dimensional finite differential method, is one of calculation methods of ground motion analysis considering three-dimensional heterogeneous underground structures and time change of ground displacement. The time change in ground displacement may be calculated by a ground motion analysis that uses the earthquake ground motion analytical tool GMS to take into account three-dimensional heterogeneous underground structures.

The data on three-dimensional underground structures may be downloaded from, for example the National Research Institute for Earth Science and Disaster Resilience's Earthquake Hazard Station. These data include all land and sea areas around Japan, and may be used for ground motion analysis that takes into consideration three-dimensional underground structures.

4.2.2.2. Tsunami analysis accounting for time change in sea bottom displacement

A method that sets the time change of ground displacement is shown below.

Continuity equation:

$$\frac{\partial(\eta-\zeta)}{\partial t}+\frac{\partial M}{\partial x}+\frac{\partial N}{\partial y}=0$$

where, x, y are horizontal axes, t is time, η is water surface elevation, M, N are discharge fluxes in the x- and y- directions, and ζ is sea bottom vertical displacement.

Discretization of the above continuity equation gives the following.

$$\eta_{i,j}^{k+1} = \eta_{i,j}^{k} + \left(\zeta^{k+1} - \zeta^{k}\right) - \frac{\Delta t}{\Delta x}\left(M_{i+1/2,j}^{k+1/2} - M_{i-1/2,j}^{k+1/2}\right) - \frac{\Delta t}{\Delta y}\left(N_{i,j+1/2}^{k+1/2} - N_{i,j-1/2}^{k+1/2}\right)$$
$$= \eta_{i,j}^{k} + \Delta\zeta^{k+1} - \frac{\Delta t}{\Delta x}\left(M_{i+1/2,j}^{k+1/2} - M_{i-1/2,j}^{k+1/2}\right) - \frac{\Delta t}{\Delta y}\left(N_{i,j+1/2}^{k+1/2} - N_{i,j-1/2}^{k+1/2}\right)$$

where, k is number of calculation steps.

In cases where the time change of sea bottom displacement is taken into account, the results of calculations of three-dimensional sea bottom movement analyses are used to find the moment-by-moment vertical displacement increase amount $\Delta\zeta$ so that this may be given.

4.2.2.3. Case studies of tsunami analyses using three-dimensional sea bottom movement analysis (Tsuchiya et al., 2013)

Case studies of earthquake ground motion analyses, which took into account three-dimensional heterogeneous underground structures using GMS, as well as case studies of tsunami analyses, which used these calculation results, are presented below.

(1) Tsunami source model

The target earthquake is the 1923 Kanto earthquake, and the tsunami source model by Aida (1993) is adopted. The fault plane is represented by a total of 732 point sources (arranged at intervals of 2.5km), the rupture point was configured as 35.3°N and 139.1°E, depth as 11.7km (compiled by the National Astronomical Observatory, 2007), the rupture velocity as 3.0km/s, hypocenter time function as a triangular pattern, and the rise time for point sources as 4 seconds.

(2) Underground structure model

Three types of underground structure models have been created: the uniform physical properties model, horizontal stratification model, and three-dimensional underground structure model. For the values of physical properties in the uniform physical properties model, ρ was configured the value by the Central Disaster Management Council (2002), the Q value was the value by Sato et al. (1999), Vs was configured using $\mu=\rho V_s^2$ with rigidity $\mu=4.00\times10^{10}\mathrm{N/m^2}$, and V_p was $V_p=\sqrt{3}Vs$. In addition, the values for the physical properties in the horizontal stratification model have been configured with reference to Sato et al. (1999). For the values of the physical properties in the three-dimensional underground structure model, data on boundary surface and depth distribution for three layers beginning with the ground surface have been prepared by synthesizing with Suzuki (2002) as well as Yamada and Yamanaka (2003), and layers from the fourth and later layers from the ground surface have been set with reference to Sato et al. (1999).

(3) Conditions for calculation of three-dimensional sea bottom movements

The computation region is a range extending 240km east to west and 240km north to south encompassing the tsunami source, and the depth is between 0km and 104km. Of this, the nonreflecting boundary is 24km to the side and 24km downward. The grid size is $\Delta x=\Delta y=\Delta z$=400m, extending from a depth of 0km to 44km, and $\Delta x=\Delta y=\Delta z$=1,200m for grid sizes deeper than 44km. The computation time interval is 0.02 seconds, and the simulating time is up to 180 seconds after the earthquake occurred.

(4) Results of calculation of three-dimensional sea bottom movements

The final vertical displacement of GMS results was compared with the method proposed by Mansinha and Smylie (1971), and there was a maximum difference of 15%, excluding points far from the tsunami source. Also, no clear trends were respect to differences in methods or locations.

In addition, in a time series of vertical displacement in underground structure models as shown in Tsuchiya et al. (2013) Figure-5, areas also emerge where maximum amplitude of displacement is twice that of the final displacement. Moreover, the amplitude increased at the peak with the horizontal stratification model and three-dimensional underground structure model in comparison to the uniform physical properties model. When the maximum displacement at point D is compared, the three-dimensional underground structure model is approximately 1.5 times that of the uniform physical properties model, but the cycle of the displacement waveform is less than 10 seconds, and the infulense of such displacement on the tsunami will be only in the area vely close to the wave source region.

However, the cycle of the displacement waveform that occurs here is thought to depend significantly on the source time function (rise time at point sources), an appropriate configuration needs to be set in keeping with the target earthquake.

(5) Tsunami calculation conditions and calculation cases

According to the method of Manshinha and Smylie (1971) and the results of analyses and calculations of three-dimensional sea bottom movements given in (4) sets an initial condition, is given to perform tsunami calculations.

The computation region is a range that encompasses the area from the Chiba Prefecture to Aichi Prefecture. The grid sizes have been subdivided successively (1,600m ~ 800m ~ 400m ~ 200m ~100m), and the coastline from Chiba Prefecture to Aichi Prefecture used a land run-up model with a grid size of 50m. Also, the conditions of the offshore boundary were a nonreflecting boundary. The time interval was set at 0.5 seconds, and the simulating time extended up to six hours after the earthquake occurred.

Tsunami analyses were performed of a total of five cases: Case 1 which used vertical

displacement by Mansinha and Smylie (1971), Case 2s which used final vertical displacement in the GMS results using the uniform physical properties model, Case 2d which used the time change of vertical displacement in the GMS results using the uniform physical properties model, Case 3d which used the time change of vertical displacement in the GMS results using the horizontal stratification model, and Case 4d which used the time change of vertical displacement in the GMS results using the three-dimensional underground structure model.

(6) Tsunami calculation results

1) Impact of time change in sea bottom displacement on tsunami

A comparison was conducted of the tsunami results from Case 1, which use the method of Mansinha and Smylie (1971), as well as Case 2d and Case 2s, which used GMS results based on the physical properties model, and the impact, which time change in sea bottom displacement has on the maximum water level of a tsunami, was examined.

From the time series of the water level of Case 1 and Case 2d as well as time series of the sea bottom displacement by GMS result, shown in Tsuchiya et al. (2013) Figure-8, the water level in Case 2d appears to be greater than that in Case 1 at first glance, but the ground itself has risen, so a tsunami does not necessarily occur that is excessively larger than that in Case 1 immediately after an earthquake occurs. Also, at any points as well, the water level in Case 2d corresponds to the ground formation immediately after an earthquake occurs, but a significant difference is no longer seen when compared to Case 1 as the ground deformation converges. This is because the initial displacement waveform has a 10-second period and there is almost no contribution to the tsunami, and the long-period wave, which occurs due to the final displacement distribution, accounts for the principal component of the tsunami. Also, a comparison of the maximum water levels at points along the coastline from Tokyo Bay to Sagami Bay showed that the maximum water levels at points in Case 2d were at the most 10% greater than those in Case 1, and, even when compared with Case 2s, the difference was a maximum of 10% (mean of 5%).

2) Impact of differences in underground structures on tsunami

Comparisons were performed of the results of tsunami calculations from Case 1, which use the method proposed by Mansinha and Smylie (1971), and Cases 2d, 3d and 4d, which use the GMS results based upon the three types of underground structure models, to examine the effect that differences in underground structures have on tsunami.

The results showed that the maximum water levels of the three respective types of underground structure models were at the most 15% (mean of 5%) higher than that in Case 1, and, even when compared with the three types of underground structure models, the maximum difference was 20% (mean of 5%).

4.3. Wave front condition, calculation grid size, friction coefficient and coefficient of eddy viscosity

4.3.1. Wave front condition

Moving boundaries need to be configured to represent sea bottom exposure accompanying tsunami run-up onto land and drawback. The method of Iwasaki and Mano (1979) has been widely used for the algorithm and discrete format of moving boundaries. This method approximates the topography in the area of the tsunami head in a stepwise fashion for grid size widths and distinguishes between whether or not there is water at the stage at each time step in the calculation process. The specific points are presented below (Figure 4.3.1-1).

- The tsunami head is located at the boundary between the cell in which the sum of the water depth and maximum still water depth at the cell boundaries (four sides) is positive, and the cell in which the sum is either zero or negative.
- The total water depth at the cell boundary for calculating the flow rate per unit width is given as the sum of the still water depth at the cell boundary and the higher water depth in the two neighboring cells.
- The flow rate per unit width is estimated using the momentum equation by assuming that the line connecting the water level of the wave head and the bottom height in the neighboring cell gives the surface slope to a first-order approximation. When the total water depth is zero or negative, the flow rate per unit width should be assumed to be zero.
- When the total water depth approaches zero, the advection term is neglected.

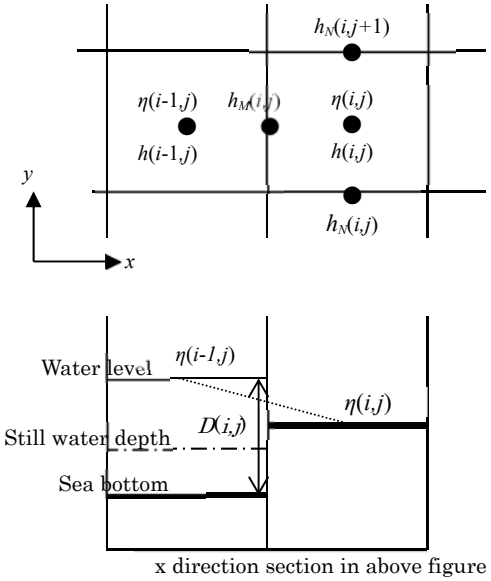

Legend
i,j : Cell number in direction of x,y
η : Water level
h : Still water depth (Addition of the subscript of M and N is water depth in the boundary.)
D : Total water depth ($\eta+h$)
M,N : Discharge flux

Figure 4.3.1-1 Iwasaki and Mano (1979)

Kotani et al. (1998) revised the above calculation method and proposed the following method (Figure 4.3.1-2).

- The total water depth for calculation of the flow rate is the difference between the water level at the head and the ground height at dry calculation points. In cases where this difference is negative, the flow rate is zero (no run-up).
- In cases where the total water depth is zero or below a minimum value when calculating the advection term, only items where the total water depth is the denominator are omitted and the advection term is calculated.

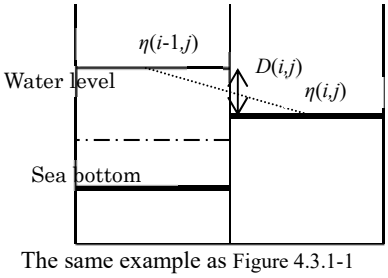

Figure 4.3.1-2 Kotani et al. (1998)

4.3.2. Grid sizes

4.3.2.1. Grid size in the propagation area

If the sea bottom topography is straightforward, the grid size can be 1/20 or less than one wavelength of a spatial tsunami (Hasegawa et al., 1987), However, it is the complex sea bottom topography, attention needs to be given to the following and other matters that have been pointed out.

- It is important to accurately express wave refraction in order to improve the precision of tsunami propagation calculations (Sayama et al., 1986).
- The actual topography is unable to be sufficiently represented using rough grid sizes, and calculation results will often shift very greatly (Imamura and Li, 1998).

Here, for the actual topography off the coast of Shimoda, the method by Goto is used to conduct an empirical examination and show the impact that calculation grid sizes for sea areas have on the maximum water level ascent in the propagation process.

(1) Study sea area and examined tsunami

1) Study sea area

• The area off the coast of Shimoda, where it is considered difficult to represent refractive phenomena resulting from the sea bottom topography, is the sea area to be examined.

• The area for which calculations are to be performed is the sea area that is approximately 16km east to west and 24km north to south extending from near the Izu Peninsula to the northern part of Shimoda City.

2) Examined tsunami

The 1854 Ansei-Tokai earthquake and tsunami will be examined.

(2) Grid sizes and boundary conditions

1) Grid sizes

Uniform grid sizes have been configured for six cases using 50m, 100m, 200m, 400m, 800m, and 1600m.

2) Boundary conditions

• Incident wave at open boundary: The results of calculations of the 1854 Ansei-Tokai earthquake and tsunami using the Ishibashi (1976) model implemented across a wide area are provided along an open boundary.

• Shoreline: Vertical wall

(3) Comparisons of maximum water level ascent

1) Tsunami propagation route

The tsunami propagation paths, obtained by calculation each grid size, were compared in Figure 4.3.2-1. The propagation times and propagation paths in cases where the grid sizes were set at 50m, 400m and 800m are shown in Figure 4.3.2-2 along with the water depths. At the results, knowledge has been gained such as:

• Because of the geographical features of this sea area, tsunami head toward Shimoda City while going around in the process of propagation, so wave refraction needs to be reproduced with good precision for accurate calculations.

• Calculation of wave refraction having good accuracy are possible if 400m grids are used for water depths of 100m and grid sizes ranging from 200 ~ 50m for water depths of 50m or shallower.

2) Maximum water level ascent along wave direction lines

From the relation between the maximum water level ascent and grid size along the propagation paths (Figure 4.3.2-3), almost no impact is observed even when grid sizes of 800m are set for water depths of 100 m or greater, but grid sizes need to be set at 200m or less for water depths between 50m and 100m, and grid size set at 50m for water depth of 50m or shallower.

3) Summary

To obtain a convergence value, it is necessary to select grid sizes on the order of:

Shallow sea areas 100m or deeper : Maximum 800m

Waters depths between 100 ~ 50m : Maximum 200m

Shallow areas of 50m or less : 100 ~ 50m

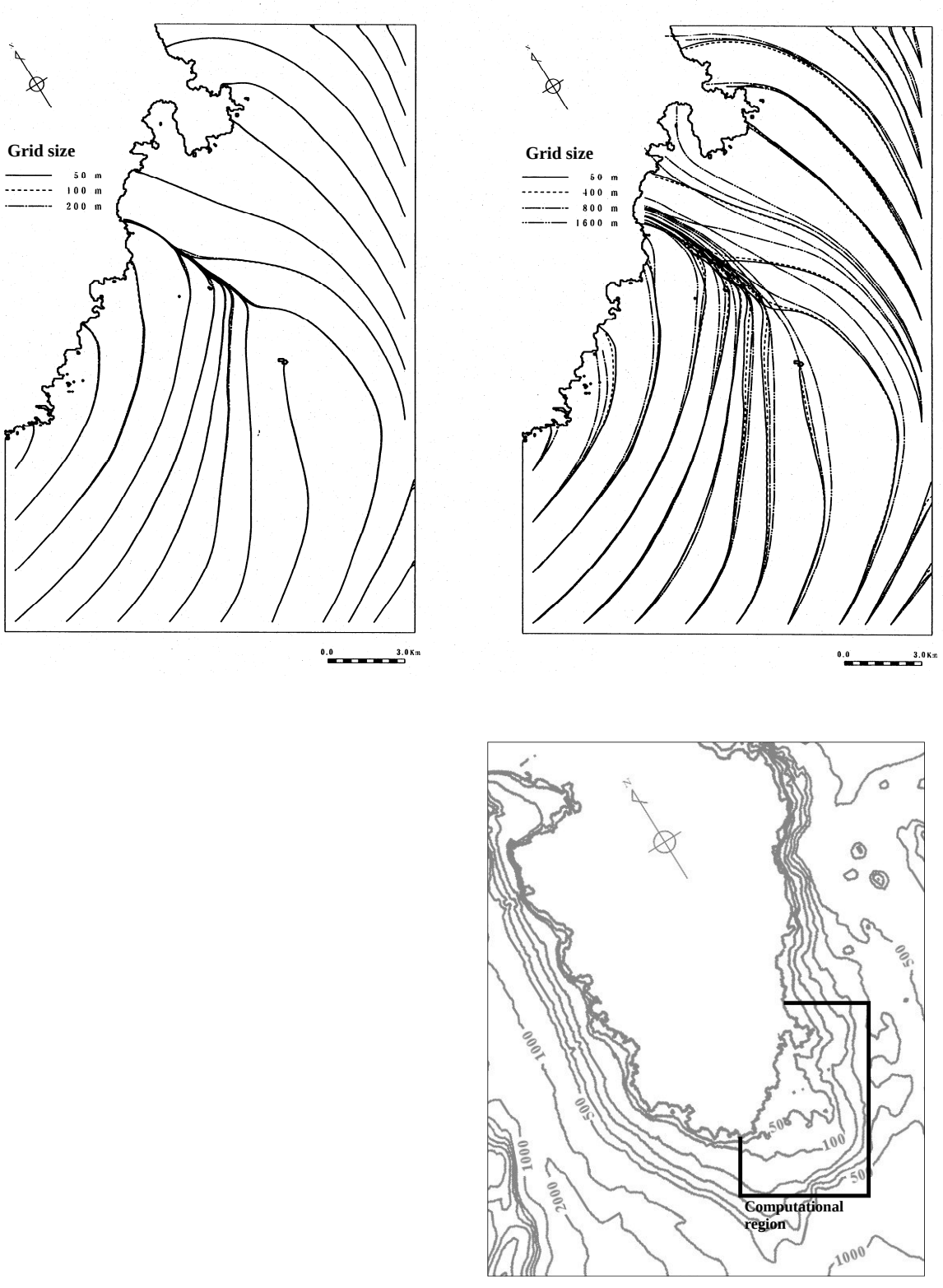

Figure 4.3.2-1 Comparison of tsunami propagation

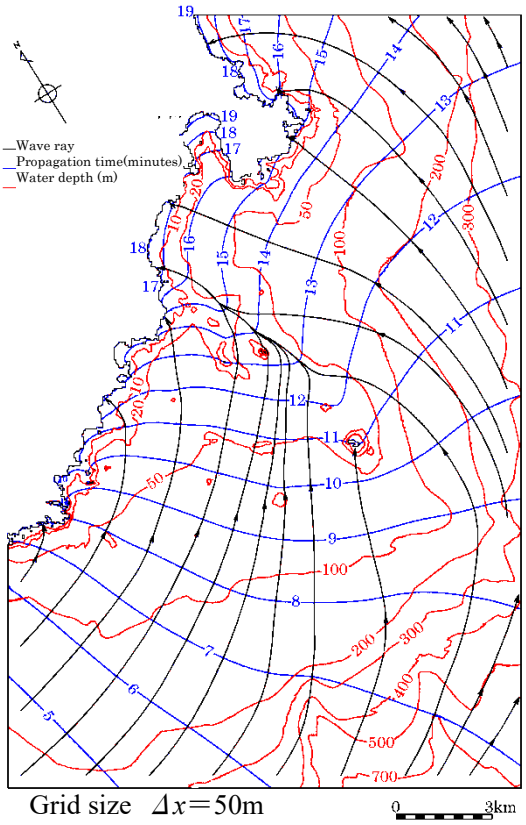

Grid size $\Delta x = 50$m

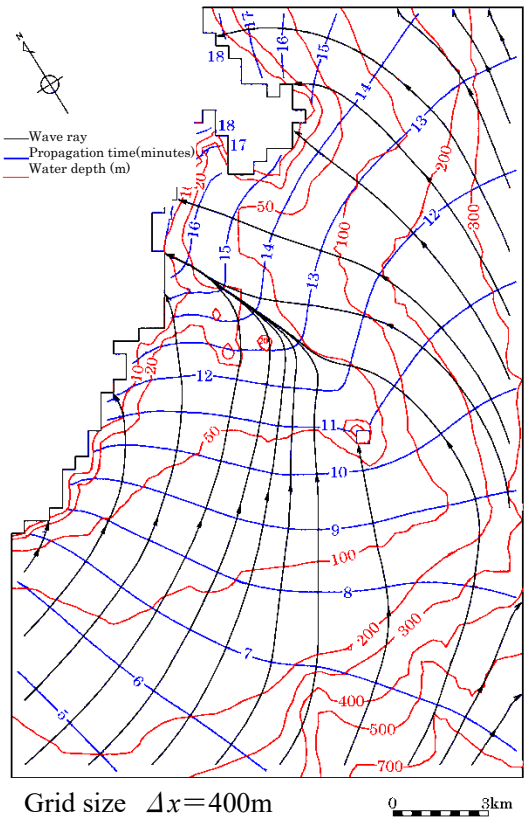

Grid size $\Delta x = 400$m

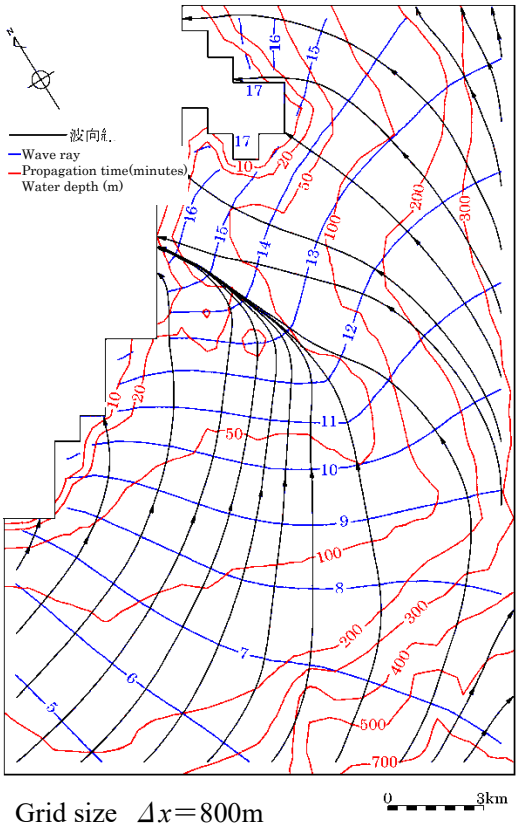

Grid size $\Delta x = 800$m

Figure 4.3.2-2 Water depth, propagation time, and propagation path

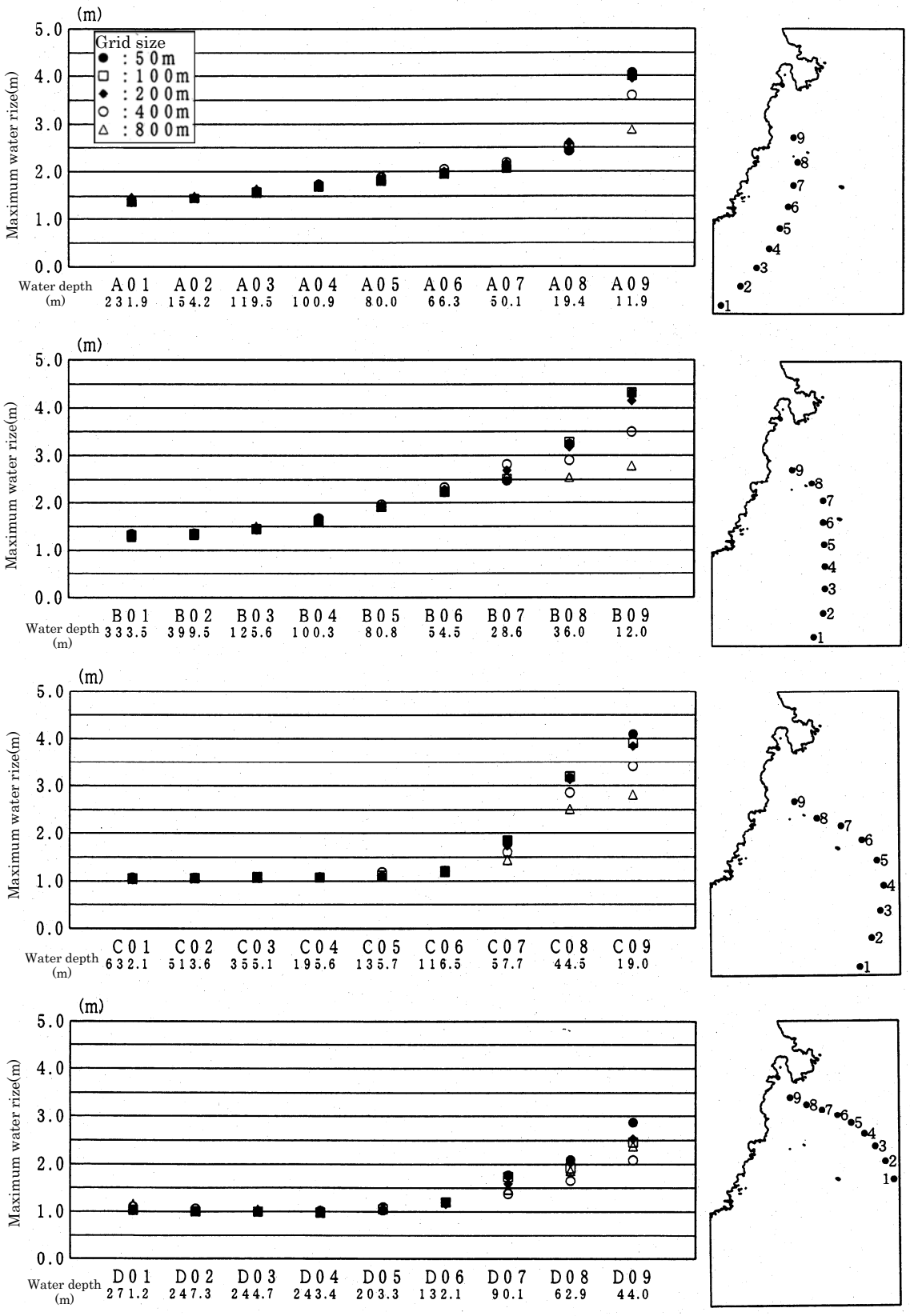

Figure 4.3.2-3 Relation between the maximum water level ascent and grid size along propagation path

4.3.2.2. Grid size of sea areas around target sites

(1) Harbours and ports

Inagaki et al. (2001) analyzed the influence of grid size to the maximum water level ascent inside a ports, such as the facility of the nuclear power plants.

The following characteristics from the results of a comparison of flow patterns and maximum water level ascent.

- The water level inside a port rises as the grid sizes are greater, and, particularly in cases where a port or harbor opening is modeled as one grid (Δx=150m), this tendency is pronounced.
- When focusing on current velocity vectors and water level distribution, the smaller the grid size around the port opening, the more complex the flow patterns become. Futhermore the characteristics of the water level distribution are also in harmony with differences in the flow patterns.
- As for the time series of the water level and current velocity in the center of the port opening, the difference when the grid size is set at 75m or less is not that pronounced, but there is clearly a difference in the velocity distribution pattern.
- In the case of the grid size of 25m and 150m phase was a significant difference.

The reason why smaller grid sizes result in lower water levels inside a port appears to be because the smaller the grid size is, the more pronounced the vortex at the port opening and the accompanying dead water region become and the inflow width of the main channel narrows, inhibiting entry of flow accompanying the tsunami.

Judging from the aforementioned analytical results, even where the grid size per wavelength satisfies the basic conditions (in this model, where the number of grids per wavelength is 20 even for cases where the incident wave period is set at 5 minutes), cases where a comparatively large grid width is set in comparison to the port opening width are subject to significant constraint in the flow pattern, so it is desirable to create a model of the area around the harbor using grid sizes that are 1/5 of the port opening width.

(2) In the case of V-shaped harbours

Noticeably higher run-up height record of historical tsunami have been seen in small V-shaped harbors along deeply indented coastlines in comparison with the surrounding area. At a minimum, detailed grid models need to be used to verity such high water records. Also, adjusting the run-up height with rough grid mode is to high levels on the records of historical tsunami may be overestimate the fault slippage, so sea areas where inappropriate grids are used should be excluded from the area where reproducibility will be assessed.

Within such a background, Inagaki et al. (2001) analyzed the sensitivity of small V-shaped

harbors where significant tsunami hight is thought to occur, and the following knowledge was gained with respect to grid partitioning.

The variables indicated below are utilized in arranging the calculation results.

Intra-harbor mean wave length : $Lv(=T(gh/2)^{1/2})$

Mean wave length from harbor center to back : $Lo(=T(gh/4)^{1/2})$

where, T is incident wave period, g is acceleration of gravity, h is water depth at the harbour mouth, and λ is distance from harbor mouth to the innermost area, and Δx is spatial grid size. Characteristics observed in the relationship between grid size and maximum water level ascent are presented below.

1) Distribution of maximum water level rise inside harbors

In most cases, the maximum water level rise inside a harbor tends to be more amplified in the innermost area than in the center of the harbor, regardless of harbor shape or length of the incident wave. However, in cases where ratio Lv/λ between the intra-harbor mean wave length Lv and distance λ to the innermost area of the harbor is 20, there is almost no amplification for the harbor as a whole. In cases where Lv/λ is the same even though the length of the input wave and the length to the innermost area of the harbor are different (for example, λ=1,000m : T=5min, λ=2,000m : T=10min, λ=4,000m : T=20min), the maximum water level rise is almost the same when the horizontal distance is made dimensionless.

2) Distribution of maximum water level rise from harbor mouth to center

Within the range of the grid size as configured here, the maximum water level ascent does not vary significantly, and, if the grid size Δx is set at 1/40 of the intra-harbor mean wave length, the calculation may be performed within an error of 5% inspite of the value of Lv/λ.

3) Maximum water level rise at the innermost part of the harbor

The maximum water level ascent at the innermost part of the harbor depends significantly on the relationship between the intra-harbor mean wave length Lv and the distance from the harbor mouth to the innermost part of the harbor.

• In the case of $Lv/\lambda < 6$

The incident wave amplifies suddenly at the innermost part of the harbor, and the calculation results vary greatly depending upon grid size. It is necessary to gradually bring the grids smaller from the center of harbor and to set a grid size of 1/100 or less of Lo at the innermost part of the harbor.

• In the case of $6 \leq Lv/\lambda < 10$

Although the sudden amplification of the incident wave occurs slightly at the innermost part of the harbor, if a grid size that is 1/50 of Lo is used, then it is possible to keep calculation error at around 5%.

• In the case of $10 \ll Lv/\lambda$

There is gentle amplification of the incident wave, and, if a grid size is utilized that is 1/40 of mean wave length *Lo* at the innermost area of the harbor from the central area, then the calculation may be performed such that error is less than 5%.

(3) Run-up area

According to Goto and Shuto (1983), the grid size mean the head of run-up waves is reguired to satisfy the condition; $\Delta x/\alpha g T^2 < 4\times10^{-4}$ (Δx is gird size, T is wave period, α is bottom slope) Here, the range from the shallow sea area to the run-up area is the focus, and a sensitivity analysis is conducted of the grid size to obtain a guide for error that appears to include the grid size used for these areas.

1) Governing equations and numerical scheme

[1] Governing equations

The following basic equations are used.

• Continuity equation

$$\frac{\partial \eta}{\partial t} + \frac{\partial M}{\partial x} = 0$$

• Momentum equation

$$\frac{\partial M}{\partial t} + \frac{\partial}{\partial x}\left(\frac{M^2}{D}\right) + gD\frac{\partial \eta}{\partial x} + (gn^2 / D^{1/3})\frac{M|M|}{D^2} = 0$$

where, x is spatial coordinates for a static water surface, h is still water depth, D is total water depth expressed by $D=h+\eta$, t is temporal coordinates, g is the gravitational acceleration, M is flow rate per unit width in the x direction, η is the vertical displacement of water surface above the still water surface, and n: Manning's coefficient of roughness.

[2] Numerical scheme

The staggered leapfrog method is the basis for the numerical scheme, and the first-order upwind difference is applied for the advection term.

2) Examination conditions

The examination model is a one-dimensional channel with a uniform depth and a slope in the edge of channel as shown in Figure 4.3.2-4. The incident wave is given by having sinusoidal wave at semi-amplitude 2a be the initial tsunami shape, and this initial tsunami shape propagates as sinusoidal waves of semi-amplitude along the coast and out to sea, respectively. Also, consideration is given so that there is no noise in the calculation by setting a sufficient propagation distance towerd offshore.

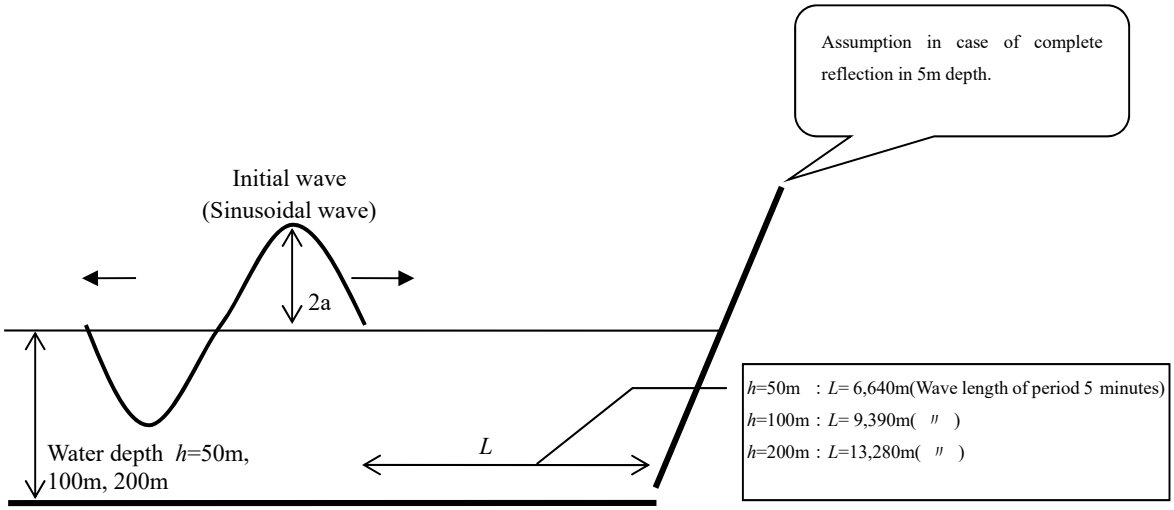

Figure 4.3.2-4 Initial wave and target topography

The examination conditions are shown in Table 4.3.2-1. According to Goto and Shuto (1983) when error within 5% is permissible, the grid size at the wave head needs to utilize Δx=1.27m for a 3-minute period, Δx=3.53m for a 5-minute period, and Δx=14.13m for a 10-minute period with respect to the grid size at the wave head. Moreover, in order to obtain a solution that generally coincides with the theoretical solution, it is necessary for the grid size to be approximately 1/4 grid size described previously when reading from the diagram shown by Goto and Shuto (1983). Accordingly, the minimum grid sizes were set at 1m for the 3- and 5-minute periods, and 2m for the 10-minute period to investigate the sensitivity of the respective grid sizes as the grid size was gradually increased up to 400m. Also, comparisons were made of cases where these grid sizes were combined to make uneven intervals.

Table 4.3.2-1 Examination conditions

Items	Contents
Amplitude and waveform of incident wave	The sinusoidal wave of the half amplitude 2m is given to the offshore boundary as initial wave.
Period T of incident wave	3, 5, 10 minutes
Wavenumber of incident wave	One wave given as initial wave
Slope of sea bottom	1/100
Manning's coefficient of roughness n	$0.03 m^{-1/3} \cdot s$
Grid size Δx	1 ~ 400m(T=3,5 minutes) 2 ~ 400m(T=10 minutes)

3) Results of sensitivity analysis

According to the results of the sensitivity analysis, the knowledge presented below was obtained. However, the correct solution for the maximum water level rise was a "convergence solution" for the value where the grid size was gradually reduced and the maximum water level ascent settled at a level that was almost constant. In addition, the convergence solution for the case of uneven intervals between grids also used this value.

[1] Case of uniform grid size

- If the error of the maximum water level ascent is kept held at about 5%, the grid size for calculation of wave run-up is reguired to be

  16m for a 3-minute period,

  20m for a 5-minute period,

  25m for a 10-minute period, as shown in Table 4.3.2-2.
- Similarly, if the grid size for a case of complete reflection is a period of 5 minutes or more is about 200m, then the error will be within 5% even using a grid size of 200m (Table 4.3.2-3).
- Contrary to Goto and Shuto (1983) which omitted bottom friction, in cases where the roughness coefficient is set at n =$0.03 m^{-1/3} \cdot s$, the grid size may be configured slightly larger, and, in order to keep error of the maximum water level ascent at about 5%, it is sufficient to set the configuration so that grid size Δx is $\Delta x / \alpha g T^2 \leq 7 \times 10^{-4}$ (Figure 4.3.2-5).

Table 4.3.2-2 Ratio to convergence solution of the maximum water level ascent

(Offshore depth: 50m, n =0.03m$^{-1/3}$・s)

Grid size Δx (m)	Run-up onto sloping land			Complete reflection		
	Period T(minute)					
	3	5	10	3	5	10
1	1.00	1.00			1.00	1.00
2	1.03	1.00	1.00		1.00	1.00
4	0.99	0.99	1.00		1.00	1.00
8	0.97	0.98	0.99		1.00	1.00
10	0.96	0.98	0.98		1.00	1.00
16	0.95	0.95	0.99		1.00	1.00
20	0.91	0.95	0.98		1.00	1.00
25	0.92	0.94	0.95		1.00	0.99
50	0.85	0.88	0.92		1.02	0.98
100	0.78	0.79	0.90		1.03	0.96

Table 4.3.2-3 The maximum grid size when error of the maximum water level ascent is assumed to be 5%

(unit(m), n = 0.03 m$^{-1/3}$s)

Offshore depth (m)	Run-up onto sloping land			Complete reflection		
	Period T(minute)					
	3	5	10	3	5	10
50	16	20	25	—	200	200
100	20	25	25	—	200	400
200	25	25	50	—	200	400

Note) -: The numeric vibration is caused and the evaluation is impossible.

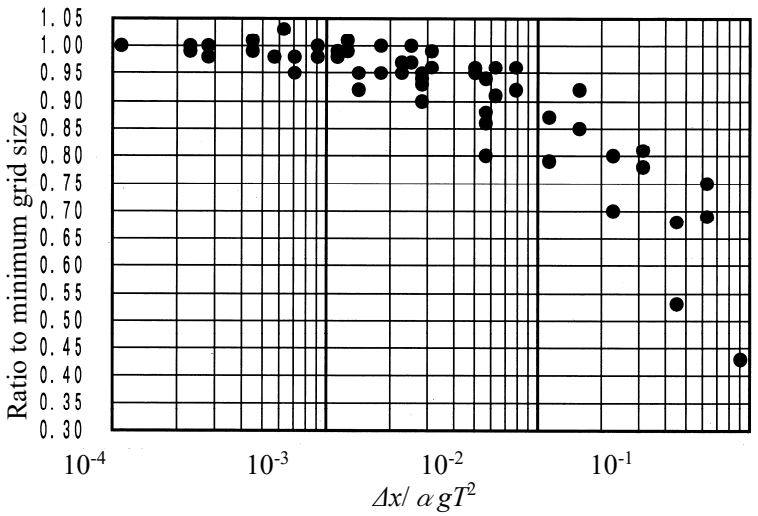

Figure 4.3.2-5 Relation between ratio to convergence solution of the maximum water rise and parametere ($\Delta x/\alpha gT^2$) of Goto and Shuto(1983)

[2] Case of nonuniform grid sizes

- For periods of 5 minutes or longer, if an appropriate grid size is selected from the partition patterns shown in Figure 4.3.2-6, then it is possible to hold calculation error to within 5% (see Table 4.3.2-4).
- In the case of a 3-minute period, in order to kept calculation error within 5%, it is often necessary to use a finer grid size than that patterns shown in Figure 4.3.2-6 (Table 4.3.2-4).

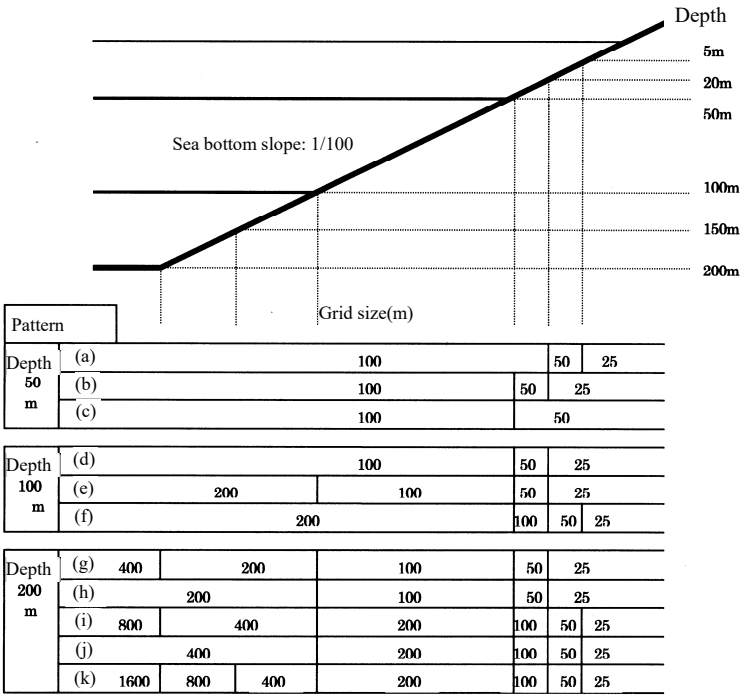

Figure 4.3.2-6 Grid size pattern of comparative calculation

Table 4.3.2-4 Relation between grid size pattern and the maximum water level ascent

Offshore depth (m)	Grid size Pattern	Run-up onto sloping land			Complete reflection		
		Period T(minute)					
		3	5	10	3	5	10
50	(a)	0.87	0.91	0.95	1.00	1.02	0.99
	(b)	0.92	0.94	0.97	1.02	1.00	1.00
	(c)	0.85	0.88	0.92	0.98	1.02	0.99
100	(d)	0.93	0.97	0.98	1.00	0.97	0.98
	(e)	0.93	0.97	0.98	1.00	1.03	0.99
	(f)	0.90	0.94	0.97	0.94	1.05	0.99
200	(g)	0.99	1.00	1.00	0.92	1.03	0.99
	(h)	0.98	0.99	1.00	0.99	1.06	0.99
	(i)	0.93	0.98	0.99	0.66	1.02	0.97
	(j)	0.96	0.96	0.98	0.81	1.06	1.00
	(k)	0.75	0.93	1.00	0.58	0.84	1.04

4) Energy balance in calculation

The calculation error was estimated by the energy balance in run-up calculation using uniform grids, when the convergence solution was obtaind. Energy balance error when the maximum water level ascent emerges is shown below. From these results, the energy balance error reaches approximately 10% in the case of a 3-minute period, but it may be observed that error will be below 5% even for a 100m spatial grid size with a period of 5 minutes or longer, and there are no issues present.

Table 4.3.2-5 Energy balance error

Period (minute)	Grid size (m)	Energy balance error (%)
3	1	11.3
	16	10.6
	100	12.8
5	1	2.4
	20	2.8
	100	5.0
10	2	0.9
	25	0.8
	100	1.1

5) Methods for an exact solution (Nagano et al., 1989)

Using the follow-up approach suggested by Richardson (Fujikawa, 1982), it is possible to estimate an exact solution for a differential equation from an approximate solution derived using numerical calculation. However, the exact solution referred to here is the convergence value of numerical solutions when grid size approaches the limit of zero.

u represents the exact solution and the approximate solutions for grid sizes Δx_1, Δx_2, and Δx_3 are u_1, u_2, and u_3 respectively. Assuming that the discretization error is proportional to the Δx power, then the equations are expressed as:

$$u - u_1 = A(\Delta x_1)^p$$
$$u - u_2 = A(\Delta x_2)^p$$
$$u - u_3 = A(\Delta x_3)^p$$

and it is sufficient to solve this system of equations to find u. For example, if $\Delta x_1 = \Delta x_2 / 2 = \Delta x_3 / 4$, then:

$$p = \log_2\left(\frac{u_3 - u_2}{u_2 - u_1}\right)$$

$$u = \frac{(\Delta x_2)^p u_1 - (\Delta x_1)^p u_2}{(\Delta x_2)^p - (\Delta x_1)^p}$$

4.3.3. Impact of bottom friction coefficient and vortex viscosity on calculation water level

4.3.3.1. Bottom friction coefficient

With the nonlinear long-wave theory equation, the sea bottom friction term indicates the component for shear force on the sea bottom (τ_x/ρ, τ_y/ρ) driven by integration of the vertical vortex viscosity term into the depth. If the frow is uniform, it is expressed as:

$$\tau_x / \rho = \frac{f}{D^2} MQ, \quad \tau_y / \rho = \frac{f}{D^2} NQ$$

where, f is bottom friction coefficient, M and N are component for flow rate per unit width in the x and y direction, Q is flow rate per unit width, and D is total water depth.

Iwasaki and Mano (1979) introduced the transformation equation $f=gn^2/D^{1/3}$ between friction coefficient f and Manning's coefficient of roughness n, and used Manning's coefficient of roughness n to express the friction term. Here, the sensitivity of the roughness coefficient is analyzed and the impact that it has on calculation water level is examined.

(1) Examination conditions

The examination is carried out with one-dimensional water channel having a uniform depth (run-up calculation) (Figure 4.3.2-4). The incident wave is provided by having sinusoidal wave at semi-amplitude 2a be the initial tsunami shape, and this initial tsunami shape propagates as sinusoidal waves of semi-amplitude along the coast and out to sea, respectively. Also, consideration is given so that there is no noise in the calculation by setting a sufficient propagation distance out to sea. The principal examination conditions are shown in Table 4.3.3.1-1.

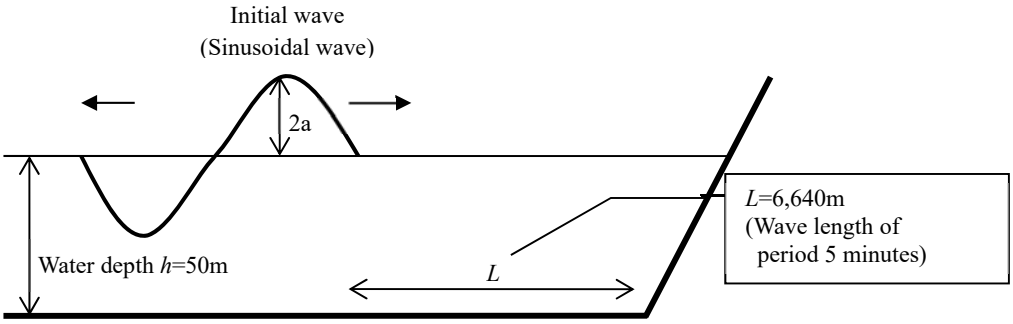

Figure 4.3.3.1-1 Initial wave and target topography

Table 4.3.3.1-1 Examination conditions

Items	Contents
Amplitude and waveform of incident wave	The sinusoidal wave of the half amplitude 2m is given to the offshore boundary as initial wave.
Period T of incident	5, 10, 20, 30 (minute)
Wavenumber of incident wave	One wave given as initial wave
Slope of sea bottom	1/10, 1/50, 1/100
Grid size Δx	22.1359m (1/300 of wave length of period 5 minutes)
Manning's coefficient of roughness n	0.0, 0.01, 0.02, 0.03, 0.04, 0.05$m^{-1/3}\cdot s$

(2) Results of comparative calculations

Tables 4.3.3.1-2 and 4.3.3.1-3 show comparisons of the maximum water level ascent and descent for cases where Manning's coefficient of roughness was varied. Also, Figure 4.3.3.1-2 shows the distribution of maximum water level ascent and descent for a case where the sea bottom slope incline was set at 1/100. From the results of these comparative calculations, characteristics have been summarized and presented below.

- In a case where the sea bottom slope is set at 1/10, even if roughness coefficient n is varied between 0 and 0.05, the change in the maximum water level ascent and descent is limited to a maximum of approximately 9%.
- In a case where the sea bottom slope is set at 1/50 when the periods for the incident wave are

5 minutes and 10 minutes and in a case where the sea bottom slope is set at 1/100 when the periods for the incident wave are 5 minutes, 10 minutes and 20 minutes, a variance is yielded of close to a maximum of 50% in sea areas having a depth of 10m or shallower.

Table 4.3.3.1-2 Comparison of maximum water level rise and fall

Sea bottom slope	Manning's coefficient of roughness $n(m^{-1/3}\cdot s)$	Period T and maximum water level ascent and descent (m)							
		T=5 minutes		T=10 minutes		T=20 minutes		T=30 minutes	
		Ascent	Descent	Ascent	Descent	Ascent	Descent	Ascent	Descent
1/10	0.00	2.45	-2.23	2.01	-2.09	2.01	-2.01	2.01	-2.01
	0.01	2.45	-2.23	2.01	-2.09	2.01	-2.01	2.01	-2.00
	0.02	2.45	-2.22	2.01	-2.08	2.01	-1.99	2.01	-1.98
	0.03	2.44	-2.21	2.01	-2.06	2.01	-1.97	2.01	-1.94
	0.04	2.43	-2.20	2.01	-2.03	2.01	-1.94	2.00	-1.89
	0.05	2.42	-2.17	2.01	-2.00	2.00	-1.89	2.00	-1.84
1/50	0.00	4.77	-4.71	3.65	-3.40	2.53	-2.41	2.42	-2.09
	0.01	4.60	-4.63	3.48	-3.39	2.53	-2.40	2.42	-2.08
	0.02	4.21	-4.28	3.46	-3.38	2.52	-2.37	2.42	-2.06
	0.03	3.84	-4.11	3.42	-3.35	2.52	-2.16	2.41	-2.04
	0.04	3.49	-3.58	3.36	-3.30	2.52	-2.13	2.41	-2.02
	0.05	3.33	-3.25	3.27	-3.10	2.52	-2.10	2.39	-2.00
1/100	0.00	5.27	-4.39	4.88	-4.83	3.56	-3.50	2.92	-2.55
	0.01	4.66	-3.85	4.48	-4.66	3.55	-3.49	2.92	-2.55
	0.02	3.79	-3.23	4.00	-4.09	3.37	-3.47	2.92	-2.53
	0.03	3.18	-2.77	3.57	-3.56	3.33	-3.40	2.91	-2.42
	0.04	2.74	-2.42	3.17	-3.13	3.12	-3.21	2.89	-2.38
	0.05	2.44	-2.14	2.91	-2.80	2.91	-2.97	2.69	-2.34

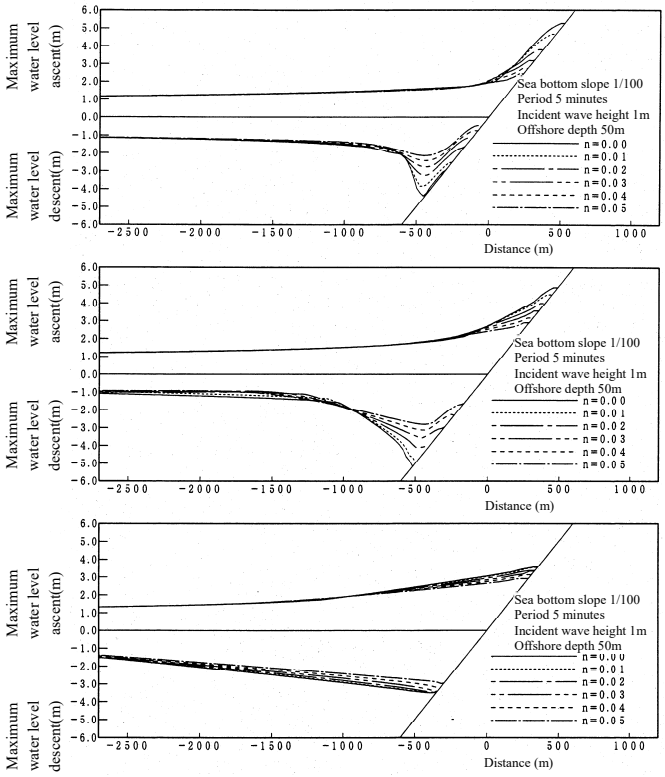

(n : $m^{-1/3}s$)

Figure 4.3.3.1-2 Comparison of the maximum water level ascent and descent by difference of Manning's coefficient of roughness

4.3.3.2. Eddy viscosity coefficient

With respect to a horizontal eddy viscosity term, there are many cases where the position is taken that a sufficiently precise solution may be obtained even if it is disregarded, provided that the tsunami water level is the principal object (Shuto, 1986). However, examples have also been seen where simulations have been performed that take this term into account in the basic equation (see for example Tanaka, 1985 and Shibaki, 1994). Also, based upon recognitions such as:

- The impact of the eddy viscosity term needs to be examined using a numerical calculation scheme and set so that it is indicated in the numerical calculation scheme and truncated error terms.
- The impact of the eddy viscosity needs to be examined with respect to plane issues.

Comparative calculations have been carried out of the impact that the eddy viscosity coefficient has on calculation water level, and the knowledge gained is given below.

(1) Examination conditions

The principal examination conditions are given in Table 4.3.3.2-1.

Table 4.3.3.2-1 Examination conditions

Items	Contents
Topography	Harbor shown in Figure 4.3.3.2-1 is assumed.
Computational region	Direction of cross shore : 3,000m, Direction of shoreline : 6,000m
Water depth	10m (Uniformity)
Grid size	25m (50, 75, 150m partially was used referring.)
Amplitude and waveform of incident wave	The sinusoidal wave of the half amplitude 2m is given to the offshore boundary as initial wave.
Period of incident wave	5, 10, 20 minutes
Direction of incident wave	Cross to the shoreline
Eddy viscosity coefficient	$0.0 \sim 10^2 m^2/s$
Manning's coefficient of roughness	n: $0.03 m^{-1/3} s$
Boundary conditions	Land/breakwater : Complete reflection, Offshoreboundary : Open boundary

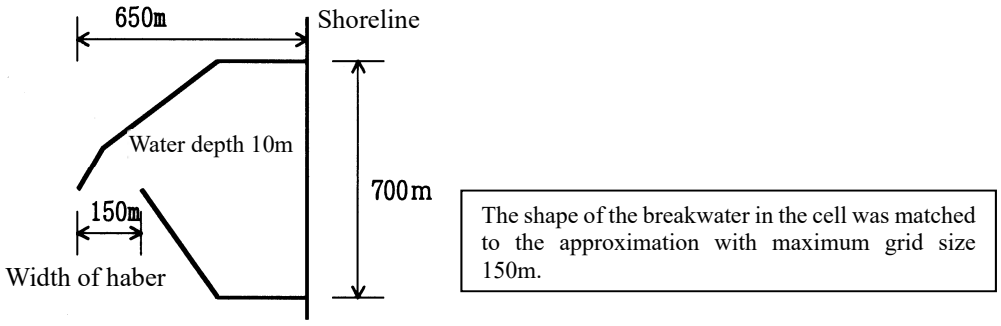

Figure 4.3.3.2-1 Shape of the breakwater

(2) Results of comparative calculations

1) Impact of eddy viscosity coefficient on maximum water level ascent (Figure 4.3.3.2-2)

- With a eddy viscosity coefficient of $1m^2/s$ or less, almost no impact has been observed on the maximum water level ascent due to differences in the eddy viscosity coefficient.
- When the grid size is varied, the level of the absolute value of the maximum water level ascent changes, and the impact due to the eddy viscosity coefficient shows the same tendency.
- The maximum water level ascent is 5 to 10% lower in a case where the eddy viscosity is $0.0m^2/s$ than when it is $10m^2/s$, and is becomes significantly lower when it is $10^2m^2/s$.
- The extent of the impact of the eddy viscosity coefficient differs depending upon the order of current velocity, geomorphic change, calculation scheme and other factors, so any generalization is difficult, but the maximum water level ascent is lower at $10m^2/s$ or greater according to the scales of the models shown here.

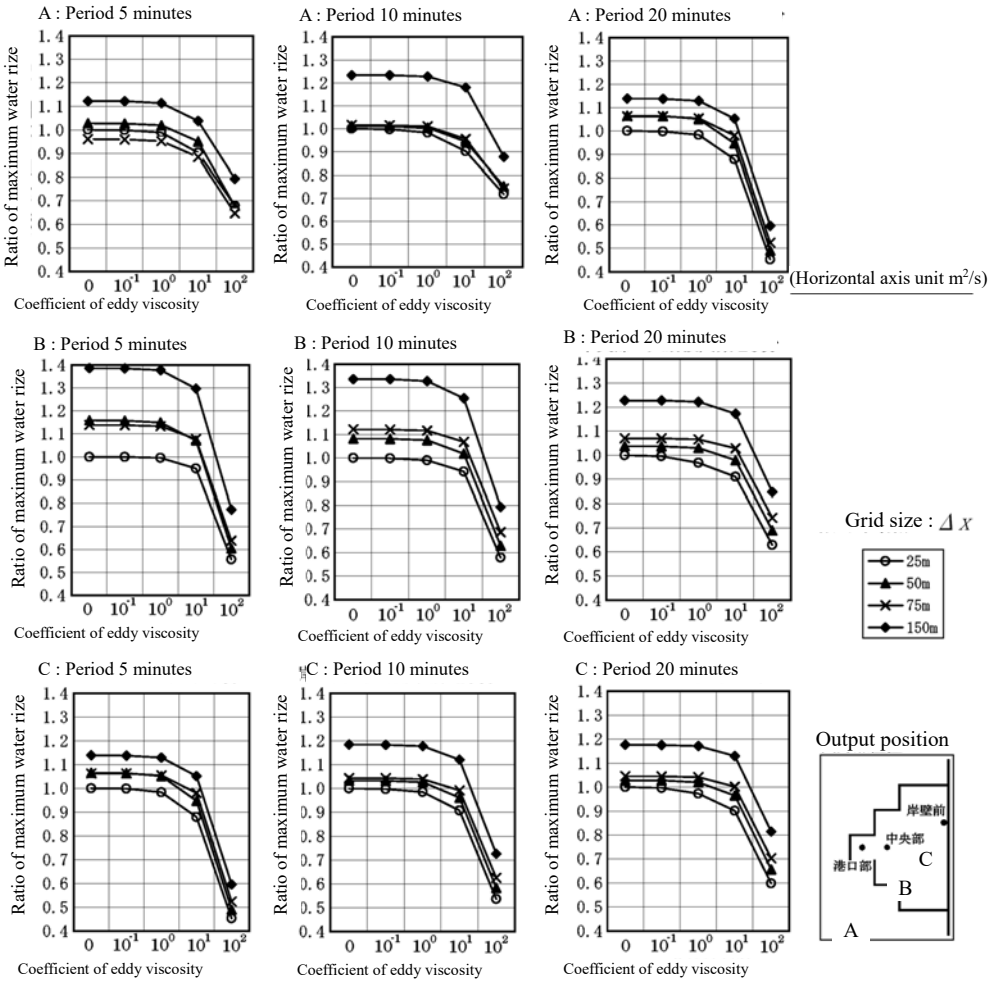

Figure 4.3.3.2-2 Comparison of the maximum water level ascent based on the case of grid size 25m and eddy viscosity coefficient 0.0m^2/s

2) Impact of eddy viscosity coefficient on flow pattern (Figures 4.3.3.2-3 and 4.3.3.2-4)

- Almost no difference is observed in the flow pattern with a eddy viscosity coefficient of 10m^2/s or less, and the circling drift disappears at the harbor mouth at 10^2m^2/s.
- When focusing on the absolute value of the current velocity in the central part of the harbor mouth, similarly, almost no difference is observed with a eddy viscosity coefficient of 10m^2/s or less, but, at 10^2m^2/s, the current velocity value decreases substantially and the flow direction also changes.

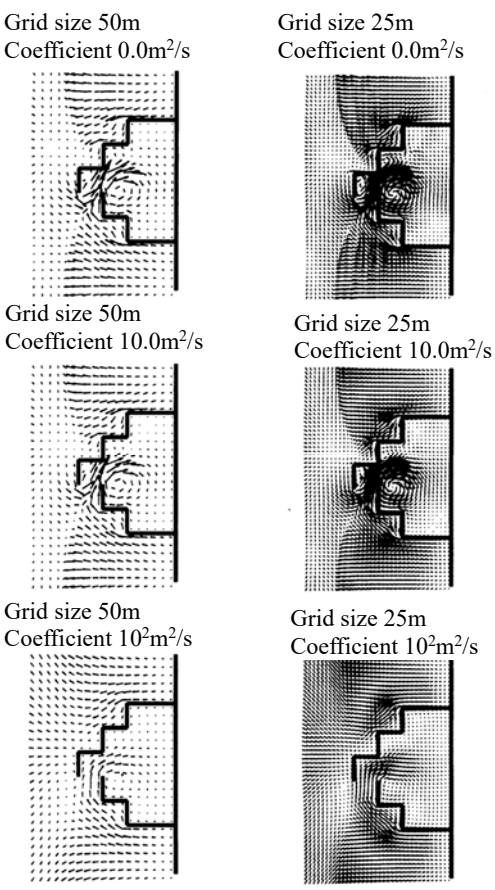

Figure 4.3.3.2-3 Coefficient of eddy viscousity and flow pattern (Period 5 minutes)

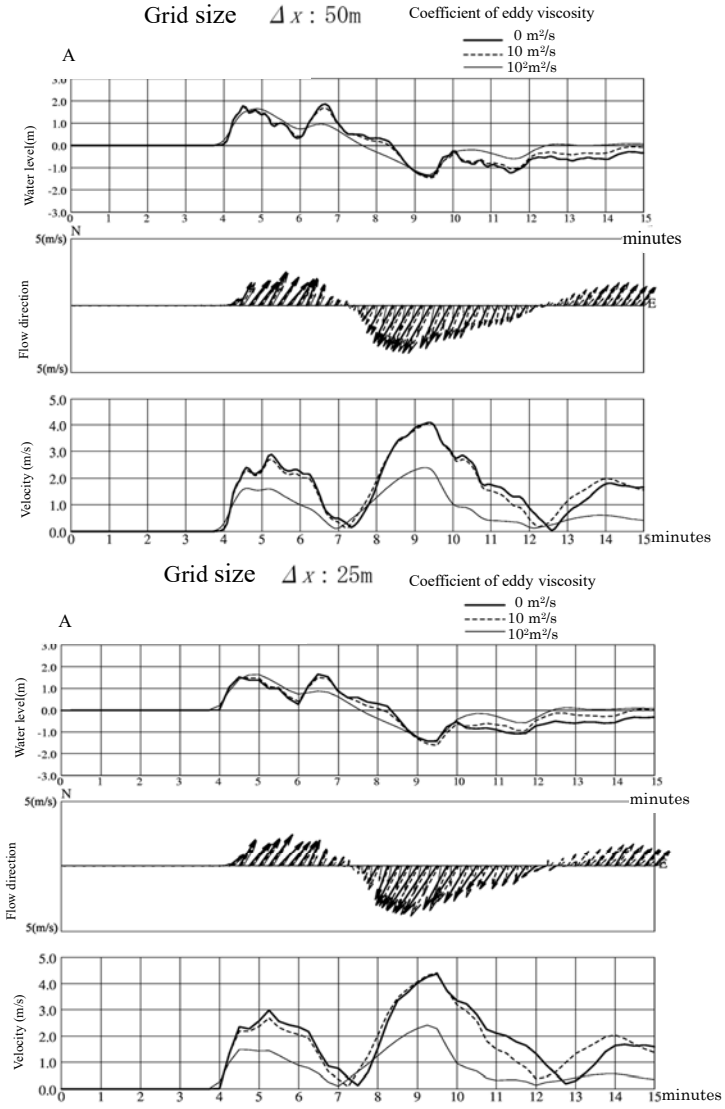

Figure 4.3.3.2-4 Water level, flow direction, velocity in output position A (Period 5 minutes)

4.4. Numerical method for tsunami generated by submarine landslides, slope failure and flank collapse

4.4.1. Overviews of the numerical methods and examples of applications

This section presents overviews of numerical methods for tsunami occurrence along with submarine landslides, slope failures and flank collapses and examples of applications.

Not all of the methods described in this section are currently usable. As new methods are proposed in the future, available ones should be investigated again when numerical simulation of tsunami is performed.

4.4.1.1. Flow rate model

(1) Overview

In the flow rate model, the inflow of sediment from land into the sea is treated as that of water. At the boundary where sediment flows in, a tsunami is caused by setting flow rate that vary over time. The flow rate is given by:

$$q = Q_m \{(l - y/l)\} \sin(\pi t/\tau) = Q \sin(\pi t/\tau), \quad 0 \le t \le \tau, -l \le y \le l$$

Where y is taken along the coastline, $\pm\ l$ for the range of inflow, and τ for the duration. Q_m is the maximum flow rate in the central part of the inflow, and q is the flow rate at position y.

(2) Examples

Aida (1975) applied this method to the 1792 Shimabara flank collapse. For the unit length of the coastline, a maximum flow rate of 18,000m^3/min is given for a period between 2 and 4 minutes. When the duration of the inflow is 2 minutes, this corresponds to 4.6×10^7m^3 for the total inflow.

4.4.1.2. Circular slip failure method

(1) Overview

The circular slip failure method deduces the topography before and after a landslide on an unstable slope, and reflects the topography in the water level of the sea surface. Direct lines are connected so that depressions are covered where traces of landslides are presumed as deduced from charts showing the submarine topography. The connected lines are set as a cross-section of the sea bottom before a virtual landslide, and the circular arc slip method is used to perform calculations of the stability of the slope. Cases, in which the safety factor is less than one and the computer cross-section coincides for the most part with a cross-section deduced from current

traces of submarine landslides, are regarded as cross-sections of landslides to be incorporated into tsunami analysis. Sediment, which has moved along a slope as a submarine landslide has occurred, is deposited below the slope, and the mass of the sediment is incorporated into the tsunami analysis in a form where it is preserved. A tsunami is caused as a change in the water surface occurs that is similar to the change in the seabed due to movement of sediment. With respect to a direction perpendicular to the direction of the landslide, a cross-section is provided using the COS function so that the volume of the landslide decreases toward both ends. To configure the motion of the landslide, the period of time for the landslide is introduced beginning from when landslide occurs until the movement of the landslide is completed. The volume of the landslide sediment, which is estimated using the circular arc slip method, is regarded as an integral value of landslides that have occurred multiple times and is used by multiplying by a factor of 1 or less.

(2) Examples

Hiraishi et al. (2001) apply this method to the Meiwa Yaeyama tsunami, assuming the simultaneous occurrence of fault motion and landslide. Provisional calculations are needed for setting the landslide time, and, in the calculations performed by Hiraishi et al. (2001), three values were set: 30, 60 and 90 seconds. A range of 0.2 to 1.0 times has been provided for the landslide volume factor with reference to previous values estimating the number of times landslides have occurred.

4.4.1.3. Kinematic landslide model

(1) Overview

The kinematic landslide model (KLS) was proposed by Satake and Kato (2002). The model utilizes detailed topography changes obtained from bathymetric surveys. Displacements at each point are assumed to occur during rise time T. Moreover, this change is regarded as moving from the top of the landslide body at propagation velocity U (Satake and Kato, 2002). The evolution of topographic variations, which are obtained using this method, are taken into consideration in a mass conservation expression as change in the water depth. Propagation velocity U and rise time T are parameters that are analogous to the failure propagation velocity and rise time of the earthquake fault model.

The approaches to propagation velocity are the case where the vertical direction component Uz is provided (Satake and Kato, 2001; Satake and Kato, 2002; Satake et al., 2002) and case where the horizontal direction component U is provided (Satake, 2007).

In the model described above, the slide (missing volume) first appears, then the deposit

(additional volume) results. Tonomo et al. (2015) focused on this point and proposed a model in which collapse and sedimentation proceed simultaneously.

Satake (2007) varied propagation velocity U in a horizontal direction within a range of 10~100m/s, referencing the configuration in examinations of observations and past occurrences, in a case study involving a numerical simulation of the 1741 Kanpo tsunami. Also, with respect to rise time T, Satake (2007) also discussed the difficulty of estimating using propagation velocity U, and set it to within a range from 1 to 5 minutes.

(2) Examples

Table 4.4.1-1 shows parameters in the case studies where the KLS model is applied to tsunami originating in submarine landslides, flank collapses and slope failures.

Table 4.4.1-1Parameters for KLS model in the previous studies

*1 Uz=20m/s for Satake and Kato (2002)

Events(Reference)	Parameter		Note
	U (Uz) (m/s)	T (min)	
Submarine landslides around Hawaii (Satake et al., 2002)	U = 20,50,100	5	
1741 Kampo tsunami (Satake and Kato, 2001; Satake and Kato, 2002)	Uz = 2,5,10,20*1	1, 2, 5	The observed values are best explained for the combination of Uz=10m/s and T=2min.
1741 Kampo tsunami (Satake,2007)	U = 10, 20, 40, 50, 60, 80, 100	1, 2, 5	The observed values are best explained for the combination of U=40m/s and T=2min.

4.4.1.4. Landslide motion analysis model

(1) Overview

This method gives the movement of landslide sediment, which is obtained using the landslide analysis model, as sea surface fluctuation for the tsunami analysis model. The movement of landslide sediment is analyzed using either plane two-dimensional or three-dimensional models such as LSFLOW, TITAN2D or FLOW3D. The tsunamis are caused by giving changes in the thickness of landslide sediment, which are obtained from the results of analysis of landslide movement, as a time-series sea surface fluctuation.

Sasahara (2004) combined the Public Works Research Institute's quasi-three-dimensional landslide motion analysis program LSFLOW and program for computing fluid flow using a long wave equation, and then analyzed the tsunami that resulted from the 1792 Shimabara sector collapse. The calculation component of the continuity equation has been revised to address time variation for layer thickness of landslide sediment.

(2) Examples

In the case study by Sasahara (2004) applying the model to the tsunami accompanying the 1792 Shimabara sector collapse, the acceleration, duration, period and other characteristics of the earthquake are given in order to analyze landslide motion using the LSFLOW model. Also, the physical properties for the ground have been set using such values as 2.0t/m^3 for density, 0.2~0.7° as the friction angle for the sliding surface (underwater), and 9.0~23° as the angle of internal resistance.

4.4.1.5. Two-layer flow model

(1) Overview

The two-layer flow model was proposed by Imamura and Imteaz (1995) as a basic equation for the motion of fluids where the density differs in two-layers, the upper and lower.

Matsumoto et al. (1998) enhanced the two-layer flow model developed by Imamura and Imteaz (1995) to apply it to tsunami occurring due to debris flow. Specifically, terms were added to the basic equation for expressing bottom friction force, interfacial shear force, and form drag at the head of the debris flow in the sea area. Also, an artificial viscosity term was introduced to suppress vibration that occurs when the debris flow plunges into the sea. The interfacial resistance coefficient f_{inter} was introduced for the term expressing interfacial shear force, and the drag coefficient C_{D} was introduced for the term expressing form drag at the head of the debris flow. The proposed two-layer flow model has been applied to simulation of hydraulic model experiments with hydraulic models as well as past tsunami (1741 Kampo tsunami).

Hashi and Imamura (2000) applied the two-layer flow model to the 1998 Papua New Guinea tsunami, and examined the position and magnitude of landslides for cases where submarine landslides are taken into consideration as a factor causing the tsunami.

Imamura et al. (2001) conducted hydraulic model experiments of debris flow plunges in a one-dimensional water route, and used the two-layer flow model to perform simulation calculations. The Manning roughness formula has been used in expressions of bottom friction force. Also, this experiment did not take into consideration form drag based on a determination that the head of the debris flow was not in a form that would give rise to significant resistance. In this research, parametric studies were conducted that varied bottom roughness within a range of 0.08~0.12m$^{-1/3}$s, the diffusion coefficient for the sediment layer within a range of 0.005~0.01m^2/s, and the interfacial resistance coefficient within a range of 0~1.0. Based on the results of a comparison of the results of measurements using hydraulic model experiments and those of simulation calculations, the optimum combination for this case study was found to be a

bottom friction coefficient of $0.12m^{-1/3}s$ and a horizontal eddy viscosity coefficient of $0.01m^2/s$.

Kawamata et al. (2005) used the two-layer flow model to perform simulations of hydraulic model experiments and past tsunami (1741 Kanpo tsunami). The hydraulic model experiments were carried out using a configuration that was the same as that set by Imamura et al. (2001). The most appropriate value pairs were proposed as a result of trials of several settings for parameters included in the two-layer flow model. More precisely, the optimum values were a combination where the bottom Manning's roughness coefficient in the air was $0.01m^{-1/3}s$, the horizontal eddy viscosity coefficient was $0.01m^2/s$, the bottom Manning's roughness coefficient in the water was $0.012m^{-1/3}s$, $C_D = 10$, $f_{inter} = 0.2$, and the duration of the force of interaction was 0.37 seconds. Multiple calculations were performed for a calculation of the 1741 Kanpo tsunami using differing bottom roughnesses. When the bottom Manning's roughness coefficient in the air and in the water was $0.4m^{-1/3}s$, the results best coincided with the traces marking the height of the tsunami. The other settings were $0.1m^2/s$ for the horizontal eddy viscosity coefficient, for the bottom Manning's roughness coefficient in the water $0.4m^{-1/3}s$, and $C_D = 2.0$. Based upon an analysis of the results of this simulation, it has been pointed out that there is a strong directivity toward a direction in which the debris flow traveled (northward), and the reproducibility in this northward direction is not necessarily good in comparison to the Japan Sea as a whole.

Maeno and Imamura (2007) conducted a study of tsunami during the formation of the Kikai Caldera approximately 7,300 years ago. The study used tsunami that occurred due to pyroclastic flow, which accompanied eruption when the caldera was formed, that plunged into the sea, and used the two-layer flow model to perform calculations of the motion of the pyroclastic flow and tsunami. The horizontal eddy viscosity coefficient and interfacial resistance coefficient were set at $0.01m^2/s$ and 0.2, respectively, based upon Matsumoto et al. (1998) and Kawamata et al. (2005). Manning's roughness coefficient for the bottom was set at $0.01m^{-1/3}s$ for the air and $0.08m^{-1/3}s$ for water based upon a comparison of the results of experiments that focused on pyroclastic flow by McLeod et al. (1999) and the results of numerical simulations performed in this study. Form drag was not taken into consideration.

Maeno and Imamura (2011) applied the two-layer flow model to the tsunami triggered by the pyroclastic flow following eruption of Krakatoa in 1883. This study examined both cases where the density of the pyroclastic flow was greater than that of water and where it was less than that of water, and applied basic equations that differed according to the respective case. Manning's roughness coefficient for the bottom did not depend on the density of the pyroclastic flow, and was set at $0.01 \sim 0.06m^{-1/3}s$ for when in the air, and $0.06 \sim 0.08m^{-1/3}s$ for when in the water. The values of 0.06, 0.18 or 0.20 were given for the interfacial resistance coefficient. The horizontal eddy viscosity coefficient was given according to an expression dependent upon the thickness of water or the pyroclastic flow, the velocity of the pyroclastic flow, and other elements.

The coefficient β of the viscosity term to suppress numerical vibration was set at 1.2. Form drag was not taken into consideration.

Yanagisawa et al. (2014) applied the two-layer flow model to the tsunami in the Ariake Sea, which originated in the sector collapse of Mt. Mayuyama in 1792. This study increased the precision of landslide calculations by taking a soil parameter into account in the basic equation for the sediment layer. More specifically, the study applied the law of friction using Coulomb's equation and the coefficient of earth pressure generally utilized in numerical models of landslides and debris flow. Also, to stabilize the calculation, the outflow rate was limited with respect to mesh for which clod thickness was negative. Horizontal eddy viscosity and form drag were not taken into consideration.

As described above, multiple basic equations have been proposed which differ in their treatment of bottom friction force and the force of interaction between seawater and sediment layers. Here, a description is given of the basic equation presented by Maeno and Imamura (2007) as one formulation*. The basic equation for the upper layer (seawater layer) is expressed as:

$$\frac{\partial(\eta_1-\eta_2)}{\partial t}+\frac{\partial M_1}{\partial x}+\frac{\partial N_1}{\partial y}=0$$

$$\frac{\partial M_1}{\partial t}+\frac{\partial}{\partial x}\left(\frac{M_1^2}{D_1}\right)+\frac{\partial}{\partial y}\left(\frac{M_1N_1}{D_1}\right)+gD_1\frac{\partial \eta_1}{\partial x}-INTF_x=0$$

$$\frac{\partial N_1}{\partial t}+\frac{\partial}{\partial x}\left(\frac{M_1N_1}{D_1}\right)+\frac{\partial}{\partial y}\left(\frac{N_1^2}{D_1}\right)+gD_1\frac{\partial \eta_1}{\partial y}-INTF_x=0$$

The basic equation for the lower layer (sediment layer) is expressed as:

$$\frac{\partial \eta_2}{\partial t}+\frac{\partial M_2}{\partial x}+\frac{\partial N_2}{\partial y}=0$$

$$\frac{\partial M_2}{\partial t}+\frac{\partial}{\partial x}\left(\frac{M_2^2}{D_2}\right)+\frac{\partial}{\partial y}\left(\frac{M_2N_2}{D_2}\right)+gD_2\left(\alpha\frac{\partial D_1}{\partial x}+\frac{\partial \eta_2}{\partial x}-\frac{\partial h}{\partial x}\right)+\frac{\tau_x}{\rho_2}+\alpha INTF_x=DIFF_x$$

$$\frac{\partial N_2}{\partial t}+\frac{\partial}{\partial x}\left(\frac{M_2N_2}{D_2}\right)+\frac{\partial}{\partial y}\left(\frac{N_2^2}{D_2}\right)+gD_2\left(\alpha\frac{\partial D_1}{\partial y}+\frac{\partial \eta_2}{\partial y}-\frac{\partial h}{\partial y}\right)+\frac{\tau_y}{\rho_2}+\alpha INTF_y=DIFF_y$$

*Partial supplementation and revisions have been made in comparison with the descriptions given of the basic equations in other literature.

where, the subscripts 1 and 2 represent the upper and lower layers, respectively. η_1 is the water level of the upper layer and η_2 the thickness of the lower layer. h is the still water depth of the upper layer, D_1 the total water depth ($=h+\eta_1$), and D_2 the thickness of the lower layer. M and N are the flow rates per unit width in the x and y directions, respectively. ρ_1 is the density of the upper layer, ρ_2 the density of the lower layer, α the density ratio ($=\rho_1/\rho_2$), and τ/ρ_2 the bottom friction term for the lower layer. $INTF$ indicates the interfacial resistance force and

$DIFF$ the horizontal diffusion term. The bottom friction term, interfacial resistance force and horizontal diffusion term are expressed as:

$$\frac{\tau_x}{\rho} = \frac{gn^2}{D^{7/3}} M\sqrt{M^2 + N^2}\ ,\quad \frac{\tau_y}{\rho} = \frac{gn^2}{D^{7/3}} N\sqrt{M^2 + N^2}$$

$$INTF_x = f_{\text{inter}}\,\overline{u}\sqrt{\overline{u}^2 + \overline{v}^2}\ ,\quad INTF_y = f_{\text{inter}}\,\overline{v}\sqrt{\overline{u}^2 + \overline{v}^2}$$

$$DIFF_x = \nu\left(\frac{\partial^2 M}{\partial x^2} + \frac{\partial^2 M}{\partial y^2}\right),\quad DIFF_y = \nu\left(\frac{\partial^2 N}{\partial x^2} + \frac{\partial^2 N}{\partial y^2}\right)$$

where, n is Manning's roughness coefficient for bottom friction. f_{inter} indicates the interfacial resistance coefficient, $\overline{u},\overline{v}$ the interlayer relative velocities in the x and y directions, respectively, and ν the horizontal diffusion coefficient.

To suppress the vibration that occurs when debris flow plunges into the sea, the artificial viscosity term, which is shown below, is introduced into the mass conservation expression.

$$\beta\Delta x^3\sqrt{\frac{g}{D}}\left\|\frac{\partial^2\eta}{\partial x^2}\right\|\frac{\partial^2\eta}{\partial x^2}$$

where, β is a constant.

(2) Examples

Table 4.4.1-2 shows parameters in the case studies where the two-layer flow model has been applied to tsunami originating in submarine landslides, sector collapses and slope failures.

Table 4.4.1-2 Parameters in two-layer flow model in the previous studies

- : not described, *: Basic equations are not described

Event(Reference)	Parameter						Note
	α	n ($m^{-1/3}s$)	ν (m^2/s)	f_{inter}	C_D	β	
1998 Papua New Guinea Tsunami (Tachibana and Imamura, 2000)	-	-	-	-	-	-	Parameters and basic equations are not described in the paper
1741 Kampo tsunami (Matsumoto et al.,1998)	-	-	*	0.025	2.0	3.0	Assumption of dilatant fluid leads to bottom friction coefficient in the paper
1741 Kampo tsunami (Kawamata et al.,2005)	-	0.25, 0.4, 0.6	0.1	0.0	2.0	*	The best fit was obtained for n=0.4.
1792 Unzen-Mayuyama landslide tsunami (Yanagisawa et al.,2014)	-	*	*	0.01, 0.05, 0.10, 0.20	*	*	The lower bottom friction is computed using friction Coulomb's theory
Hydraulic model experiment for Tsunami (Imamura et al.,2001)	-	0.08, 0.10, 0.12	0.005, 0.01, 0.02, 0.03	0.0, 0.05, 0.20, 1.00	*	*	The best fit was obtained for the combination of n=0.12 and ν=0.01.
Hydraulic model experiment for Tsunami (Kawamata et al.,2005)	-	Air:0.01 Water:0.12	0.01	0.2	10	*	

4.4.1.6. Methods for estimating initial water level

(1) Overview

Grilli and Watts (2005) and Watts et al. (2005) proposed methods that assess the initial water level distribution of tsunami generated by submarine landslides. Submarine landslides can be classified as slides and slumps with different equations proposed. With respect to the estimation equation for initial water level distribution, equations have been proposed for estimating amplitude and wavelength in cases where the landslide is a two-dimensional cross-section. Moreover, an equation has been proposed for estimating the distribution of the amount of water level fluctuation in a case where the landslide movement is three-dimensional based upon its amplitude and wavelength.

The equation for estimating amplitude when the landslide is a two-dimensional cross-section has been computed by approximating multiple numerical solutions in a functional form that is based upon theoretical consideration.

The tsunami amplitude and wavelength for slides are given below.

$$\eta_{o,2D} = S_o(0.0574 - 0.043\,1\sin\theta)\left(\frac{T}{b}\right)\left(\frac{b\sin\theta}{d}\right)^{1.25}\left(1 - e^{-2.2(\gamma-1)}\right)$$

$$\lambda_o = t_o\sqrt{gd}$$

Where, $\eta_{0,2D}$ is the maximum water level fall immediately above the initial position of the landslide, S_0 the characteristic distance, T the maximum thickness of the landslide, b the length when the cross-sectional shape of the movement of the landslide is approximated using a Gaussian distribution, θ the slope incline, d the initial submergence depth of the landslide, γ the underwater relative density of the landslide, and t_0 the characteristic time. A series of equations for computing S_0 and t_0 have been proposed as shown below.

$$S_o = \frac{u_t^2}{a_o},\quad t_0 = \frac{u_t}{a_o},$$

$$u_t = \sqrt{gd}\sqrt{\frac{B\sin\theta}{d}\frac{\pi(\gamma-1)}{2C_d}\left(1 - \frac{\tan\psi}{\tan\theta}\right)},$$

$$a_o = g\sin\theta\left(\frac{\gamma-1}{\gamma + C_m}\right)\left(1 - \frac{\tan\psi}{\tan\theta}\right)$$

where, u_t is the final velocity, a_o the initial acceleration, g the acceleration of gravity, B the length when the landslide is elliptically approximated, C_d the drag coefficient, C_m the additional mass coefficient, and ψ the angle of friction. In addition, $C_d \approx 1$, $C_m \approx 1$, and $\psi \approx 0$ have been proposed as appropriate values obtained from experiments. The scope of applicability for this estimation equation has been given as coinciding with the scope of the calculation conditions for numerical experiments used when finding approximate equations. In other words, $\vartheta \in [5,30]^\circ$, $d/b \in [0.06,1.5]$, $T/b \in [0.008,0.2]$, $R/b \in [1,2]$, and $\gamma \in [1.46,2.93]$.

The amplitude and wavelength for slumps are given below.

$$\eta_{o,2D} = S_o\left(\frac{0.131}{\sin\theta}\right)\left(\frac{T}{b}\right)\left(\frac{b\sin\theta}{d}\right)^{1.25}\left(\frac{b}{R}\right)^{0.63}(\Delta\Phi)^{0.39}(1.47 - 0.35(\gamma-1))(\gamma-1)$$

$$\lambda_o = t_o\sqrt{gd}$$

where, R is the radius of curvature, and $\Delta\Phi$ the rotation angle. In modeling, S_o is half of the distance until the landslide stops. A case study gives the value for half of the distance over which the landslide moves. The following have been proposed as equations for computing R, $\Delta\Phi$, and t_0.

$$R = b^2/(8T) \quad \text{or} \quad R = b,$$

$$\Delta\Phi = 2S_o / R,$$

$$t_0 = \sqrt{\frac{R}{g}}\sqrt{\frac{\gamma + C_m}{\gamma - 1}}$$

In addition, $C_d \approx 0$ and $C_m \approx 1$ have been proposed. The application scopes are $\vartheta \in [10,30]^\circ$, $d/b \in [0.34,0.5]$, $T/b \in [0.10,0.15]$, $R/b \in [1,2]$, $\Delta\Phi \in [0.1,0.52]$, and $\gamma \in [1.46,2.93]$.

The following equation has been proposed for estimating the distribution of the water level fluctuation in a case where the landslide phenomenon is three-dimensional, which is based on amplitude and wavelength in a case where the landslide phenomenon is a two-dimensional cross-section. First, amplitude $\eta_{0,3D}$, which is directly above the landslide term in a case where the landslide phenomenon is three-dimensional, is given as:

$$\eta_{0,3D} = \eta_{0,2D}\left(\frac{w}{w + \lambda_0}\right)$$

where, w is the width of the landslide. Next, most of the tsunami energy at the $t = t_0$ stage is potential energy, and a double Gaussian distribution is used for the water level distribution in this case, which may be expressed as follows.

$$\eta(x,y) = \frac{\eta_{0,3D}}{\eta_{\min}} \sec h\left(\kappa \frac{y - y_0}{w + \lambda_0}\right)\left(\exp\left\{-\left(\frac{x - x_0}{\lambda_0}\right)^2\right\} - \kappa' \exp\left\{-\left(\frac{x - \Delta x - x_0}{\lambda_0}\right)^2\right\}\right)$$

where, $\eta_{\min}$ is the minimum value for the right-hand side excluding amplitude, κ the parameter yielding the shape of the distribution in a direction perpendicular to the direction of the landslide movement, x_g the coordinates for the initial position of the landslide, Δx the parameters governing the distance between the peaks of the rise and fall, x_0 the coordinates of $x_0 \approx x_g + \Delta x$, y_0 the coordinate of the landslide position in the y direction. κ' is the parameter governing the ratio of the positive and negative peaks, but the determination method is not indicated.

(2) Examples

Watts et al. (2005) applied the proposed formulas to the estimation of several tsunamis from previous case studies. The parameters used in the previous studies are given in Table 4.4.1-3.

Table 4.4.1-3 Parameters for Watts et al. (2005) in the previous studies

* : S_0 is not used in slide type

Event	Configuration							
	Type	γ (-)	T (m)	b (m)	w (m)	$2S_0$ (m)	d (m)	θ (degree)
1998 Papua New Guinea	slump	1.85	760	4,500	4,500	766	1,200	12
1994 Skagway, Alaska	slide	1.85	15-20	180-600	340-390	*	24-150	9-24
1999 Izmit Bay	slump	1.85	500	5,000	5,000	230	218	5
1946 Unimak, Alaska	slump	1.85	400	40,000	25,000	358,000	1,600	4.3

4.4.1.7. Distinct element method

(1) Overview

A method has been proposed that addresses landslide (solid phase) and seawater (fluid phase) respectively with the distinct element method and the particle method, and takes into consideration the interaction between both phases to calculate landslide tsunami. Goto et al. (2011) proposed a solid-liquid two-phase flow model for application to flank collapse tsunami.

(2) Examples

Goto et al. (2011) used the proposed model to reproduce hydraulic model experiments simulating flank collapse tsunami, and reported on the basis of the results that the height and other characteristics of tsunami that occurred as well as the motion process from plunge of the particle group through sedimentation corresponded well overall with the empirical results.

4.4.2. Examination of appropriate grid size

In this section, the two-layer flow model and the KLS model are addressed, and an examination conducted of the appropriate grid size when performing calculations using both models. For this examination, a virtual topography is to be prepared that illustrates submarine landslides, slope failures and flank collapses, and both models will be applied.

4.4.2.1. Illustration of landslide body

The formula set forth by Lynett and Liu (2005) was adopted to illustrate the formation of landslide body.

4.4.2.2. Examination of tsunami originating in submarine landslides

(1) Calculation conditions

1) Topographical conditions

Figure 4.4.2-1 shows a topography for a submarine landslide. The flat shallow area of water depth H_f and the flat deep area of water depth H_b are connected with the inclining slope θ, and the landslide body is arranged on this inclination. The length of the inclination is twice the initial length of the landslide body. For the final depositional landform, the KLS model yields a distribution that moved in a horizontal direction only in a distance equivalent to length L of the landslide body from the initial position of the landslide body (zone of depletion). These parameters have been compiled and given in Table 4.4.2-1.

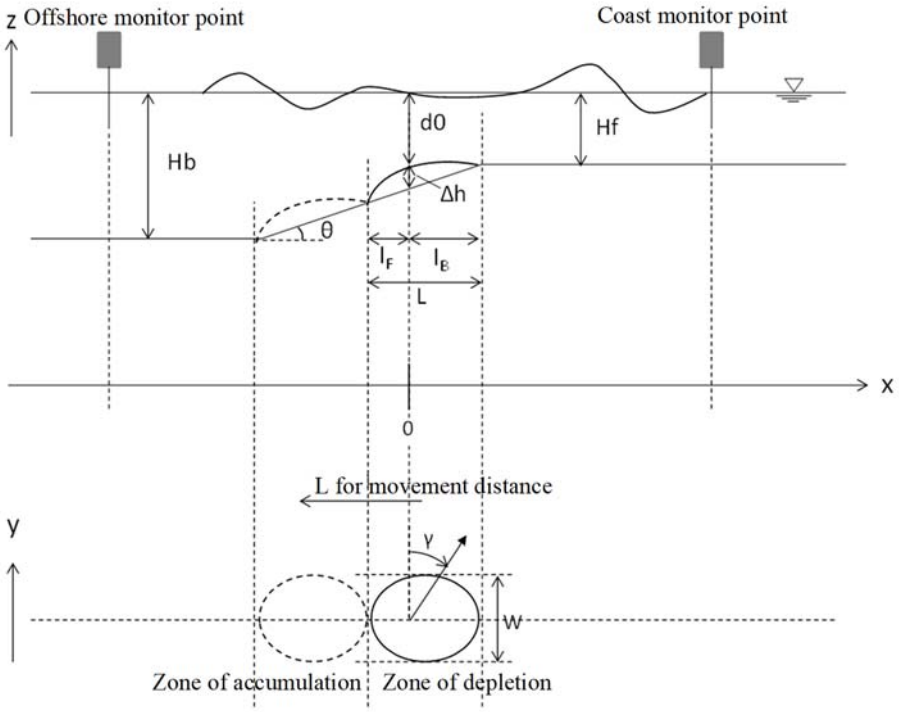

Figure 4.4.2-1 Model for submarine landslide

Table 4.4.2-1 Parameters for submarine landslide

Parameter	Value
Δh (m)	30
H_f (m)	500
H_b (m)	$H_f + 2L\tan\theta$
θ (°)	3, 6, 12
κ (= l_F/l_B)	1.0
L (m)	600
W (m)	600
γ (= ρ_s/ρ_{water})	1.85
b	0.5L

2) Other conditions

The grid size is based on landslide length L, and set at L/40, L/20, L/10, and L/5 (=15, 30, 60, and 120m). The appropriate grid size is examined by comparing solutions obtained using different grid sizes. Tables 4.4.2-2 and 4.4.2-3 show the other calculation conditions.

Table 4.4.2-2 Calculation conditions (Submarine landslide)

Parameter	Value
Grid sizes (m)	15,30,60,120
Computation time interval (s)	0.05
Manning's roughness coefficient between water and bottom ($m^{-1/3}s$)	0.03
Kinematic viscosity for water (m^2/s)	10.0
Calculation method	Tanaka(1985)'s method

Table 4.4.2-3 Calculation conditions for each model (Submarine landslide)

Model	Parameter	Symbol	Value
Two-layer flow model	Manning's roughness coefficient for lower layer (soil layer)	n ($m^{-1/3}s$)	0.2, 0.3, 0.4
	Kinematic viscosity for lower layer (soil layer)	ν(m^2/s)	0.01
	resistance coefficient	C_D (-)	0
	coefficient for interface resistance force	f_{inter} (-)	0
KLS model	Horizontal slide velocity	U (m/s)	10, 20, 40
	Rise time	T (s)	120, 240, 480

(2) Results

First, the results of the two-layer flow model are shown. Convergence is verified of the maximum water level ascent and descent when the grid sizes are set at $L/5$, $L/10$, $L/20$, and $L/40$. The slope incline is fixed at an angle of 6° and roughness coefficient n for the sediment layer at $0.4 m^{-1/3} \cdot s$.

The maximum water level changes at target sites offshore are shown in Table 4.4.2-4. The maximum water level changes at target sites along the coastline are shown in Table 4.4.2-5. Because of the strong directivity that emerged in the solutions using the two-layer flow model, the rise is dominant for target sites offshore and the fall for target sites along the coastline. Accordingly, when convergence is verified for the rise at target sites offshore and the fall at target sites along the coastline, cases where $\Delta x=L/10$ show a large difference from cases where $\Delta x=L/40$, and cases where $\Delta x=L/20$ showed a difference of ±5% or less than cases where $\Delta x=L/40$.

From the above, this calculation example resulted in the maximum water level change converging for the most part in cases where the size of the landslide area is set at 1/20 in the configuration of grid sizes for the two-layer flow model.

Next, the results for the KLS model are shown. Similar to the case of the two-layer flow model, convergence is verified of the maximum water level ascent and descent when the grid sizes are set at $L/5$, $L/10$, $L/20$, and $L/40$. The slope incline is fixed at an angle of 6°, and the propagation velocity U and duration T at 40m/s and 120s, respectively. The maximum water level

changes at target sites offshore are shown in Table 4.4.2-6. The maximum water level changes at target sites along the coastline are shown in Table 4.4.2-7. Cases where $\Delta x=L/20$ showed a difference of ±5% or less in comparison to cases where $\Delta x=L/40$.

From the above, this calculation example resulted in the maximum water level change converging for the most part in cases where the size of the landslide area was set at 1/20 in the configuration of grid sizes for the KLS model.

Table 4.4.2-4 Maximum water level ascent and descent (Two-layer flow model, offshore)

Grid sizes Δx (m)	Water level (m)		Relative error for Δx=15m	
	Maximum water level ascent	Maximum water level descent	Maximum water level ascent	Maximum water level descent
15 (=L/40)	0.05219	-0.00679	—	—
30 (=L/20)	0.05453	-0.00748	+4.5%	10.2%
60 (=L/10)	0.04963	-0.00779	-4.9%	14.7%
120 (=L/5)	0.03675	-0.02206	-29.6%	224.9%

Table 4.4.2-5 Maximum water level ascent and descent (Two-layer flow model, coast)

Grid sizes Δx (m)	Water level (m)		Relative error for Δx=15m	
	Maximum water level ascent	Maximum water level descent	Maximum water level ascent	Maximum water level descent
15 (=L/40)	0.00703	-0.04920	—	—
30 (=L/20)	0.00916	-0.04801	+30.3%	-2.4%
60 (=L/10)	0.01685	-0.04158	+139.7%	-15.5%
120 (=L/5)	0.02347	-0.02750	+233.9%	-44.1%

Table 4.4.2-6 Maximum water level ascent and descent (KLS model, offshore)

Grid sizes Δx (m)	Water level (m)		Relative error for Δx=15m	
	Maximum water level ascent	Maximum water level descent	Maximum water level ascent	Maximum water level descent
15 (=*L*/40)	0.05057	0.06758	—	—
30 (=*L*/20)	0.0496	0.07097	-1.9%	+5.0%
60 (=*L*/10)	0.05327	0.06701	+5.3%	-0.8%
120 (=*L*/5)	0.06338	0.05289	+25.3%	-21.7%

Table 4.4.2-7 Maximum water level ascent and descent (KLS model, coast)

Grid sizes Δx (m)	Water level (m)		Relative error for Δx=15m	
	Maximum water level ascent	Maximum water level descent	Maximum water level ascent	Maximum water level descent
15 (=*L*/40)	0.0176	-0.03334	—	—
30 (=*L*/20)	0.01758	-0.03372	-0.1%	1.1%
60 (=*L*/10)	0.01797	-0.0388	2.1%	16.4%
120 (=*L*/5)	0.01968	-0.03807	11.8%	14.2%

4.4.2.3. Examination of tsunami originating in slope failures and flank collapses

(1) Calculation conditions

1) Topographical conditions

Figure 4.4.2-2 shows a topography for a slope failure and flank collapse. The topography is configured so that the inclination of slope θ connects to the flat sea bottom having water depth *Hb*. On this inclination, the illustrated landslide body has been arranged so that the edge touches the water surface in its initial state. For the final depositional landform, the KLS model yielded a distribution that moved in a horizontal direction only in a distance equivalent to length *L* of the landslide body from the initial position of the landslide body (zone of depletion). These configurations have been compiled and given in Table 4.4.2-8.

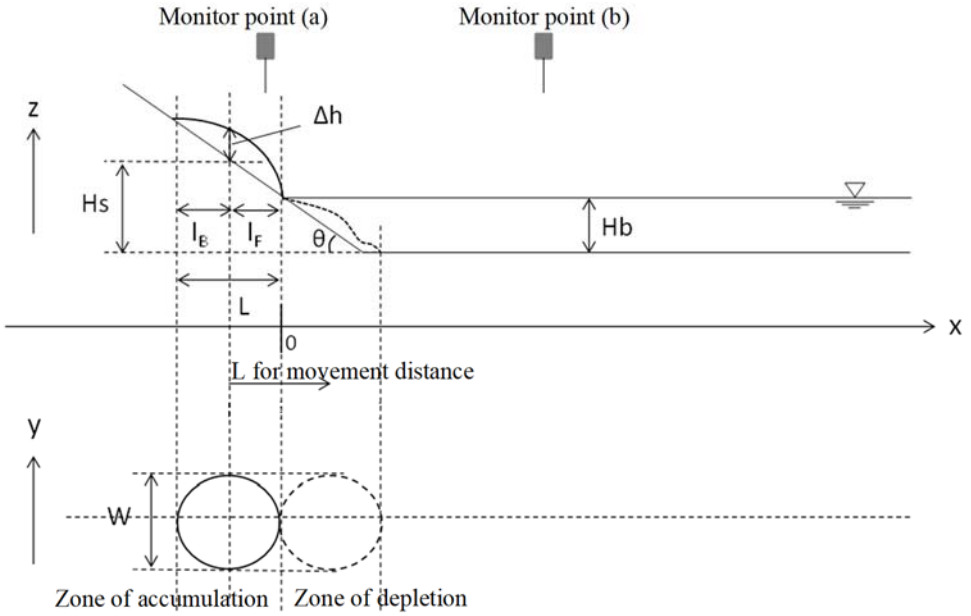

Figure 4.4.2-2 Model for slope failure and flank collapse

Table 4.4.2-8 Parameter (slope failure and flank collapse)

Parameter	value
Δh (m)	40
H_b (m)	80
θ (degree)	20,30,40(two-layer flow model), 30(KLS model)
κ (= l_F/l_B)	1.0
L (m)	400
W (m)	400
γ (= ρ_s/ρ_{water})	1.94(=2.0/1.03)
b	0.5L

2) Other conditions

The grid size is based on landslide length L, and was set at L/80, L/40, L/20, L/10 and L/5 (=5, 10, 20, 40 and 80m). The appropriate grid size is examined by comparing solutions obtained using different grid sizes. Tables 4.4.2-9 and 4.4.2-10 show the other calculation conditions.

Table 4.4.2-9 Calculation conditions (Slope failure and flank collapse)

Parameter	Value
Grid sizes (m)	5,10,20,40,80
Manning's roughness coefficient between water and bottom ($m^{-1/3}s$)	0.03
Kinematic viscosity for water (m^2/s)	10.0
Calculation method	Tanaka(1985)'s method

Table 4.4.2-10 Calculation conditions for each model

(Slope failure and flank collapse)

Model	Parameter	Symbol	Value
Two-layer flow model	Computation time interval	Δt (s)	0.025
	Manning's roughness coefficient for lower layer (soil layer)	n ($m^{-1/3}s$)	0.4
	Kinematic viscosity for lower layer (soil layer)	ν(m^2/s)	0.01
	resistance coefficient	C_D (-)	0
	coefficient for interface resistance force	f_{inter} (-)	0
KLS model	Computation time interval	Δt (s)	0.1
	Horizontal slide velocity	U (m/s)	40
	Rise time	T (s)	120

(2) Results

The appropriate grid size is examined based upon the results of calculations performed using the conditions indicated in the previous section.

First, the results of the two-layer flow model are shown. convergence is verified of the maximum water level ascent and descent when the grid sizes are set at L/5, L/10, L/20, L/40, and L/80.

The water level time history and maximum water level changes at position x=800m have been examined. Table 4.4.2-11 shows the maximum water level change in a case where the slope incline is 20°. Table 4.4.2-12 shows the change in case where the slope incline is 30°, and Table 4.4.2-13 for the case where the slope incline is 40°.

A case study of these results showed that, when the grid size was set between 1/40 and 1/20 (=10~20m) for size L of the landslide area, the difference in the maximum water level change was, for the most part, ±10% or less in comparison to a case where the grid size was set at the smallest Δx=L/80 (=5m).

Next, the results for the KLS model are shown. Similar to the case of the two-layer flow model, convergence is verified of the maximum water level ascent and descent when grid sizes

are set at $L/5$, $L/10$, $L/20$, $L/40$, and $L/80$.

The water level time history and maximum water level change at position x=800m have been examined. Table 4.4.2-14 shows the maximum water level change in a case where the slope incline is 30°. Because a value for the fall was not able to be obtained, this calculation verified the values with respect to rise.

The case of these results showed that, when the grid size was set between 1/40 and 1/10 (=10~40m) for size L of the landslide area, the difference in the maximum water level change was, for the most part, ±10% or less in comparison to a case where the grid size was set at the smallest $\Delta x=L/80$ (=5m).

Table 4.4.2-11 Maximum water level ascent and descent

(Two-layer flow model, θ=20°, x=800m)

Grid sizes Δx (m)	Water level (m)		Relative error for Δx=5m	
	Maximum water level ascent	Maximum water level descent	Maximum water level ascent	Maximum water level descent
5 (=$L/80$)	2.767	0.607	—	—
10 (=$L/40$)	3.066	0.654	10.8%	7.9%
20 (=$L/20$)	3.143	0.690	13.6%	13.7%
40 (=$L/10$)	2.098	1.030	-24.2%	69.7%
80 (=$L/5$)	1.166	0.461	-57.9%	-24.0%

Table 4.4.2-12 Maximum water level ascent and descent

(Two-layer flow model, θ=30°, x=800m)

Grid sizes Δx (m)	Water level (m)		Relative error for Δx=5m	
	Maximum water level ascent	Maximum water level descent	Maximum water level ascent	Maximum water level descent
5 (=$L/80$)	5.196	2.033	—	—
10 (=$L/40$)	5.268	2.139	1.4%	5.2%
20 (=$L/20$)	5.237	1.418	0.8%	-30.2%
40 (=$L/10$)	4.012	1.785	-22.8%	-12.2%
80 (=$L/5$)	1.864	0.696	-64.1%	-65.8%

Table 4.4.2-13 Maximum water level ascent and descent

(Two-layer flow model, θ=40°, x=800m)

Grid sizes Δx (m)	Water level (m)		Relative error for Δx=5m	
	Maximum water level ascent	Maximum water level descent	Maximum water level ascent	Maximum water level descent
5 (=L/80)	8.570	2.948	—	—
10 (=L/40)	9.210	2.942	7.5%	-0.2%
20 (=L/20)	7.799	3.480	-9.0%	18.1%
40 (=L/10)	6.196	3.266	-27.7%	10.8%
80 (=L/5)	2.308	1.488	-73.1%	-49.5%

Table 4.4.2-14 Maximum water level ascent and descent

(KLS model, θ=30°, x=800m)

Grid sizes Δx (m)	Water level (m)		Relative error for Δx=15m	
	Maximum water level ascent	Maximum water level descent	Maximum water level ascent	Maximum water level descent
5 (=L/80)	0.32	—	—	—
10 (=L/40)	0.33	—	+2.7%	—
20 (=L/20)	0.33	—	+1.4%	—
40 (=L/10)	0.30	—	-8.6%	—
80 (=L/5)	0.26	—	-20.4%	—

4.4.2.4. Summary

Case studies were conducted of the appropriate grid size when applying the two-layer flow model and the KLS model to tsunami originating in submarine landslides as well as slope failures and flank collapses. The results of the case studies are following:

<Submarine landslides>

With both the two-layer flow model and the KLS model, the maximum water level change converged for the most part in these calculation case studies when the grid size was set at 1/20 of size L of the landslide area.

<Slope failures and flank collapses>

With the two-layer flow model, the maximum water level ascent change converged for the most part when the grid size was set at 1/20 of size L of the landslide area. With respect to the maximum water level descent, there was convergence for the most part in the case where the grid size was set at 1/40 of size L of the landslide area. However, when compared with the results of the examination using tsunami triggered by submarine landslides, the results showed that a

relatively large difference remained in comparison to a case where the grid size was configured more minutely.

With the KLS model, the maximum water level ascent converged for the most part when the grid size was set at 1/10 of size L of the landslide area.

In many cases the length of the tsunami wave following a slope failure or flank collapse was shorter than that of a tsunami following an earthquake. Attention needs to be given so that the grid size for the area surrounding the tsunami source region is configured with the precision sufficient for expressing the spatial tsunami shape of the water level.

4.4.3. Relationship between the calculation tsunami height and the topographical conditions as well as various parameters

An investigation was conducted for the effects of topographical conditions and various parameters on calculation tsunami height for the purpose of ascertaining characteristics of numerical methods. The numerical methods are the two-layer flow model and KLS model. These methods were applied to the calculation of submarine landslides in accordance with the virtual topography given in Appendix Section 4.4.2.2. The following perspectives were adopted for the investigation.

- Relationship of maximum water level change to slope incline
- Directivity of maximum water level change
- Characteristics of attenuation over distance of the maximum water level change
- Relationship between the maximum water level change and the slide velocity
- Relationship of maximum water level change to rise time (KLS model)

(1) Relationship of maximum water level change to slope incline

Calculations were performed in which slope incline was varied under the following conditions, and the relationship between slope incline and maximum water level was analyzed.

- Slope incline $\theta = 3, 6, 12°$
- Two-layer flow model: Sediment layer roughness coefficient n=0.4m$^{-1/3}$s
- KLS model: U = 40m/s, T = 120s

The other conditions are the same as those for the calculations in Appendix Section 4.4.2.2.

The target sites were x = -2,400m offshore and x = 2,400m along the shore (see Figure 4.4.2-1).

The relationship between slope incline and maximum water level is shown in Figure 4.4.3-1.

- With the two-layer flow model, as the slope incline becomes steeper, the intensity of the tsunami becomes greater.

• With the KLS model, increase in slope incline does not necessarily contribute to an increase in tsunami intensity. Because of this, it has been suggested that attention needs to be given so that the propagation velocity may be configured in accordance with the slope incline and other settings aligned in keeping with the parameters.

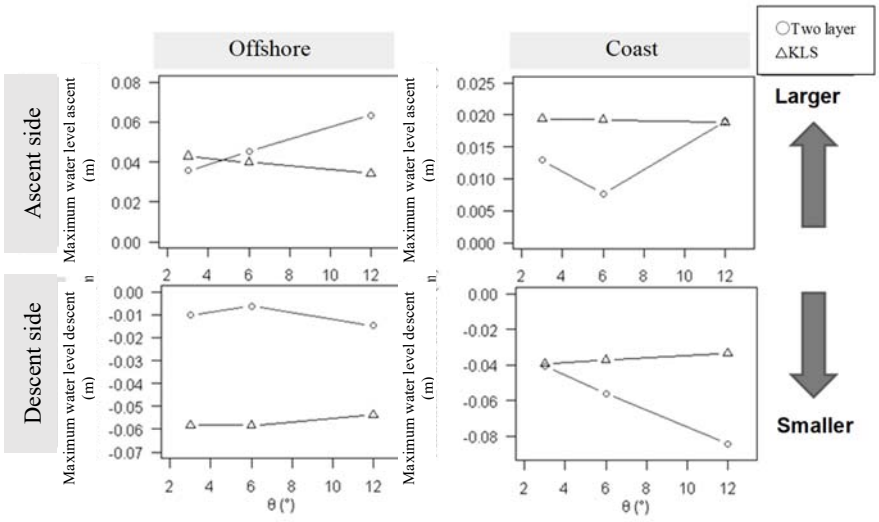

Figure 4.4.3-1 Slope gradient and maximum water level variations

(2) Directivity of maximum water level change

The relationship between tsunami propagation distance and maximum water level change has been examined for calculations performed under the following conditions, and the characteristics related to directivity of each model verified.

• Slope incline $\theta = 6°$

• Two-layer flow model: Sediment layer roughness coefficient n=0.4m$^{-1/3}$s

• KLS model: U = 40m/s, T = 120s

The other conditions are the same as those for the calculations in Appendix Section 4.4.2.2.

The target sites were arranged at 5° intervals on a circle having a radius of 2,400m with its center at the initial apex of the landslide body (see Figure 4.4.2-1).

Figure 4.4.3-2 shows the relationship between tsunami propagation direction and maximum water level change. The orientation parallel to the shore is γ=0°, the orientation heading perpendicular to the shore is γ=90°, and the orientation heading in the opposite direction out to sea is γ= -90°. The directivity of the maximum water level ascent in the direction out to sea was verified by both methods. With respect to the maximum water level descent, the two-layer flow model was in the direction of the shore, and directivity in the direction out to sea was verified for

the KLS model. In particular, directivity verified with the two-layer flow model was more pronounced than that verified with the KLS model.

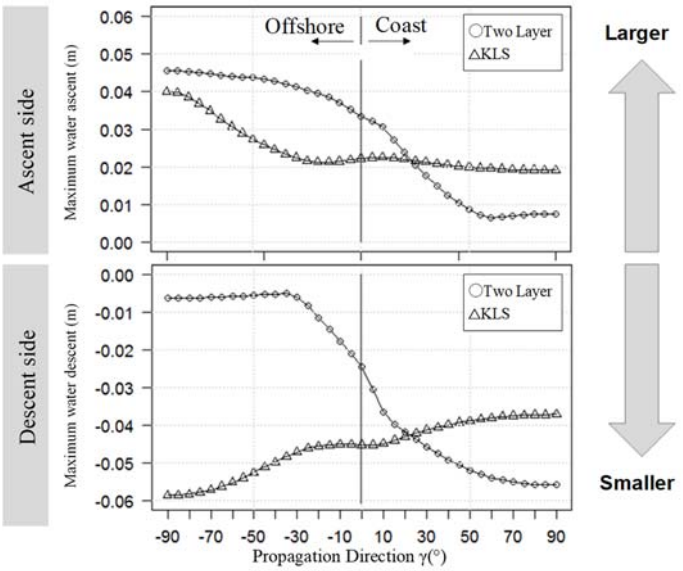

Figure 4.4.3-2 Directivity for maximum water level
(Two-layer flow model, KLS model)

(3) Characteristics of attenuation over distance for maximum water level change

The relationship between tsunami propagation distance and maximum water level change has been examined for calculations performed under the following conditions, and the characteristics verified as pertains to attenuation over distance for each model.

- Slope incline $\theta = 6°$
- Two-layer flow model: Sediment layer roughness coefficient n=0.4m$^{-1/3}$s
- KLS model: U = 40m/s, T = 120s

The other conditions are the same as those for the calculations in Appendix Section 4.4.2.2. The target sites are points along the linear y=0 (see Figure 4.4.2-1).

Figure 4.4.3-3 shows the maximum water level ascent at the target sites. The axis of abscissas is x, and the origin is the point of maximum topographic prominence. The absolute value of coordinate x is regarded as the propagation distance.

In order to quantitatively express the characteristics of attenuation over distance, the relationship between propagation distance $|x|$ and maximum water level ascent y was regressed in equation $y = a \times |x|^b$. The results are as follows.

- In the case where the coefficient of the regression equation was determined for the section out to sea -3,000 < x < -1,500:

- Two-layer flow : a = 2.13, b = -0.494
- KLS : a = 3.21, b = -0.514

• In the case where the coefficient of the regression equation was determined for the section along the shore 1,500 < x < 3,000:

- Two-layer flow : a = 0.10, b = -0.336
- KLS : a = 1.98, b = -0.512

In the case of the point tsunami source, theoretically, the water level is inversely proportional to the square root of the distance. The regression value of coefficient b is on the order of -1/2 with the exception of along the shore for the two-layer flow model where amplitude is particularly small. It was verified that, along the linear y=0, the numerical solution provided by both models was in accordance for the most part with the theoretical attenuation characteristics of the point tsunami source.

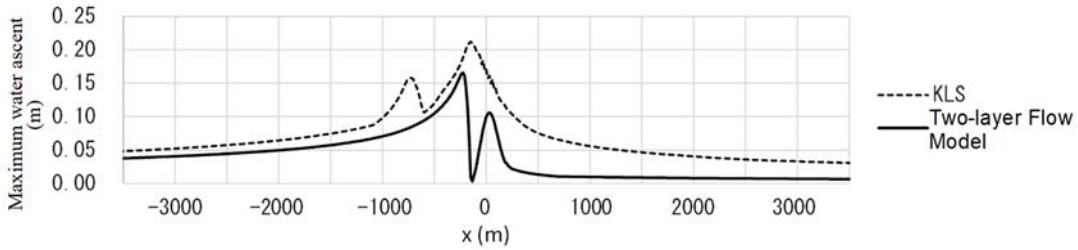

Figure 4.4.3-3 Distribution of maximum water level ascent (Two-layer flow model, KLS model, y=0)

(4) Relationship between maximum water level change and slide velocity

The relationship between slide velocity and maximum water level has been examined for the two-layer flow model, and the relationship between propagation velocity and maximum water level for the KLS model. The calculations were performed using the following conditions.

• Slope incline θ = 6°
• Two-layer flow: n=0.2, 0.3, 0.4m$^{-1/3}$s
• KLS: U = 10, 20, 40m/s, T = 120s

The other conditions are the same as those for the calculations in Appendix Section 4.4.2.2.

The target sites were x= -2,400m offshore and x=2,400m along the shore (see Figure 4.4.2-1).

The slide velocity in the two-layer flow model is the mean velocity defined as L/S where S is the time required for the point of maximum thickness to move distance L (= 600m) in each time series.

Figure 4.4.3-4 shows the relationship between slide velocity and maximum water level

change. From this examination, it was found that, for both the two-layer flow model and KLS model, the greater U is, the greater the tsunami intensity becomes. However, the water level in the KLS model had a greater sensitivity to velocity U. Also, particularly along the shore where it is anticipated a power station will be located, a tendency was observed where the KLS model assessed the scale of the rise greater, and the two-layer flow model assessed the scale of the fall to be greater.

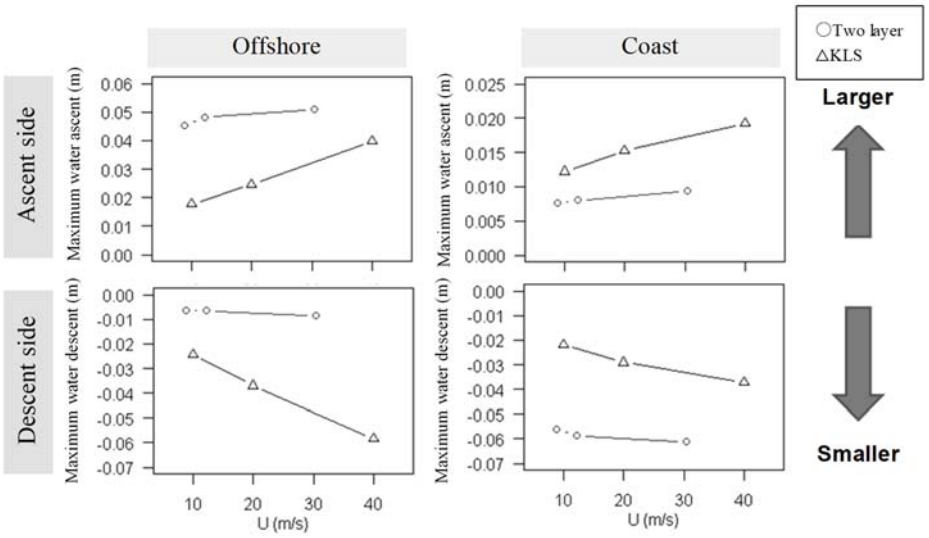

Figure 4.4.3-4 Horizontal slide velocity and maximum water level variations

(5) Relationship of maximum water level change to rise time (KLS model)

Calculations were performed where rise time T was varied for the KLS model, and the relationship between duration and maximum water level was examined. The calculation conditions were as given below.

- Slope incline $\theta = 6°$
- KLS: $U = 40$m/s, $T = 120$, 240, 480s

The other conditions are the same as those for the calculations in Appendix Section 4.4.2.2.

The target sites were x= -2,400m offshore and x=2,400m along the shore (see Figure 4.4.2-1).

Figure 4.4.3-5 shows the relationship between duration and maximum water level.

From this examination, it was able to be verified that the shorter the duration, the greater the tsunami intensity becomes with the KLS model.

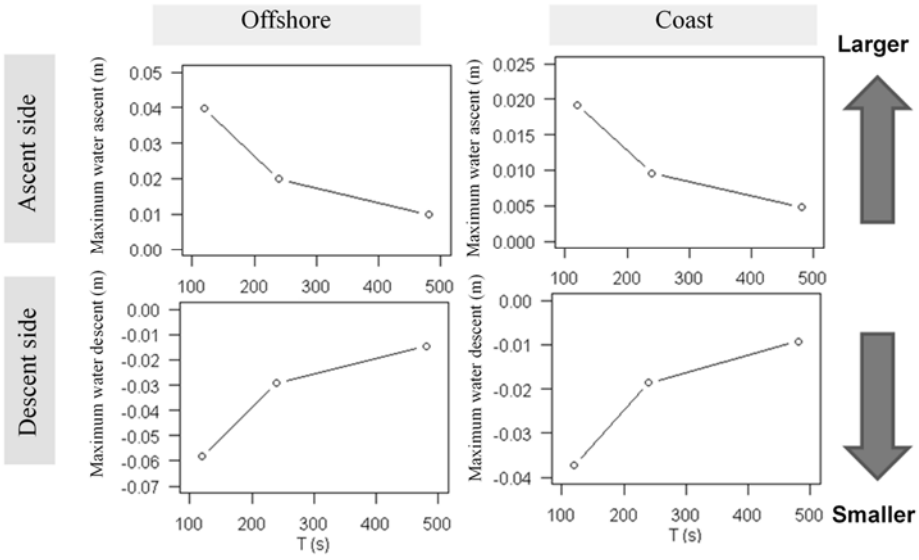

Figure 4.4.3-5 Rise time and maximum water level variations (KLS model)

4.4.4. Case studies of historical tsunami caused by factors other than fault motion

The majority of the factors causing tsunami are due to the vertical displacement occurring in the seafloor following fault motion. However, although relatively few in number*, there are also tsunamis that occur due to factors other than fault motion, such as submarine landslides, slope failures and volcanic phenomena (flank collapse, caldera collapse, etc.), some of which have caused enormous damage. This section examines, according to causal factor, notable examples of tsunami that have occurred due to factors other than fault motion.

* According to Imamura (1998), tsunami caused by factors other than fault motion account for less than 10% of all tsunami.

4.4.4.1. Tsunami caused by volcanic phenomena (flank collapse)

Name	Ariake Sea Tsunami (torment at Shimabara and strife at Higo)	Date	May 21, 1792 (1st day of 4th month in 4th year of the Kansei era)
Summary	• A volcanic earthquake, which occurred on the night of May 21, 1792 (first day of the 4th month in 4th year of the Kansei era), caused a large flank collapse at Mt. Tengu, which is a peak of Mt. Mayuyama located approximately 4 km to the east of Mt. Unzen-Fugen, and the flow of debris turned into a flow of earth and stone that plunged into Ariake Sea, triggering a tsunami. • The large tsunami, which descended on the coastal area of Kumamoto Prefecture (Higo Province) on the other side as well as the coastal area of the Ariake Sea over the entire Shimabara region, is known as the greatest volcanic disaster in Japan in recorded history with the tsunami reaching heights exceeding 30 to 50 meters at Shimabara and between 15 and 20 meters in Kumamoto City, and a total of 15,000 people either missing or dead.		
Previous case studies, etc.	Aida, I. (1975) Numerical Experiments of the Tsunami Associated with the Collapse of Mt. Mayuyama in 1792, Zisin (Journal of the Seismological Society of Japan. 2nd ser.), Vol.28, pp.449-460 (in Japanese), https://www.jstage.jst.go.jp/article/zisin1948/28/4/28_4_449/_pdf Sasahara, N. (2004) Numerical Simulation of the Tsunami caused by the sector Collapse of Mt. Mayuyama, Shimabara Peninsula, Kyushu in 1792, REPORT OF HYDROGRAPHIC AND OCEANOGRAPHIC RESEARCHES No.40 March, pp. 63-72. http://www1.kaiho.mlit.go.jp/GIJUTSUKOKUSAI/KENKYU/report/rhr40/rhr40-02.pdf Togashi, H., Y. Hirayama, U. Taniguchi, and S. Matsumoto (1992) Hydraulic experiments of Ariake Sea tsunami in 1792, Proceedings of Coastal Engineering, JSCE, Vol.39, pp. 221-225 (in Japanese), https://www.jstage.jst.go.jp/article/proce1989/39/0/39_0_221/_article/-char/ja/. Tsuji, Y. and T. Hino (1993) Damage and Inundation Height of the 1792 Shimabara Landslide Tsunami along the Coast of Kumamoto Prefecture, Bulletin of the Earthquake Research Institute, University of Tokyo, Vol.68(2), pp.91-176, https://repository.dl.itc.u-tokyo.ac.jp/?action=repository_action_common_download&item_id=32721&item_no=1&attribute_id=19&file_no=1 Tsuji, Y. and Y. Murakami (1997) Run up height of Ariake Sea tsunami on Shimabara peninsula generated by collapse of Mt. Mayuyama in 1792, Proceedings of Historical Earthquake Studies, JSCE, Vol. 13, pp.135-173 (in Japanese).		

Name	Oshima-Oshima Tsunami	Date	August 29, 1741 (19th day of 7th month in 1st year of the Kanpo era)
Summary	• The Oshima-Oshima tsunami occurred in the sea adjacent to Oshima-Oshima early in the morning of August 29, 1741 (19th day of 7th month in 1st year of the Kanpo era). The tsunami height has been estimated to have been between 3 and 15 meters along the coastline of the Oshima Peninsula and between 4 and 7 meters along the Tsugaru Peninsula. Estimates have also put the tsunami height between 2 and 5 meters at Sado, 4 meters along the Noto Peninsula, 1 meter at Obama in Fukui Prefecture, 2 meters at Gotsu in Shimane Prefecture, and between 3 and 4 meters along the eastern coastline of South Korea. • This tsunami is said to have resulted in the deaths of 1,467 people (over 2,000 when Ainu and people living on Honshu are included). • There are various theories about the cause of the tsunami. It has been pointed out that, at the time, no major earthquakes had been felt and there is the possibility that the tsunami was triggered by an avalanche of debris resulting from a flank collapse following an eruption that began in the western mountains of Oshima-Oshima around August 18, 1741.		
Previous case studies, etc.	Aida, I. (1984) An Estimation of Tsunamis Generated by Volcanic Eruptions - The 1741 Eruption of Oshima-Ohshima, Hokkaido., Bulletin of the Earthquake Research Institute, University of Tokyo, Vol.59(4), pp.519-531 (in Japanese), http://tsunami-dl.jp/document/133 Hatori, T. (1984) Reexamination of Wave Behavior of the Hokkaido-Oshima (the Japan Sea) Tsunami in 1741 : Their Comparison with the 1983 Nihonkai-Chubu Tsunami., Bulletin of the Earthquake Research Institute, University of Tokyo, Vol.59(1), pp.115-125 (in Japanese with English abstract), https://www.researchgate.net/publication/29773100_beihaidaodudaochongjinbo1741niannojudongnozaijiantao_1983nianribenhaizhongbudezhenjinbotonobijiao Imamura, F. and T. Matsumoto (1998) Field Survey of the 1741 Oshima-Ohshima Volcanic Tsunami, Tsunami engineering Technical Report, Tohoku University , Vol.15, pp.85-105 (in Japanese). Katsui, Y., I. Yokoyama, S. Ehara, H. Yamashita, K. Niida, and M. Yamamoto (1977) Oshima-Ohshima. Report of the Volcanoes in Hokkaido, part 6 Committee for Prevention of the Natural Disasters of Hokkaido, Sapporo, 82 pp. (in Japanese). Japan Meteorological Agency (2013) National Catalogue of The Active Volcanoes in Japan (The fourth edition), http://www.data.jma.go.jp/svd/vois/data/tokyo/STOCK/souran_eng/menu.htm Satake, K. and Y. Kato (2001) The 1741 Oshima-Oshima Eruption: Extent and Volume of Submarine Debris Avalanche, Geophysical Research Letters, Vol. 28, No.3, pp.427-430. Satake, K. and Y. Kato (2002) Collapse of the Oshima-Ohshima Island triggered the 1741 Kampo tsunami, Kaiyo Monthly, Extra ed.,28, pp.150-160. (In Japanese). Tsuji, Y., W. S. Beak, K.S. Chu, and H. S. An (1984) Earthquake-induced tsunamis attacked on the eastern coast of Korea, Kaiyo-kagaku Monthly, 16, pp.527-537. (In Japanese).		

Name	Hokkaido-Komagatake Tsunami	Date	July 31, 1640 (13th day of 6th month in 17th year of the Kan'ei era)
Summary	• In the afternoon of July 31, 1640 (13th day of 6th month in 17th year of the Kan'ei era), part of the crest of a mountain collapsed following a large eruption of the Hokkaido-Komagatake Volcano. An avalanche of debris rushed into Onuma Lake and Uchiura Bay, causing a tsunami that descended upon Usu Zenkoji Temple on the opposite side and drowned some 700 people. • Historical descriptions, tsunami deposits, numerical simulations and various other sources of knowledge have been taken into account in estimating the height of the tsunami, which has been put at between 6 and 8 meters along the coastline of Uchiura Bay extending from the west to the north of Komagatake, between 8 and 11 meters from Usu to Muroran, and between 6 and 8 meters from Shiraoi to Tomakomai to the east.		
Previous case studies, etc.	Hatori, T. (1984) Reexamination of Wave Behavior of the Hokkaido-Oshima (the Japan Sea) Tsunami in 1741 : Their Comparison with the 1983 Nihonkai-Chubu Tsunami., Bulletin of the Earthquake Research Institute, University of Tokyo, Vol.59(1), pp.115-125 (in Japanese). https://www.researchgate.net/publication/29773100_beihaidaodudaochongjinbo1741niannojudongnozaijiantao_1983nianribenhaizhongbudezhenjinbotonobijiao Hokkaido Disaster Management Council (1975) Komagatake – Geological Map, Historical Activity, Volcanic Activity, and Disaster Prevention, Report of the volcanoes in Hokkaido, part 4. Committee for Prevention of the Natural Disaster of Hokkaido, 194p (in Japanese). Nishimura, Y. and K. Satake (1993) Numerical computations of tsunamis from the past and future eruptions of Komagatake Volcano, Hokkaido, Japan., Proceedings of the IUGG/IOC International Tsunami Symposium, pp.573-583. Nishimura, Y. and N. Miyaji (1998) On Height Distribution of Tsunami Caused by the 1640 Eruption of Hokkaido-Komagatake, Northern Japan., Kazan, Bulletin of the Volcanological Society of Japan, Vol.43, pp.239-242 (in Japanese), https://www.jstage.jst.go.jp/article/kazan/43/4/43_KJ00001052578/_pdf/-char/ja Tsuji, Y. (1989) Tsunami from the Eruption of Hokkaido Komagatake on July 31, 1640, The Seismological Society of Japan, 1989 Meeting, Proceedings (1) 261p (in Japanese). Yohimoto, M., Hurukawa, R., Nanayama, H., Nishimura, Y., Nishina, K., Uchida, Y., Takarada, S., Takahashi, R., Kinoshita, H(2003): Subaqueous distribution and volume estimation of the debris-avalanche deposit from the 1640 eruption of Hokkaido-Komagatake volcano, southwest Hokkaido, Japan, The Journal of the Geological Society of Japan, Vol.109,No.10, pp.595-606 (in Japanese), https://ci.nii.ac.jp/els/contents110003009762.pdf?id=ART0003416282		

4.4.4.2. Tsunami caused by volcanic phenomena (caldera collapse)

Name	Tsunami following eruption of Krakatoa Volcano (Sunda Strait, Indonesia)	Date	August 27, 1883
Summary	• Following a major eruption of Krakatoa Volcano which occurred at 9:58 local time on August 27, 1883, two-thirds of the island disappeared and a large tsunami occurred in the Sunda Strait that flooded the surrounding islands. The results of investigations of the traces of this tsunami have found that the maximum run-up height reached over 30 meters and over 36,000 people died, making it the largest tsunami disaster in the Indian Ocean until the earthquake off of Sumatra Island in 2004. • The mechanism, which generated this tsunami, is not clearly understood. If it is assumed that the cause was a caldera collapse, then the tsunami may be explained by records of tidal observations that, among other things, show a predominance of short-period waves inside the Sunda Strait and a predominance of long-period waves outside the strait. • Also, based on the results of numerical simulations, it has been pointed out that a tsunami source model entailing a phreatic explosion underwater is able to explain the results of actual measurements of the tsunami.		
Previous case studies, etc.	Aida, I (1995) The 1883 Krakatau eruption tsunami, Document Editing Society of Diet (Editorial supervisor: Rikitake, T.), pp.198-199. Kawamata, S., F. Imamura, and N. Shuto (1992) Numerical simulation of the 1883 Krakatau tsunami, Proceedings of Coastal Engineering, JSCE, Vol.39, pp.226-230 (in Japanese), https://www.jstage.jst.go.jp/article/proce1989/39/0/39_0_226/_pdf Nomanbhoy, N. and K. Satake (1995) Generation mechanism of tsunami from the 1983 Krakatau eruption, Geophysical Research Letters, Vol.22, No.4, pp.509-512. Simkin, T. and R.S. Fiske (1983) Krakatau 1883, The volcanic eruption and its effects, Smithsonian Institution Press, 464p. Winchester, S. (2005) Krakatoa: THE DAY THE WORLD EXPLODED: AUGUST 27, 1883, Harper Perennial; 1st Harper Perennial Ed. Publ. 2005 edition, 416p.		

4.4.4.3. Tsunami caused by submarine landslide

Name	Meiwa Yaeyama Earthquake Tsunami	Date	August 24, 1771 (10^{th} day of 3^{rd} month in 8^{th} year of the Meiwa era)
Summary	• Following an earthquake that occurred around 8 AM on April 24, 1771 (10th day of 3rd month in 8th year of the Meiwa era), a tsunami occurred that resulted in approximately 12,000 dead or missing on the Miyako Islands and Yaeyama Islands as well as more than 2,000 homes swept away. Based on the results of investigations of the height of traces of the tsunami, it has been found that the run-up height of the tsunami reached approximately 30 meters in the southern part of Ishigaki Island and approximately 18 meters in the southern part of Miyako Island. • Based on the results of numerical simulations, it is difficult to explain the run-up height records of tsunami only from fault displacement on the basis of the earthquake magnitude. Investigations of the sea bottom topography in the seas around the Yaeyama Islands have confirmed traces of submarine landslides, and it has been pointed out that it is highly possible the tsunami was caused by a submarine landslide.		
Previous case studies, etc.	Goto, K. and A. Shimabukuro (2012) The 1771 Meiwa tsunami revealing by multidisciplinary researches, Kagaku, 82, pp.208-214 (in Japanese). Hatori, T(1987) Tsunami magnitudes and source areas along the Ryukyu islands, Zisin (Journal of the Seismological Society of Japan. 2nd ser.), Vol.41, pp. 541-547, (in Japanese), https://www.jstage.jst.go.jp/article/zisin1948/41/4/41_4_541/_article Hiraishi, T., H. Shibaki, and N. Hara (2001) Numerical Simulation of Meiwa-Yaeyama Earthquake Tsunami in Landslide Model with Circular Rupture, Proceedings of Coastal Engineering, JSCE, Vol.48, pp.351-355 (in Japanese), http://library.jsce.or.jp/jsce/open/00008/2001/48-0351.pdf Kawana, T., N. Date, T. Nakata, Y. Masaki, N. Simabukuro, R. Hagino, N. Nakasone, and N. Oohashi (2000) Run up height and movement of reef boulders in Ishigaki island caused by the 1771 Meiwa tsunami, Proceedings of Historical Earthquake Studies, JSCE, Vol. 17, pp.38-41 (in Japanese). Matsumoto, T., Kimura, M. (1993) Detailed bathymetric survey in the sea region of the estimated source area of 1771 Yaeyama earthquake tsunami and consideration of the mechanism of its occurrence, Zisin (Journal of the Seismological Society of Japan. 2nd ser.), Vol.45, pp. 417-426 (in Japanese), https://www.jstage.jst.go.jp/article/zisin1948/45/4/45_4_417/_article/-char/ja/ Nakata, T. and T. Kawana (1986) Seismic tsunami in 1771, Proceedings of Historical Earthquake Studies, JSCE, Vol. 2, pp.141-147 (in Japanese).		

4.4.4.4. Tsunami caused by flank (slope) collapse

Name	Lituya Bay Tsunami (Alaska, United States)	Date	July 10, 1958
Summary	• Following the M_W 8.3 earthquake on July 10, 1958, a massive slope failure occurred in the interior of Lituya Bay along the southern coast of Alaska, and a large quantity of earth, sand and lumps of ice plunged into the sea, causing a massive tsunami. • Lituya Bay is a long, narrow and steep fjord that is approximately 11.3 km long and approximately 3.2 km wide at the widest point, and fronts the Pacific Ocean. The tsunami, from which there was no place to escape, ran up the slope on the opposite coast and reached an elevation of 524 meters, which is the highest observation ever recorded. However, as the run-up height of the tsunami approach the bay opening, it suddenly decreased, and no traces of any impact outside the bay have been observed. • At Lituya Bay, six flank collapses have been recorded due to similar slope failures.		
Previous case studies, etc.	Aida, I. (1982) Tsunami caused by a sector collapse, Monthly marine sciences, Vol.9, No.2, pp.31-38 (in Japanese). Aida, I. (1995) The 1958 Lituya Bay tsunami in Alaska, Document Editing Society of Diet (Editorial supervisor: Rikitake, T.), pp.202-203 (in Japanese). Fritz, H.M., F. Mohammed, and J. Yoo (2009): Lituya Bay Landslide Impact Generated Mega-Tsunami 50th Anniversary, Pure and Applied Geophysics, Feb. 2009, 166, pp.153-175. Unoki, S. and M. Kubota (1996) Science of Ocean Waves and Currents, Tokai University Press, 356p (in Japanese).		

4.4.4.5. Tsunami caused by other factors

Name	Papua New Guinea Earthquake Tsunami (Sissano coast, West Sepik Province)	Date	July 17, 1998
Summary	• At around 18:49 local time on July 17, 1998, a M7.1 earthquake occurred causing a tsunami that resulted in more than 2,000 deaths along the Sissano coast. The maximum height of the tsunami was over 10 meters, and there was damage over an area extending along 30 kilometers of coastline. • In comparison to the earthquake magnitude, the intensity of the tsunami was greater. While it has been pointed out that events other than fault displacement such as landslides triggered by the earthquake were factors causing the tsunami, detailed investigations of the sea bottom topography found distinct geographical features suggesting that tsunami are more prone to be concentrated along the Sissano coast than other areas. • Calculations have been performed using multiple models of the tsunami occurrence and propagation, but they have not been able to completely explain the results of actual observations, and a conclusion on the factors causing the tsunami has still not been reached.		
Previous case studies, etc.	Hashi, K., and Imamura, F(2000), Study on the Multi-Tsunami Source in the Case of the 1998 Papua New Guinea Tsunami, Proceedings of Coastal Engineering, JSCE, Vol.47, pp.346-350 (in Japanese), http://library.jsce.or.jp/jsce/open/00008/2000/47-0346.pdf Kawada, K., Takahashi, T., Imamura, H., Matsutomi, H., Hujima, K and Matsuyama, M. (1999), Proceedings of Coastal Engineering, JSCE, Vol.46, pp.391-395 (in Japanese), https://www.jstage.jst.go.jp/article/proce1989/46/0/46_0_391/_article/-char/ja/ Matsuyama, M., Imamura, H., Hash Matsuyama, M., Imamura, H., Hashi, K., Matsumoto and T., Tsuji (1999), Proceedings of Coastal Engineering, JSCE, Vol.46, pp. 386-390 (in Japanese), https://www.jstage.jst.go.jp/article/proce1989/46/0/46_0_386/_article/-char/ja/ Matsuyama, M., Satake, K. and Matsumoto, T(1999), Proceedings of Coastal Engineering, JSCE, Vol.48, pp. 366-370 (in Japanese), https://www.jstage.jst.go.jp/article/proce1989/48/0/48_0_366/_article/-char/ja/ Tappin, D. R., T. Matsumoto, P. Watts, K. Satake, G. M. McMurty, M. Matsuyama, Y. Lafoy, Y. Tsuji, T. Kanamatsu, W. Lus, Y. Iwabuchi, H. Yeh, Y. Matsumoto, M. Nakamura, M. Mahoi, P. Hill, K. Crook, L. Anton, and J. P. Walsh (1999): Offshore surveys identify sediment slump as likely cause of devastating Papua New Guinea Tsunami 1998, EOS, American Geophysical Union, pp.329-340.		

Name	Kocaeli Earthquake Tsunami (Coast of Izmit Bay, Turkey)	Date	August 17, 1999
Summary	• At around 3:02 local time on August 17, 1999, a tsunami occurred following the M_W 7.4 earthquake with a seismic center near Izmit City in Turkey. Traces of the tsunami have been confirmed at heights of 1 to 2.5 meters at the innermost part of Izmit Bay. • The mechanism of this earthquake was a side slip, which not regarded as often resulting in a tsunami. However, based on the results of field investigations and numerical simulations, speculation has been proffered that the earthquake caused fault displacement as well as ground subsidence and coastal landslides, which occurred in the southern part of Izmit Bay following the earthquake. These compounded and overlapped, triggering a tsunami.		
Previous case studies, etc.	Altinok, Y., B. Alpar, S. Ersoy, and A. C. Yalciner (1999): Tsunami generation of the Kocaeli earthquake (August 17th 1999) in the Izmit bay; coastal observations, bathymetry and seismic data, Turkish Journal of Marine Science, Vol.5, No.3, pp.131-148. Imamura, H., Koshimura, S. and Ahmet C. Yalciner(2000), Proceedings of Coastal Engineering, JSCE, Vol.47, pp. 331-335 (in Japanese), https://www.jstage.jst.go.jp/article/proce1989/47/0/47_0_331/_pdf Yalciner A. C., C. E. Synolakis, J. Borrero, Y. Altinok, P. Watts, F. Imamura, U. Kuran, S. Ersoy, U. Kanoglu and S. Tinti(1999): Tsunami generation in Izumit bay by 1999 Izumit earthquake, Proc. Int. Conf. on Kocaeli earthquake, ITU, Dec. 2-5, Istanbul, pp.217-221.		

4.5. Basic equations and illustrative calculations for water level fluctuation of sea water intake and outlet

4.5.1. Basic equation

(1) Open channel flow

Basic equations for unsteady flows, which have been utilized for inundation flow, etc., are utilized for the continuity equation as well as the momentum equation for open channel flow.

a. Continuity equation for open channel flow

$$\frac{\partial A}{\partial t} + \frac{\partial Q}{\partial x} = 0$$

b. Momentum equation for open channel flow

$$\frac{\partial Q}{\partial t} + \frac{\partial}{\partial x}\left(\frac{Q^2}{A}\right) + gA\,\frac{\partial H}{\partial x} + gA\left(\frac{n^2 \mid v \mid v}{R^{4/3}} + \frac{1}{L} f\,\frac{|v|v}{2g}\right) = 0$$

Of those calculation methods for water channels in Section 6.3.2.1 of the Main Volume, the above basic equations have been applied in the following cases.

Main Volume Section 6.3.2.1 (2): Of those cases where all sections are ordinarily open channel flow, method applying an equation for one-dimensional unsteady flow through an open channel

Main Volume Section 6.3.2.1 (3): Of those cases of both sections with open channel flow and sections with pipeline flow,

- Calculation method based on the slot model
- Section of open channel flow with a calculation method separating the open channel section and pipeline section

(2) Pipeline flow

In sections where there is pipeline flow (flow in a completely filled state without a free water surface), the flow cross sectional area fluctuation in the length direction and flow rate fluctuation are very small, so an expression is used that assumes the first term on the left side of the continuity equation and the second term on the left side of the momentum equation are each 0 for the aforementioned open channel flow.

a. Continuity equation for pipeline flow

$$\frac{\partial Q}{\partial x} = 0$$

b. Momentum equation for pipeline flow

$$\frac{\partial Q}{\partial t} + \frac{\partial}{\partial x}\left(\frac{Q^2}{A}\right) + gA\,\frac{\partial H}{\partial x} + gA\left(\frac{n^2 \mid v \mid v}{R^{4/3}} + \frac{1}{L} f\,\frac{|v|v}{2g}\right) = 0$$

Of those calculation methods for water channels in Section 6.3.2.1 of the Main Volume, the above basic equations have been applied in the following cases.

Main Volume Section 6.3.2.1 (1): Cases where all sections are ordinarily pipeline flow

Main Volume Section 6.3.2.1 (3): Of those cases of both sections with open channel flow and sections with pipeline flow,

- Section of pipeline flow with a calculation method separating the open channel section and pipeline section

where, t: time, Q: flow rate, v: flow velocity, x: coordinate along the water channel, A: flow cross sectional area, H: pressure head + potential head (case of pipeline flow), potential head (case of open channel flow), z: water channel bed height, g: acceleration of gravity, n: Manning's roughness coefficient, R: hydraulic radius, L: length of water channel flow direction, and f: local loss coefficient.

4.5.2. Illustrative calculation conditions

An examination is conducted of the water intake facility model shown in Figure 4.5.2-1.

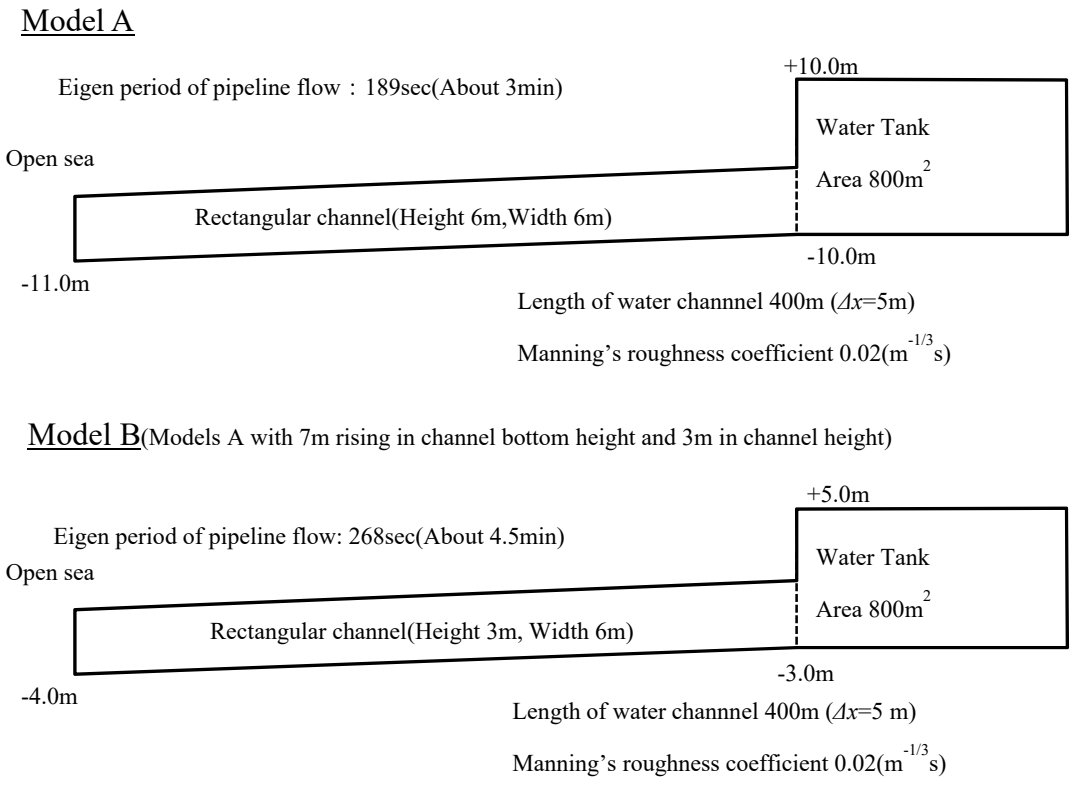

Figure 4.5.2-1 The water intake facility model

The principal calculation conditions are given below.

- The numerical methods are a numerical method that separates the water channel portion into a section for open channel flow and a section for pipeline flow, and a numerical method for the water tank portion that is based upon a model taking into account only fluctuations in water volume inside the tank (see Main Volume Section 6.3.2).
- Data on the perimeter water level in the open sea is the following three types.
  [1] Inherent period 30sec., sine wave having a semi-amplitude of 2m
  [2] Inherent period 20min., sine wave having a semi-amplitude of 2m
  [3] Simulated tsunami waveform (see Figure 4.5.2-2)

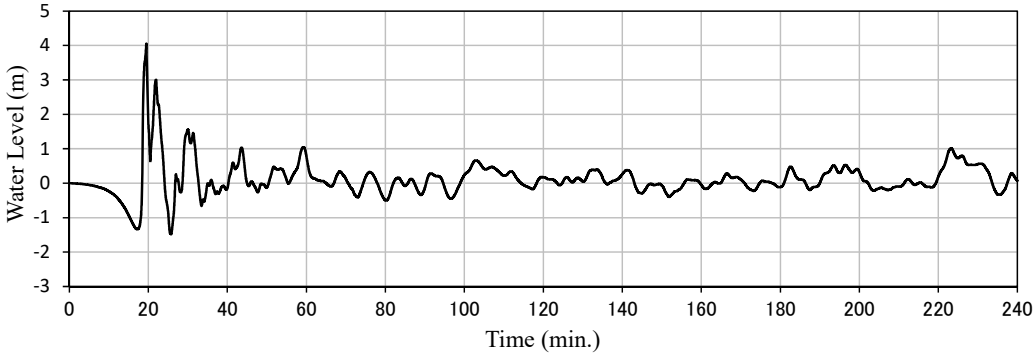

Figure 4.5.2-2 Simulated Tsunami waveform

- Pump water intake volume: 0.0m^3/s
- Computation time interval: 0.05sec

The cases examined are the four cases indicated in Table 4.5.2-1.

Table 4.5.2-1 List of calculation of water level fluctuation of the sea water intake and outlet

Case	Model	Waveform of open sea	Flow
Case1	Model A	Sine wave（Period 30 sec.）	All sections are pipeline flow
Case2	Model A	Sine wave（Period 20 min.）	All sections are pipeline flow
Case3	Model A	Simulated tsunami waveform	All sections are pipeline flow
Case4	Model B	Simulated tsunami waveform	Both sections with open channel flow and sections pipeline flow

4.5.3. Results of illustrative calculations

Table 4.5.3-1 shows the maximum and minimum water levels based upon the results of

calculations for the four cases indicated in Table 4.5.2-1. Figure 4.5.3-1 shows a time series graph for each case. The examination results are consolidated below.

- From the results of Case 1 shown in Figure 4.5.3-1(a), there is almost no change in the water level of the water intake tank. This is because the inherent period (30 seconds) of the open sea water level tsunami waveform is a shorter period than the eigen period for the facility (3 minutes), so the water tank water level did not respond to changes in the water level in the open sea.
- From the results of Case 2 shown in Figure 4.5.3-1(b), the fluctuation in the water level of the water intake tank is the same as that for the open sea. This is because the longer the inherent period becomes of the open sea water level tsunami waveform in comparison to the eigen period of the facility, change in the water level of the water tank becomes coincides more with the water level in the open sea.
- From the results of Case 3 shown in Figure 4.5.3-1(c), it is able to be verified that the composition of the inherent period of 3 minutes, which is included in the water level for the open sea (= eigen period for the facility), is amplified in the water tank.
- In the results of Case 4 shown in Figure 4.5.3-1(d), all sections are in a state of open channel flow due to initial drawback, and the subsequent sudden leading wave forms a bore within the water channel which then immediately becomes a state of pipeline flow. The water intake tank water level subsequently reaches its highest height, and, thereafter as well, fluctuation in the water level in the open sea results in a mix of open channel flow and pipeline flow.

Figure 4.5.3-1 List of the maximum and minimum water levels based upon yhe results of calculations

Case	Model	Waveform of open sea	Water level of open sea(m)		Water level of water tank (m)	
			max	min	max	min
Case1	Model A	Sine wave（Period 30 sec.）	2.00	-2.00	0.06	-0.06
Case2	Model A	Sine wave（Period 20 min.）	2.00	-2.00	2.05	-2.05
Case3	Model A	Simulated tsunami waveform	4.05	-1.48	6.72	-3.99
Case4	Model B	Simulated tsunami waveform	4.05	-1.48	4.60	-1.94

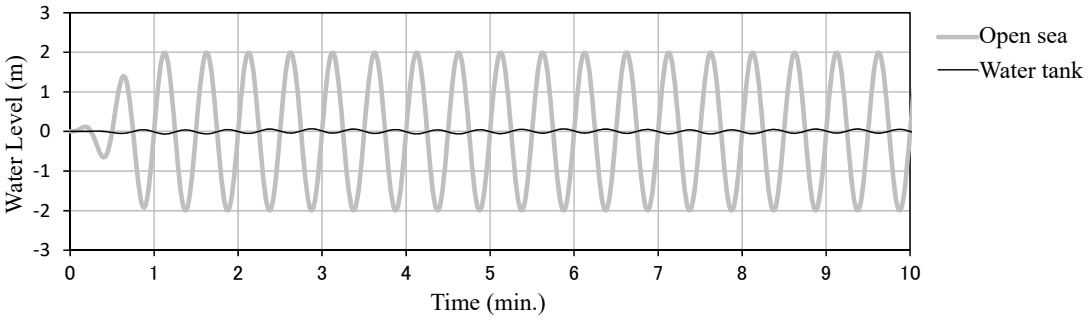

(a) Case1 (Model A, Sine wave (Period 30 sec.))

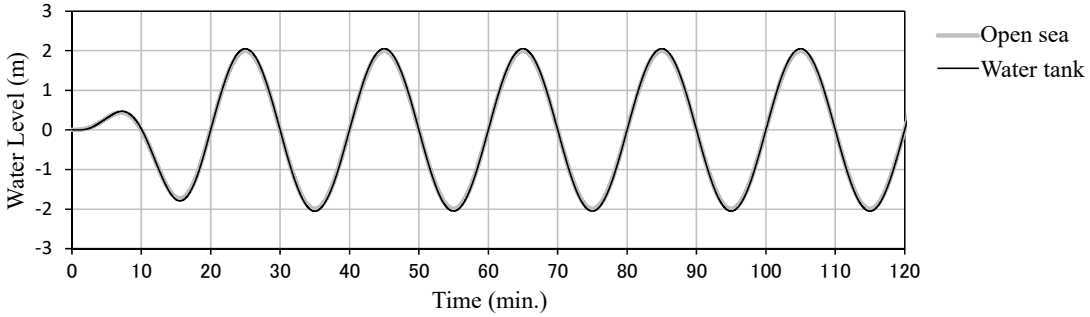

(b) Case2 (Model A, Sine wave (Period 20 min.))

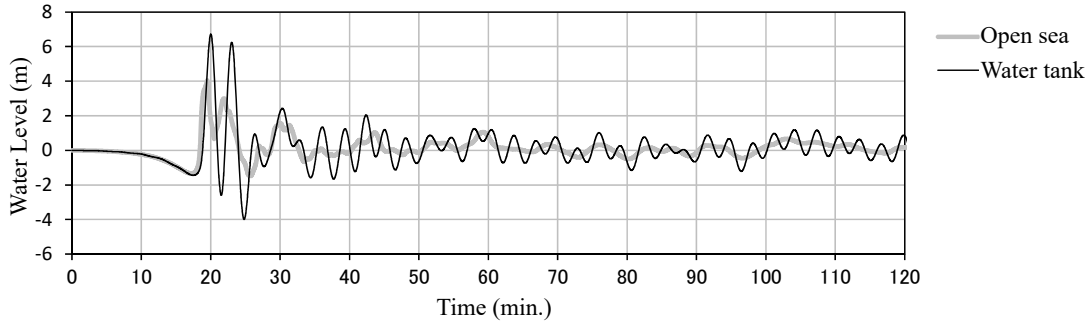

(c) Case3 (Model A, Simulated tsunami waveform)

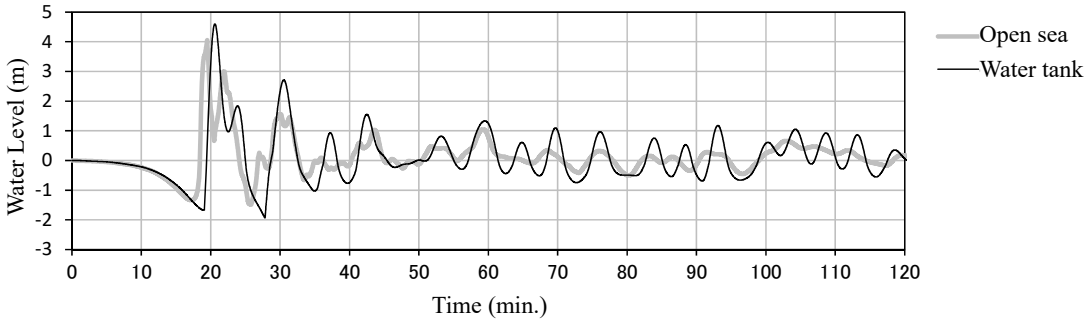

(d) Case4 (Model B, Simulated tsunami waveform)

Figure 4.5.3-1 A time series graph for each case

4.6. Heights of traces of historical tsunami and tide gauge records

4.6.1. Methods for classifying the reliability of historical tsunami trace heights

The confidence of data on the heights of traces of historical tsunami varies in each individual case depending upon how well defined the traces are and the certainty of information sources. In an investigation of tsunami height after the 1960 Chile earthquake tsunami, data on the height of the tsunami traces was classified based upon the standards described in levels A, B and C of Table 4.6.1-1 in accordance with the degree to which the traces were defined and the magnitude of the measurement error (Chile Tsunami Joint Investigation Team, 1961). Subsequent investigations have also followed this classification for the most part. Moreover, when an investigation was conducted of the earthquake tsunami off the eastern coast of Hokkaido in 1994, level D in Table 4.6.1-1 was added (Shuto and Unohana, 1995).

Based upon a similar approach, Table 4.6.1-2 is presented as a standard for classifying the heights of traces of historical tsunami prior to the 1960 Chilean tsunami, which are described in historical material and other sources (Japan Society of Civil Engineers, 2002).

The descriptions given in levels A and B concerning confidence are used in comparisons with tsunami calculations. In cases where there are very few traces of a tsunami, those descriptions in level C or below may be the focus.

Table 4.6.1-1 Classification of confidence levels of run-up height records of tsunami (After 1960 Chilean Tsunami)

		Judgment criteria
Confidence	A	High confidence level. Clear traces with minor survey errors.
	B	Moderate confidence level. Traces are obscure, but the surrounding conditions and witnesses indicate a reliable water level. Survey errors are insignificant.
	C	Low confidence level. Traces indicating waves having abnormally landed a sand beach, etc. or traces with significant survey errors due to survey points located away from the seashore.
	D	Extremely low confidence level. Obscure traces overlapped by the effect of high water or typhoons etc. or folklore or other ungrounded information.

Table 4.6.1-2 Classification of confidence levels of run-up height records of tsunami (Before 1960 Chilean Tsunami)

Japan Society of Civil Engineers (2002)

[Notes on the confidence of ancient document records (Nobuo Shuto)]

		Judgment criteria
Confidence	A	High confidence level. Trace Information is described in ancient texts and local historical documents, etc., as well as site can be confirmed at present.etc., as well as site can be confirmed at present. Furthermore, trace height is surveyed and determined in recent years.
	B	Moderate confidence level. Trace Information is described in ancient texts and local historical documents, etc., as well as site can be confirmed at present. However, trace height is not re-surveyed in recent years.
	C	Low confidence level. Trace Information is described in ancient texts or told from mouth to mouth. However, the information is only limited to the name of regions and villages. Location of trace cannot be tacked.
	D	Only as reference. Information speculated from relevant phenomena and descriptions on damage described in ancient texts.

4.6.2. Relationship between heights of traces of historical tsunami and tide gauge records

Depending upon the frequency response characteristics of tidal wells which are attributable to the structure of the tidal well, tide gauge records omit short period elements of tsunami (this is known as a “hydraulic filter”). Satake et al. (1988) show the typical structure of a tidal well in Japan. The tide gauge itself is set inside the tidal well, and the well is connected with the open sea by means of a

conduit. The conduit functions to remove short period elements that also result from ocean tides. Accordingly, these conduits also affect tsunami records (Satake, 1991).

After the 1983 Nihonkai-Chubu earthquake, the response characteristics of tidal wells were investigated, and a method proposed for correcting tide gauge records. For an example of the correction of tide gauge records and the response characteristics of tidal wells, see Satake et al. (1988).

Kajiura (1983) investigated the relationship between the peak overall amplitude in the tide gauge records and the run-up height around tide gauges, which was:

(Run-up height) ≃ (Tide gauge record peak overall amplitude)

If the water level ascent and descent due to tsunami is almost equal, then this shows that the maximum water level ascent based upon tide gauge records is equivalent to approximately half of the run-up height on average. In other words, the relationship is:

(Run-up height) ≃ (Tide gauge record maximum water level ascent) × 2

4.6.3. Inversion Analysis of Tsunami

References on tsunami inversion can be found in Satake et al. (2013). This case study is presented of a linear inversion analysis that takes into consideration shallow water deformation based upon the method presented by Annaka et al. (1999) for the 1944 Tonankai Earthquake.

(1) Analysis method

1) Configuration of tsunami source model

The tsunami source model, which would serve as the foundation, was configured as indicated below.

- Subduction zone surface: The subduction zone depth (10~30 km) was adopted based upon Kaneda and Baba (2006)
- Slip direction: Configured with reference to Sagiya (1999) and Nishimura et al. (1999)

2) Configuration of calculation grid model

For verification of the reproducibility of tsunami observation records, the results were utilized of calculations performed using a land run-up model with a grid size of 50m along the coastline (Pacific coastline from Chiba Prefecture to Kyushu was partitioned into four regions). For the inversion analysis, calculation of Green's function and a series of tsunami iterations were necessary, so the simulating time was shortened by using a rough grid model with grids of 400m along the coastline (50-meter grid model only at tidal observation record points).

3) Configuration of evaluation function

Evaluation function J, which was used for inversion, is given below.

$$J = C_1 \times \frac{n_2}{n_1} \sum_{i=1}^{n_1} \left\{ \log_{10}\left(\left(A_{NL}^{O}\right)_i\right) - \log_{10}\left(k_i \times \left(A_{NL}^{C}\right)_i\right) \right\}^2 + C_2 \times \sum_{l=1}^{n_0} \sum_{i=1}^{n'_{2l}} \left(\left(Z_{NL}^{O}\right)_{i,l} - \left(Z_{NL}^{C}\right)_{i+ts_l,l} \right)^2 + W \times \sum_{l=1}^{n_0} \left(ts_l\right)^2$$
$$+ C_3 \times \frac{n_2}{n_3} \sum_{i=1}^{n_3} \left\{ B_i^O - B_i^C \right\}^2 + \gamma^2 \sum \left(\nabla^2 m_{i,j}\right)^2$$

where,

n_1: total data number of the height of tsunami traces,

n_2: total data number of tidal observation records,

n_3: total data number of crustal movement,

n_0: number of tidal observation records point,

n'_{21}: number of data per tidal observation records point ,

A^O_{NL}: height of tsunami traces,

A^C_{NL}: the calculation maximum water level (shallow water equation),

Z^O_{NL}: height of tidal observation records at arbitrary time,

Z^C_{NL}: the calculation height at tidal observation records point (shallow water equation),

B^O: observed crustal movement data,

B^C: the calculation crustal movement data,

k: conversion coefficient of calculation result of rough grid model and detailed grid model,

C_1: weight for SSR of the height of tsunami traces,

C_2: weight for SSR of tidal observation records,

C_3: weight for SSR of crustal movements,

ts: the calculation tsunami waveform time shift,

W: weight for the calculation tsunami waveform time shift, and

γ: weight for the smoothing constraint.

$$\nabla^2 m_i = \sum_{j=1}^{n_{si}} m_{bi,j} - n_{si} \times m$$

m_i: slip amount of i th segment, and

$m_{bi,j}$: the j th slip amount adjacent to the i th segment

The height of tsunami traces, tidal observation records and the amount of crustal movement were reproduced, and $C_1 : C_2 : C_3$, which was weighted for the sum of the squared residuals of these, were all 1. Also, the inversion was performed using zero for W weighted for the extent of the calculation tsunami waveform time shift and γ weighted for the smoothing constraint. Tsunami calculations were performed using grid models based upon a model having uniform slippage in all tsunami source regions, and the coefficient for each point, which was used to convert the results of calculations using a rough grid model with 400-meter grids along the coastline into the results of calculations using a detailed grid model with 50-

meter grids along the coastline, was the ratio of the calculation maximum water level for each point marking a trace of the tsunami.

(2) Reproduced data

1) Run-up height of past tsunami

From data for points where traces of the tsunami were identified on the tsunami calculation grid (50-meter grid), those points which appeared to have originated due to river run-up or other such circumstances were omitted, and the data for tsunami traces at 64 sites was adopted.

2) Tidal observation records

The target records are for the following 10 points: Mera, Yokosuka, Ito, Uchiura, Fukue, Morozaki, Matsusaka, Shimotsu, Muroto and Tosashimizu.

A band pass filter having inherent periods ranging from 5 minutes to 3 hours was applied to remove short period elements included due to digitalization and tide elements. The tsunami waveform data intervals were set at 10 seconds.

3) Crustal movement

The values for 12 points based upon Omote (1946) were used as the observed values for crustal movements.

(3) Inversion results

Figure 4.6.3-1 shows a map of the locations of faults of the 1944 Tonankai earthquake and the observation locations. Figure 4.6.3-2 shows crustal movement and site locations. Because setting a configuration for each small fault is difficult due to the relationship of the amount of observation data, the fault slippage, which was estimated by inversion, was computed by grouping together small faults for a total of 18 slippage groups.

Figure 4.6.3-3 shows the fault slippage distribution estimated by inversion. Moreover, Figure 4.6.3-4 shows a comparison of the observation results and calculation results using detailed 50m grids along the coastline based upon the configured tsunami source model. The indices K and κ, which were set forth by Aida (1977) based upon the configured tsunami source model are given below.

K=1.14, κ=1.44 (number of sites: 64)

Although K did not really satisfy the compatibility conditions, κ, which was the indicator for variance, satisfied the conditions of $0.95 < \kappa < 1.45$ (Japan Society of Civil Engineers, 2002). Also, tidal records and crustal movement were able to reproduce, for the most part, observation records.

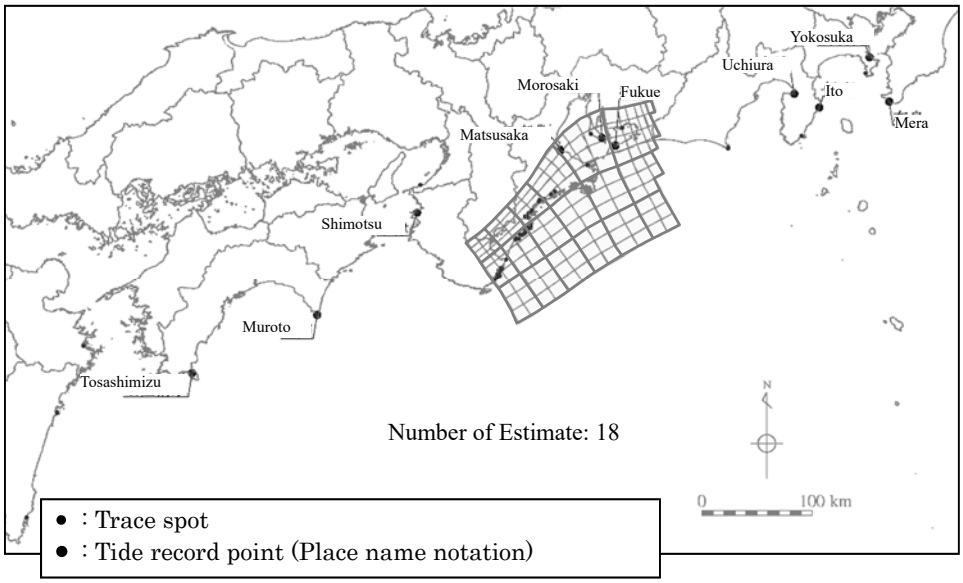

Figure 4.6.3-1 Locations of faults of the 1944 Tonankai Earthquake and Tsunami observation

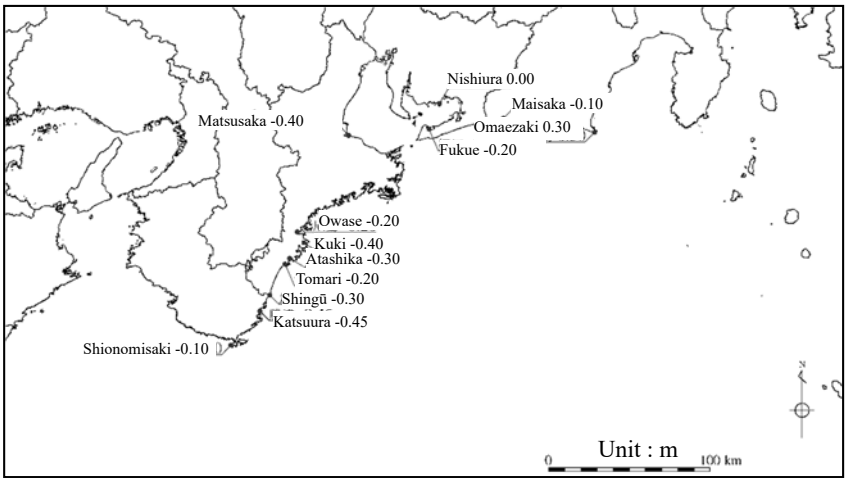

Figure 4.6.3-2 Crustal movements of the 1944 Tonankai Earthquake

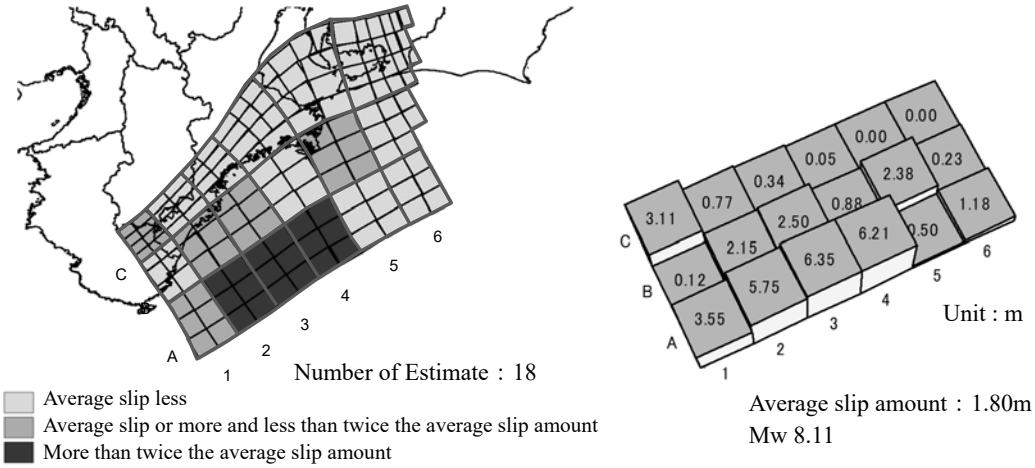

Figure 4.6.3-3 Fault slippage distribution estimated by inversion of the 1944 Tonankai Earthquake

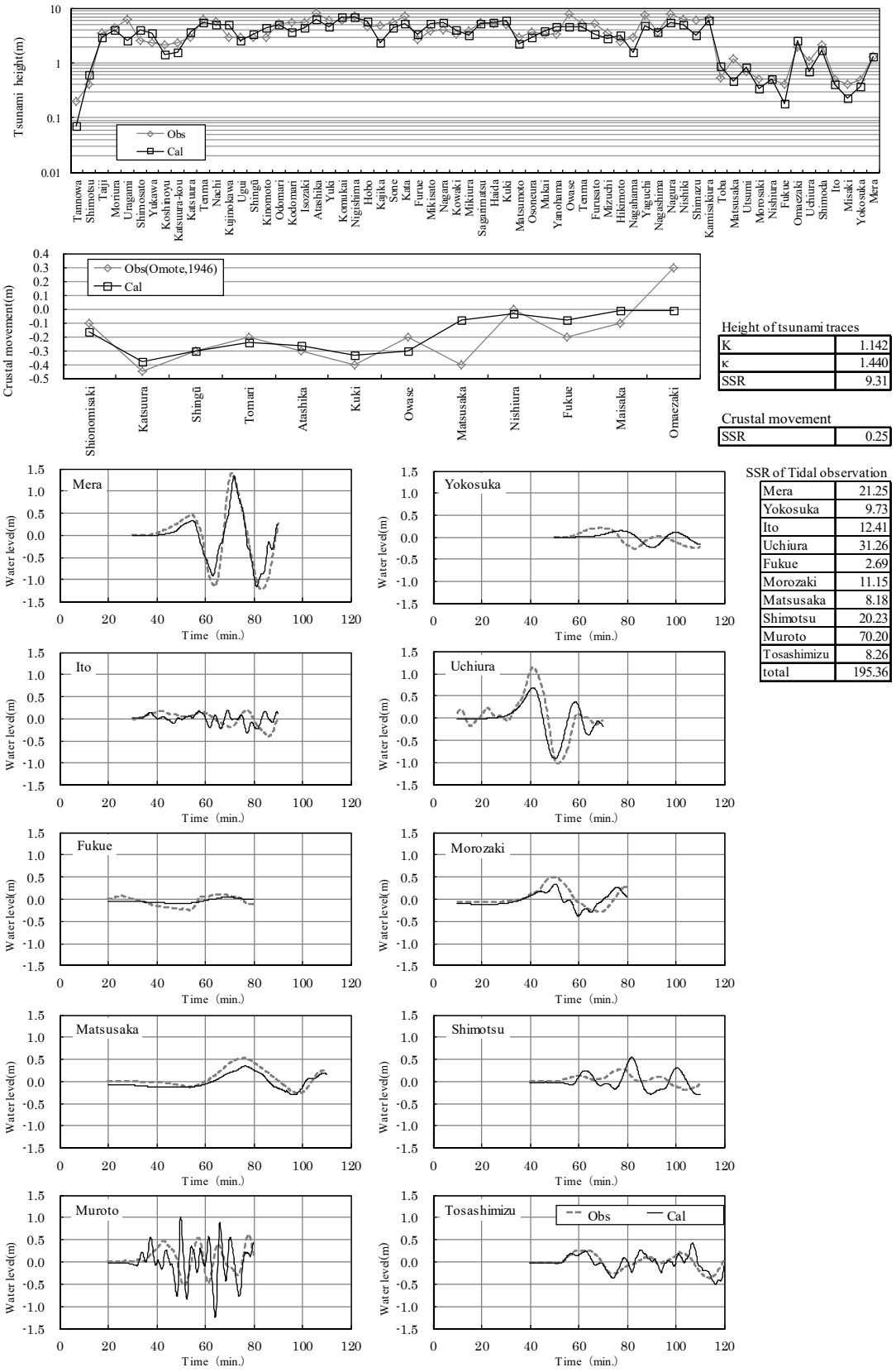

Figure 4.6.3-4 Reproduction result by inversion of the 1944 Tonankai Earthquake

[Appendix 4 References]

Aida, I. (1975): Numerical Experiments of the Tsunami Associated with the Collapse of Mt. Mayuyama in 1792, Zisin (Journal of the Seismological Society of Japan. 2nd ser.), Vol. 28, pp. 449-460 (in Japanese).
https://www.jstage.jst.go.jp/article/zisin1948/28/4/28_4_449/_pdf

Aida, I. (1977): Simulations of Large Tsunamis Occurring in the Past off the Coast of the Sanriku District., Bulletin of the Earthquake Research Institute, University of Tokyo, Vol. 52(1), pp. 71-101 (in Japanese)
https://repository.dl.itc.u-tokyo.ac.jp/?action=repository_action_common_download&item_id=33218&item_no=1&attribute_id=19&file_no=1

Aida, I. (1993): Historical Tsunamis and their Numerical Models which Occurred in the North-Western Part of Sagami Bay, Journal of Geography, Vol. 102, No. 4, pp. 427-436 (in Japanese).
https://www.jstage.jst.go.jp/article/jgeography1889/102/4/102_4_427/_pdf

Annaka, T., K. Ohta, H. Motegi, I. Yoshida, M. Takao and H. Soraoka (1999): Tsunami Inversion Based on the Shallow Water Theory, Proceedings of Coastal Engineering, JSCE, Vol. 46, pp. 341-345 (in Japanese).
https://www.jstage.jst.go.jp/article/proce1989/46/0/46_0_341/_pdf/-char/ja

Arikawa, T., F. Yamada and M. Akiyama (2005): Study of Applicability of Tsunami Wave Force in Three-Dimensional Numerical Wave Tank, Proceedings of Coastal Engineering, JSCE, Vol. 52, pp. 46-50 (in Japanese).

Arimitsu, T., Kazuya Ooe and Koji Kawasaki (2012): Proposal of Evaluation Method of Tsunami Wave Pressure Using 2D Depth-Integrated Flow Simulation, Journal of Japan Society of Civil Engineers, Ser. B2 (Coastal Engineering), Vol. 68, No. 2, pp. I-776-I-780 (in Japanese).

Arimitsu,T., T. Deguchi, K. Ooe and K. Kawasaki (2013): Applicability of Evaluation Method of Tsunami Wave Pressure Using Hydraulic Quantities at Front of Land Structure to Multiple Structures, Journal of Japan Society of Civil Engineers, Ser. B2 (Coastal Engineering), Vol. 69, No. 2, pp. I-321-I-325 (in Japanese).

Boussinesq, J. (1872): Théorie des ondes et des remous qui se propagent le long d'un canal rectangulaire horizontal, au communiquant an liquide contenue dans ce canal des vitesses sensiblement pareilles de la surface au fond, Liouvilles Journal de mathématiques pures et appliquées, Vo. 17, pp. 55-108.

Central Disaster Management Council (2002): The 6th meeting of Tonankai/Nankai Earthquake Countermeasure Expert Committee (in Japanese).
http://www.bousai.go.jp/kaigirep/chuobou/senmon/tounankai_nankaijishin/6/pdf/siryou1.pdf

Coastal Development Institute of Technology (2010): Research and Development on CADMAS-SURF/3D, Report of Study Group on Application of Three-Dimensional Numerical Wave Tank to Maritime Structures Design, Coastal Technology Library, No. 39 (in Japanese).

Committee for the Field Investigation of the Chilean Tsunami of 1960 (1961): The Chilean tsunami of May 24, 1960, Earthquake Research Institute, The University of Tokyo, 397p. (in Japanese).

Fujikawa, Y. (1982): Method for Solving of the partial differential equation with the computer, pp. 144-145, SAIENSU-SHA Co., Ltd. (in Japanese).

Goto, C. and Y. Ogawa (1982): Tsunami numerical simulation with leapfrog scheme, School of Engineering, Tohoku University, 52p. (in Japanese).

Goto, C. and N. Shuto (1983): Numerical simulation of tsunami propagations and run-up, Tsunamis: Their Science and Engineering, pp. 439-451.

Goto, C. (1984): EQUATIONS OF NONLINEAR DISPERSIVE LONG WAVES FOR A LARGE URSELL NUMBER, Journal of Japan Society of Civil Engineers, Volume 1984, Issue 351, pp. 193-201 (in Japanese).
https://doi.org/10.2208/jscej.1984.351_193

Goto, C., F. Imamura and N. Shuto (1988): Study on Numerical Simulation of the Transoceanic Propagation of Tsunami Part 1: Governing Equation and Mesh Length, Journal of the Seismological Society of Japan. 2nd ser., Volume 41, Issue 4, pp.515-526 (in Japanese).
https://doi.org/10.4294/zisin1948.41.4_515

Goto, C. and K. Sato (1993): Development of Tsunami Numerical Simulation System for Sanriku Coast in Japan, Report of the Port and Harbor Research Institute, Vol. 32, No. 2, pp. 3-44 (in Japanese).
http://www.pari.go.jp/search-pdf/vol032-no02-01.pdf

Goto, H., H. Ikari, T. Matsubara and T. Ito (2011): Numerical Simulation on Tsunami due to Sector Collapse by Solid-Liquid Two-Phase Flow Model Based on Accurate Particle Method, Journal of Japan Society of Civil Engineers, Ser. B2 (Coastal Engineering), Vol. 67, No. 2, pp. I_196-I_200 (in Japanese).
https://doi.org/10.2208/kaigan.67.I_196

Grilli, S. T. and P. Watts (2005): Tsunami Generation by Submarine Mass Failure. I: Modeling, Experimental Validation and Sensitivity Analyses, Journal of Waterway, Port, Coastal, and Ocean Engineering, 131:6(283), 283-297.

Hasegawa, K., T. Suzuki, K. Inagaki and N. Shuto (1987): A STUDY ON THE MESH SIZE AND TIME INCREMENT IN THE NUMERICAL SIMULATION OF TSUNAMIS, Journal of Japan Society of Civil Engineers, Volume 1987, Issue 381, pp. 111-120 (in Japanese).
https://doi.org/10.2208/jscej.1987.381_111

Hashi, K. and F. Imamura (2000): Study on the Multi-Tsunami Source in the Case of the 1998 Papua

New Guinea Tsunami, Proceedings of Coastal Engineering, JSCE, Vol. 47, pp. 346-350 (in Japanese).
http://library.jsce.or.jp/jsce/open/00008/2000/47-0346.pdf

Hiraishi, T., H. Shibaki and N. Hara (2001): Numerical Simulation of Meiwa-Yaeyama Earthquake Tsunami in Landslide Model with Circular Rupture, Proceedings of Coastal Engineering, JSCE, Vol. 48, pp. 351-355 (in Japanese).
http://library.jsce.or.jp/jsce/open/00008/2001/48-0351.pdf

Imamura, F. and M. M. A. Imteaz (1995): Long waves in two-layers: Governing equations and numerical model, Science of Tsunami Hazards, Vol. 13, pp. 3-24.

Imamura, F. (1998): Development of tsunami numerical calculation in 15 years and future, Kaiyo extra (15), pp. 89-98 (in Japanese).

Imamura, F. and H. J. Lee (1998): State-of Arts of Numerical Simulations for Generation and Propagation of Tsunamis, Bulletin on Coastal Oceanography, Vol. 36, No. 1, pp. 91-101 (in Japanese).
https://projects.repo.nii.ac.jp/?action=repository_uri&item_id=47487&file_id=21&file_no=1

Imamura, F., D. Goto, Y. Shigihara, Y. Kitamura, T. Matsubara, K. Takaoka and K. Ban (2001): Study on the Tsunami Generation due to Rush of a Landslide into Water, Proceedings of Coastal Engineering, JSCE, Vol. 48, pp. 321-325 (in Japanese).
http://library.jsce.or.jp/jsce/open/00008/2001/48-0321.pdf

Inagaki, K., M. Koba, H. Tanaka and M. Takao (2001): Study on the Grid Size for V-Shaped Bay and Port in Tsunami Computation, Proceedings of Coastal Engineering, JSCE, Vol. 48, pp. 336-340 (in Japanese).
http://library.jsce.or.jp/jsce/open/00008/2001/48-0336.pdf

Ishibashi, K. (1976): Reexamination of a major earthquake expected in the Tokai district - About Gulf of Suruga major earthquake-, The Seismological Society of Japan, 1976 Meeting, Proceedings (2) pp. 30-34 (in Japanese).

Iwasaki, T. and A. Mano (1979): Two-dimensional numerical simulation of tsunami run-ups in the Eulerian description, Proceedings of Coastal Engineering, JSCE, Vol. 26, pp. 70-74 (in Japanese).
http://library.jsce.or.jp/jsce/open/00008/1979/26-0070.pdf

Iwase, H., M. Fukasawa and C. Goto (2001): Hydraulic Experiment and Numerical Simulation for Breaking Wave Transformation of Disintegrated Soliton Waves, Proceedings of Coastal Engineering, JSCE, Vol. 48, pp. 306-310 (in Japanese).
http://library.jsce.or.jp/jsce/open/00008/2001/48-0306.pdf

Iwase, H., C. Goto, K. Fujima and K. Iida (2002): THE DISPERSION EFFECT ON THE PROPAGATION OF TSUNAMI IN DEEP SEA REGION, Journal of Japan Society of Civil

Engineers, Volume 2002, Issue 705, pp. 101-114 (in Japanese).
https://doi.org/10.2208/jscej.2002.705_101

Kajiura, K. (1983): Some statistics related to observed tsunami heights along the coast of Japan, Tsunamis-Their Science and Engineering, Iida, K. and T. Iwasaki (ed.), pp. 131-145.

Kawamata, K., K. Takaoka, K. Ban, F. Imamura, S. Yamaki and E. Kobayashi (2005): Model of tsunami generation by collapse of volcanic eruption: The 1741 Oshima-Oshima tsunami, Tsunamis: Case Studies and Recent Developments, pp. 79-96, L. Satake (ed.), Springer.

Kawasaki, K., S. Yamaguchi, M. Hakamata, N. Mizutani and S. Miyajima (2006): Wave Pressure Acting on Drifting Body after Collision with Bore, Proceedings of Coastal Engineering, JSCE, Vol. 53, pp. 786-790 (in Japanese).

Kawasaki, K. and M. Hakamata (2007): Development of Three-Dimensional Numerical Model of Multiphase Flow "DOLPHIN-3D" and Dynamic Analysis of Drifting Bodies under Wave Actions, Proceedings of Coastal Engineering, JSCE, Vol. 54, pp. 31-35 (in Japanese).

Kawasaki, K., S. Matsuura and T. Sakatani (2013): Validation of Free Surface Analysis Method in Three-Dimensional Computational Fluid Dynamics Tool "OpenFOAM", Journal of Japan Society of Civil Engineers, Ser. B3 (Marine Development) Vol. 69, No. 2, pp. I_748-I_753 (in Japanese).

Kaneda, Y. and T. Baba (2006): REGIONAL CHARACTERIZATION OF THE CRUST IN METROPOLITAN AREAS FOR PREDICTION OF STRONG GROUND MOTION, "Special Project for Earthquake Disaster Mitigation in Urban Areas", Ministry of Education, Culture, Sports, Science and Technology (MEXT), Japan, pp. 490-500 (in Japanese).
http://www.eri.u-tokyo.ac.jp/daidai/h17seika-hokokusho/honbun_final/3_3_3_10(pp.490-500).pdf

Kihara, N. and M. Matsuyama (2010): On applicability of the hydrostatic 3-D tsunami analysis system Tsunami to tsunami-induced sediment transport-Simulations of sediment transport around the Kirinda port induced by the Indian Ocean tsunami, Central Research Institute of Electric Power Industry Reports, N09004 (in Japanese).

Kihara, N., N. Fujii and M. Matsuyama (2012): Three-dimensional sediment transport processes on tsunami-induced topography changes in a harbor, Earth Planets Space, Vol. 64, pp. 787-797.

Kotani, M., F. Imamura and N. Shuto (1998): Tsunami Run-Up Simulation and Damage Estimation by Using GIS, Proceedings of Coastal Engineering, JSCE, Vol. 45, pp. 356-360 (in Japanese).
http://library.jsce.or.jp/jsce/open/00008/1998/45-0356.pdf

Lynett, P. and P. L.-F. Liu (2005): A numerical study of the run-up generated by three-dimensional landslides, Journal of geophysical research, Vol. 110, C03006.

Madsen, P.A. and O. R. Sørensen (1992): A New Form of the Boussinesq Equation with Improved Linear Dispersion Characteristics, Part 2, A Slowly-Varying Bathemetry, Coastal Engineering,

Vol. 18, pp. 183-204.

Maeno, F. and F. Imamura (2007): Numerical investigations of tsunamis generated by pyroclastic flows from the Kikai caldera, Japan, Geophysical Research Letters, 34:L23303.

Maeno, F. and F. Imamura (2011): Tsunami generation by a rapid entrance of pyroclastic flow into the sea during the 1883 Krakatau eruption, Indonesia, Journal of Geophysical Research, Vol. 116, doi:10.1029/2011JB008253.

Mansinha, L. and D. E. Smylie (1971): The displacement fields of inclined faults, Bulletin of the Seismological Society of America, Vol. 61, No. 5, pp. 1433-1440.

Matsumoto, T., K. Hashi, F. Imamura and N. Shuto (1998): A Development of a Numerical Model of Two Layers Flow to Simulate a Tsunami Generation Caused by a Debris Flow, Proceedings of Coastal Engineering, JSCE, Vol. 45, pp. 346-350 (in Japanese).
http://library.jsce.or.jp/jsce/open/00008/1998/45-0346.pdf

Matsuyama, M., M. Ikeno, T. Sakakiyama, K. Yanagisawa and N. Fujii (2005): Study on Wave Breaking Criterion of Tsunami Soliton Fission Based on Undistorted Experiment, Annual Journal of Coastal Engineering, JSCE, Vol. 52, pp. 241-245 (in Japanese).
http://library.jsce.or.jp/jsce/open/00008/2005/52-0241.pdf

Matsuyama, M., M. Ikeno, T. Sakakiyama and T. Takeda (2006): Wave Breaking Model after Soliton Fission on a Continental Shelf in Tsunami Numerical Simulation, Annual Journal of Coastal Engineering, JSCE, Vol. 53, pp. 226-230 (in Japanese).
http://library.jsce.or.jp/jsce/open/00008/2006/53-0226.pdf

McLeod, P., S. Carey and R. S. J. Sparks (1999): Behaviour of particle-laden flows into the ocean: Experimental simulation and geological implications, Sedimentology, Vol. 46, pp. 523–536.

Nagano, O., F. Imamura and N. Shuto (1989): Numerical Simulation of the Chilean tsunami in the area along the shore, Proceedings of Coastal Engineering, JSCE, Vol. 36, pp. 183-187 (in Japanese).
http://library.jsce.or.jp/jsce/open/00008/1989/36-0183.pdf

National Astronomical Observatory of Japan (2007): Chronological Scientific Tables 2008, Maruzen Publishing Co., Ltd., 278p. (in Japanese).

Nishimura, S., M. Ando and S. Miyazaki (1999): Inter-plate Coupling Along the Nankai Trough and Southeastward Motion Along Southern Part of Kyushu, Journal of the Seismological Society of Japan. 2nd ser., Vol. 51 (1998-1999), Issue 4, pp. 443-456 (in Japanese).
https://www.jstage.jst.go.jp/article/zisin1948/51/4/51_4_443/_pdf/-char/en

Okada, Y. (1985): Surface deformation due to shear and tensile faults in a half-space, Bulletin of the Seismological Society of America, Vol. 75, No. 4, pp. 1135-1154.

Omote, T. (1946): The Tsunami, the Earthquake Sea Waves, that Accompanied the Great Earthquake of Dec. 7, 1944, Bulletin of the Earthquake Research Institute, University of Tokyo, Vol. 24(1-

4), pp. 31-57 (in Japanese).
https://repository.dl.itc.u-tokyo.ac.jp/?action=repository_uri&item_id=34294&file_id=19&file_no=1

Peregrine, D.H. (1967): Long waves on a beach, Journal of the Fluid Mechanics, Vol. 27, Part4, pp. 815-827.

Pham, V.P., M. Hasebe and I. Takahashi (2012): A Study on Three-Dimensional Tsunami Analysis Using VOF Method, Journal of Japan Society of Civil Engineers, Ser. B2 (Coastal Engineering), Vol. 68, No. 2, pp. I_071-I_075 (in Japanese).

Sagiya, T. (1999): Interplate coupling in the Tokai District, Central Japan, deduced from continuous GPS data, Geophysical Research Letters, Vol. 26, No. 15, pp. 2315-2318.

Sasahara, N. (2004): Numerical Simulation of the Tsunami caused by the sector Collapse of Mt.Mayuyama, Shimabara Peninsula, Kyushu in 1792, REPORT OF HYDROGRAPHIC AND OCEANOGRAPHIC RESEARCHES No.40 March, http://www1.kaiho.mlit.go.jp/GIJUTSUKOKUSAI/KENKYU/report/rhr40/rhr40-02.pdf

Satake, K., M. Okada and K. Abe (1988): Tide gauge response to tsunamis: Measurements at 40 tide gauge stations in Japan, Journal of Marine Research, Vol. 46, pp. 557-571.

Satake, K. (1991): Recent Studies on Tsunamis, Journal of the Seismological Society of Japan. 2nd ser., Volume 44 (1991) Issue Supplement, pp. 99-112 (in Japanese). https://www.jstage.jst.go.jp/article/zisin1948/44/Supplement/44_Supplement_99/_pdf/-char/en

Satake, K. and Y. Kato (2001): The 1741 Oshima-Oshima Eruption: Extent and Volume of Submarine Debris Avalanche, Geophysical Research Letters, Vol. 28, No. 3, pp. 427-430.

Satake, K. and Y. Kato (2002): The 1741 Kanpo-Tsunami Occurred Because of Sector Collapse of Oshima-Oshima, Monthly Kaiyo No. 28, pp. 150-160 (in Japanese).

Satake, K., J.R. Smith and K. Shinozaki (2002): Three-Dimensional Reconstruction and Tsunami Model of the Nuuanu and Wailau Giant Landslides, Hawaii, in Hawaiian Volcanoes: Deep Underwater Perspectives, edited by Takahashi et al., AGU Geophysical Monograph, 128, pp. 333-346.

Satake, K. (2007): Volcanic origin of the 1741 Oshima-Oshima tsunami in the Japan Sea, Earth Planets Space, Vol. 59, pp. 381-390.

Sato, S. (1995): Numerical Computation of the Tsunami in Consideration of Division and Breaking Wave, Proceedings of Coastal Engineering, JSCE, Vol. 42, pp. 376-380 (in Japanese). http://library.jsce.or.jp/jsce/open/00008/1995/42-0376.pdf

Sato, T., R. W. Graves and P. G. Somerville (1999): Three-dimensional finite-difference simulations of long-period strong motions in the Tokyo metropolitan area during the 1990 Odawara earthquake (MJ 5.1) and the great 1923 Kanto earthquake(MS 8.2) in Japan, Bulletin of the

Seismological Society of America, Vol. 89, No. 3, pp. 579-607.

Sayama, J., T. Goto and N. Shuto (1986): Error of the Tsunami Numerical Computation about the Refraction, Proceedings of Coastal Engineering, JSCE, Vol. 33, pp. 204-208 (in Japanese). http://library.jsce.or.jp/jsce/open/00008/1986/33-0204.pdf

Shibaki, H., T. Mikami and T. Goto (1994): Propagation characteristics of Hokkaido Nansei−Oki Earthquake Tsunami, Proceedings of Coastal Engineering, JSCE, Vol. 41, pp. 226-230 (in Japanese). http://library.jsce.or.jp/jsce/open/00008/1994/41-0226.pdf

Shuto, N. (1986): TSUNAMIS AND COUNTERMEASURES, Journal of Japan Society of Civil Engineers, Volume 1986, Issue 369, pp. 1-11 (in Japanese). https://doi.org/10.2208/jscej.1986.369_1

Shuto, N. and M. Uhana (1995): The run-up heights for the 1994 Hokkaido Toho-Oki earthquake tsunami, Research Report of Tsunami Engineering Vol.12, Part 2, p. 1 (in Japanese). http://www.tsunami.civil.tohoku.ac.jp/hokusai3/J/publications/pdf/vol.12_7.pdf

Steketee, J.A. (1958): On Volterra's dislocations in a semi-infinite elastic medium, Canadian Journal of Physics, Vol. 36, pp. 192-205.

Suzuki, H. (2002): Underground Geological Structure beneath the Kanto Plain, Japan, Report of the National Research Onstitute for Earth Science and Disaster Prevention, Vol. 63, pp. 1-19 (in Japanese). http://dil-opac.bosai.go.jp/publication/nied_report/PDF/63/63suzuki.pdf

Takahashi, K. and T. Tomita (2013): Simulation of the 2011 Tohoku Tsunami in Kuji Bay Using Three-Dimensional Non-Hydrostatic Numerical Model, Journal of Japan Society of Civil Engineers, Ser. B2 (Coastal Engineering), Vol. 69, No. 2, pp. I_166-I_170 (in Japanese).

Tanaka, H. (1985): Development of Mathematical Models for Tsunami Behavior on Coastal Zones, CRIEPI Research Report, No. 385017 (in Japanese). http://criepi.denken.or.jp/jp/kenkikaku/report/detail/385017.html

Tomita, T. and T. Kakinuma (2005): Storm Surge and Tsunami Simulator in Oceans and Coastal Areas (STOC), Report of the Port and Airport Research Institute, Vol. 44, No. 2, pp. 83-98 (in Japanese).

Tomita, T. and K. Honda (2008): Application of Three-Dimensional Non-Hydrostatic Numerical Model to Tsunamis in Coastal Areas, Proceedings of Coastal Engineering, JSCE, Vol. 55, pp. 231-235 (in Japanese).

Tonomo, K., T. Shikata and Y. Murakami (2015): ACCURACY STUDY OF NUMERICAL SIMULATION OF TSUNAMI APPLIED TO THE SUBMARINE LANDSLIDE MODEL, Journal of Japan Society of Civil Engineers, Ser. B3 (Ocean Engineering), Volume 71 (2015), Issue 2, pp. 557-562 (in Japanese).

https://doi.org/10.2208/jscejoe.71.I_557

Tsuchiya, S., Y. Satou, M. Matsuyama and Y. Tanaka (2013): The Effect Generated by Calculation Method of the Sea Bottom Displacement on Tsunami Estimation - Three-dimensional Sea Bottom Crustal Movement Analysis -, Journal of Japan Society of Civil Engineers, Ser. B2 (Coastal Engineering), Volume 69 (2013), Issue 2, pp. I_441-I_445 (in Japanese). https://doi.org/10.2208/kaigan.69.I_441

Tsunami Evaluation Subcommittee, The Nuclear Civil Engineering Committee, JSCE (2002): Tsunami Assessment Method for Nuclear Power Plants in Japan. http://committees.jsce.or.jp/ceofnp/system/files/JSCE_Tsunami_060519.pdf

Tsunami Evaluation Subcommittee, The Nuclear Civil Engineering Committee, JSCE (2007): RESEARCH FOR DEVELOPING TSUNAMI EVALUATION METHODS – PROBABILISTIC TSUNAMI HAZARD ANALYSIS /NUMERIAL SIMULATION METHODS WITH DISPERSION AND WAVE BREAKING, Journal of Japan Society of Civil Engineers, Ser. B, Vol. 63, No. 2, pp. 168-177 (in Japanese). https://www.jstage.jst.go.jp/article/jscejb/63/2/63_2_168/_pdf/-char/ja

Watts, P., S. T. Grilli, D. R. Tappin and G. J. Fryer (2005): Tsunami Generation by Submarine Mass Failure II: Predictive Equations and Case Studies, Journal of Waterway, Port, Coastal, and Ocean Engineering, 131:6(298), 298-310.

Yamada, N. and H. Yamanaka (2003): Ground Motion Simulations of Moderate Earthquakes for Comparison of Performance of 3D Subsurface Structural Models in Kanto Plain for Strong Motion Prediction, Journal of the Seismological Society of Japan. 2nd ser., Volume 56 (2003-2004), Issue 2, pp. 111-123 (in Japanese). https://www.jstage.jst.go.jp/article/zisin1948/56/2/56_2_111/_pdf/-char/en

Yanagisawa, H., A. Aoki, K. Sassa and K. Inoue (2014): Numerical Simulation of 1792 Ariake-Kai Tsunami using Landslide-Tsunami Model, Journal of Japan Society of Civil Engineers, Ser. B2 (Coastal Engineering), Volume 70 (2014), Issue 2, pp. I_151-I_155 (in Japanese). https://doi.org/10.2208/kaigan.70.I_151

Yoneyama, N., H. Nagashima and K. Toda (2008): Numerical Analysis for the Behavior of the Driftage with Tsunami Run-up Using FAVOR Method, Annual Journal of Hydraulic Engineering, Vol. 52, pp. 1399-1404 (in Japanese).

Yoneyama, N. and H. Nagashima (2009): Development of a Three-Dimensional Numerical Analysis Method for the Drift Behavior in Tsunami, Journal of Japan Society of Civil Engineers, Ser. B2 (Coastal Engineering), Vol. B2-65, No. 1, pp. 266-270 (in Japanese).

Chapter 5. Probabilistic Assessment Methods

5.1. Standard deviation and truncation threshold of estimation error

5.1.1. Statistics of variance between calculation results and run-up height records of tsunami

To view the statistical properties of variance between calculation results by tsunami simulation and the run-up height records of tsunami, the results of calculations simulating 10 historical earthquake tsunami (total of 1,505 trace points), which are given in Table 5.1.1-1, have been analyzed in two patterns:

- Difference between the run-up height records and calculated value
- Ratio of run-up height records to calculated value (logarithm).

The results are shown in Figure 5.1.1-1. However, both are also displayed using a 1:18 scale factor for standard deviation for all data along the vertical access.

When the data given in Figure 5.1.1-1 are expressed as a distribution of the frequency of the difference or ratio (logarithm) for each representation, the diagram given in Figure 5.1.1-2 is yielded. The chi-square test for normality is carried out. The result is as shown in Table 5.1.1-2 and this logarithm is closer to the normal distribution. In other words, the ratio of the run-up height records to calculated value generally conforms to the logarithmic normal distribution.

Table 5.1.1-1 Fault models and number of data

Earthquake Tsunami	Number of Data
1707 Hoei	61
1854 Ansei-Tokai	88
1854 Ansei-Nankai	60
1896 Meiji-Sanriku	83
1933 Showa-Sanriku	325
1944 Tonankai	41
1946 Nankai	149
1968 Tokachi-Oki	273
1983 Nihonkai-Chubu	209
1993 Hokkaido Nansei-Oki	216
Total	1,505

Note) restricted tsunami height estimations below 12m.

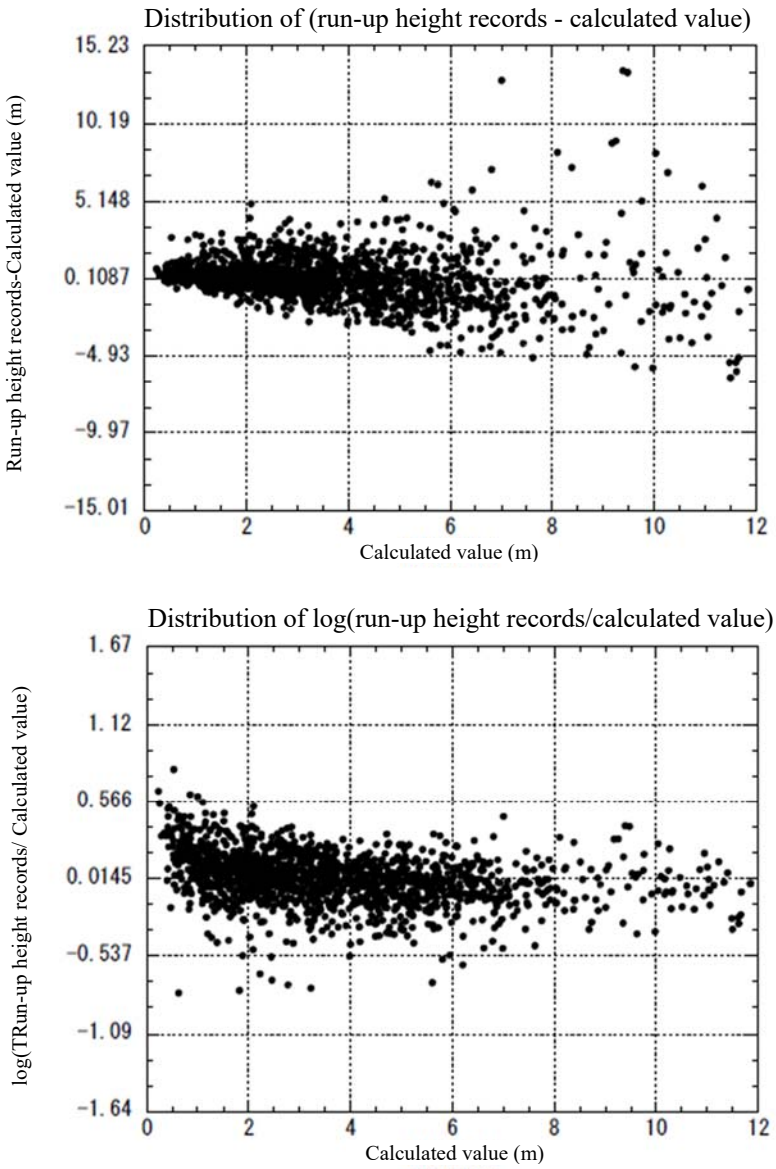

Figure 5.1.1-1 Scatter diagram of run-up height records and calculated values

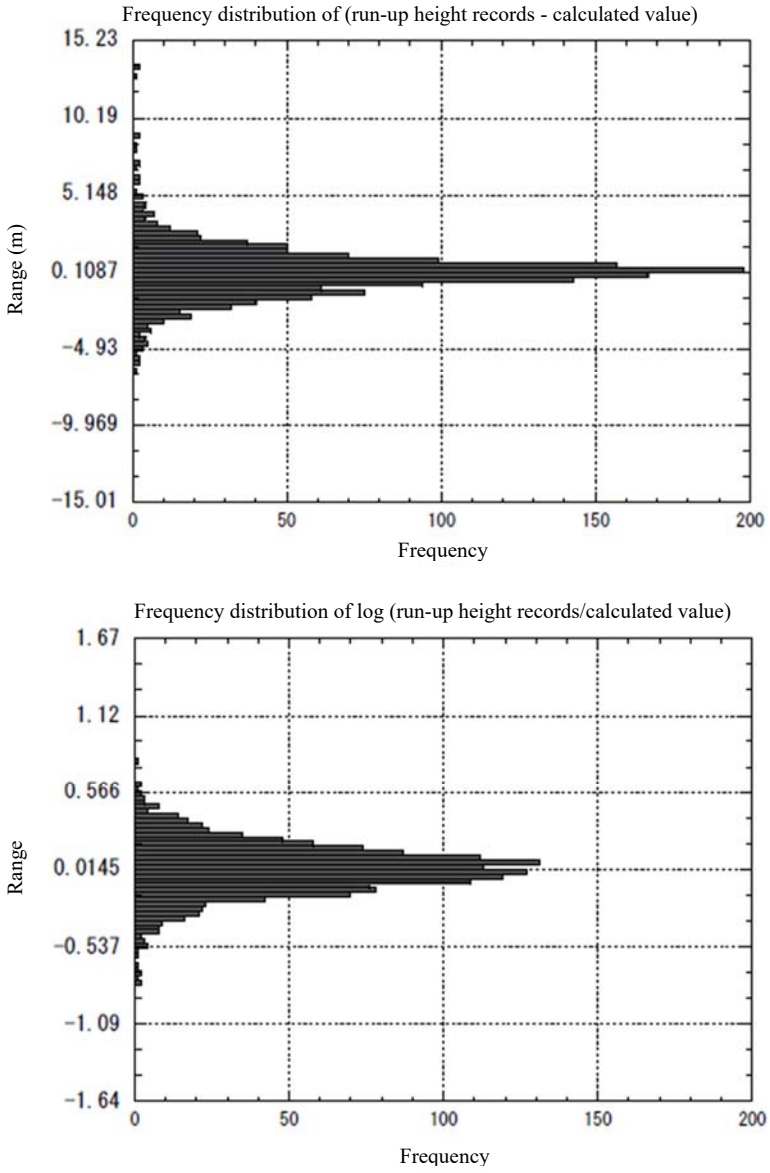

Figure 5.1.1-2 Histogram of run-up height records and calculated values

Table 5.1.1-2 χ^2 test of fitness to normal distribution

Type	χ^2 -value	Result
trun-up height records-calculated value	393.53	NG
log(run-up height records-calculated value)	226.09	OK

Note) The range of mean ± 2.3×S.D. is divided into 200 sections in the test. OK means that the null hypothesis "Data follow a normal distribution" is not rejected with significant level 5%. (The critical value of χ^2 distribution for the P-value, 0.05, conducting the right-tailed test is 235 in case of 201 DOF. If χ^2 value greater than the critical value, the hypothesis is rejected.)

5.1.2. Examination of variance in estimated tsunami heights

With respect to the variance in calculations of tsunami height using in PTHA, an attempt was made to ascertain the extent of variance in numerical simulations of the 2011 off the Pacific coast of Tohoku Earthquake (2011 Tohoku earthquake).

The Cabinet Office's inversion model (see Figure 5.1.2-1), which is able to provide a good representation of tsunami traces, was used to perform a numerical simulation of the 2011 Tohoku Earthquake. Distributions of the ratio of observed values to calculated values ("O/C") were examined according to the degree of data reliability and distance from the coastline.

The Japanese main island of Honshu was the only region examined, and the minimum grid size for the coastal region was set at 50m.

The O/C distribution, which only used tsunami trace data of reliability level A, is shown in Figure 5.1.2-2. In the diagram, the boundary from the geometric mean to the nth factor of standard deviation is indicated by a broken line. There are no results that exceed the mean+4β. There are some points where the mean+3β is exceeded, but, the following two phenomena arose, as shown in Figures 5.1.2-3 through 5.1.2-5, with regard to these locations where O/C significantly deviates.

- Although the calculation results are generally constant, the observed values differ significantly only for the locations in question.
- Although the observed values are generally constant, the calculated values differ significantly only for the locations in question.

It is surmised that it is likely both of these cases originate in the reproducibility of topography using 50-m grids, and it would be difficult for such phenomena to occur in cases where the grid size is narrowed down, such as in tsunami assessments for nuclear power plants.

In Figure 5.1.2-6, the ratio of number of data where the mean±nβ is exceeded to total number of data (Cabinet Office model; only Honshu) is shown. Here, the theoretical value of the probability that the truncation threshold of the logarithmic normal distribution may be exceeded is shown in Table 5.1.2-1. The ratio of O/C exceeding the mean±nβ in the numerical simulation results was confirmed to consistent generally with the theoretical exceedance probability of the logarithmic normal distribution.

When setting the truncation threshold for the tail of the logarithmic normal distribution, the aforementioned examination results may be used as a reference.

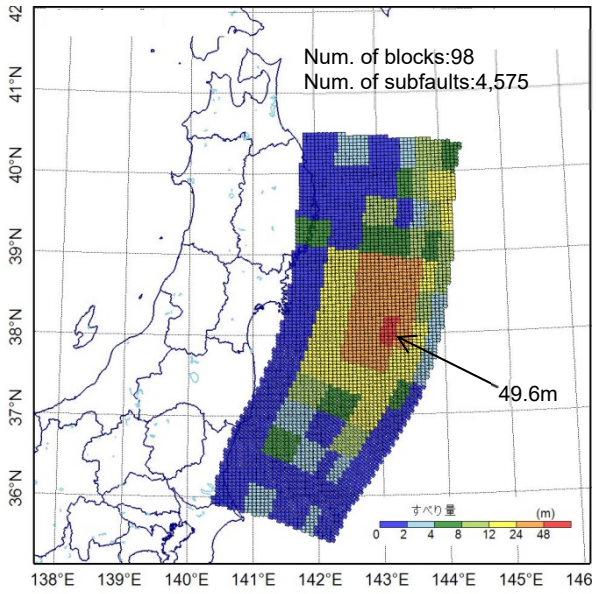

Figure 5.1.2-1 Cabinet Office's inversion model

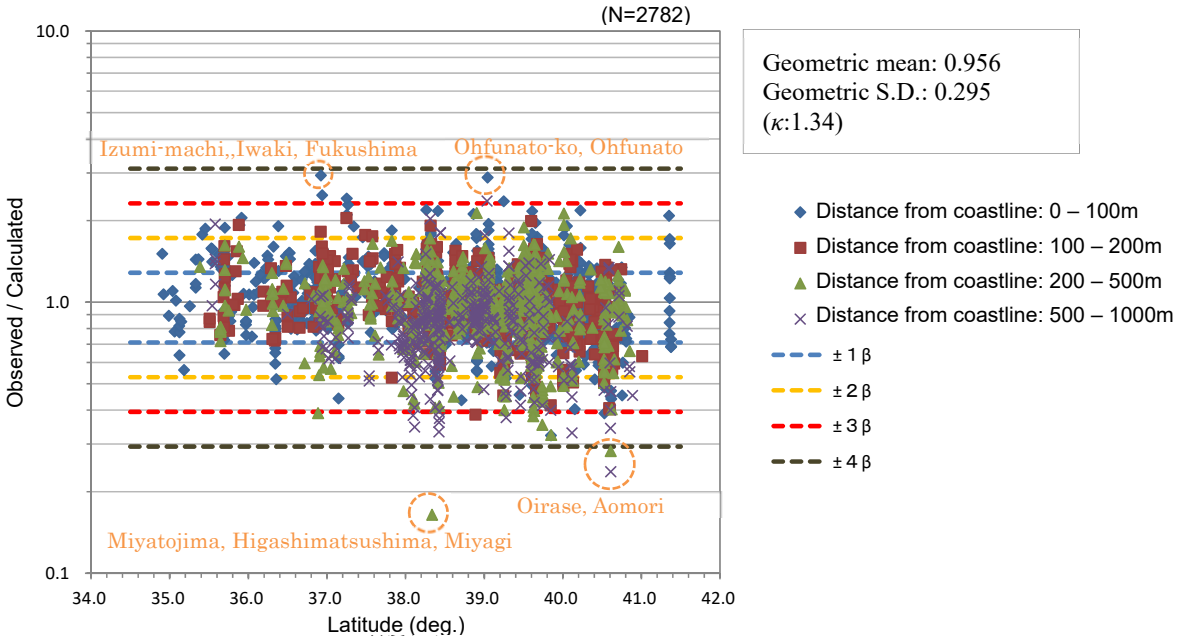

Figure 5.1.2-2 The O/C distribution, which only used tsunami trace data of reliability level A (Cabinet Office model; only Honshu)

Figure 5.1.2-3 Tsunami trace points in Izumi-machi, Iwaki, Fukushima (Reliability; A, No.690)

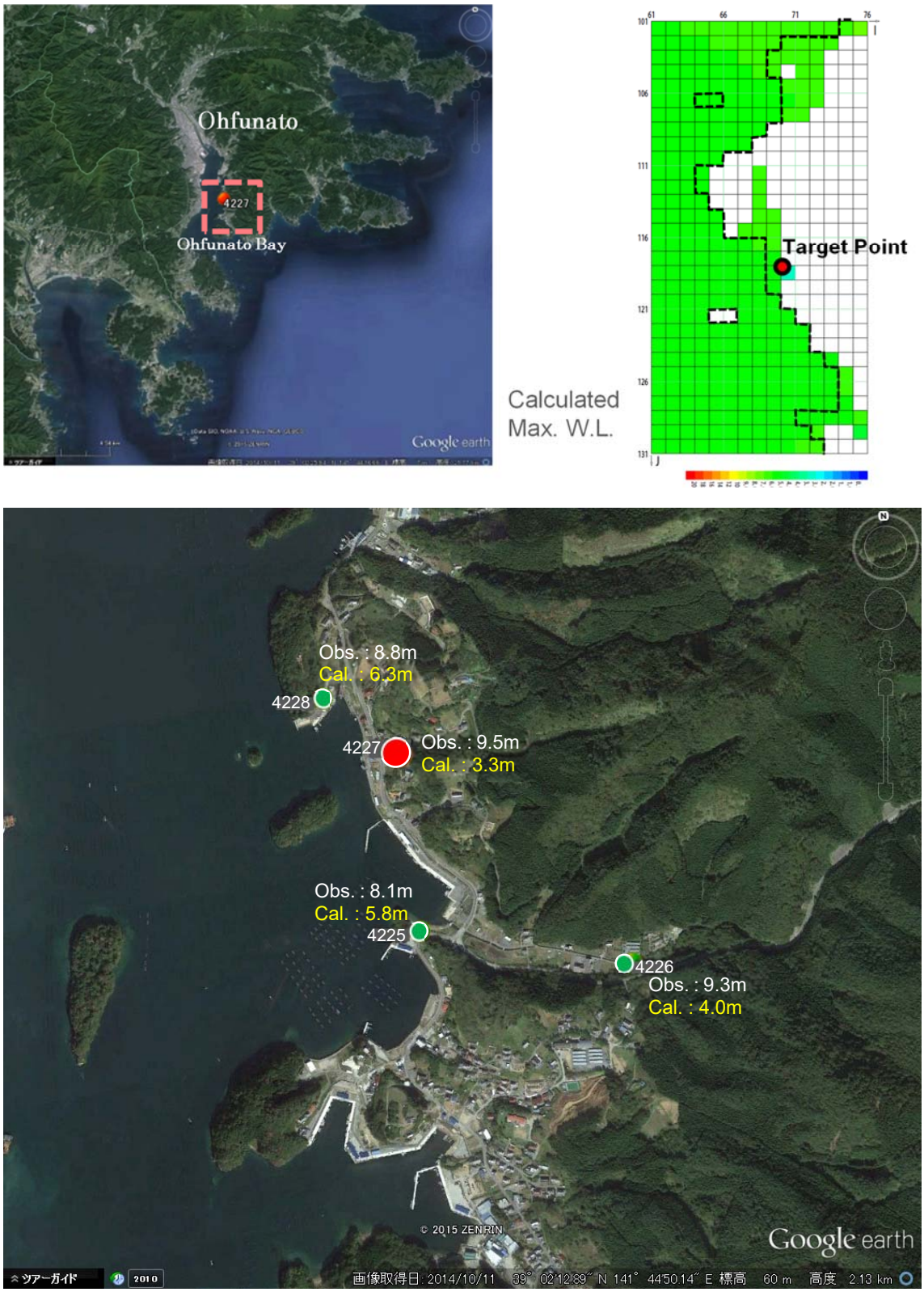

Figure 5.1.2-4 Tsunami trace points in Ohfunato-ko, Ohfunato (Reliability: A, No.4227)

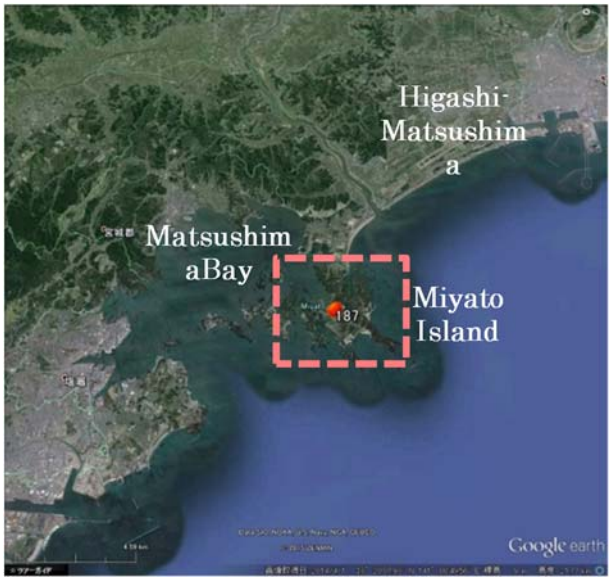

Figure 5.1.2-5 Tsunami trace points in Miyatojima, Higashimatsushima, Miyagi

(Reliability: A, No.187)

Table 5.1.2-1 Theoretical probability to exceed the truncation threshold of normal distribution

Truncation threshold	Exceedance probability (%)
mean±1β	15.866
mean±2β	2.275
mean±2.3β	1.072
mean±3β	0.135
mean±4β	0.003

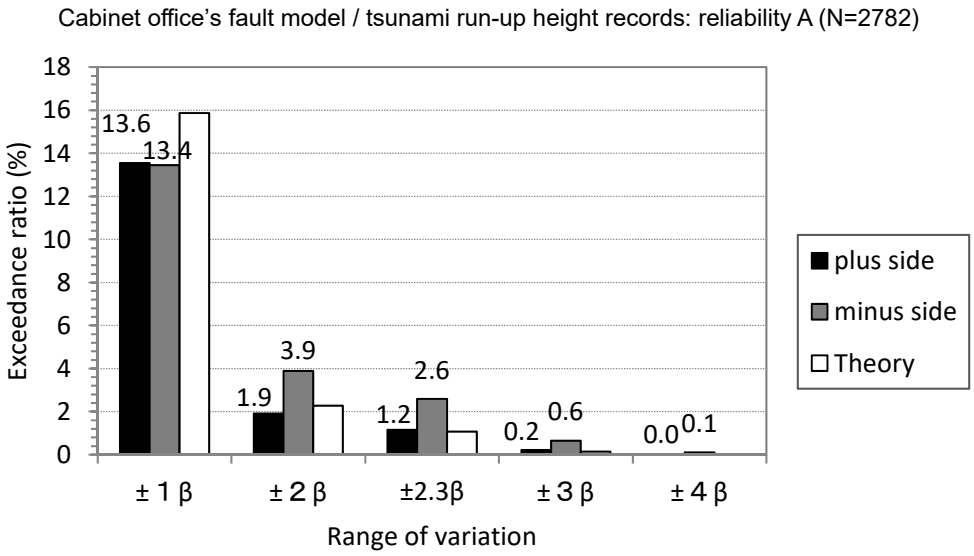

Figure 5.1.2-6 Ratio of the number of data to exceed the mean±nβ to total number of data (Cabinet office's fault model; only Honshu)

The followings are examples of truncation thresholds configured for the logarithmic normal distribution.

[1] Atomic Energy Society of Japan (2015): Upper limit truncation for seismic ground motion

- "Ground motion intensity is phenomenally finite. Accordingly, the range in which the logarithmic normal distribution is valid needs to be configured to be finite, so a truncation threshold is set. In cases where a sufficient basis cannot be obtained for setting a truncation threshold, the range of the level of ground motion acceleration, which affects core damage frequency, may be taken into consideration and the truncation threshold set at a sufficiently large value (for example, up to five times the standard deviation)".
- "The truncation threshold of the logarithmic normal distribution was a uniform distribution

within a range from ±2.0σ to ±4.5σ".

[2] Japan Nuclear Energy Safety Organization (2014): Setting truncation for logarithmic normal distribution in a tsunami propagation model

- "For example, in cases where a 'phenomenon, in which 1% is reached on both sides of the distribution, does not actually occur,' 1% is the cutoff on both sides of the distribution" (Truncation at =2.3β).

[3] National Research Institute for Earth Science and Disaster Prevention (2005): Truncation of the tail of the distribution in an examination of methods for the National Seismic Hazard Maps for Japan

- "In cases where the target is up to a level of probability where there is a 5% probability of exceedance in 50 years or a 3% probability of exceedance in 30 years… what is considered to have a substantial impact on the results is a range within +2σ. Based on this, data from observation records that exceeds a range of ±3σ is regarded as statistical outliers, and the tail of the logarithmic normal distribution is truncated along this range".

5.2. Previous studies about the *b* value in the G-R equation

When focusing on multiple earthquake swarms, the G-R model assumes that:

$$\log n = a - bM$$

holds between magnitude M and the number of earthquakes n for each magnitude (hereinafter, this expression is referred to as the "G-R equation"). Here, the *b* value may be found by applying the G-R equation to statistics for earthquakes that occur in sea regions, which are the objects of the assessment, and, in cases where the *b* value included in the G-R equation is 1, it signifies that, when the magnitude increases 1, the number of earthquakes will be 1/10 the magnitude.

The *b* value varies depending upon the sea regions that is targeted. Ogata (2015) showed the *b* value distribution globally, and stated that, broadly speaking, the *b* value was larger along oceanic ridges and smaller in subduction zones, and that the regional characteristics are quite detailed when viewed in more detail.

In formulating a nationwide seismic ground motion prediction map, the Headquarters for Earthquake Research Promotion (2013) assessed the probability distribution of earthquake magnitude on the assumption that the distribution observed the relationship in the G-R model, which has a maximum value, and used 0.9, which is considered to be the mean for the *b* value for the area around Japan. In addition, it has been pointed out that the *b* value also varies over time in response to seismic cycles. For example, Kusuki et al. (2011) observed a decline in the *b* value before the main shock for the source region of the 2011 Tohoku earthquake.

5.3. Effect of storm surge on Probabilistic Tsunami Hazard Analysis

5.3.1. Objectives

In a Probabilistic tsunami hazard analysis, the distribution of the probability of exceedance of the tsunami tide level is found by combining (convoluting) the tsunami height distribution and the tide level distribution in order to find the probability that the tide level will be exceeded at a power generation facility.

This tide level distribution is prepared using any of the following:

- Prepared by means of statistical processing using records of tide measurements around the power generation facility
- Artificially calculated using the harmonic constant

The issue when using a tide level distribution is the possibility that, storm surges and other phenomena that "have a low occurrence frequency, but a large tide level deviation when they occur" may not be sufficiently reflected. In this examination, we focus on storm surge, which is assumed to have the largest impact except for tsunamis, and we evaluate impact of storm surge deviation on a Probabilistic tsunami hazard analysis.

5.3.2. Design of probabilistic typhoon models

(1) Data used for statistical analysis

The typhoon for probabilistic model design is extracted from the Japan Meteorological Agency Best Track Data for the period from 1951 to 2005.

(2) Formulation

1) Typhoon occurrence

The number of typhoons occurring during a one-year period is modeled as a Poisson distribution for each period of time. In other words, in cases where the average number of typhoons occurring during the one-year period is λ, then the probability of n typhoons occurring during a one-year period is given with the following equation.

$$f(n) = \frac{e^{-\lambda}\lambda^{n}}{n!}$$

The locations where typhoons occur and central pressure when they occur are assumed to follow the cumulative frequency distribution set by the observation data.

2) Time evolution of Typhoon

The time evolution for the probabilistic typhoon model is determined in the following

manner using the autoregressive process (AR) model.

$$p_i = p_{i-1} + \Delta p_i$$
$$\vec{x}_i = \vec{x}_{i-1} + \vec{v}_i dt$$
$$\Delta p_i = \langle \Delta p_i \rangle + \delta p_i$$
$$\vec{v}_i = \langle \vec{v}_i \rangle + \delta \vec{v}_i$$

p_i is the central pressure, x_i is the central coordinates of the typhoon, and v_i is the velocity at which the typhoon travels. The degree to which the central pressure changes is calculated using the sum of the mean field (Δp_i) and deviation δp_i at the point where the typhoon is situated, and velocity v_i, which is rate at which the coordinates change, is also calculated using the sum of the mean field (v_i) and deviation δv_i. Deviation is expressed by the following autoregressive process model:

$$\delta p_i = a_1 \delta p_{i-1} + a_2 \delta p_{i-2} + a_3 \delta p_{i-3} + \varepsilon_p$$
$$\delta \vec{v}_i = A_1 \delta \vec{v}_{i-1} + A_2 \delta \vec{v}_{i-2} + \vec{\varepsilon}_v$$

The order of the autoregressive process model is determined by trial and error, so there is room for optimization. The coefficient of the autoregressive process model is determined by multiple linear regression analysis using past observation data. Velocity coefficients $A_1$and A_2 are 2 x 2 matrices. ε_p and ε_v indicate random errors, and are given using a normal distribution of mean 0. Variance of the normal distribution is the mean of the sum of squared errors between observation data and the given regression equation.

3) Configuration of typhoon radius

The shape of a developed typhoon is almost circular. For this reason, in the cases where the central pressure and the typhoon radius are given, a simplified approach has been proposed for finding the gradient wind distribution and the pressure distribution on land by assuming a concentric distribution (there are also cases where an elliptical distribution is assumed). This examination uses the typical Myers equation to find the pressure decrease. The pressure, at points that are r distance away from the typhoon center, is approximated using the following equation:

$$p = p_c + (1010 - p_c) \exp\left(-\frac{r_0}{r}\right)$$

p_c is the central pressure and r_0 is the typhoon radius.

(3) Calculation of storm surge deviation

In this examination, the storm surge deviation is calculated with the following simplified equation, which is published in the Tide Table (2003 edition):

$$H = a(1010 - P) + bW \cos\theta + c$$

P is the minimum pressure (hPa), W is the maximum wind velocity, and θ is the angle formed by

the harbor and wind direction. The coefficients *a*, *b*, and *c* of the simplified equation have been given for major harbors in Japan based on statistics for the past storm surges.

1) Results

• Typhoon track distribution

Figure 5.3.2-1 shows the results of a probabilistic typhoon model that was run for a period of 100 years to generate typhoon tracks. It was found that the generated typhoon tracks correspond to the distribution of tracks from observation data.

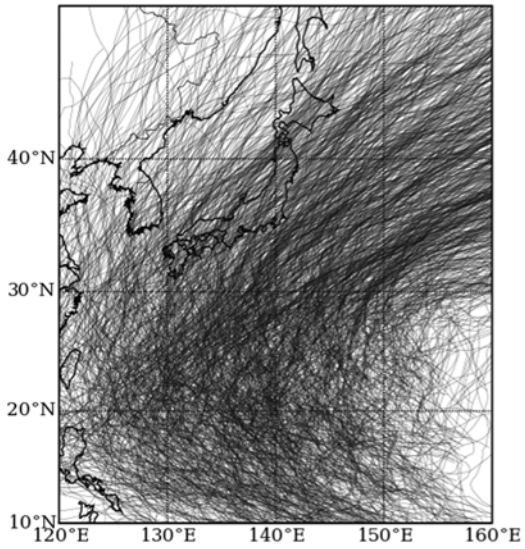

Figure 5.3.2-1 Generated typhoon track over a period of 100 years

2) Minimum pressure distribution

Figure 5.3.2-2 shows the distribution of minimum pressure over a period of 100 years, which was generated using a probabilistic typhoon model.

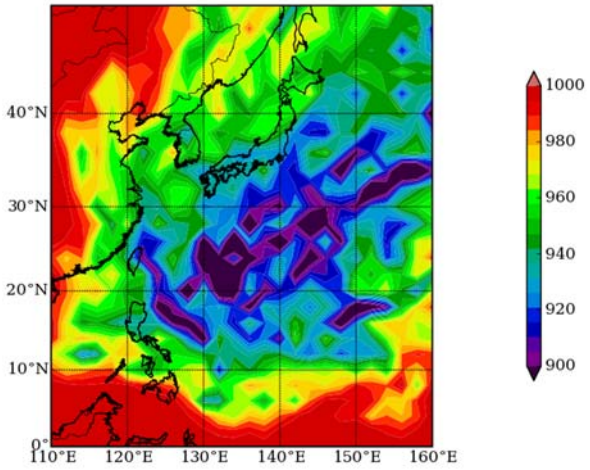

Figure 5.3.2-2 The distribution of minimum pressure over period of 100 years, generated using a probabilistic typhoon model (hPa)

5.3.3. Calculation of typhoon theoretical maximum intensity

In this section, we calculate probabilistic typhoons over a long period of 1,000 years in order to examine the effect of storm surge on hazard analysis. However, in the formulation of probabilistic typhoons as previously described, powerful typhoons occur that appear to be unrealistically extreme. Accordingly, the limit of the physical development of tropical cyclones is calculated in accordance with the characteristics of the meteorological field during each period of time, and this is used as the limit for development in the probabilistic typhoon model.

The Maximum Potential Intensity of typhoons is calculated with reference to Holland (1997), and the surrounding meteorological conditions are used to find the pressure of the typhoon center by means of iterative calculation. For the meteorological data used in calculating the maximum typhoon intensity, the NCEP/NCAR re-analysis data is used for three variables: vertical profile of temperature, temperature near land surface, and sea level pressure.

5.3.4. Effect of storm surge on tsunami hazard analysis

(1) Assessment procedure

In a standard tsunami hazard assessment, the tide level deviation in front of a site is found by superimposing the distribution of tsunami deviation which assumes a logarithmic normal distribution onto the tide level distribution, which is prepared based upon tide measurement records and other sources. Since the objective of this examination is to assess the effect that abnormal tide levels due to typhoon have on a tsunami hazard analysis, the tide level distribution

is expressed by combining astronomical tide levels and storm surge deviation. Of these, the astronomical tide levels are prepared artificially by using a harmonic constant, and the storm surge deviation is found by using the probabilistic typhoon model (Inoue et al., 2013).

(2) Case studies of configuration of astronomical tide levels

An artificial tide level distribution is prepared using the harmonic constant published in the 2007 edition of the Tide Table. The prepared tide level distribution is combined with the tide level deviation prepared using the probabilistic typhoon model.

Using harmonic analysis, the astronomical tide level is represented by linear superposition of trigonometric function. Tide level $\eta(t)$ for time t at a certain point is calculated using the following equation:

$$\eta(t) = \sum_i H_i \cos\left(\frac{2\pi t}{T_i} + \mu_i - \kappa_i\right)$$

where, H_i is the amplitude of the tidal constiuent components, and T_i is the inherent period. μ_i is known as the phase angle, which expresses the difference in phase of the tide producing force itself. This is a constant that does not depend upon the location point. κ_i is known as the lag angle and indicates the shift in phase determined for each location point.

(3) Assessment of effect of storm surge deviation on tide level distribution

The probabilistic typhoon model is used to assess the effect of storm surge deviation on tide level distribution. For the distribution of the astronomical tide levels, two locations, Nagoya (representing the Pacific Ocean side) and Maizuru (representing the Japan Sea side) are used. In running the probabilistic-model, the following procedures are used:

- Three time periods are covered: 10 years, 100 years, and 1,000 years,
- Random numbers are varied and 10 trial calculations conducted for each time period.

First, a distribution of tide levels is prepared, which combines astronomical tide levels and storm surge deviation, to investigate the relative impact of storm surge. The probability density function of the combined tide levels is found by finding the probability density function of the astronomical tide levels and storm surge deviation and then calculating their convolution. Figure 5.3.4-1 shows results indicating the probability of exceedance calculated based upon the probability density function. The red line is the distribution in a case where storm surge is not included, and the black lines are the results after adding storm surge based on the probabilistic typhoon model (10 trial calculations). The calculation results are able to verify the following properties.

[1] A noticeable difference in the distribution profile emerges in the case of probability smaller than 10^{-3}.

[2] It is found that lengthening the calculation period of the probabilistic typhoon model is able to suppress variance, which typhoons have, and make a more reliable assessment.

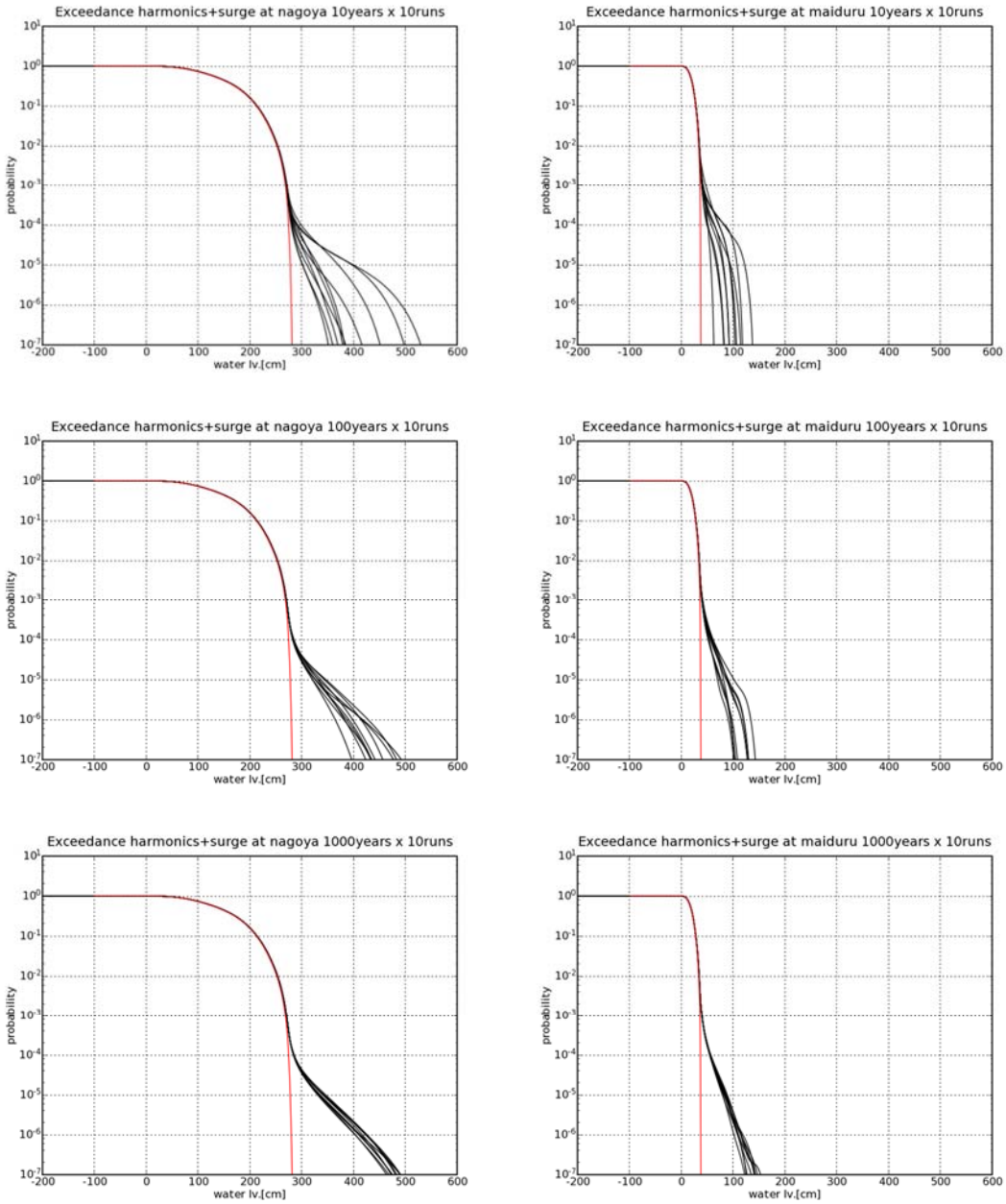

Figure 5.3.4-1 Exceedance probability distribution of astronomical tide levels and storm surge deviation on Nagoya and Maizuru
(10 trial calculations with probabilistic typhoon model for 10years, 100 years, and 1000 years)

(4) Assessment of effect on hazard analysis of case where tsunami height is assumed

In tsunami hazard analysis, a tsunami height distribution is often used that truncates the edge

of the logarithmic normal distribution so that various types of errors that occur in numerical simulations of tsunami may be taken into account. Accordingly, the impact of storm surge is examined for a case where the truncated height of the distribution and the magnitude of variance in the distribution are varied and superimposed on the tide level.

- Tsunami height median value (μ): 5m, 1m
- Variability (κ): 1.25, 1.45
- Truncated water level (σ_{co}): 2.3σ, 10σ

Figure 5.3.4-2 shows the probability density function and probability of exceedance in a case where the median value of the tsunami height is set at 5m.

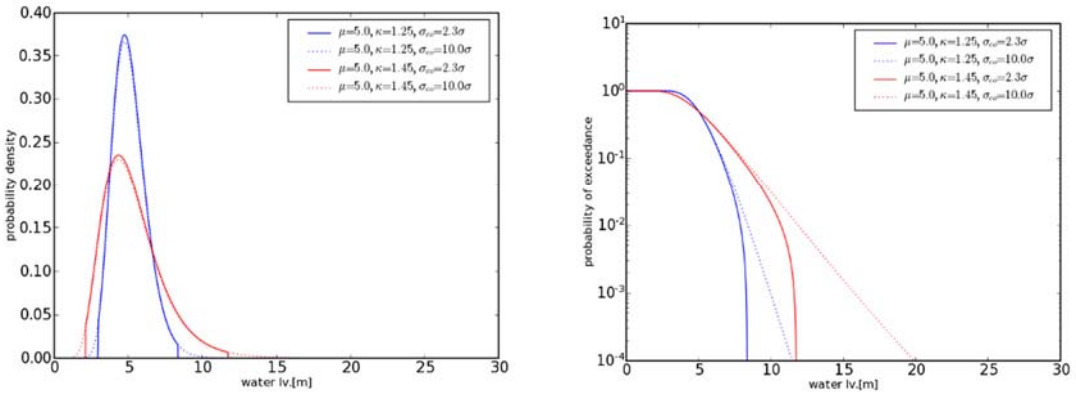

Figure 5.3.4-2 The probability density function (Left) and exceedance probability (Right) in a cases where the median value of the tsunami height is set at 5m

Figures 5.3.4-3 and 5.3.4-4 show the exceedance probability of the tide level when a tsunami occurs is found based upon the aforementioned conditions. The following properties are observed.

1) Case where the truncated water level is 2.3σ
   - The impact of storm surge occurs at a probability of 10^{-5}~10^{-7} (Table 5.3.4-1).

   -> If it is assumed that a tsunami occurs once every 100 years, then the occurrence frequency ranges from 10^{-7} times/year to 10^{-9} times/year, so the impact of storm surge does not pose an issue at a level covered in a typical tsunami hazard analysis.
   - The higher the tsunami height is, the less effect storm surge has.
   - The greater the variance in tsunami is, the less effect storm surge has.

2) Case where the truncated water level is 10σ
   - If tsunami height is equal or larger than storm surge deviation, then the effect of storm surge may be almost completely disregarded.
   - If tsunami height is smaller than storm surge deviation, then the tide level is exceeded, but the storm surge effect is small.

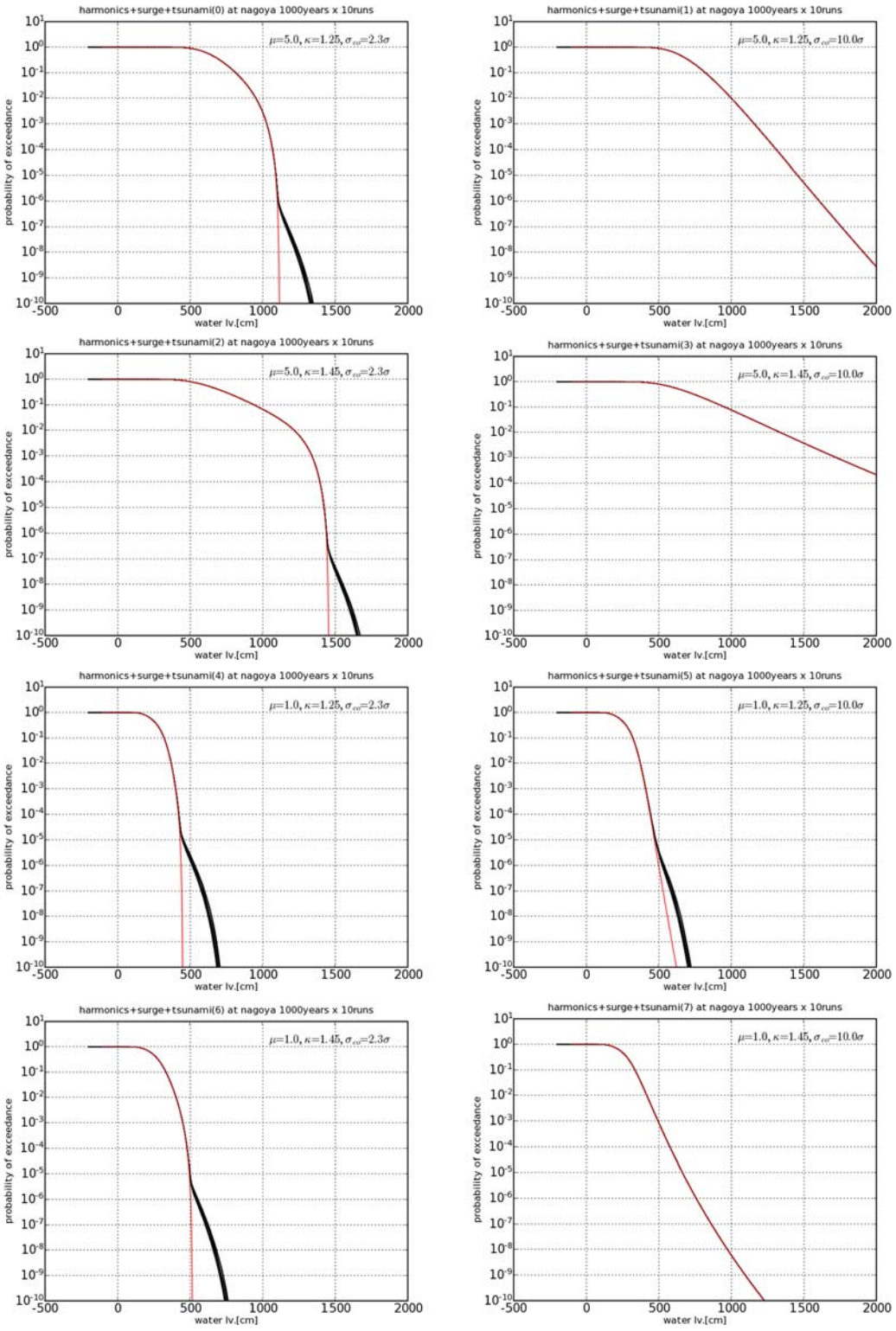

Figure 5.3.4-3 Tide level exceedance probability distribution when a tsunami occurs on Nagoya (Truncation water level: 2.3σ(Left), 10σ(Right))

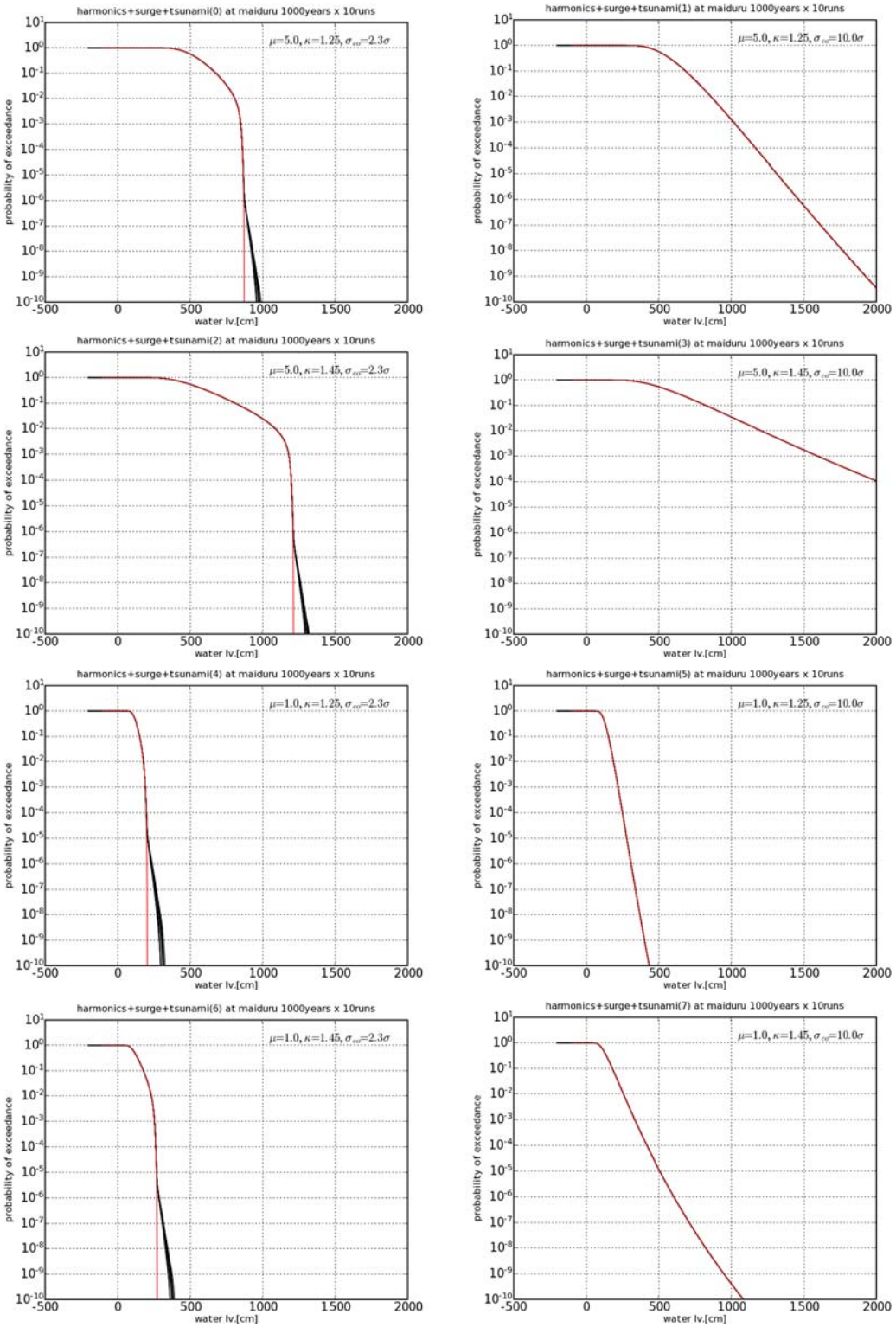

Figure 5.3.4-4 Tide level exceedance probability distribution when a tsunami occurs on Maizuru (Truncation water level: 2.3σ (Left), 10σ (Right))

Table 5.3.4-1 Frequency which storm surge effects on to tsunami hazard analysis (exponential notation)

	Tsunami height	Variability	Truncated water level with logarithmic normal distribution	
			2.3σ	10σ
Nagoya	5m	κ=1.25	-6	-
		κ=1.45	-6.5	-
	1m	κ=1.25	-5	-5
		κ=1.45	-5.5	-
Maizuru	5m	κ=1.25	-6	-
		κ=1.45	-6.5	-
	1m	κ=1.25	-5	-
		κ=1.45	-5.5	-

5.3.5. Summary

A study using the probabilistic typhoon model has been able to verify that the effect of storm surge due to a typhoon on tsunami hazard analysis is very small with the exception of special cases. It is found that the effect of storm surge is relatively large in:

- Cases where tsunami height is small in comparison to the storm surge deviation
- Cases where variance in tsunami height is small

Also, the degree of storm surge effect varies also depending upon the truncated water level of the tsunami height distribution. It is found that the greater the truncated tsunami height is and the closer it is to the logarithmic normal distribution, the smaller the effect of storm surge is which is offset by error in the tsunami simulation.

[Appendix 5 References]

Atomic Energy Society of Japan (AESJ) (2015): A Standard for Procedure of Seismic Probabilistic Risk Assessment for Nuclear Power Plants, AESJ-SC-P006:2015, pp. 374-375 (in Japanese).

Atomic Energy Society of Japan (AESJ) (2015): A Standard for Procedure of Seismic Probabilistic Risk Assessment for Nuclear Power Plants, AESJ-SC-P006:2015, 426p. (in Japanese).

Atomic Energy Society of Japan (AESJ) (2015): A Standard for Procedure of Seismic Probabilistic Risk Assessment for Nuclear Power Plants, AESJ-SC-P006:2015, 60p. (in Japanese).

Headquarters for Earthquake Research Promotion (2013): Study on ground motion hazard assessment

of future (in Japanese).
http://www.jishin.go.jp/evaluation/seismic_hazard_map/shm_report/shm_report_2013

Holland, G. J. (1997): The Maximum Potential Intensity of Tropical Cyclones, Journal of the Atmospheric Sciences, vol. 54, No. 21, pp. 2519-2541.

Inoue, T., N. Fujita, M. Matsuyama, and Y. Tanaka (2013): A STUDY ON THE SIMULTANEOUS OCCURRENCE PROBABILITY OF TSUNAMI AND STORM SURGE, Journal of Japan Society of Civil Engineers, Ser. B3 (Ocean Engineering), Volume 69 (2013) Issue 2, pp. I_425-I_430 (in Japanese).
https://www.jstage.jst.go.jp/article/jscejoe/69/2/69_I_425/_pdf/-char/en.

Iwabuchi, Y., H. Sugino, and K. Ebisawa (2014): Guidelines for Developing Design Basis Tsunami based on Probabilistic Approach, Japan Nuclear Energy Safety Organization, JNES-RE-2013-2041 (in Japanese with English abstract).

Nanjo, K.Z., N. Hirata, K. Obara, and K. Kasahara (2011): Spatiotemporal change in b values around the hypocenter of the 2011 Tohoku-Oki earthquake, Report of the Coordinating Committee for Earthquake Prediction, Japan, Vol. 86, 3-17, pp. 121-122 (in Japanese).
http://cais.gsi.go.jp/YOCHIREN/report/kaihou86/03_17.pdf.

National Research Institute for Earth Science and Disaster Prevention, Japan (2005): A Study on Probabilistic Seismic Hazard Maps of Japan, Technical Note of the National Research Institute for Earth Science and Disaster Prevention No. 275 (in Japanese).
http://dl.ndl.go.jp/view/download/digidepo_9682770_po_n275.pdf?contentNo=1&alternativeNo=.

Ogata, Y. (2015): Stochastic Prediction of Earthquakes - A Strategy for the Research, Proceedings of the Institute of Statistical Mathematics Vol. 63, No. 1, pp. 3–27 (in Japanese).
http://www.ism.ac.jp/editsec/toukei/pdf/63-1-003.pdf.

Chapter 6. Examples of Applications of Deterministic Hazard Analysis

"Notes: Examples of Applications of Deterministic Hazard Analysis"

The examples of applications of deterministic tsunami hazard analysis, which are presented in this chapter, are premised on tsunami source locations, intensity and other characteristics given as conditions, and illustrate the procedures and results of parametric studies for taking into account uncertainty and configuration of the standard fault models presented in Chapter 4 of the main volume.

In accordance with the aforementioned purpose, it should be kept in mind that these application examples neither specify in detail the causes, locations, intensities or other characteristics of tsunami that may occur in the future nor negate other assessment procedures. Also, the parameters and other information presented in these application examples are entirely illustrative. In actual deterministic tsunami hazard analyses, sufficient consideration needs to be given to the appropriateness of parameter configurations and other elements in the analysis.

Covering the sea region extending from the Kuril-Kamchatka Trench to the Japan Trench, an example is presented of a deterministic tsunami hazard analysis based upon a method for considering uncertainty, which takes into account knowledge gained from the 2011 Tohoku earthquake.

6.1. Basic matters

(1) Examination method

The examination method is given in Table 6.1-1. First, the standard fault model is prepared based upon tectonic data and other information about the target region. Next, as described in section 4.2.3.1(1) of the main volume, a simplified parametric study is carried out of major factors, and the locations of large slip areas, which significantly affect the region assessed, are selected. Lastly, a detailed parametric study is conducted of subordinate factors, and the effect of uncertainty is studied as concerns kinematic parameters of fault rupture.

Table 6.1-1 Investigation method for the sea area along the Kuril trench and the Japan trench

Step	Content		Remarks
1. standard fault model	Large slip area and super large slip area are modeled under the method proposed by Cabinet office.		-
2. Simplified parametric study	Overlap the half of the large slip area with the next fault model. (Seto and Takahashi, 2014)		Rise time: 30s Rupture velocity: ∞
3. Detailed parametric study	Rupture velocity	1.0km/s, 2.0km/s, 2.5km/s, 3.0km/s	Rise time:30s (fixed vale)
	Hypocenter	Setting 6 points along the outer border of large slip area and in the super large slip area	-
	Rise time	30s, 60s, 180s, 300s	Rupture velocity: ∞, 2.5km/s

(2) Analysis conditions for the numerical simulation

The analysis conditions used in the numerical simulation of tsunami are given in Table 6.1-2.

Table 6.1-2 Analysis condition

Specification	Description
Calculation area	Pacific ocean from northern Kuril islands to Boso peninsula
Calculation mesh grid size	Offshore 1,350m, 450m, 150m, coastal area 50m
Basic equation	Nonlinear long wave theory
Initial displacement of sea bottom	The elasticity theory of dislocation (Mansinha and Smylie, 1971)
Boundary condition	Offshore: free transmission, Landward: wave front (dry-wet) condition
Overflow condition	Breakwater: Honma model, revetment:Aida model
Horizontal eddy viscosity coefficient	Not considered
Friction Coefficient	Manning's coefficient of roughness Sea area: $0.03m^{-1/3}\cdot s$, land area; $0.03m^{-1/3}\cdot s$
Tide level	T.P.±0.0m (T.P.: Tokyo peil)
Computation time interval	0.5s
Simulating time	4 hours after the occurrence of earthquake

(3) Computational region and grid size in FDM

Figure 6.1-1 shows the grid size of the computational region used in the numerical simulation of tsunami. The grid size for the offing region is 1,350m, becoming more finely divided closer to the coastal area so that it is 50m along the coastline.

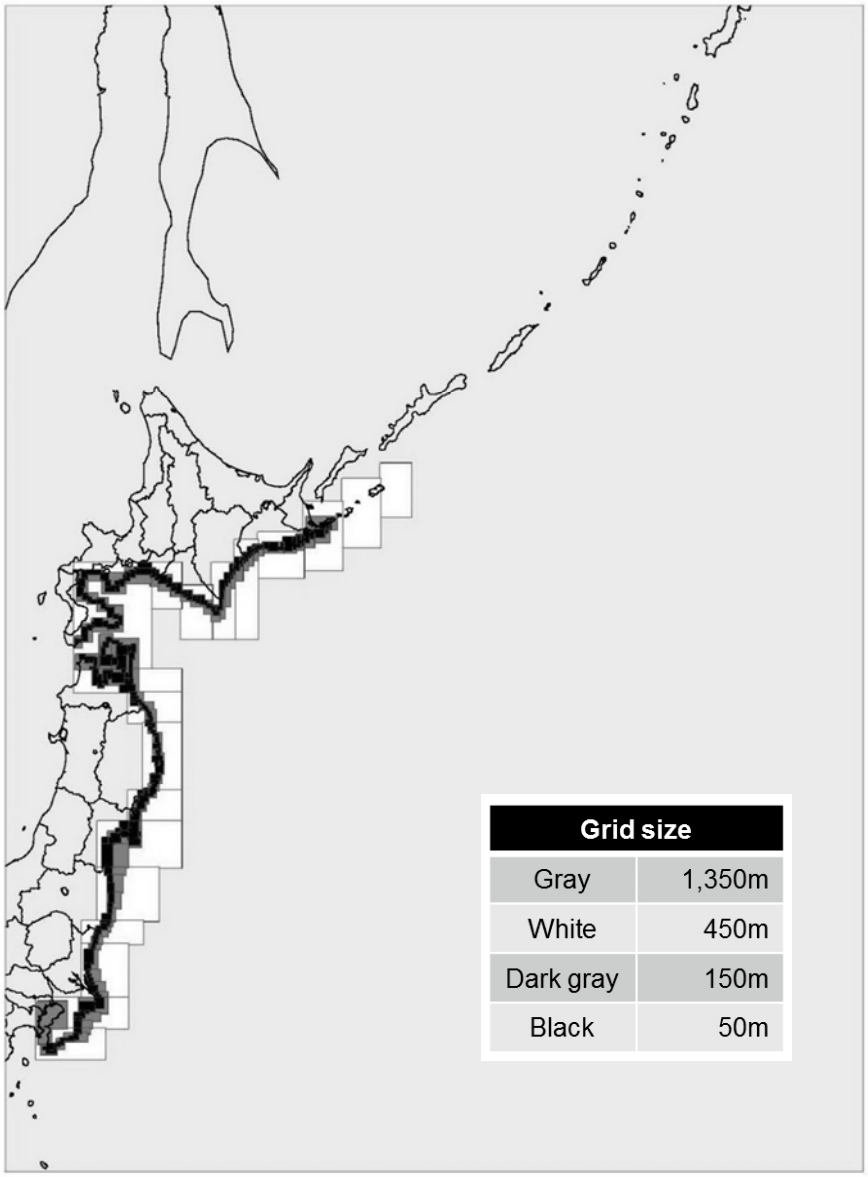

Figure 6.1-1 Grid size of computational region in FDM

6.2. Configuration of standard fault model

According to the Headquarters for Earthquake Research Promotion (2004), earthquakes, which occurred in the region ranging from Off Tokachi to Off Nemuro, may have been multi-segment ruptures occurring at intervals between 400 and 500 years (500-year interval earthquakes), and the time of the most recent occurrence was during the 17th century. Based on this, the focus in the sea region ranging from the Kuril-Kamchatka Trench to the Japan Sea Trench is on a region that includes the 500-year interval earthquakes off the coast of Hokkaido, which is considered to be the area where the occurrence of a megathrust earthquake presents the greatest urgency.

The conditions for fault model were as follows.

[Configuration conditions]

- Fault area: Junction with the Japan Trench to the Bussol Strait (assuming an earthquake occurring along the boundary between the Kuril forearc sliver (DeMets, 1992) and Pacific plate)
- Mean stress drop: $\Delta\sigma$=3(MPa)
- Slip distribution: Large slip areas and very-large slip areas are set based on the approach set forth in Cabinet Office (2012)

Table 6.2-1 shows the basic information of fault model for a *M*9-class megathrust earthquake along the Kuril-Kamchatka Trench, as configured according to the aforementioned conditions.

Figure 6.2-1(1) shows the standard fault model. Also, Figures 6.2-1(2) through (5) show fault models when large slip areas, which also include super large slip areas, move in accordance with previously described method for a simplified parametric study.

Table 6.2-1 Basic information of standard fault model

Specification	Values
Length (km)	848
Area(×1,000km^2)	159
Area ratio of the super large slip area and large slip area (%)	20.1
Average slip of whole area (m)	10.0
Displacement of super large slip area (m)	40.0
Displacement of large slip area (m)	20.0
Displacement of background zone (m)	5.8
M_W	9.2
$\Delta\sigma$ (MPa)	3.0
Number of subfaults	1,961

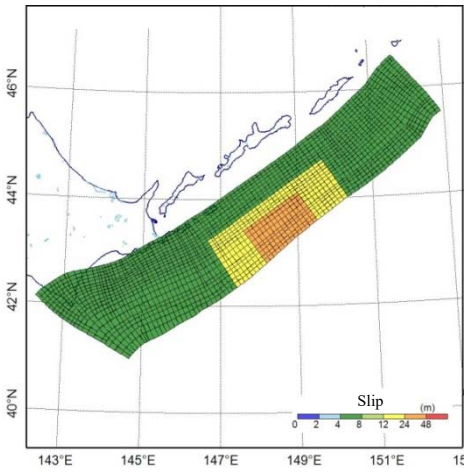

(1) Centered large slip area (basic model)

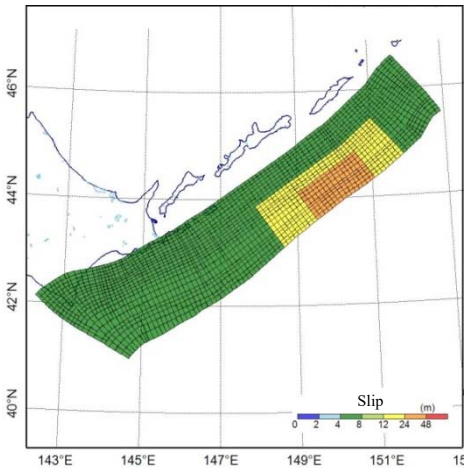

(2) Large slip area placed at the half point to east

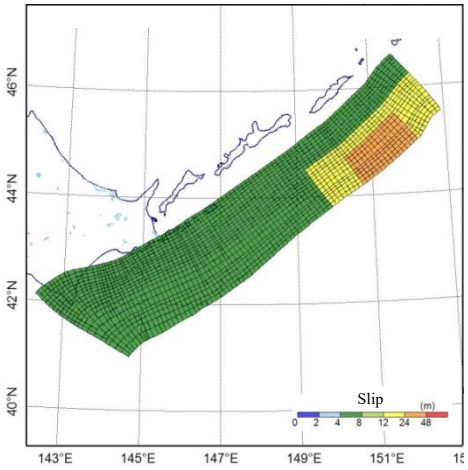

(3) Large slip area placed at the eastern edge

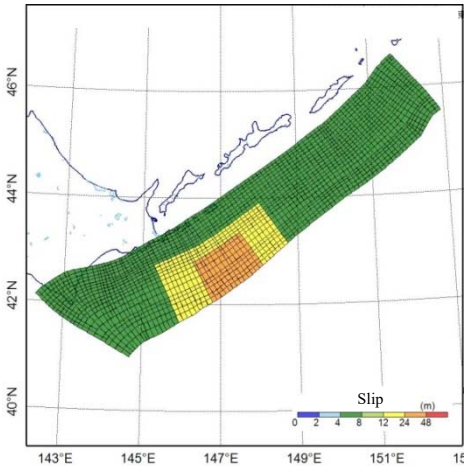

(4) Large slip area placed at the half point to west

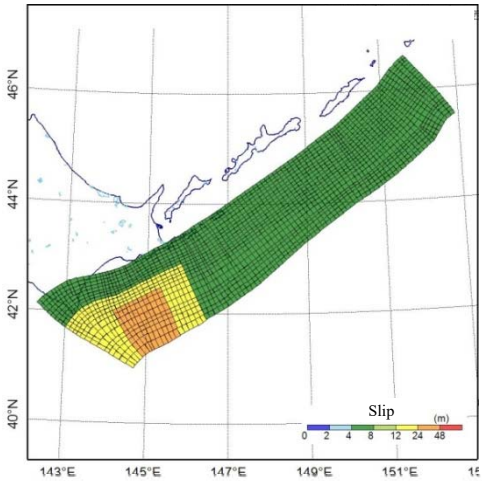

(5) Large slip area placed at the western edge

Figure 6.2-1 Standard fault model and trial fault models for simplified parametric study

6.3. Simplified parametric study

The simplified parametric study and detailed parametric study compared the analysis results with the results of surveys of tsunami deposits ("run-up height records (deposits)"). The run-up height records (deposits), which were used, were based on Hokkaido Government(2012), MEXT and Hokkaido University (2010), MEXT and Hokkaido University (2011), and MEXT and Hokkaido University (2012). Here, other than Hokkaido Government(2012), the position data were digitalized from the reports as elevation values, so the values from the reports are treated as sample values.

Distribution of the run-up height records (deposits) is shown in Figure 6.3-1. Detailed data of run-up height records (deposits) is also listed in Table 6.3-1.

Figure 6.3-1 Distribution of run-up height records (tsunami deposits) (Hokkaido government, 2012)

Figure 6.3-2 shows a comparison of the run-up height records (deposits) and the calculation results where the position of large slip area was moved. Here, in the vicinity of Nemuro City, when the large slip area placed at the half point to west, calculated tsunami heights exceeded the run-up height records (deposits). At most of the other trace points, when a large slip area was placed at "western edge", the tsunami run-up height records (deposits) were either exceeded, or at the same level. Based on the aforementioned results, the detailed parametric study verified the effect of

uncertainty on the kinematic parameters of fault rupture by using models where large slip area was placed at “western edge”.

In Figure 6.3-2, all of the values calculated for trace points in the Hidaka region and Funka Bay were lower than the tsunami run-up height records (deposits). As shown in Figure 6.3-3, it is considered that tsunami occurring along the Kuril-Kamchatka Trench (southern part) are obstructed by Cape Erimo and most large waves do not propagate in the Hidaka region or Funka Bay, which are located west of Cape Erimo.

Table 6.3-1 Detailed data of tsunami run-up height records (deposits)

No.	Tsunami Height (m)	Latitude (deg.)	Longitude (deg.)	Place	Source
01	15.0	43.34	145.72	Nemuro-shi	Hokkaido Government (2012)
02	4.0	43.24	145.55	Nemuro-shi	Hokkaido Government (2012)
03	10.0	43.24	145.55	Nemuro-shi	Hokkaido Government (2012)
04	10.0	43.19	145.41	Nemuro-shi	Hokkaido Government (2012)
05	15.5	43.19	145.41	Nemuro-shi	Hokkaido Government (2012)
06	1.0	43.03	144.84	Hamanaka-cho	Hokkaido Government (2012)
07	5.0	43.03	144.84	Hamanaka-cho	Hokkaido Government (2012)
08	12.0	43.03	144.84	Hamanaka-cho	Hokkaido Government (2012)
09	8.0	42.99	144.20	Kushiro-shi	Hokkaido Government (2012)
10	5.0	42.92	144.00	Shiranuka-cho	Hokkaido Government (2012)
11	12.0	42.92	144.00	Shiranuka-cho	Hokkaido Government (2012)
12	4.0	42.88	143.92	Kushiro-shi-Onbetsu	Hokkaido Government (2012)
13	7.0	42.88	143.92	Kushiro-shi-Onbetsu	Hokkaido Government (2012)
14	8.0	42.88	143.92	Kushiro-shi-Onbetsu	Hokkaido Government (2012)
15	12.0	42.83	143.84	Urahoro-cho	Hokkaido Government (2012)
16	7.0	42.79	143.80	Urahoro-cho	Hokkaido Government (2012)
17	10.0	42.76	143.76	Urahoro-cho	Hokkaido Government (2012)
18	12.0	42.60	143.55	Toyokoro-cho	Hokkaido Government (2012)
19	15.0	42.60	143.55	Toyokoro-cho	Hokkaido Government (2012)
20	10.0	42.54	143.48	Taiki-cho	Hokkaido Government (2012)
21	15.0	42.54	143.48	Taiki-cho	Hokkaido Government (2012)
22	18.0	42.54	143.48	Taiki-cho	Hokkaido Government (2012)
23	11.0	42.45	143.41	Taiki-cho	Hokkaido Government (2012)
24	12.0	42.45	143.41	Taiki-cho	Hokkaido Government (2012)
25	17.0	42.45	143.41	Taiki-cho	Hokkaido Government (2012)
26	9.0	42.39	143.37	Hiroo-cho	Hokkaido Government (2012)
27	10.0	42.39	143.37	Hiroo-cho	Hokkaido Government (2012)
28	12.0	42.39	143.37	Hiroo-cho	Hokkaido Government (2012)
29	5.0	42.33	142.38	Shin-Hidaka-cho	Hokkaido Government (2012)
30	5.0	42.49	142.03	Hidaka-cho	Hokkaido Government (2012)
31	7.0	42.57	141.91	Mukawa-cho	Hokkaido Government (2012)
32	5.0	42.35	141.05	Cape Washibetsu	Hokkaido Government (2012)
33	4.5	42.39	140.91	Date-shi-Kogane	Hokkaido Government (2012)
34	5.0	42.12	140.54	Mori-machi-Washinoki	Hokkaido Government (2012)
35	2.3	42.71	143.68	Urahoro-cho-Toyokita (sample)	MEXT & Hokkaido University (2010-2012)
36	15.5	43.19	145.41	Nemuro-shi-Bettoga (sample)	MEXT & Hokkaido University (2010-2012)
37	4.9	42.86	143.87	Nemuro-shi-Kinashibetsu (sample)	MEXT & Hokkaido University (2010-2012)
38	4.9	42.88	143.92	Nemuro-shi-Onbetsu (sample)	MEXT & Hokkaido University (2010-2012)
39	4.7	42.88	143.92	Nemuro-shi-Onbetsu (sample)	MEXT & Hokkaido University (2010-2012)
40	1.4	43.07	144.80	Akkeshi-cho-Shirahama (sample)	MEXT & Hokkaido University (2010-2012)

Note) Tsunami heights of No.35-40 are sample only, since these are digitized altitude from the report

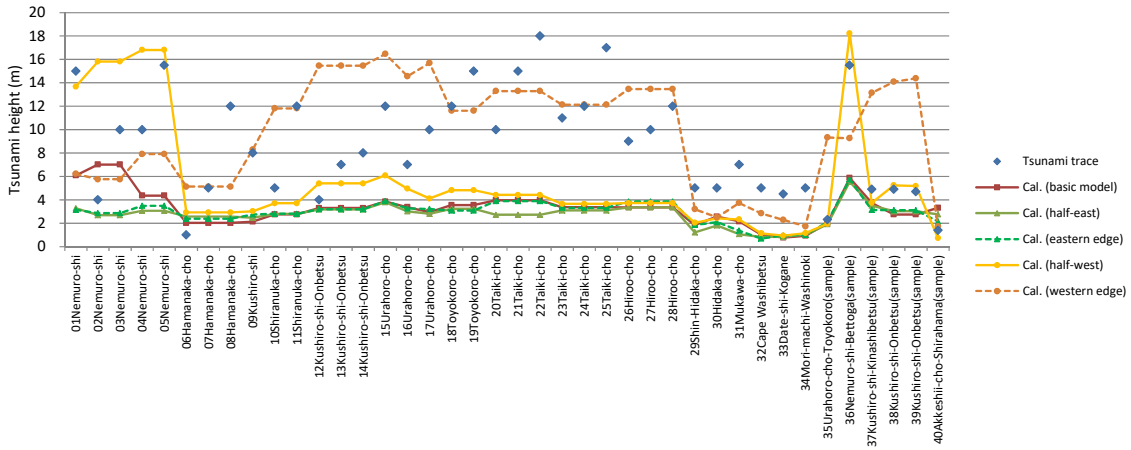

Figure 6.3-2 Comparison of the calculated tsunami heights obtained from the parametric study with respect to the location of large slip area and the tsunami run-up height records (deposits)

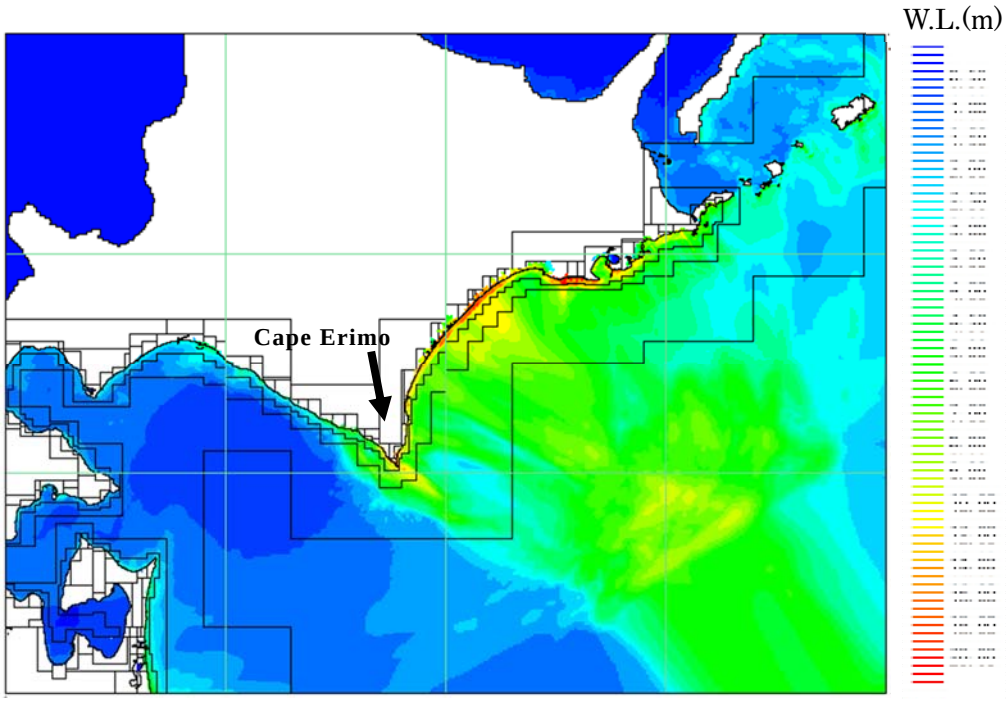

Figure 6.3-3 Distribution map of maximum water level in the calculation case in which large slip area placed at the eastern edge

6.4. Detailed parametric study

The detailed parametric study examined the uncertainty of kinematic parameters for fault rupture.

Based on the results of the simplified parametric study, it was decided to use a “model where a large slip area was placed at the western edge” for the fault model in the study.

(1) Effect of hypocenter and rupture velocity on tsunami height

The positions of hypocenters are as shown in Figure 6.4-1, and there were five points around large slip areas and one point in the center of a super large slip area. Also, four cases were set for rupture velocity: V_r: V_r=1.0(km/s), V_r=2.0(km/s), V_r=2.5(km/s), and V_r=3.0(km/s). Figure 6.4-2 shows an example of a rupture propagation time distribution for a fault in keeping with the rupture velocities in the case of hypocenter (d).

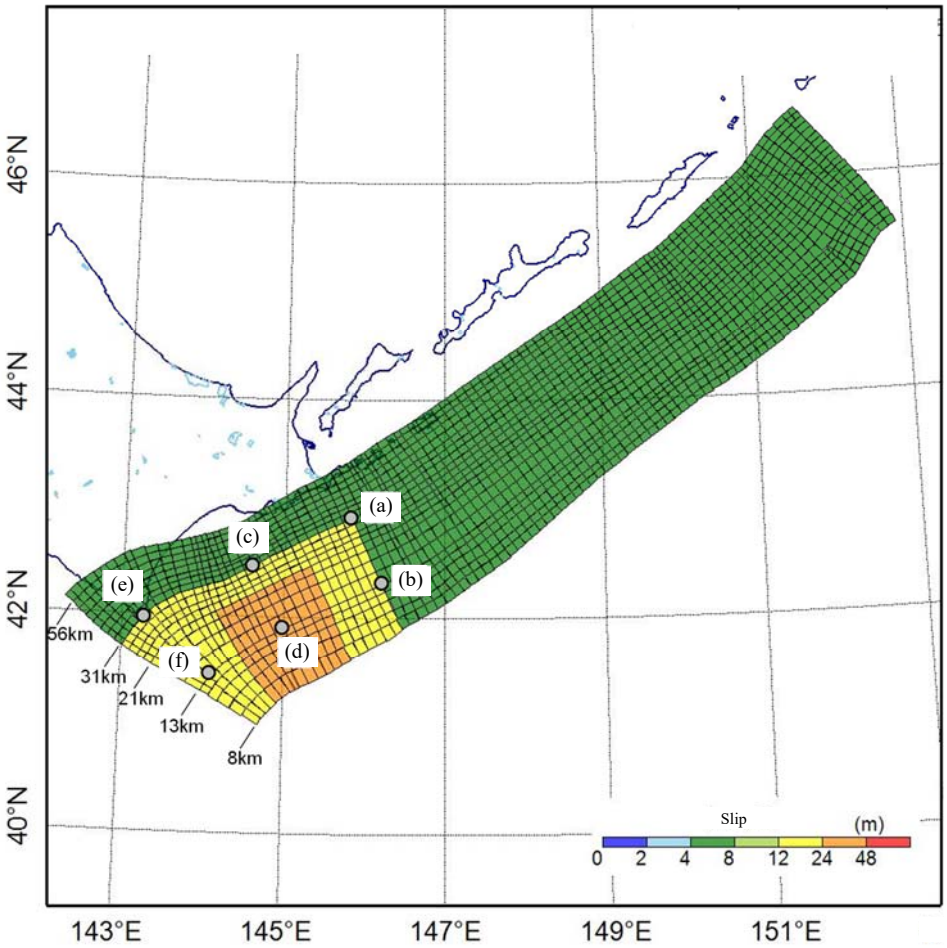

Figure 6.4-1 Location of the hypocenters (Large slip area placed at the eastern edge)

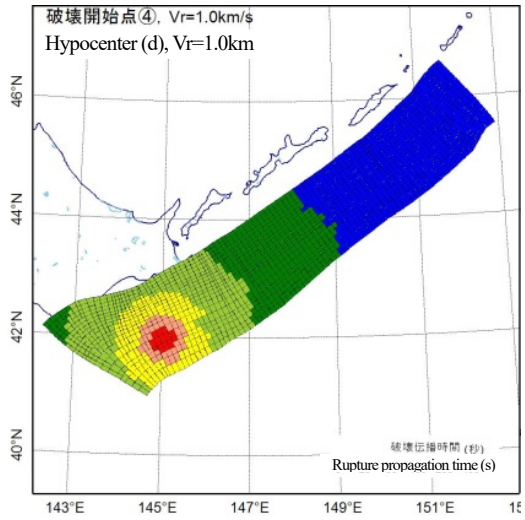

(1) V_r=1.0(km/s)

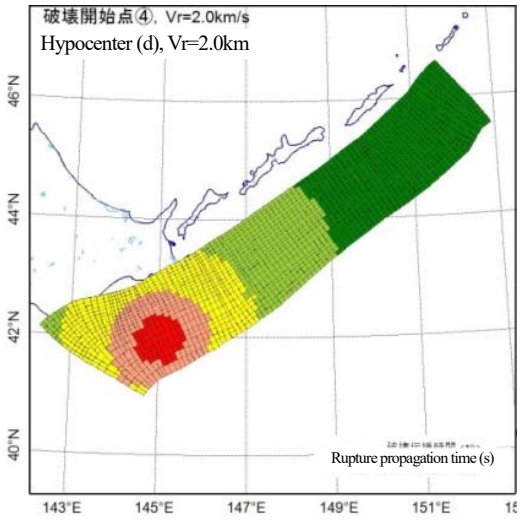

(2) V_r=2.0(km/s)

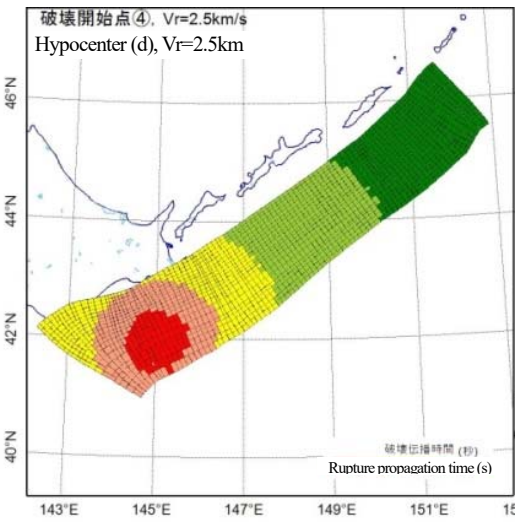

(3) V_r=2.5(km/s)

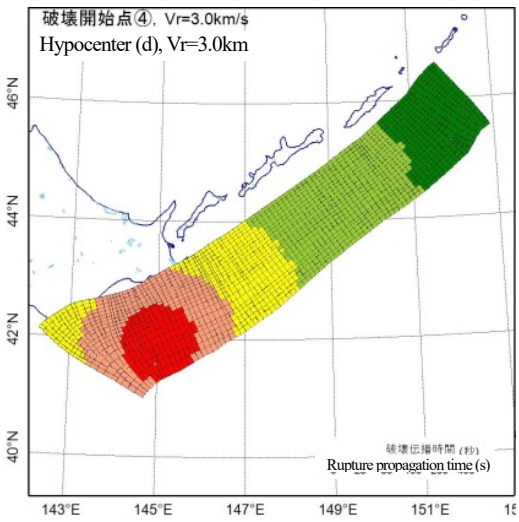

(4) V_r=3.0(km/s)

Figure 6.4-2 Distribution of rupture propagation time in the case of hypocenter (d) (Large slip area placed at the eastern edge)

Figure 6.4-3 shows the results of parametric studies of hypocenters and rupture velocities. It was found that, over a range extending from Kushiro City to Hiroo Town which is located in front of a large slip area, the tsunami height level varied significantly due to the effects of location of hypocenter and rupture velocity.

Figure 6.4-4 shows a comparison of the maximum water levels from the parametric study results with the tsunami run-up height records (deposits). Figure 6.4-4(1) shows a comparison of the maximum water levels from the detailed parametric study with the tsunami run-up height records (deposits), and Figure 6.4-4(2) shows the maximum water levels from all parametric studies, which is a combination of the simplified parametric study and detailed parametric study, with the tsunami run-up height records (deposits). At most of the run-up height records (deposits) with the exception of the area ranging from the Hidaka region to Funka Bay, the result was that the maximum envelope of the calculated values exceeded the tsunami run-up height records (deposits).

Of the sites where surveys were conducted for tsunami trace values (tsunami deposits), three representative sites (Hamanaka-cho, Taiki-cho, and Mori–machi-Washinoki) were targeted to verify the effect that location of rupture initiation pointhypocenter and rupture - velocity have on tsunami height. The results are given in Figure 6.4-5. A trend was observed where tsunami height increased in cases where the rupture initiated from a location close to the trench axis ((b), (d) and (f)). With regard to the effect of rupture velocity, the trend differed depending upon the location of the rupture initiation pointhypocenter, and, in cases where the rupture initiated in the vicinity of the trench axis ((b), (d) and (f)), a trend was observed where the tsunami height would be larger the smaller the rupture velocity was. On the other hand, in cases where the rupture initiated along the coast ((a), (c) and (e)), the opposite trend was observed.

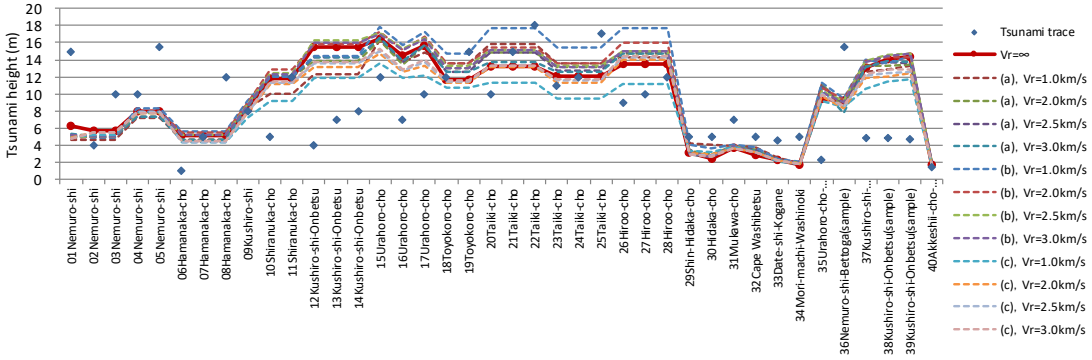

(1) Results in the case of hypocenter (a) ~ (c)

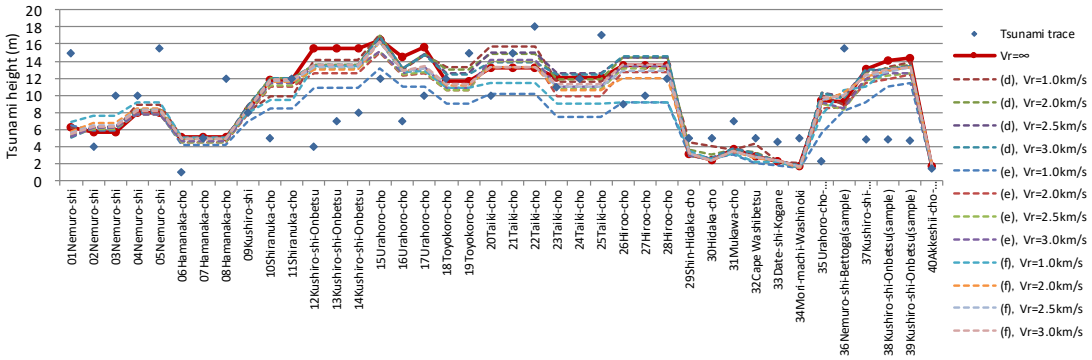

(2) Results in the case of hypocenter (d) ~ (f)

Figure 6.4-3 Results of parametric studies with respect to the hypocenter and the rupture velocity

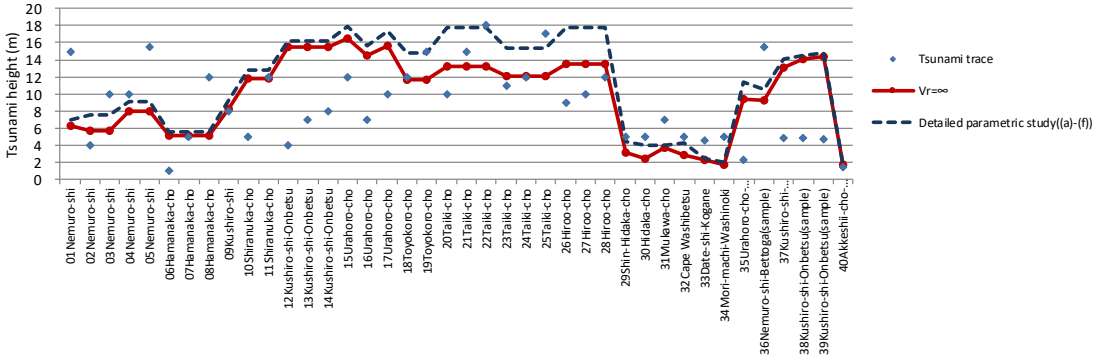

(1) Results of detailed parametric study

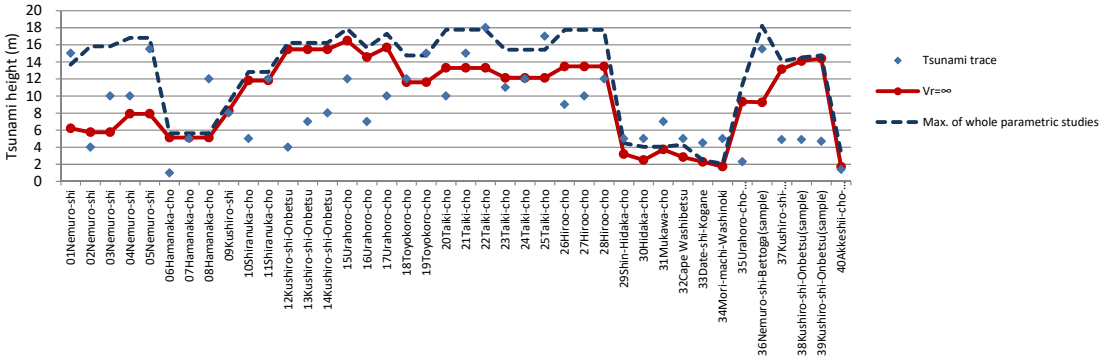

(2) Results of whole parametric study (simplified and detailed)

Figure 6.4-4 Comparison of calculated tsunami heights obtained from the parametric study and the tsunami run-up height records (deposits)

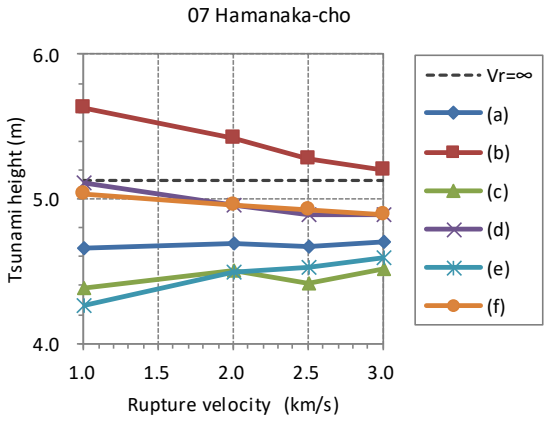

(1) Effect of rupture velocity on tsunami height in Hamanaka-cho

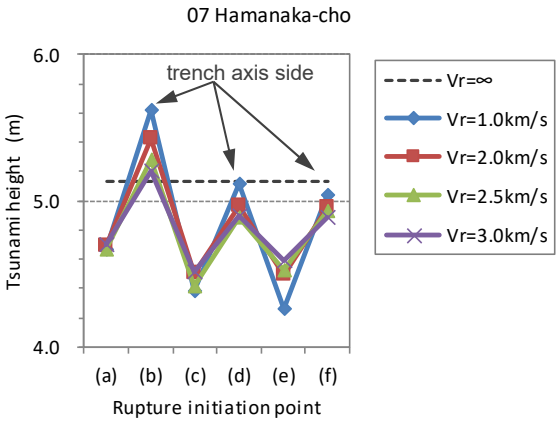

(2) Effect of location of hypocenter on tsunami height in Hamanaka-cho

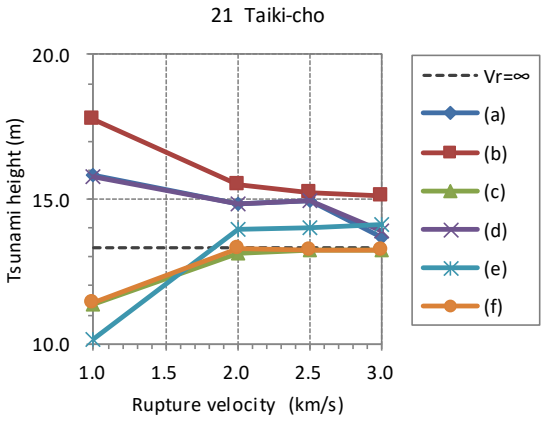

(3) Effect of rupture velocity on tsunami height in Taiki-cho

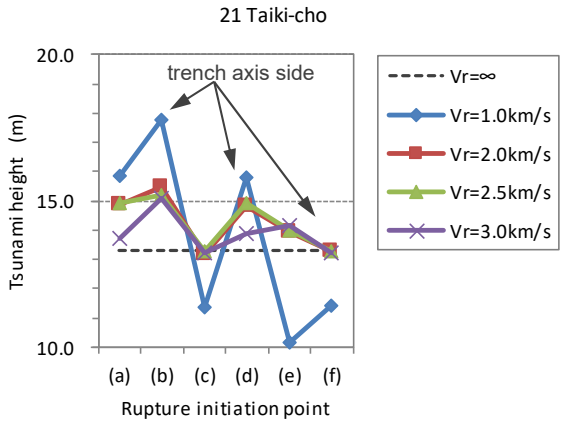

(4) Effect of location of hypocenter on tsunami height in Taiki-cho

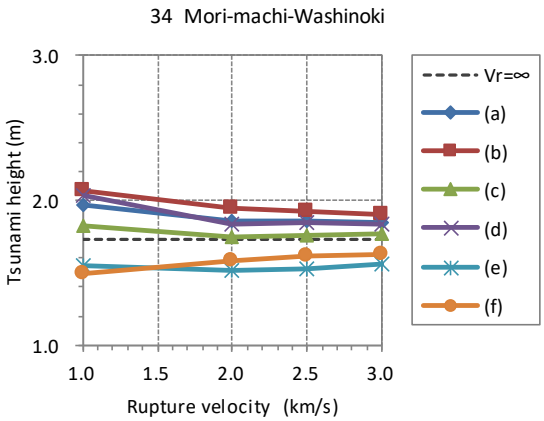

(5) Effect of rupture velocity on tsunami height in Mori-machi-Washinoki

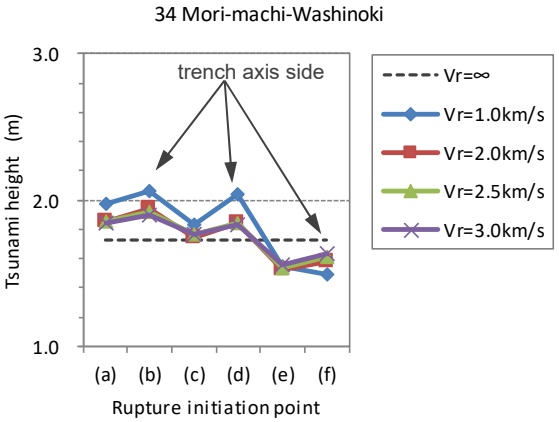

(6) Effect of location of hypocenter on tsunami height in Mori-machi-Washinoki

Figure 6.4-5 Effect of hypocenter and rupture velocity on tsunami heights

(2) Effect of rise time on tsunami height

A parametric study of rise time was conducted. Here, four scenarios were examined setting the rise time at 30 seconds, 60 seconds, 180 seconds, and 300 seconds, and two cases were examined: a case where rupture velocity was not considered (V_r=∞) and a case where rupture velocity was set at V_r=2.5(km/s) with the hypocenter (b).

Figure 6.4-6 shows the results of the case where rupture velocity was not considered (V_r=∞). Figure 6.4-7 shows the results of a case where the rupture velocity was set at V_r=2.5(km/s) and the hypocenter was (b). Based on a comparison of the results, a trend was observed with respect to the effect of rise time where the tsunami height decreased the longer the rise time was. However, the effect on tsunami height was not very pronounced within a range where the rise time was not extremely long (30 ~ 60 seconds).

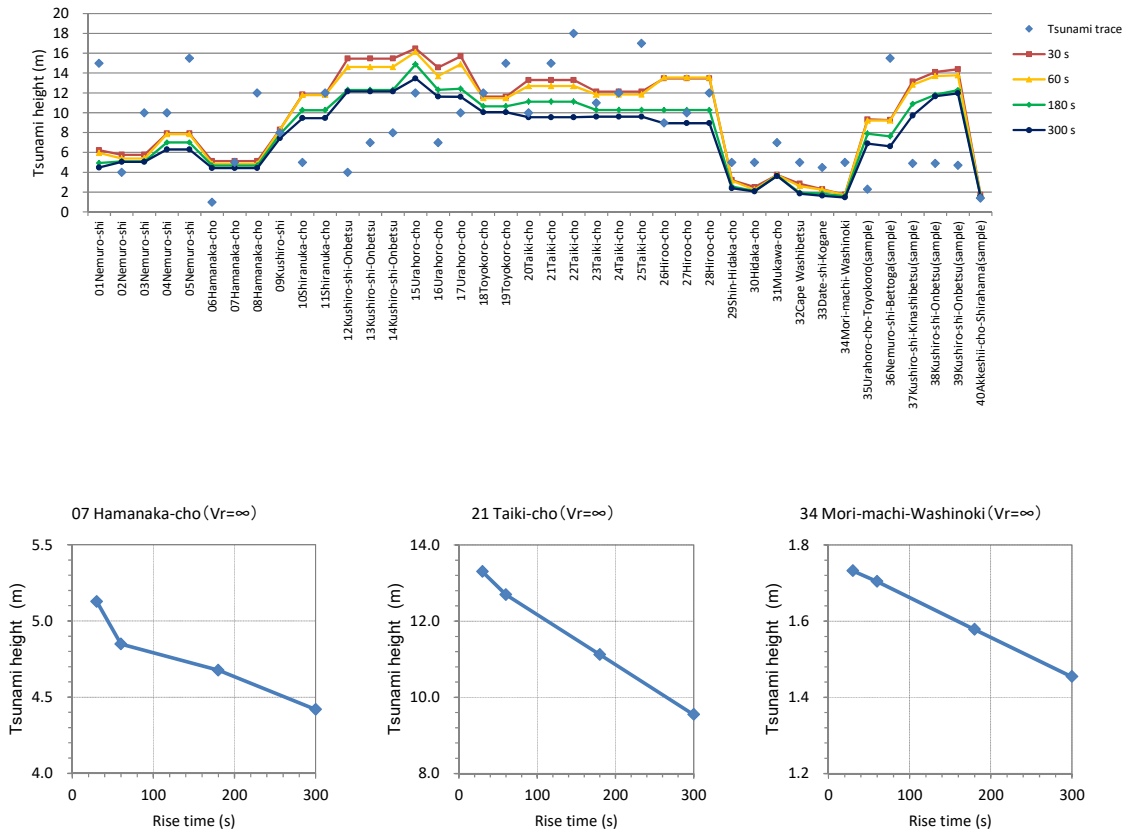

Figure 6.4-6 Effects of rise time on tsunami heights (V_r=∞)

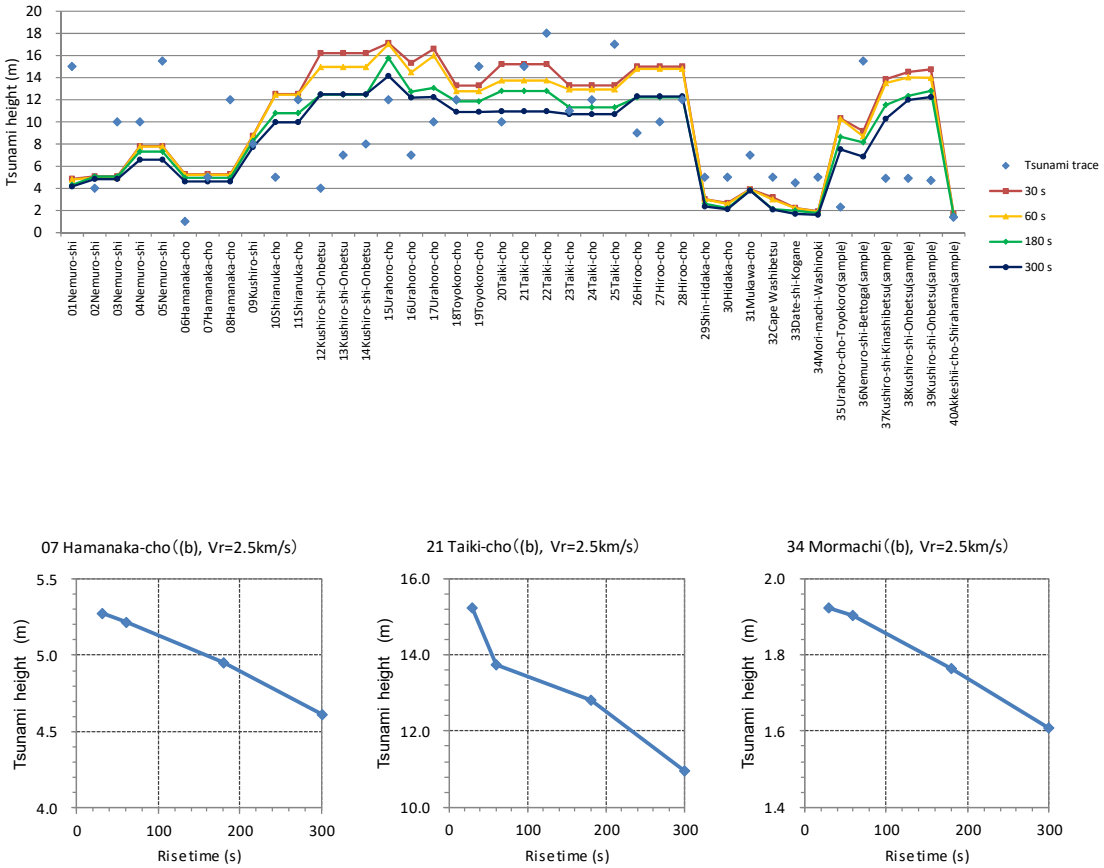

Figure 6.4-7 Effects of rise time on tsunami heights (hypocenter (b), V_r=2.5km/s)

6.5. Summary

The findings that was obtained from an examination of deterministic tsunami hazard analysis, which focused on the sea area extending from the Kuril-Kamchatka Trench to the Japan Sea Trench, is summarized below.

- For a region that includes the source region of the 500-year interval earthquakes in the Off Hokkaido, a standard fault model (M_W9.2), which was based upon the approach presented by Cabinet Office (2012), was considered and a deterministic hazard analysis was conducted.
- The results of simplified and detailed parametric studies showed that the maximum envelope of the calculated values exceeded tsunami run-up height records (tsunami deposits) at most of the tsunami trace points with the exception of the area ranging from the Hidaka region to Funka Bay.
- A detailed parametric study was conducted in order to verify the effects of kinematic parameters of fault rupture (hypocenter, rupture velocity, and rise time) on tsunami heights along the coastline.
  - In an area of open coastline that front large slip areas (comparison point: Taiki-cho), it was found that, while kinematic parameters act greatly on tsunami height, the tsunami height is not easily affected by these within a harbor (comparison points: Mori–machi-Washinoki and Hamanaka-cho).
  - With regard to the effect that location of hypocenter has on tsunami height along the coastline, a trend was observed where tsunami height increased when rupture initiated at locations close to the trench axis.
  - With regard to the effect of rupture velocity, a trend was observed where the tsunami height would be larger the smaller the rupture velocity was in cases where the rupture initiated in the vicinity of a trench axis.
  - With regard to the effect of rise time, a trend was observed where the tsunami height decreased the longer the rise time was. However, the effect on tsunami height was not very pronounced within a range where the rise time was not extremely long (30 ~ 60 seconds).

[Appendix 6 References]

Committee for Evaluating the Rupture Model of Megathrust Earthquakes along the Nankai Trough under Cabinet Office, Government of Japan (2012): The 2nd Report of Committee for Evaluating the Rupture Model of Megathrust Earthquakes along the Nankai Trough: Tsunami Fault Model Version -Tsunami Fault Model, Tsunami Height, Tsunami Flooded Area and etc.- (in Japanese).

http://www.bousai.go.jp/jishin/nankai/model/pdf/20120829_2nd_report01.pdf (Accessed on August 2014).

DeMets, C. (1992): Oblique Convergence and Deformation Along the Kuril and Japan Trenches, Journal of Geophysical Research, Vol. 97, No. B12, pp. 17615-17625.

Headquarters for Earthquake Research Promotion (2004): Long-term Evaluations of seismic activities along the Kuril Trench (2nd edition), pp. 1-81 (in Japanese).

Hokkaido Government (2012): Report on the Development of Hazard Maps of Tsunami Inundation along the Pacific Coast of Hokkaido, Japan (in Japanese).

Mansinha, L. and D. E. Smylie (1971): The displacement fields of inclined faults, Bulletin of the Seismological Society of America, Vol. 61, No. 5, pp. 1433-1440.

MEXT (Ministry of Education, Culture, Sports, Science and Technology, Japan) and Hokkaido University (2010): Annual Report 2009 on the Investigation and Research into the Off Nemuro Earthquakes, Japan (in Japanese).

MEXT (Ministry of Education, Culture, Sports, Science and Technology, Japan) and Hokkaido University (2011): Annual Report 2010 on the Investigation and Research into the Off Nemuro Earthquakes, Japan (in Japanese).

MEXT (Ministry of Education, Culture, Sports, Science and Technology, Japan) and Hokkaido University (2012): Annual Report 2011 on the Investigation and Research into the Off Nemuro Earthquakes, Japan (in Japanese).

Seto, S. and T. Takahashi (2014): Recipe of Predicting Multi Tsunami Scenarios in the Nankai Trough and Its Application, Journal of JSCE, B2 (Coastal Engineering), Vol. 70, No. 2, pp. I_351-I_355 (in Japanese).

Shuto, N. and M. Uhana (1984): Height of the 1983 Japan Sea Earthquake-Tsunami, Research Report of Tsunami Disaster Prevention Laboratory, School of Engineering, Tohoku University, Vol. 1 (in Japanese).

Chapter 7. Examples of Applications of ProbabilisticTsunami Hazard Analysis

"Notes: Examples of Applications of Probabilistic Tsunami Hazard Analysis"

The examples of applications of probabilistic tsunami hazard analysis, which are presented in this chapter, are premised on logic tree assumptions, earthquake occurrence frequency, magnitude and other characteristics given as conditions, and illustrate the procedures and results of the logic tree construction, modeling earthquake occurrence, and other matters presented in Chapter 5 of the main volume.

In accordance with the aforementioned purpose, it should be kept in mind that these application examples are neither limitations on earthquake occurrence frequency, magnitude or other characteristics nor do they negate other methods that take into consideration uncertainty. Also, the configuration of logic trees and other elements presented in these application examples are entirely illustrative. In actual probabilistic tsunami hazard analyses, sufficient consideration needs to be given to the appropriateness of logic trees and other analysis elements.

An example of a probabilistic tsunami hazard analysis for the sea region extending from the Kuril Trench to the Japan Trench is presented. Just as in with the assessment by Japan Society of Civil Engineers (2011), the target sites were Fudai Village and Yamada Town in Iwate Prefecture.

7.1. Logic tree construction

(1) Source region and occurrence pattern

Figure 7.1-1 shows the source regions. This analysis examines the multi-segment rupture type earthquakes ((a), (b), (c) and (d)), tsunami earthquakes (JTT), and normal fault earthquakes within the oceanic plate (JTNR).

With regard to the multi-segment rupture type earthquake models, branches were configured as to whether they are considered as the characteristic earthquake model identifying the region or the G-R model which does not identify the region. In addition, in case of the characteristic earthquake model, inter-regional multi-segment ruptures were also taken into account and configured as branches ((a)+(b), (b)+(c) and (a)+(b)+(c)). With regard to the position of large slip area in (c), branches were configured for those "anywhere" which varies within the region, and those "fixed" which is the same position as the 2011 Tohoku earthquake, each time.

(2) Magnitude distribution (distribution of mean stress drop)

With regard to the multi-segment rupture type earthquakes ((a)~(d)), In the case of the characteristic earthquake model, magnitude distribution was computed based upon mean stress drop and region area. Also, in the G-R model, based upon M_W computed from the area of each region where mean stress drop was 3MPa ((a): M_W8.8, (b): M_W8.7, (c): M_W9.0, and (d): M_W8.7), three branches were set for the magnitude range: up to M_W for (c) (M_W8.7~9.0), up to M_W for (b)+(c) (M_W8.7~9.2), and up to M_W for (a)+(b)+(c) (M_W8.7~9.3).

The largest historical M_W was taken into account for tsunami earthquakes (JTT) and normal fault earthquakes within the oceanic plate (JTNR) in configuring the magnitude distribution.

(3) Fault models

With regard to the multi-segment rupture type earthquakes ((a)~(d)), the characterized tsunami source model was used that configured large slip area and super large slip area based upon the approach presented in Cabinet Office (2012a). However, for the branch for "fixed in the Miyagi Prefecture offing" for (c), a model was used that reproduced the 2011 Tohoku earthquake according to Cabinet Office (2012b). A fault model, which was the same as that in Japan Society of Civil Engineers (2011), was used for the tsunami earthquakes (JTT) and normal fault earthquakes within the oceanic plate (JTNR).

(4) Mean recurrence interval

• Tokachi-oki to Nemuro-oki: region (a)

A frequency of one in six times for a multi-segment rupture in the area of the Tokachi-oki and the Nemuro-oki (the Japan Society of Civil Engineers, 2011), and a mean recurrence interval of 72.2 years for the area of the Tokachi-oki and the Nemuro-oki as postulated by the Headquarters for Earthquake Research Promotion (2004) were taken into consideration to set the mean recurrence interval at 430 years. Moreover, branches were configured for the possibility and the frequency of including tsunami earthquake regions.

• Northern Sanriku-oki: region (b)

The mean recurrence interval of interplate earthquakes in the northern area of Sanriku-oki was set at 97 years based upon the history of the past four occurrences (in 1677, 1763, 1856, and 1968), and the frequency of including tsunami earthquake regions was postulated so that it would be the same as the mean recurrence interval of (c).

• Central Sanriku-oki to Ibaraki Prefecture-oki: region (c)

A mean recurrence interval of 600 years was applied, which was for the past five earthquakes postulated by the Headquarters for Earthquake Research Promotion (2011). Branches for the frequency of including tsunami earthquake regions were configured on the

assumption that multi-segment ruptures, in four occurrences other than in 2011 out of the records of the past five occurrences, might occur four, one, and zero times.

• Ibaraki Prefecture-oki to Boso-oki: region (d)

The mean recurrence interval was set at the same as that for (c) as well as one-third of this level.

• Inter-regional multi-segment ruptures: (a)+(b), (b)+(c) and (a)+(b)+(c)

It was assumed that inter-regional multi-segment ruptures would occur one every three times each earthquake would occur. The mean recurrence interval for (a)+(b) was set based on the mean recurrence interval for (a), the mean recurrence interval for (b)+(c) was set based on the mean recurrence interval for (c), and the mean recurrence interval for (a)+(b)+(c) was set on the assumption that it would occur one in every three times that an inter-regional multi-segment rupture occurred for segments (b)+(c).

• Tsunami earthquakes: JTT

Although the Headquarters for Earthquake Research Promotion (2011) stated that tsunami earthquakes (JTT) have occurred four times in a period of 412 years (in 1611, 1677, 1896, and 2011), there is also the point of view that the 1611 tsunami was caused by a normal fault earthquake within the oceanic plate, so a branch was configured for the 1611 tsunami. For the branch where the 1611 tsunami caused by “the normal fault earthquake”, a mean recurrence interval of 100 years was set based upon the four occurrences during a period of 412 years, and a branch was configured from the section for reliability of Poisson variables. For the branch where the 1611 tsunami caused by “the tsunami earthquake”, it was configured as three occurrences during a period of 412 years.

• Normal fault earthquakes within oceanic plates: JTNR

The Headquarters for Earthquake Research Promotion (2011) stated that there was one normal fault earthquake within the oceanic plate (JTNR) that occurred during a period of 412 years. For the branch where the “1611 tsunami caused by a tsunami earthquake”, a mean recurrence interval of 410 years was set based upon one occurrence during a period of 412 years, and a branch was configured from the confidence interval of Poisson variables. For the branch where the ng a period of 412 years, normal earthquake, variables. For the branch where the occurrences during a period of 412 years.

• G-R model

As shown in Table 7.1-1, the number of M7.9 or greater earthquakes along the Japan Trench has been computed to be six with the exception of tsunami earthquakes during the period of 412 years since 1600. As shown in Figure 7.1-2, when the b value in the modified G-R equation is 0.9 and the maximum magnitude M9.3, the mean frequency is estimated to be 0.002224 = 1/450 (year) for M8.7 or greater.

(5) Error standard deviation and truncation threshold

For the error standard deviation and truncation threshold, in addition to a branch based on Japan Society of Civil Engineers (2011) (κ=1.25~1.55, truncation $\pm 2.3\beta$, $\pm 10\beta$), a branch was configured based on the results of the examination described in Appendix volume 5.1 (κ=1.3, 1.4, truncation $\pm 3\beta$).

(6) Logic trees and branch weights

Figures 7.1-3 through 7.1-15 show the logic trees constructed based upon the aforementioned approach. Branch weights were configured based upon Table 5.2.4-1 in the main volume and the 7.1-3 through 7.1-15 show the logic trees constructed based upon the aforementioned approach.

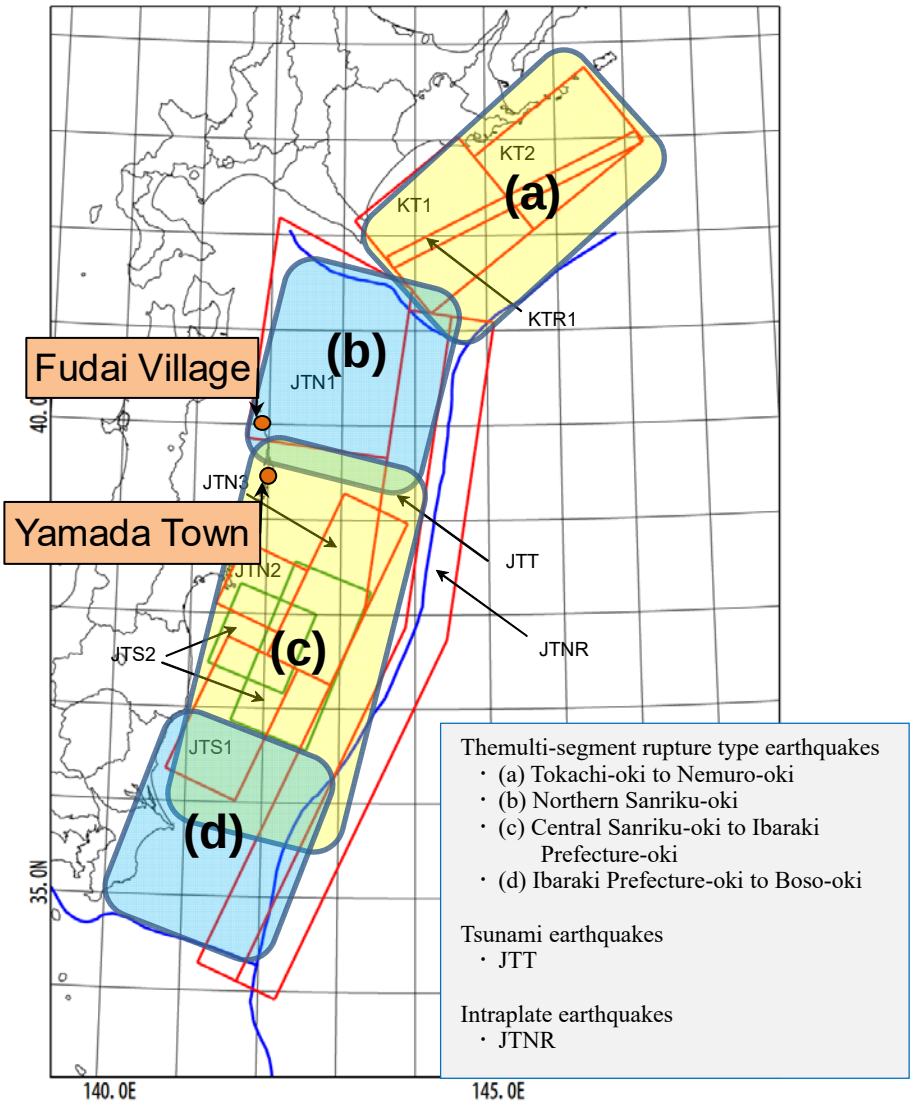

Figure 7.1-1 The target points and tsunami source regions

Table 7.1-1 Interplate earthquakes which occur in 412 years from 1600 to 2011(except tsunami earthquakes) (The Headquarters for Earthquake Research Promotion, 2011)

No.	Earthquake area	Occurrence date	Earthquake scale(M)
1	Northern Sanriku-oki	1677/4/13	$7_{3/4}$ ~ 8.0
2	Northern Sanriku-oki	1763/1/29	7.9
3	Northern Sanriku-oki	1856/8/23	7.8 ~ 8.0
4	Northern Sanriku-oki	1968/5/16	8.3 (M_W)
5	Southern Sanriku-oki closer trench	1793/2/17	7.9
6	Tohoku-oki	2011/3/11	9.0 (M_W)

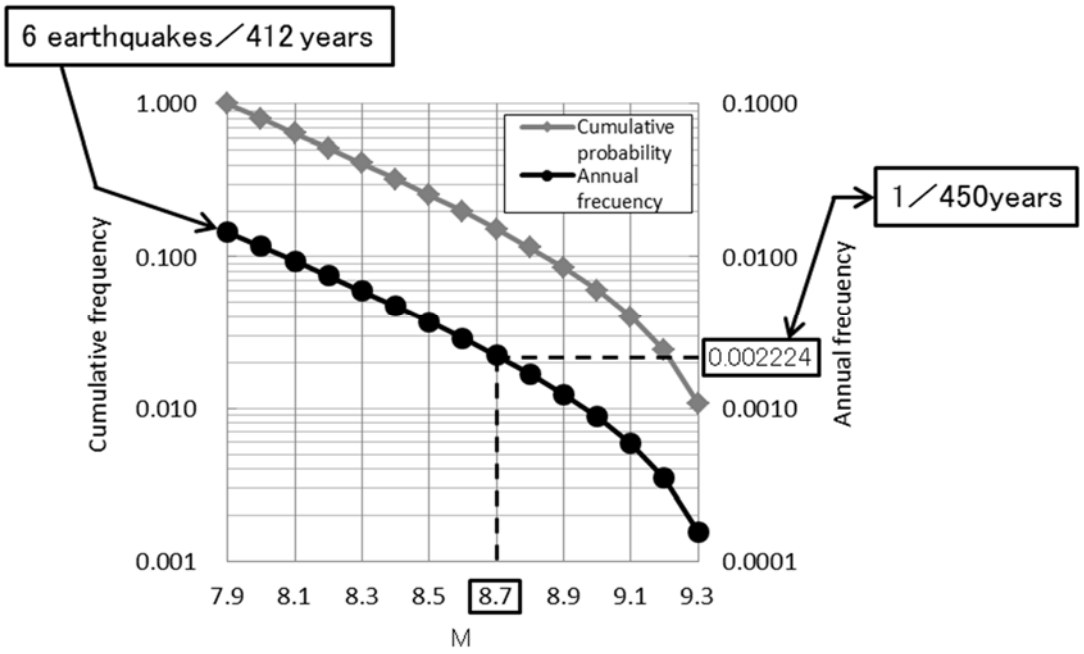

Figure 7.1-2 The results that applied modified G-R equation upper limit M9.3 to interpolate earthquakes along Japan trench

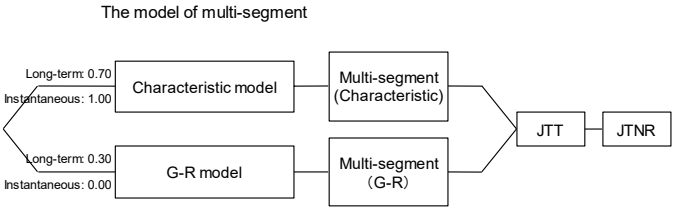

Figure 7.1-3 The basic structure of logic tree for all tsunami sources

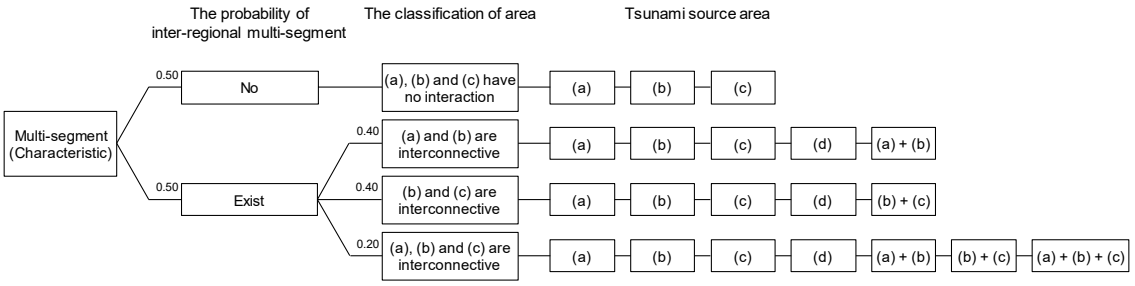

Figure 7.1-4 The logic tree of characteristic earthquake model (branches regarding inter-regional multi-segment rupture type earthquakes)

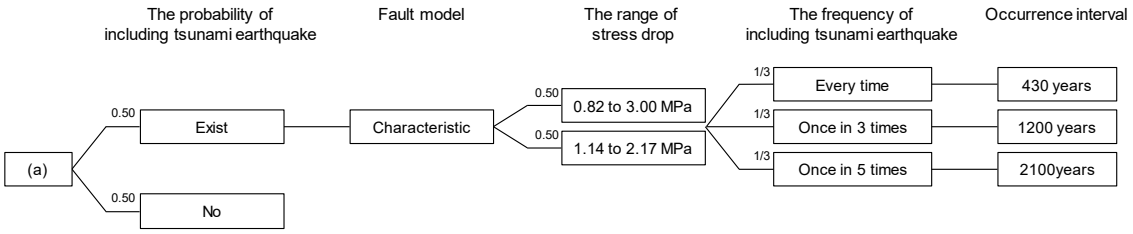

Figure 7.1-5 The logic tree of region (a)

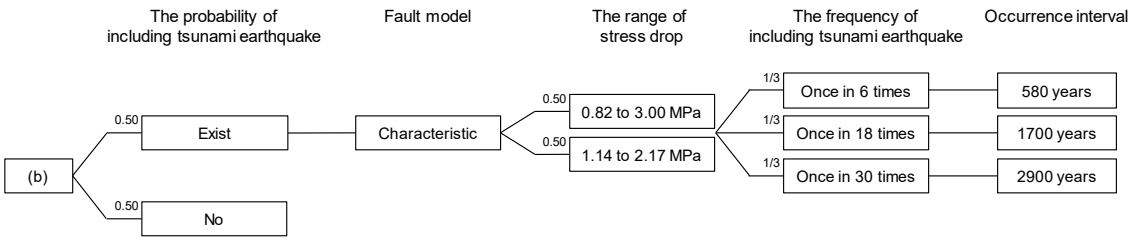

Figure 7.1-6 The logic tree of region (b)

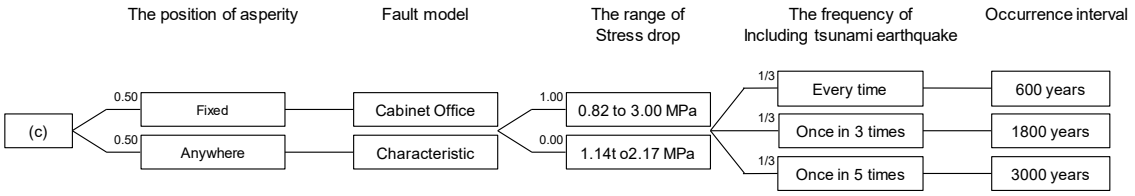

Figure 7.1-7 The logic tree of region (c)

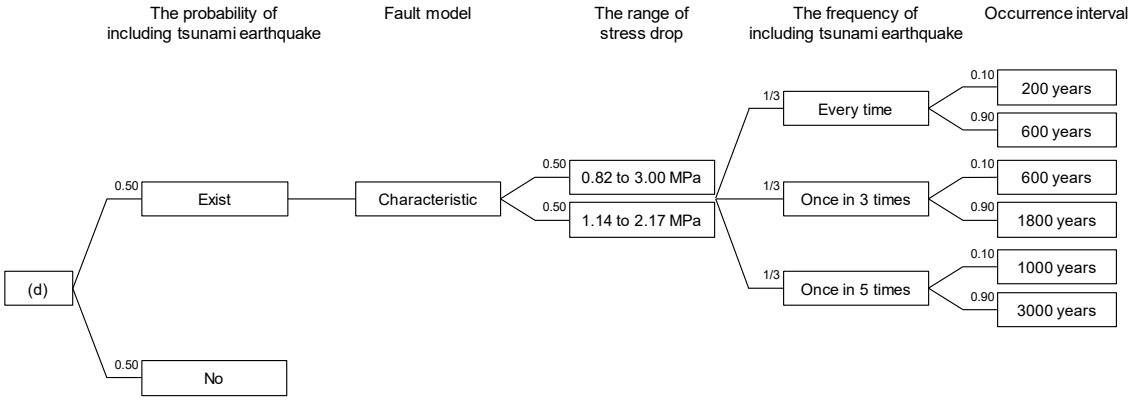

Figure 7.1-8 The logic tree of region (d)

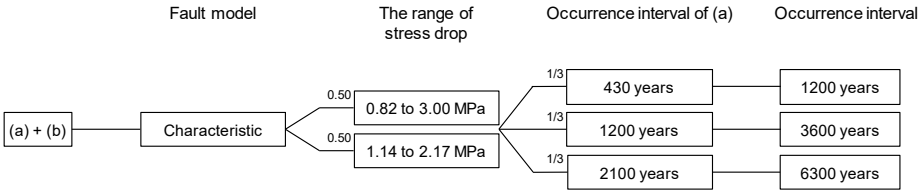

Figure 7.1-9 The logic tree of (a)+(b)

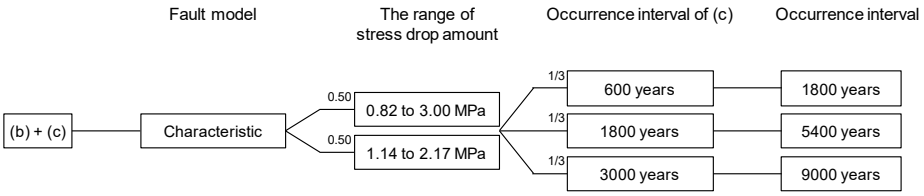

Figure 7.1-10 The logic tree of (b)+(c)

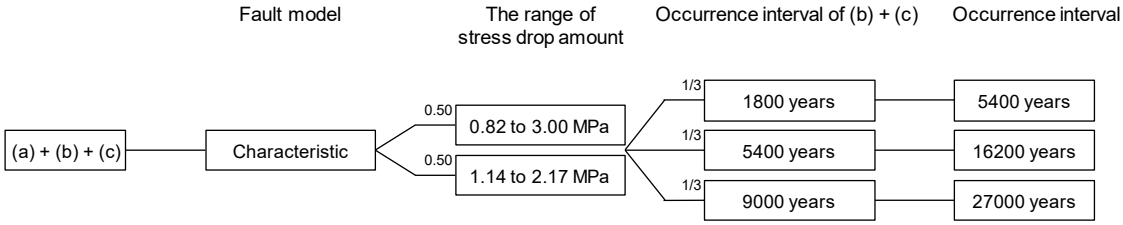

Figure 7.1-11 The logic tree of (a)+(b)+(c)

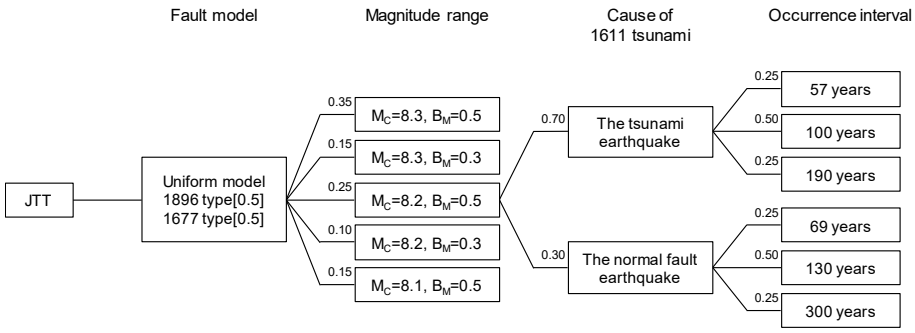

Figure 7.1-12 The logic tree of JTT

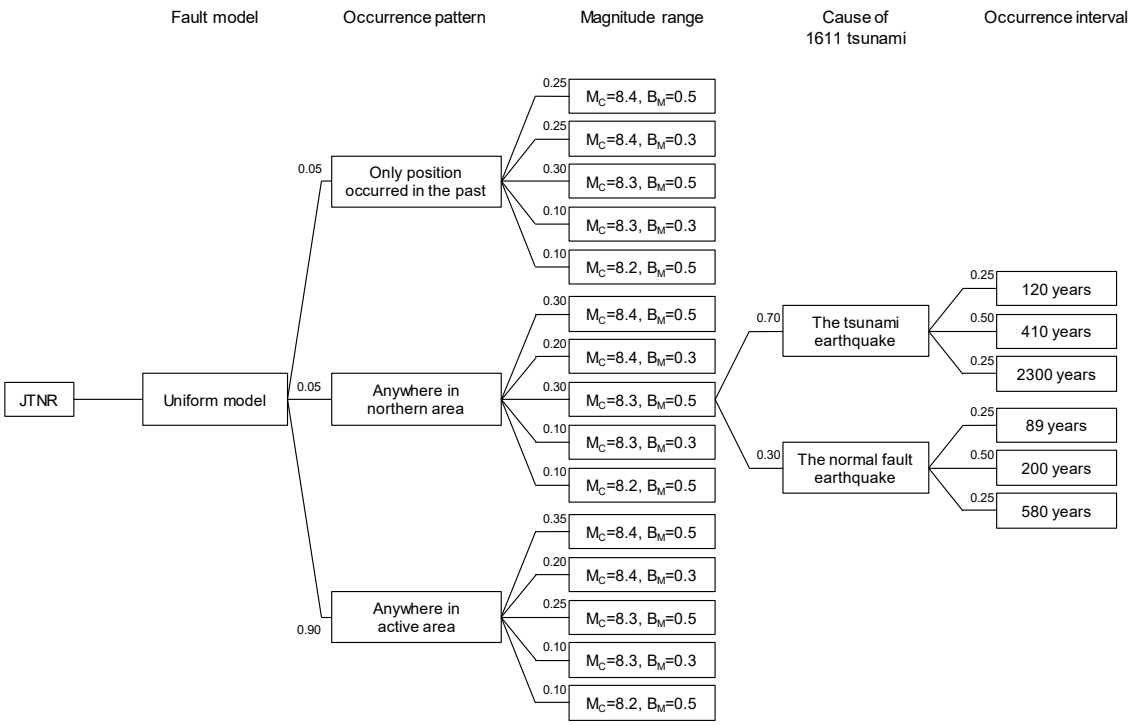

Figure 7.1-13 The logic tree of normal fault earthquakes within oceanic plate (JTNR)

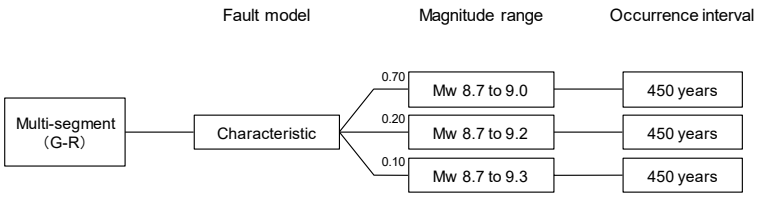

Figure 7.1-14 The logic tree of G-R model

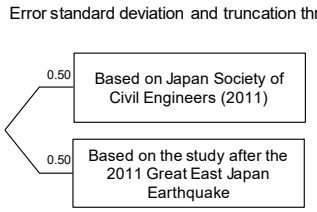

(a) The branch for disperison and censoring threshold

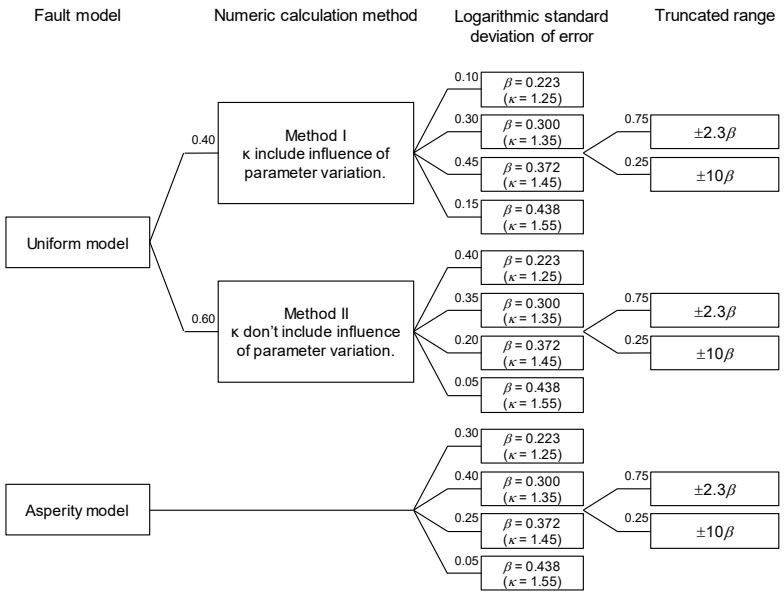

(b) The logic tree based on the Japan Society of Civil Engineers (2011)

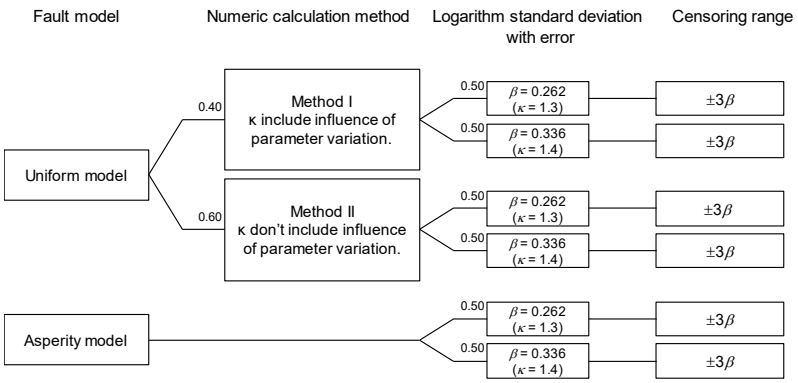

(c) The logic tree based on the study after the 2011 Tohoku earthquake

Figure 7.1-15 The logic tree for disperison and censoring threshold

7.2. Examples of analyses

Examples of analyses using the G-R model are shown.

(1) Calculation of earthquake probability

The G-R model is taken into consideration only in long-term assessments. When a Poisson process is assumed, the annual probability of an earthquake occurring in a case where the mean recurrence interval is 450 years is 1 - exp (-1/450) = 0.002220.

With the G-R model, the earthquake probability differs according to each magnitude. Table 7.2-1 shows the M_W-specific probability for each branch in the magnitude range as calculated using the modified G-R equation.

(2) Calculation of tsunami height distribution

1) Implementation of numerical tsunami simulations

Tsunami simulations were carried out to obtain tsunami height at target points. In the G-R model, the position of tsunami sources and large slip areas were moved without being constrained by regional divisions.

Figure 7.2-1 shows examples of the positions of tsunami sources for M_W9.0 earthquakes. Calculation grids are given in Figure 7.2-2. Figure 7.2-3 shows the relationship between tsunami height and M_W obtained through tsunami simulations.

2) Conversion to probability of exceedance

The exceedance probability of water level was calculated using the tsunami heights for each tsunami sources obtained in section 1). Table 7.2-2 shows examples of calculations of the annual probability of exceeding tsunami height 5m on a branch where M_W8.7~9.0, κ=1.25, and truncation threshold $\pm 2.3\beta$. When this calculation is performed in various tsunami height conditions, one tsunami hazard curve, which is shown in Figure 7.2-4, was obtained.

(3) Development of a tsunami water level hazard curves

When the aforementioned calculation is performed for all branches, a hazard analysis is completed for one tsunami source region. In the case of the G-R model, the total number of branches is 3×(4×2+2×1) = 30, so the number of hazard curves is 30. The results of calculations for all branches are given in Figure 7.2-5.

(4) Development of a fractile hazard curves

The weight of each hazard curve is given as the product of the weights of each branch. Statistical processing gives the fractile hazard curves and the arithmetic mean hazard curve as

shown in Figure 7.2-6.

Table 7.2-1 Conditional probability of M_W in each branch of M_W range (b value=0.9)

M_W	M_W8.7~9.0	M_W8.7~9.2	M_W8.7~9.3
8.7	0.3322	0.2630	0.2445
8.8	0.2700	0.2138	0.1987
8.9	0.2195	0.1738	0.1615
9.0	0.1784	0.1413	0.1313
9.1	-	0.1148	0.1067
9.2	-	0.0933	0.0867
9.3	-	-	0.0705

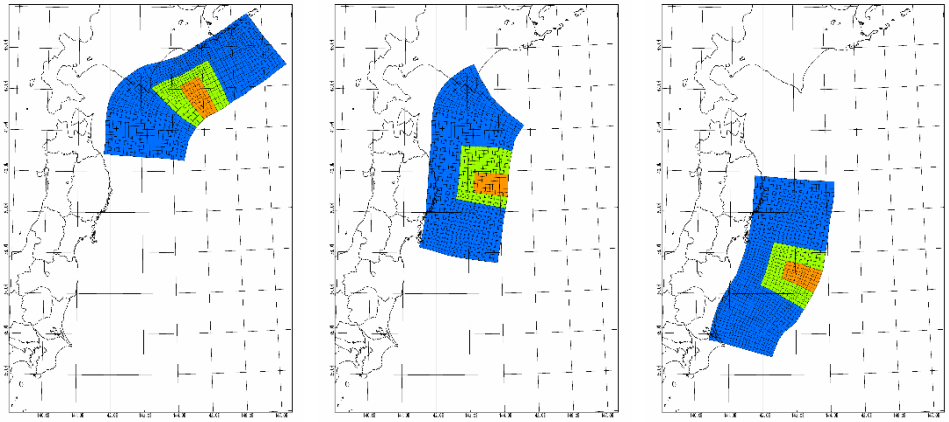

Figure 7.2-1 The examples of tsunami sources (extract from all M_W9.0 tsunami sources)

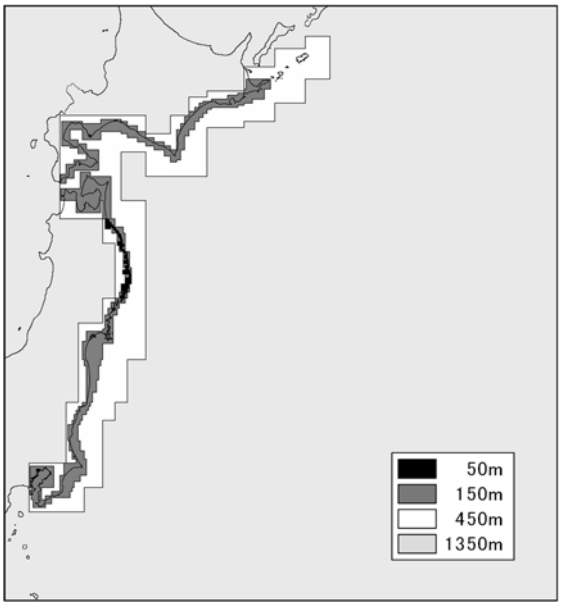

Figure 7.2-2 Grid size distribution in the computational region

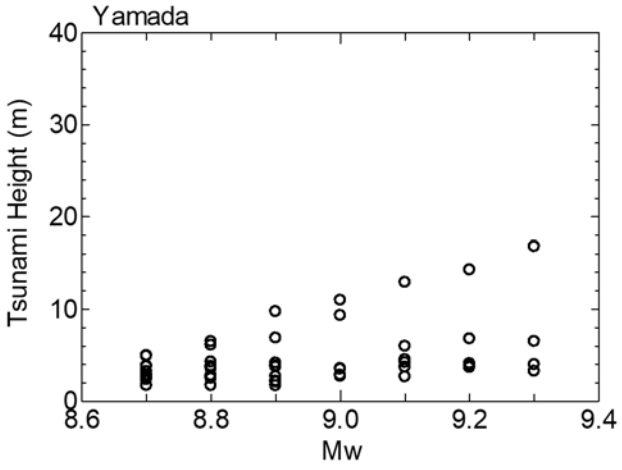

Figure 7.2-3 Example of correlation of M_W and tsunami height

Table 7.2-2 Examples for annual probability of exceeding tsunami height 5m (The branches of M_W8.7~9.0, κ=1.25, truncation threshold=±2.3β)

M_W		Calculated tsunami height (m)	Probability of exceeding 5m	Probability of exceeding 5m by an earthquake	Annual probability of exceeding 5m
8.7	1	1.703	0.0000	× 1/13 × 0.3322	× 0.002220
	2	2.356	0.0000		
	3	2.504	0.0000		
	4	2.555	0.0000		
	5	3.781	0.0965		
	6	2.595	0.0000		
	7	3.220	0.0139		
	8	4.918	0.4696		
	9	4.971	0.4894		
	10	3.838	0.1096		
	11	3.184	0.0111		
	12	2.886	0.0000		
	13	2.793	0.0000		
8.8	1	1.709	0.0000	× 1/11 × 0.2700	
	2	2.613	0.0000		
	3	2.492	0.0000		
	4	2.799	0.0000		
	5	4.270	0.2340		
	6	3.807	0.1024		
	7	6.492	0.8874		
	8	6.097	0.8198		
	9	3.541	0.0514		
	10	3.640	0.0681		
	11	2.694	0.0000		
8.9	1	2.085	0.0000	× 1/9 × 0.2195	
	2	2.205	0.0000		
	3	2.701	0.0000		
	4	3.866	0.1162		
	5	6.870	0.9321		
	6	9.757	1.0000		
	7	4.159	0.1981		
	8	3.736	0.0869		
	9	1.697	0.0000		
9.0	1	2.839	0.0000	× 1/7 × 0.1784	
	2	2.763	0.0000		
	3	3.564	0.0551		
	4	9.329	1.0000		
	5	10.984	1.0000		
	6	3.487	0.0434		
	7	2.708	0.0000		
			Summation	0.1939	0.1939×0.002220 = 0.000430

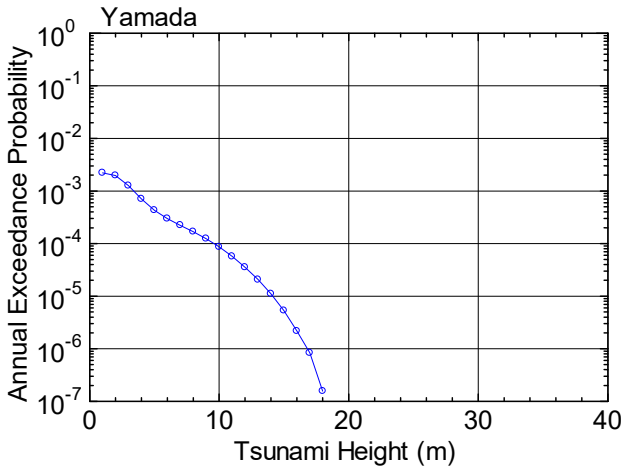

Figure 7.2-4 The hazard curve for M_W8.7~9.0, κ=1.25, truncation threshold=±2.3β

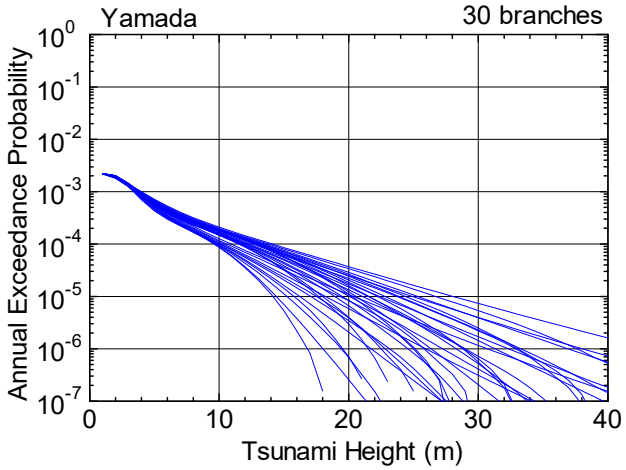

Figure 7.2-5 Group of the hazard curves

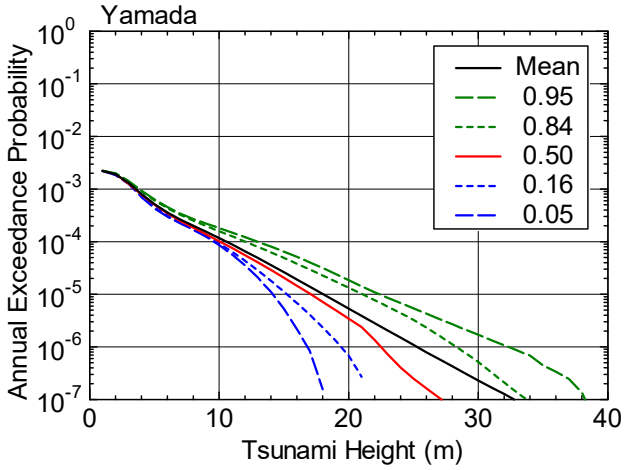

Figure 7.2-6 The fractile hazard curves and arithmetic mean hazard curve

7.3. Analysis results

Instantaneous assessment (January 1, 2016) and a long-term average assessment were performed for all tsunami sources. Table 7.3-1 shows the method for calculating the earthquake probability for each tsunami source region. The results of the assessment for all tsunami sources were computed by the Monte Carlo method.

Figure 7.3-1 shows each result from the instantaneous assessment and the long-term average assessment, and the comparisons between two arithmetic means in both assessments. In comparing the arithmetic means, the arithmetic mean for the long-term average assessment was converted into an exceedance probability in fifty years. From the comparison, no significant difference was seen at Fudai Village, but the exceedance probability in the long-term average assessment was higher at Yamada Town. In Figure 7.3-2, arithmetic mean hazard curves are shown for each tsunami source in the long-term average assessment. These figures show that the tsunami earthquakes (JTT) are dominant at Fudai Village, and the multi-segment earthquakes are dominant at Yamada Town. The probability of tsunami earthquakes (JTT) was calculated using the Poisson process, so there was no difference in the long-term average assessment and instantaneous hazard analyses. On the other hand, the probability of multi-segment earthquakes was computed using a renewal process model, and, the 2011 Tohoku earthquake occurred, so the probability decreased in instantaneous assessment for the next 50 years. Consequently, differences such as those shown in Figure 7.3-1(c) have appeared.

Table 7.3-1 The calculation methods of earthquake occurrence probability

Tsunami source region	Calculation method of occurrence probability
(a)	Poisson process
(b)	Poisson process
(c)	Renewal process (BPT distribution) The newest occurrence date: 2011/3/11
(d)	Poisson process
(a) + (b)	Poisson process
(b) + (c)	Poisson process
(a) + (b) + (c)	Poisson process
Tsunami earthquakes (JTT)	Poisson process
The normal fault earthquakes within oceanic plate (JTNR)	Poisson process

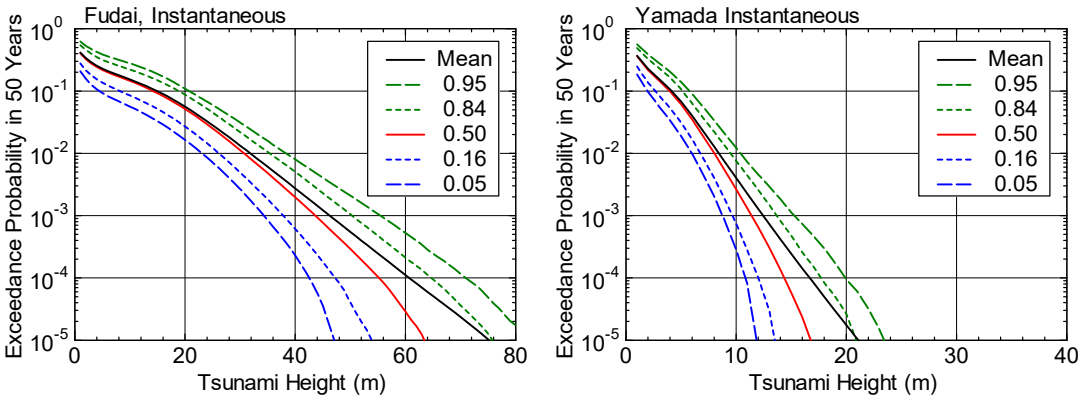

(a) The arithmetic mean and fractile hazard curves by instantaneous assessment

(Vertical axis: exceedance probability in fifty years)

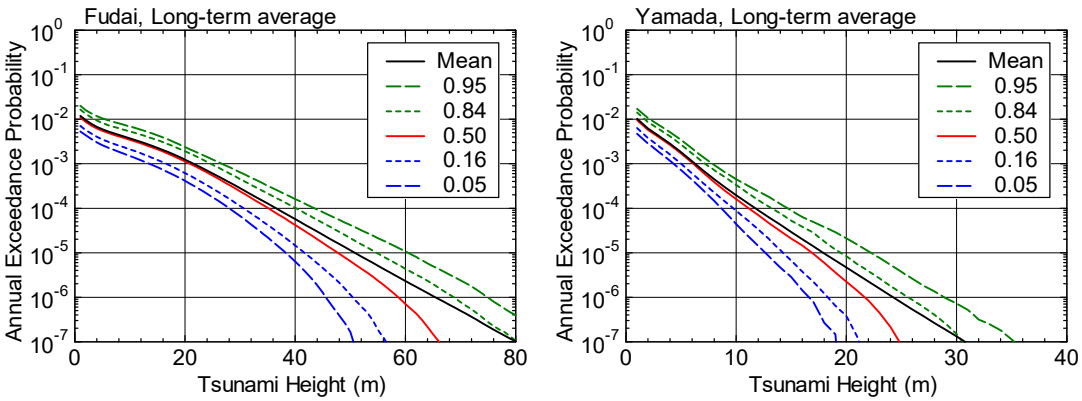

(b) The arithmetic mean and fractile hazard curves by long-term assessment

(Vertical axis: annual exceedance probability)

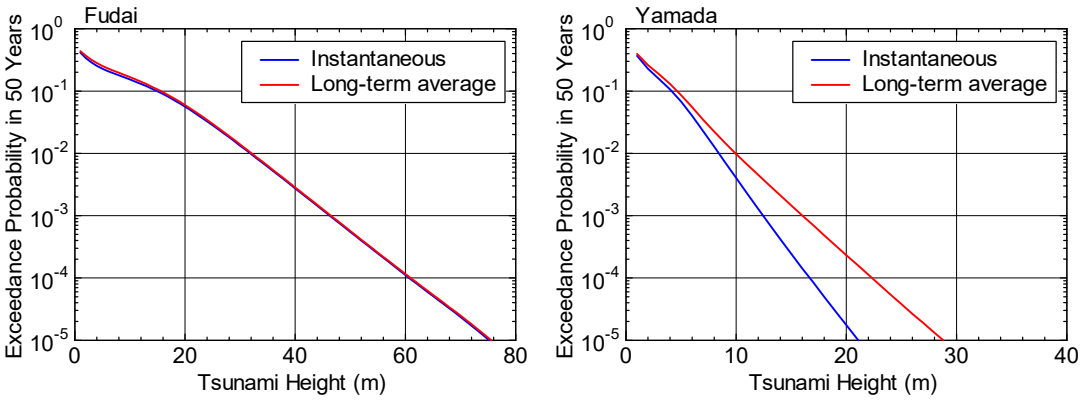

(a) The comparisons between instantaneous and long term average assessments

(Vertical axis: exceedance probability in 50 years)

Figure 7.3-1 The probabilistic hazard curves from Kuril Trench to Japan Trench

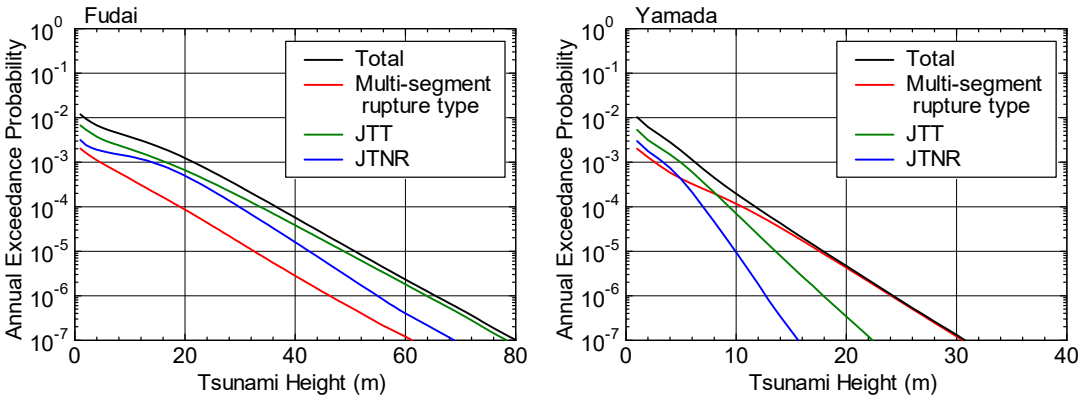

Figure 7.3-2 The arithmetic mean hazard curves according to tsunami sources by long-term average assessment

[Appendix 7 References]

Cabinet Office Nankai Trough Massive Earthquake Model Review Committee (2012a): Nankai Trough Massive Earthquake Model Review Committee (Second Report) Tsunami Fault Model Compilation: Tsunami Fault Models and Tsunami Height and Flooding Areas, etc. (in Japanese).
http://www.bousai.go.jp/jishin/nankai/model/pdf/20120829_2nd_report01.pdf (Accessed on August 2016).

Cabinet Office Nankai Trough Massive Earthquake Model Review Committee (2012b): Nankai Trough Massive Earthquake Model Review Committee (12th), Reference 1, Tsunami Fault Model for 2011 Tohoku earthquake (in Japanese).
http://www.bousai.go.jp/jishin/nankai/model/12/pdf/sub_1.pdf
(Accessed on August 2016).

Headquarters for Earthquake Research Promotion Earthquake Research Committee (2004): Long-Term Assessment of Earthquake Activity along Kuril Trench (in Japanese).
http://jishin.go.jp/main/chousa/04dec_chishima2/ (Accessed on August 2016).

Headquarters for Earthquake Research Promotion Earthquake Research Committee (2011): Long-Term Assessment of Earthquake Activity from Area Offshore of Sanriku to Area Offshore of Boso (Second Edition) (in Japanese).
http://www.jishin.go.jp/main/chousa/11nov_sanriku/
(Accessed on August 2016).

Japan Society of Civil Engineers Nuclear Civil Engineering Committee (2011): Methods of

Probabilistic Tsunami Hazard Analysis (in Japanese).
http://committees.jsce.or.jp/ceofnp/node/39 (Accessed on August 2016).

Mansinha, L. and D. E. Smylie (1971): The displacement fields of inclined faults, Bulletin of the Seismological Society of America, Vol. 61, No. 5, pp. 1433-1440.

Usami, T. (1996): Conspectus Japan Destructive Earthquakes, Tokyo University Publishing, 434p. (in Japanese).